Design Recommendations for Helical Pile Anchorages Subjected to Cyclic Load Reversals

Prepared for
Helical Piles and Tiebacks Committee

By

Sundar Chiluwal
M.S. candidate

&

Serhan Guner
Assistant Professor

The University of Toledo
Department of Civil & Environmental Engineering

COLLEGE OF ENGINEERING
THE UNIVERSITY OF TOLEDO

Sponsored by
Deep Foundation Institute (DFI)

August 2019

ACKNOWLEDGMENTS

The authors would like to thank the members of the Helical Piles and Tiebacks Committee for their feedback and support throughout this study.

DISCLAIMER

Executive Summary

Helical piles present a significant potential to create resilient, durable, and faster-to-construct foundations. Helical piles are anchored to concrete foundations with a termination bracket. Although significant research has been conducted on the cyclic-load behavior of helical piles, there is a lack of research on the helical pile anchorage zones. The current codes (e.g. ACI 318-2019, IBC-2018) have no specific design provisions for these zones. The anchorage zones are susceptible to concrete cracking when subjected to the uplift components of the cyclic loading, which may reduce the resiliency of the entire system or cause long-term durability issues.

The objective of this study is to understand and quantify the influence of anchorage zone detailing on the global behavior of concrete foundations and develop recommendations for their efficient design. Pile cap systems supported by helical piles are designed for this purpose. High-fidelity nonlinear finite element models are developed and experimentally verified with the results from nine large-scale helical foundation specimens. The verified models are employed to conduct ***162 response simulations*** for helical pile cap systems to quantify the influence of the anchorage conditions on the load, deformation, cracking, and failure behaviors. This study examines various combinations of ***bracket types*** (i.e., single, double, and studded brackets), ***embedment depths h_e*** (i.e., bottom, middle, and top for the single bracket; and bottom and middle for the studded bracket), ***longitudinal reinforcement percentages ρ_x*** (i.e., 0.2, 0.4 and 0.8%), and ***shear span to depth ratios a/d*** (i.e., 1.68, 1.42 and 1.11), and ***three loading types*** (i.e., monotonic tension, monotonic compression and reversed cyclic). The analysis of variance and the factorial design methods are employed to quantify the statistical significance of the changes in the simulation result due to the changes in the parameters examined. The simulation results, which inherently include the influence and failure modes of the helical pile anchorage zones, are compared with the traditional global analysis methods to assess the significance and consequences of considering or neglecting the anchorage zone behavior. The results are analyzed to identify the undesirable design configurations that result in anchorage zone failure and propose recommendation for their optimum design.

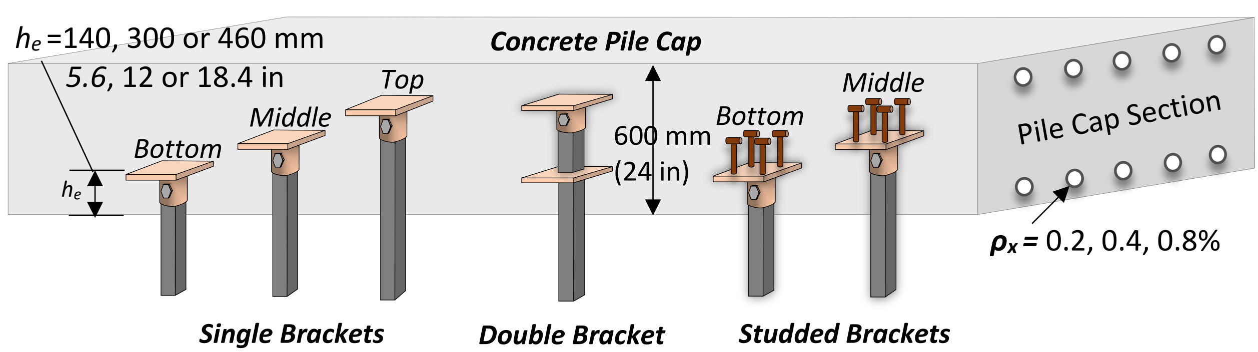

The results of the investigations demonstrate that the helical pile-to-foundation anchorages ***may govern the entire system capacity*** for the load conditions involving uplift and reversed-cyclic forces. ***The traditional global analysis methods***, which neglect the influence of the anchorage zones, are found to significantly overestimate the capacity of the helical foundations (***up to 2.2***

times in this study). ***These results justify the recommendation*** of performing an explicit capacity check of the anchorage zones in addition to the structural and geotechnical checks for the global foundation and helical pile capacities. The findings of this study are ***also applicable to micro piles*** which incorporate similar termination bracket details. Detailed conclusions and recommendations are provided below.

Monotonic and Cyclic Tension (subjected to uplift forces)

- The helical pile-to-foundation ***anchorage zone detailing*** significantly influences the global tensile capacity of the helical pile cap foundations.
- ***The tensile load capacities*** of the foundation systems (all of which are doubly and symmetrically reinforced) are found to be ***only 54%*** of their compression load capacities. If analyzed with the traditional sectional analysis methods, which neglect the influence of the anchorage zones, their load capacities in tension (i.e., a point load applied upwards) and compression (i.e., a point load applied downwards) would be incorrectly calculated as equal.
- Anchorage zone failure is predicted for ***the bottom h_e of the single bracket type***, with a decrease in the global load capacity by 25% on average. It is recommended that the middle h_e be used if the single bracket termination is to be used.
- The statistical analysis of the results indicates that the combination of ***low a/d ratios, high ρ_x, and the middle h_e*** yields the highest tension load capacity for the single bracket. These analyses also indicate that h_e dictates the effectiveness of ρ_x and *a/d* ratio. In other words, if larger tensile load capacities are desired, h_e should be changed from bottom to middle, as opposed to using the bottom h_e and increasing the ρ_x percentage or reducing the *a/d* ratio with hopes to increase the load capacity (which is not effective).
- **The double bracket type** has only one embedment depth which provides satisfactory responses with no anchorage zone failure in all simulations contained in this study.
- **The studded bracket type** has two h_e positions. While no anchorage zone failure is predicted, major anchorage zone cracking is observed for the bottom h_e. For the configurations involving the bottom h_e, the change of the bracket type from single to studded improves the foundation capacity by an average of 22%; consequently, the studded bracket may be preferred over the single bracket for the bottom h_e. For the most optimum results, however, the middle h_e is recommended for both the single and studded bracket types.
- Although ***the bottom h_e of the single bracket type*** demonstrated the least-favorable behavior, it can still be successfully used for resisting uplift forces if a special anchorage zone detailing is developed (e.g., sufficient amounts of vertical ties or stirrups in the anchorage zone). This recommendation is also applicable to the ***bottom h_e of the studded bracket type***.
- When designing the helical pile-to-foundation connections, special attention should be given to ***light and tall structures*** where one of the foundation load cases may be tensile in nature.

Monotonic and Cyclic Compression

- The helical pile-to-foundation anchorages are found to ***not influence the monotonic compression load capacity*** of the helical pile foundations in any of the bracket types examined; no anchorage failures are predicted.
- The statistical analyses show that ***the h_e parameter*** has no significant contribution on the monotonic compression capacity of the helical foundations.
- To maximize the load capacity, ***high ρ_x*** and ***low a/d ratios*** should be used for all bracket types.
- The compression capacity of the foundations examined are found, on average, to be ***1.85 times higher*** than their tension capacity. Consequently, particular attention should be paid to the connection design when there is a load case involving ***net uplift forces***.
- For the ***cyclic compression loading***, anchorage zone cracks and reduced load capacities (up to 10%) are predicted for ***the top h_e of the single bracket*** in some design configurations. It is recommended to ***follow the tension load recommendations*** (above) for the load cases involving cyclic load reversals.

Table of Contents

List of Figures

List of Tables

List of Variables

h_e	Embedment depth
ρ_x	Longitudinal reinforcement
a/d ratio	Shear span to depth ratio, which is either 1.68, 1.42, or 1.11
Tens.	Monotonic tension load
Comp.	Monotonic compression load
Cyc.	Reversed-cyclic load
T	Top embedment depth of 460 mm (18.1") for the bracket
M	Middle embedment depth of 300 mm (11.8") for the bracket
B	Bottom embedment depth of 140 mm (5.5") for the bracket
1.68 T	Helical pile with *a/d* ratio = 1.68 at top embedment depth (460 mm)
1.68 B	Helical pile with *a/d* ratio = 1.68 at bottom embedment depth (140 mm)
1.68 M	Helical pile with *a/d* ratio = 1.68 at middle embedment depth (300 mm)
P_u	Ultimate load capacity subjected to monotonic load
$P_{u\text{-}T/B}$	Ratio of P_u for the top embedment depth to that for the bottom embedment depth
$P_{u\text{-}M/B}$	Ratio of P_u for the middle embedment depth to that for the bottom embedment depth
P_t	Ultimate load capacity of the tensile curve of reversed-cyclic load
$P_{t\text{-}T/B}$	Ratio of P_t for the top embedment depth to that for the bottom embedment depth
$P_{t\text{-}M/B}$	Ratio of P_t for the middle embedment depth to that for the bottom embedment depth
P_c	Ultimate load capacity of the compression curve of reversed-cyclic load
$P_{c\text{-}T/B}$	Ratio of P_c for the top embedment depth to that for the bottom embedment depth
$P_{c\text{-}M/B}$	Ratio of P_c for the middle embedment depth to that for the bottom embedment depth
δ_u	Displacement capacity subjected to monotonic load
$\delta_{u\text{-}T/B}$	Ratio of δ_u for the top embedment depth to that for the bottom embedment depth
$\delta_{u\text{-}M/B}$	Ratio of δ_u for the middle embedment depth to that for the bottom embedment depth
δ_t	Displacement capacity of the tensile curve of reversed-cyclic load
$\delta_{t\text{-}T/B}$	Ratio of δ_t for the top embedment depth to that for the bottom embedment depth
$\delta_{t\text{-}M/B}$	Ratio of δ_t for the middle embedment depth to that for the bottom embedment depth
δ_c	Displacement capacity of the compression curve of reversed-cyclic load
$\delta_{c\text{-}T/B}$	Ratio of δ_c for the top embedment depth to that for the bottom embedment depth

$\delta_{c\text{-}M/B}$	Ratio of δ_c for the middle embedment depth to that for the bottom embedment depth
Stiff	Initial stiffness
Flexural	Flexural failure
Splt-brkt	Anchorage zone failure in tensile splitting
Bracket Infl.	Significant anchorage zone influence on the global foundation response

1. Introduction

1.1 Background

Tall and light structures such as power transmission towers, telecom towers, wind turbines, masts, and chimneys, have lower weight and experience significant cyclic loads due to wind, seismic, or vehicular traffic forces. These cyclic forces induce large overturning moments on the foundations. When the structure undergoes significant overturning, one end is subjected to compression and the other to tension forces (see **Fig 1-1**). The foundation design of such structures is typically governed by tensile demands due to the inherent weakness of the concrete in tension. Tensile uplift forces can also develop in the foundations because of hydrostatic pressure such as in submerged platforms, jetting structures, and underground water tanks. These uplift forces must be safely transmitted to the ground without creating foundation problems such as cracking, differential settlement, and excessive deformations.

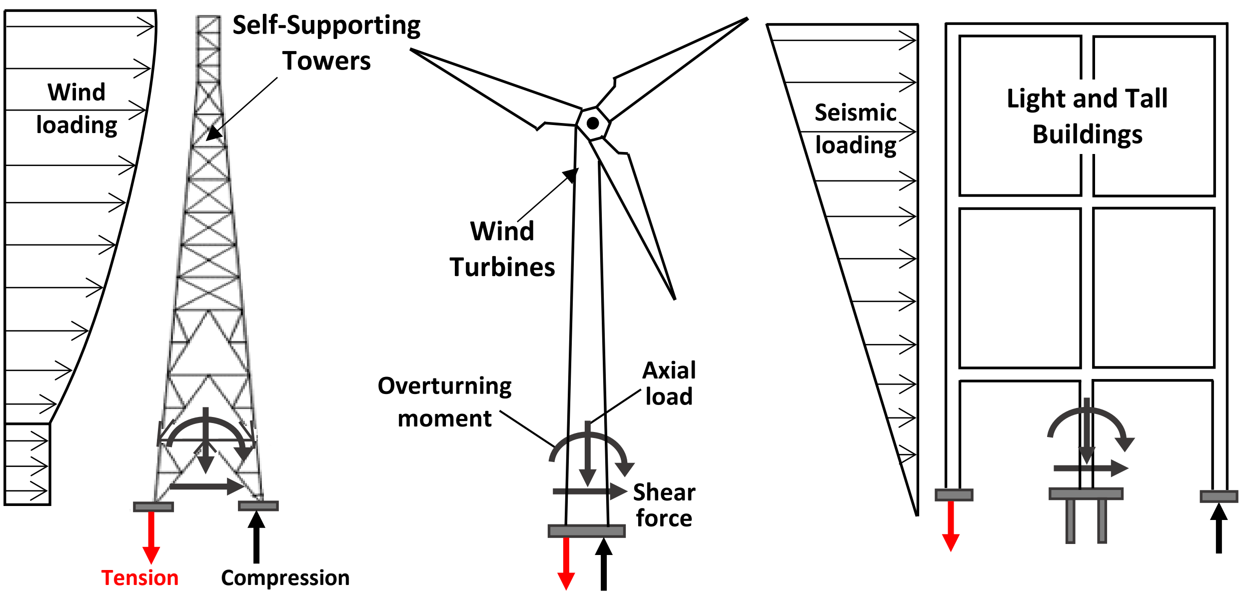

Figure 1-1: Tensile uplift force in a (a) Transmission tower subjected to wind load (Adopted from Guner and Carrière 2016), (b) Wind turbine subjected to wind load, (c) Residential building subjected to seismic load.

Helical piles (**Fig 1-2**) are typically used in these types of structures since they provide a cost-effective, practical, and resilient solution for resisting significant tension forces. Helical piles are generally connected to the superstructures through shallow concrete foundations such as pile caps, grade beams, where they are terminated with a steel bracket.

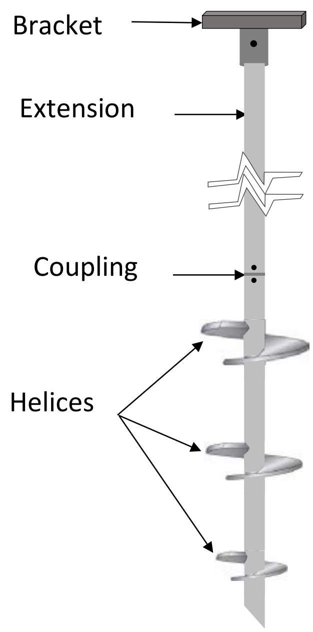

Figure 1-2: Helical pile anchored with the single bracket type.

1.2 Problem Statement

In order to develop the full potential of helical piles, it is imperative that helical pile-to-foundation connections are properly designed to resist the applied tensile loads. These connections should be able to resist major cyclic deterioration and develop the moment demands on the pile while remaining essentially rigid. Additionally, the distribution and the deformation of the concrete foundations may be influenced by these connection or anchorage zones. Ineffective anchorage zones will be susceptible to long-term cracking and deterioration subjected to cyclic loads. However, there is limited research and associated knowledge on the influence of pile-to-foundation anchorages on the holistic response of foundation systems. Consequently, helical pile anchorages are designed in practice with little confidence, using unproven approaches such as ‘assumed stress limits’ or ‘good engineering judgement.’

1.3 Research Objectives

The objective of this study is to understand the influence of pile anchorage conditions on the holistic behavior of helical foundations and develop preliminary design guidelines for the correct design of anchorage zones. The main focus will be the reversed-cyclic load conditions with reverse cycles applying net tensile uplift loads. The results of this study will demonstrate the behavior of commonly-used anchorage bracket types, indicate what bracket types are more suitable under what loading conditions, what design details should be avoided, and how the influencing parameters of the configurations affect the anchorage response. The research findings will also be applicable to micro pile-to-foundation anchorages owing to the use of similar termination brackets. The following specific tasks will be performed to achieve the objectives:

- One-way foundations (i.e., pile cap strips) will be designed to connect the helical piles with the steel column base to better isolate and understand the bracket response.
- The response of commonly-used bracket types will be investigated with an experimentally-verified numerical modeling method.
- The influence of design parameters (i.e., embedment depth, longitudinal reinforcement percentage, and shear span to depth ratio) on the load, deformation, cracking, and failure behavior of the entire foundation will be quantified in the presence of monotonic compression and tension and reversed-cyclic load conditions.
- The interaction among the parameters will be examined to quantify how the change in multiple design parameters affect the system capacity using statistical methods called the ANOVA and the factorial design.
- The capacity of the holistic helical foundations obtained from the numerical analysis will be compared with the traditional global concrete foundation checks (i.e., sectional flexure and shear checks) to assess the significance of considering/neglecting the anchorage zone behavior.

1.4 Report Outline

The report contains nine chapters and four appendices organized as follows.

Chapter 1 briefly introduces helical piles, discusses the potential issues with helical pile anchorages, and outlines the project objectives. Chapter 2 reviews the research literature and the limited past investigation on the helical pile anchorage zones. In addition, it reviews failure modes and load transfer mechanisms applicable to helical pile anchorage zones. Chapter 3 presents the design details of the helical foundations to be investigated numerically. Chapter 4 describes the 2D nonlinear finite element modelling (FEM) approach to simulate the different bracket types in the study. Chapter 5 provides the analysis detail for the numerical simulations in terms of load-displacement responses, crack patterns, and failure modes, and also compares the load capacities obtained from various design configurations. Chapter 6 presents the statistical methods (i.e., ANOVA and factorial design) to study the influence of the parameters examined in the study. Chapter 7 compares the helical foundation capacity with the traditional global concrete foundation checks (i.e., sectional flexure and shear) to assess the significance of considering/neglecting the anchorage zone behavior. Chapter 8 includes the conclusions and recommendations of this study. Chapter 9 lists the references cited.

Appendices A to C present the simulated response details for the single, double, and studded bracket types in terms of the load-displacement responses, failure modes, and crack patterns, respectively. Appendix D provides the design detailing and samples of the global concrete foundation checks performed.

2. Literature Review

2.1 Introduction

The objective of this chapter is to introduce the helical piles and investigate the past research carried out on the helical foundations (i.e., helical piles and concrete foundations). The related failure modes and load transfer mechanisms of deep foundations and headed anchors are discussed and can be of assistance in understanding the behavior of different anchorage conditions. The influencing parameters selected on this study are briefly explained at the end of the chapter.

2.2 Helical Piles

Helical piles are the steel foundation elements consisting of a shaft with one or more helical bearing plates and a termination bracket. They are also referred to as helical anchors, screw piles, helix piers, screw anchors, helical piers, torque piles, or torque anchors. A foundation system comprised of helical piles is called the *helical foundation*. Helical piles are commonly used for retrofitting existing structures, supporting tall, light, and overturning-moment-dominated structures, and creating new foundations for buildings and industrial structures.

2.3 Types of Helical Piles

The commonly used helical piles are available in round or square shapes. The square shapes have a solid cross-section, whereas the round shapes have tubular sections. The helical piles can be grouted to improve their properties (see **Fig 2-1**). If needed, the square pile can be connected with the round pile to make a hybrid pile.

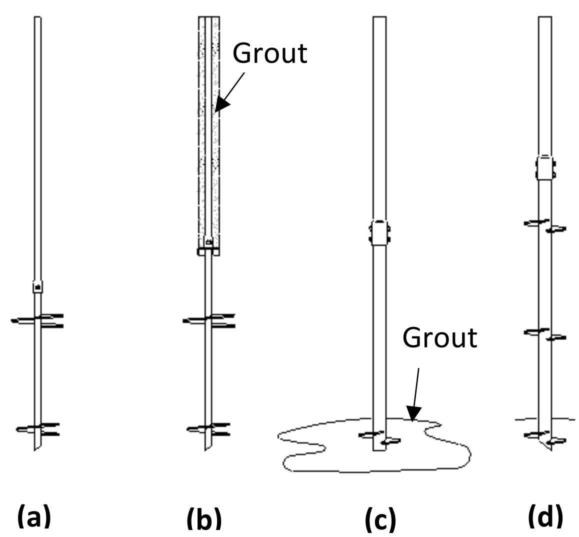

Figure 2-1: Helical piles (a) Square shaft (un-grouted); (b) Square shaft (grouted); (c) Round shaft (grouted); (d) Round shaft (un-grouted) (DFI 2014).

2.4 Components of the Helical Piles

The main components of a helical pile are helices (i.e., helical blades), a lead section (shaft), and extensions as shown in **Fig 2-2**. The helices are driven to the required bearing layer of soil with the help of a torque motor, using a number of extensions.

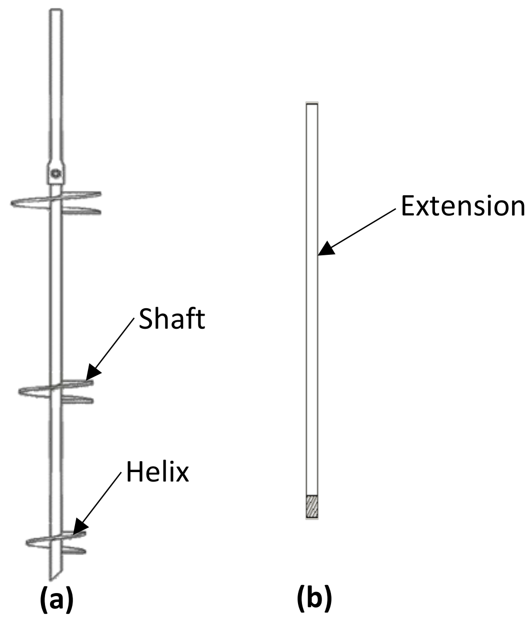

Figure 2-2: Components of a helical pile (a) Triple helix lead section; (b) Helical extension section (DFI 2014).

2.5 Research on Helical Piles and Concrete Foundations

Current studies are limited to the individual checks of the helical piles and the concrete foundations (e.g., pile caps, grade beams) without considering the influence of the anchorages.

The geotechnical literature focuses on the axial load behavior of isolated piles and consistently demonstrates the suitability of helical piles for axial loads, namely, tensile loads (e.g., Elkasabgy and El Naggar 2013, Cerato and Victor 2009, and Livneh and El Naggar 2008) and compressive loads (e.g., Elsherbiny and El Naggar 2013, and Pack 2009). There is intensive research to increase the capacity of the helical piles. New techniques are developed to increase the capacity of the helical piles such as grouted piles where cement grout around the pile shaft is introduced to increase the axial capacity (Vickars and Clemence 2000), steel fiber-reinforced grout shaft where steel fiber is added to the grout to increase the ductility capacity (El Sharnouby and El Naggar 2012), and grouted shaft enclosed in FRP tube to increase the overall pile performance (Sakr et al. 2004). The structural literature, on the other hand, exclusively focuses on the behavior of supported traditional pile caps subjected to compression (e.g., Cao 2009, Suzuki et al. 1998, Suzuki and Otsuki 2002, Suzuki et al. 2000, Otsuki and Suzuki 1996, and Adebar et al. 1990). Both the geotechnical and structural literature is lacking in accounting for the influence of the helical pile-to-foundation connections for uplift load conditions.

2.6 Research on Helical Pile Connectors for Retrofitting

The available research is limited to the retrofitting of the existing foundations. Existing foundations are connected externally with special connectors using bolts. Available research includes monotonic and cyclic lateral behavior of specialized connectors (El Naggar et al. 2007), numerical investigation of the response of expansion anchors used to attach helical pile connectors to concrete foundation (Sharnouby and El Naggar 2010), and the experimental testing of eight foundations with two types of connectors (i.e., with and without uplift brackets) under various load conditions (Youssef et al. 2006).

2.7 Anchorage Brackets for the New Foundation Constructions

Helical piles are terminated with a bracket/plate which is cast inside concrete foundations (i.e., shallow foundations, pile caps or grade beams) as shown in **Fig 2-3**. The bracket types are used to safely transfer vertical tension or compression loads from the new foundation construction to the helical piles by reducing the bearing stress induced in the helical pile shaft. There are different bracket types on the market that are available in the termination of the helical piles. Some of the commonly used bracket types are shown in **Fig 2-4**.

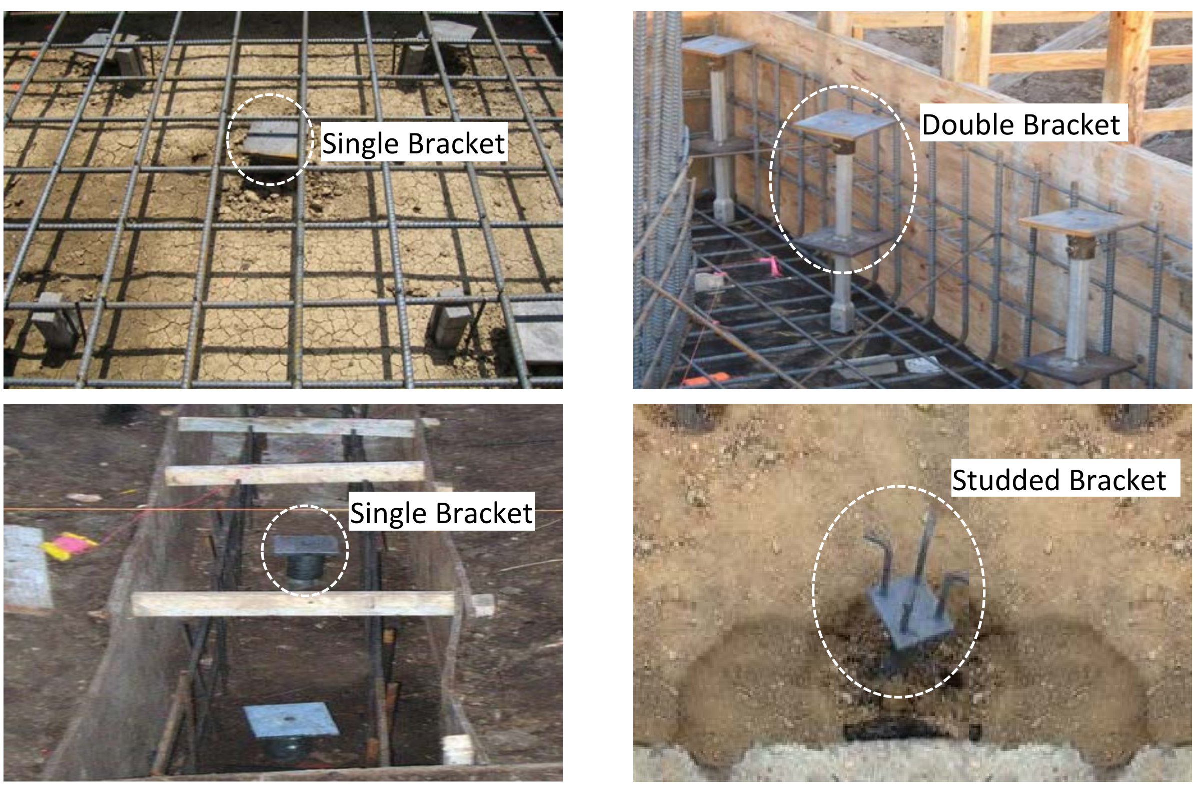

Figure 2-3: Anchorage of helical piles (Supportworks 2018).

Bracket types as shown in **Fig 2-4** are welded to a sleeve. The sleeve can be with or without the bolt holes. The sleeve without the bolt is welded directly to the helical shaft. The presence of bolts depends upon the type of loads the foundation is subjected to.

2.8 Helical Pile Anchorage Using New Construction Bracket

There is very limited research conducted on this topic. Pack (2009) investigated the bearing stresses of the concrete in front of the bracket and concluded that the ultimate bearing stress can be used as the safety limit as per the International Building Code (IBC 2018).

Labuda et al. (2013) performed a failure investigation of a helical anchor tie-down system supporting an Olympic size swimming pool where the brackets were welded to the helical shaft without the use of a sleeve. He found that the failure of the pool slab was due to the separation of the weld used to connect the helical shaft to the bracket and the crack lines propagated along the weld lines. He concluded that, even if the bracket to shaft connection had been constructed as per the original design (i.e., pinned connection using bolts), it still would have failed through other types of anchorage failures.

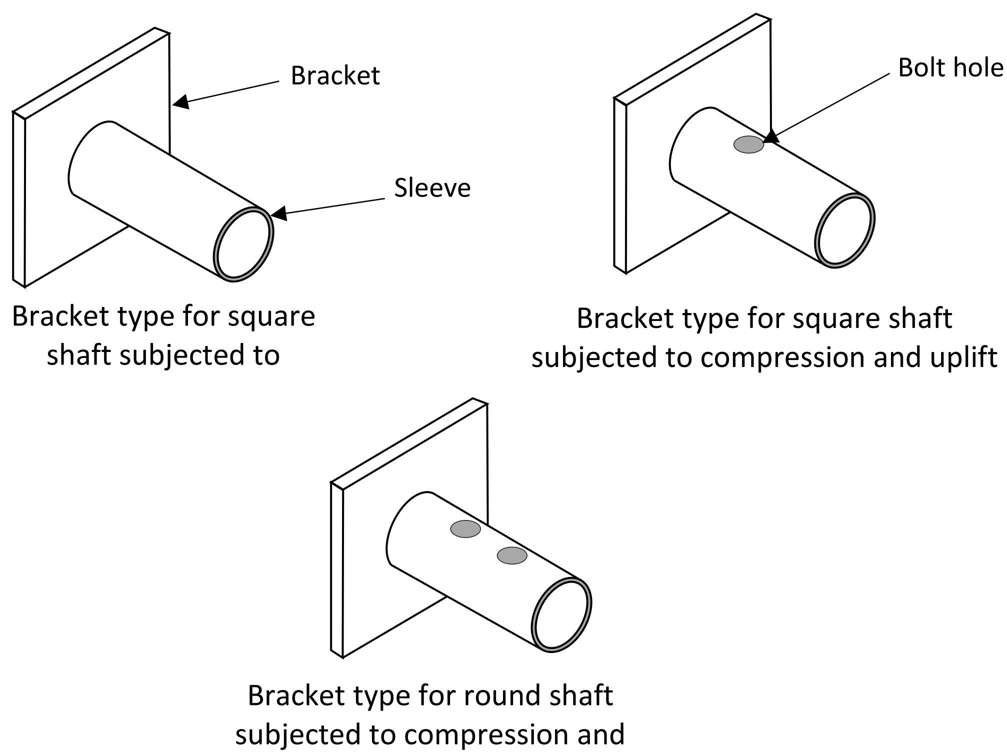

Figure 2-4: Commonly used bracket types in the new foundations construction.

Diab (2015) investigated helical piles with single bracket terminations, both experimentally and numerically. He found that the anchorage behavior is affected by the concrete compressive strength, pile embedment depth, beam reinforcement ratio, and pile cap detailing. All grade beams experienced a concrete breakout failure. Diab's study experimentally showed that the anchorage zones might govern the entire system response.

2.9 Failure Modes and Load Transfer Mechanisms

Most of the concrete foundations are deep in nature. The pile caps investigated in this research are deep beams; as such, it is necessary to investigate the shear failure mode and the load transfer mechanisms associated with it. The deep beam action may have some influence on the behavior of the anchorage conditions. A beam is classified as deep if its shear span to depth ratio (*a/d*) is smaller than 2.0 (see **Fig 2-5**).

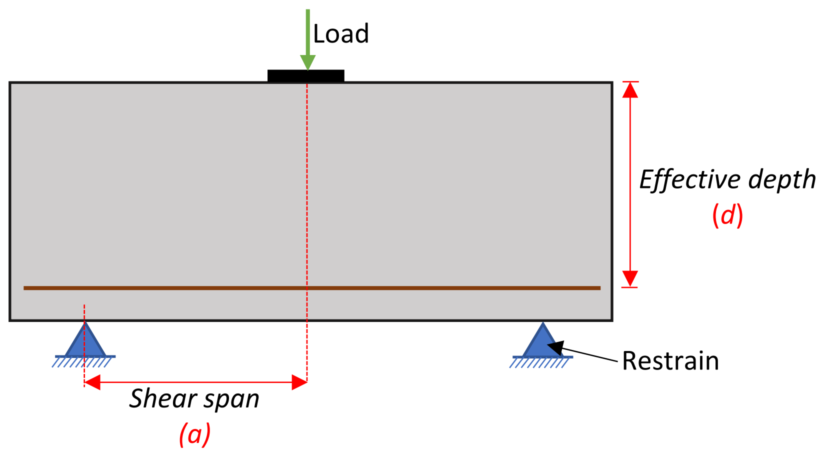

Figure 2-5: Shear span to depth depth ratio of a typical deep foundation.

Kani (1967) concluded that the shear strength of a beam increases with the decrease in the beam depth (see **Fig 2-6**). The shear capacity of the concrete depends upon the shear span to depth ratio, the longitudinal reinforcement percentage, and concrete tensile strength (MacGregor and James 2012). The failure mode of the deep beam could be either a shear-tension failure or shear compression failure after the initiation of a diagonal crack as shown in **Fig 2-7**. The presence of the longitudinal reinforcement increases the shear capacity of the beam due to dowel action.

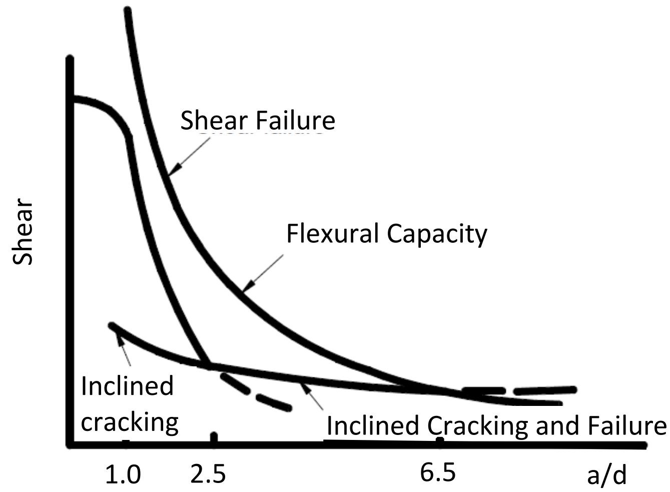

Figure 2-6: The effect of *a/d* ratio on the shear strength of beams without stirrups-shear at cracking and failure (Kani 1967).

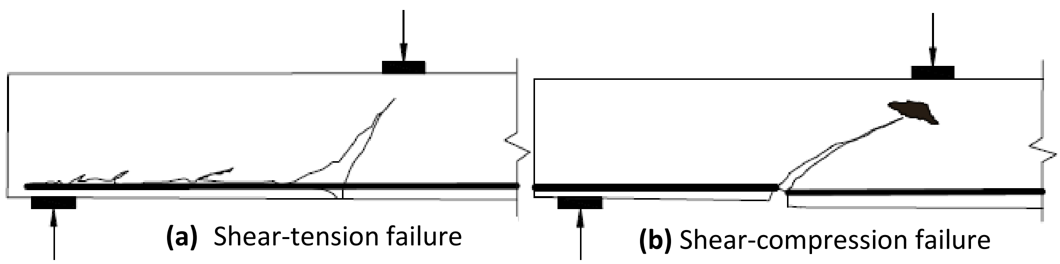

Figure 2-7: Modes of failures for deep beams with *a/d* ratio 1.5 to 2.5 (MacGregor and James 2012).

2.9.1 Headed Anchor Bolt Failure Modes Subjected to Tension Load

The helical piles act like the anchor bolts where the termination brackets behave similar to the headed anchor bolts. Anchor bolts can fail through different modes of failures when they are subjected to tensile load as shown in **Fig 2-8**.

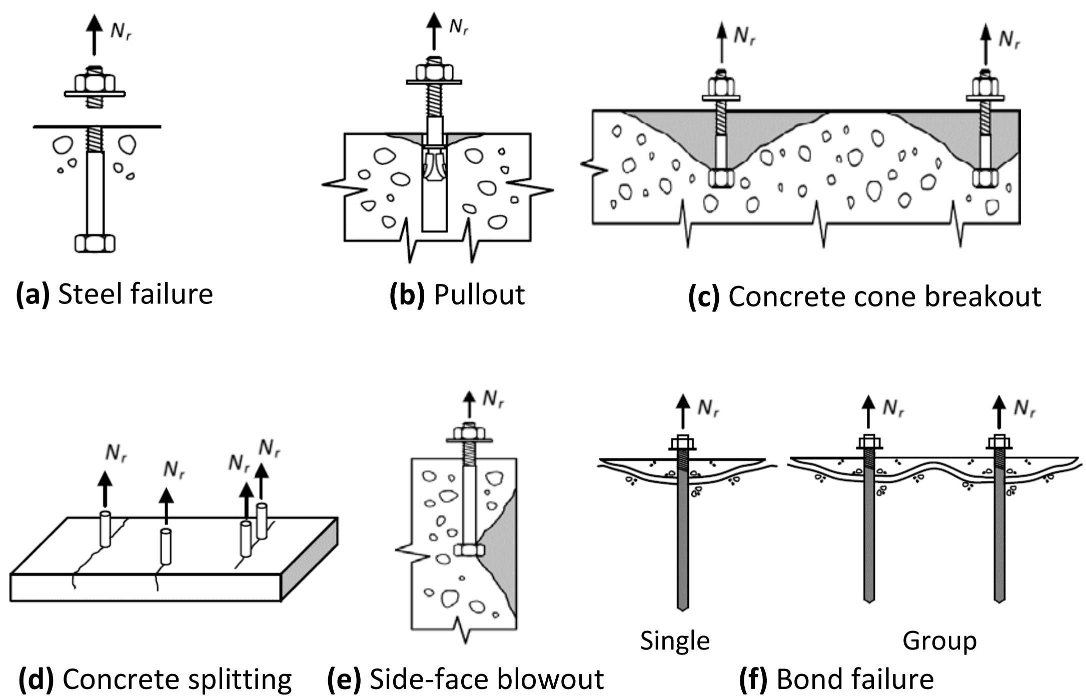

Figure 2-8: Failure modes of headed anchors subjected to tension load (ACI 318-19).

2.9.1.1 Steel Failure

When the applied load stresses the steel beyond its ultimate capacity, a steel failure occurs. The ultimate capacity of the steel depends upon the strength and the cross-sectional area of the steel. A headed anchor can yield in this manner when other modes of failures are prevented.

2.9.1.2 Pullout Failure

The pullout failure occurs due to the lack of sufficient frictional resistance, where an anchor slips out of the concrete with insignificant damage to the concrete. The pullout force depends upon the friction. Due to large termination brackets used in helical piles, this type of failure is not expected.

2.9.1.3 Concrete Cone Breakout Failure

Concrete cone breakout is a conical crack that originates from the tip of the anchor head and propagates towards the edge of the concrete due to tensile stress flow (see **Fig 2-8**). The angle of the cone varies from 35° to 45° depending on the embedment depth of the anchor bolt.

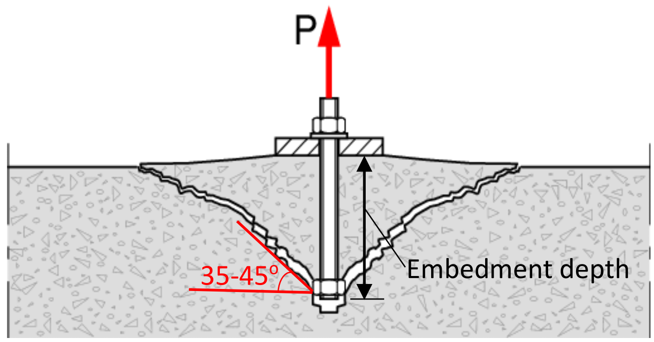

Figure 2-9: Concrete cone breakout failure subjected to tension load (Nilsson et al. 2011).

2.9.1.4 Concrete Splitting Failure

Concrete splitting failure occurs when an anchor is installed close to the edge of the concrete or the spacing between anchors is too small.

2.9.1.5 Side-Face Blowout Failure

When the headed anchors are close to an edge, the concrete between the anchor head and the concrete edge could fail resulting in side face blowout failure.

2.10 Influencing Parameters Selected for this Study

Some of the critical parameters for the concrete pile-pile cap systems are embedment depth of the piles in the pile caps (Chan and Chee 2000, Richards et al. 2011, and Xiao and Chen 2013), reinforcement ratio in the pile caps (Richards et al. 2011, and Tortola et al. 2018), and shear span to depth (*a/d*) ratios (Suzuki et al. 2000, and Tortola et al. 2018). These parameters are selected for investigating in this study to understand if they have similar influences on the helical pile-to-pile cap systems subjected to reversed-cyclic loads. In addition to the single bracket type, the studded and double brackets will also be investigated since the literature reviewed indicated that they are also used, albeit less commonly, in current construction projects.

3. Design of Helical Foundation

3.1 Introduction

The objective of this chapter is to design a one-way pile cap for the pile-to-foundation anchorage and choose the commonly used helical pile foundation components for the numerical simulations. One-way foundations (i.e., pile cap strips) supported by two helical piles are to be modeled to better isolate the anchorage zone response.

3.2 Helical Foundation Components

3.2.1 New Construction Bracket Types

Three different new construction bracket types are to be investigated as shown in **Fig 3-1**. The single bracket type has a single plate connected to a helical pile shaft as shown in **Fig 3-1a**. The dimensions and the strength of the single bracket type is listed in **Table 3-1**. The double bracket type has two plates spaced between 320 mm (12.6”) as shown in **Fig 3-1b**. The studded bracket type has a single plate with four studs as shown in **Fig 3-1c**. The length of the stud is 160 mm (6.3”) welded on the top surface of the plate. The center-to-center spacing between the studs in both directions (i.e., in-plane and out-of-plane spacing of the studs) is 160 mm (6.3”). The studs have a termination head on their top surface. The studs are No.6 steel bars of Grade 60 (2.36”) and the terminations are 60 mm (2.36”) long. To more effectively compare the bracket type responses, the same dimensions and properties are used in all the bracket types.

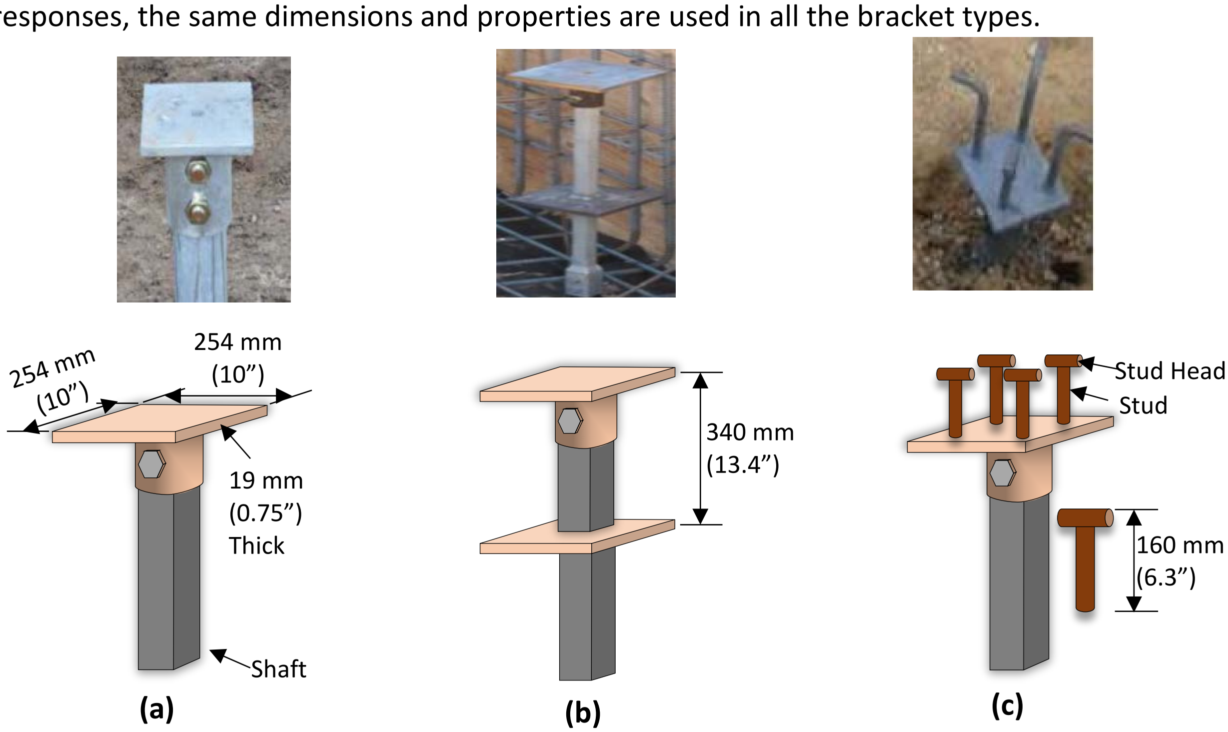

Figure 3-1: (a) Single bracket type; (b) Double bracket type; (c) Studded bracket type. (Supportworks, 2018).

Table 3-1: Properties of a single bracket type.

Length mm (in)	Breadth mm (in)	Thickness mm (in)	Area mm^2 (in^2)	Grade MPa (ksi)
260 (10.24)	260 (10.24)	20 (0.79)	67600 (105)	345 (50)

3.2.2 Helical Shaft

A square shaft (SS) is selected with properties given in **Table 3-2**.

Table 3-2: Properties of a single helical pile.

Shaft size mm (in)	Metal area mm^2 (in^2)	Uplift Capacity kN (kips)	Helix grade MPa (ksi)
51 (2)	2530 (4)	668 (150)	552 (80)

3.2.3 Pile Cap

The pile cap is 2100 mm (82.7”) thick with a cross-sectional dimension of 600 mm (23.6”) x 800 mm (31.5”). The dimension of the pile cap is similar to the dimensions recommended by Concrete Reinforcing Steel Institute (CRSI) which publishes a design guide for pile systems (CRSI 2015). A steel column (300 mm {11.8”} $\times$ 300 mm {11.8”}) anchored with four bolts is supported by the pile cap strip. The properties of the anchor bolts are shown in **Table 3-3**. The compressive strength of the concrete used was 20.7 MPa (3 ksi).

Table 3-3: Properties of an anchor bolt.

Length mm (in)	Diameter mm (in)	Area mm^2 (in^2)	Grade MPa (ksi)
460 (18.11)	38 (1.50)	1140 (1.80)	724 (105)

3.3 Helical Foundations

The designed helical foundations connected with single bracket, double bracket, and studded bracket types are shown in **Figs 3-2**, **3-3** and **3-4,** respectively.

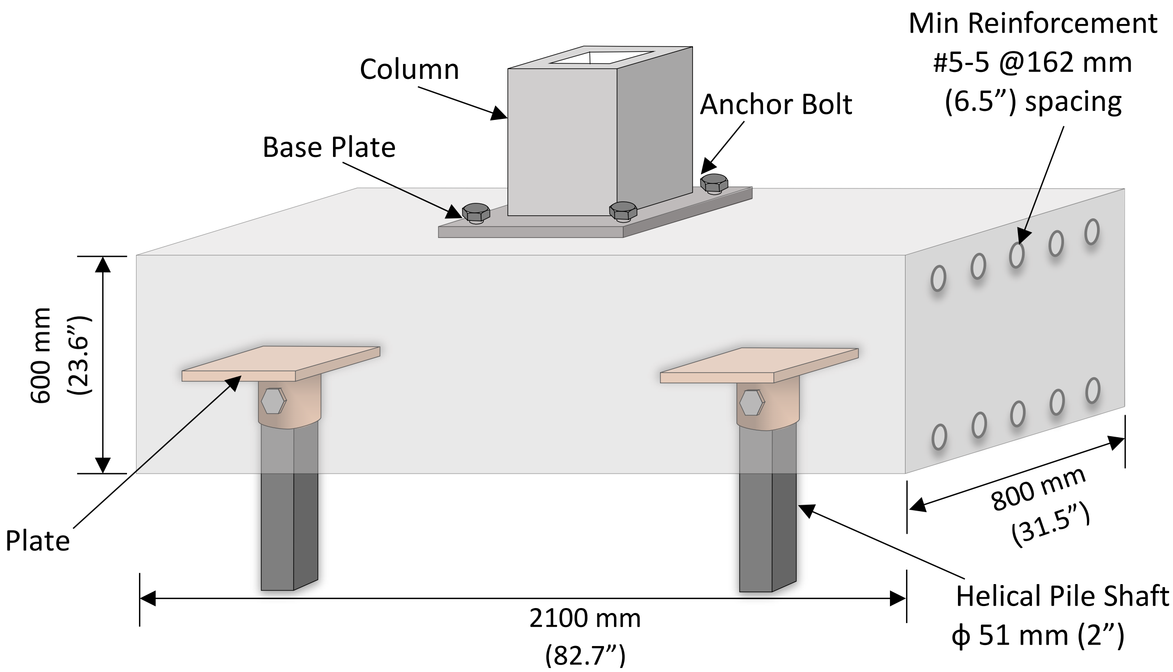

Figure 3-2: Helical pile with single bracket anchorage.

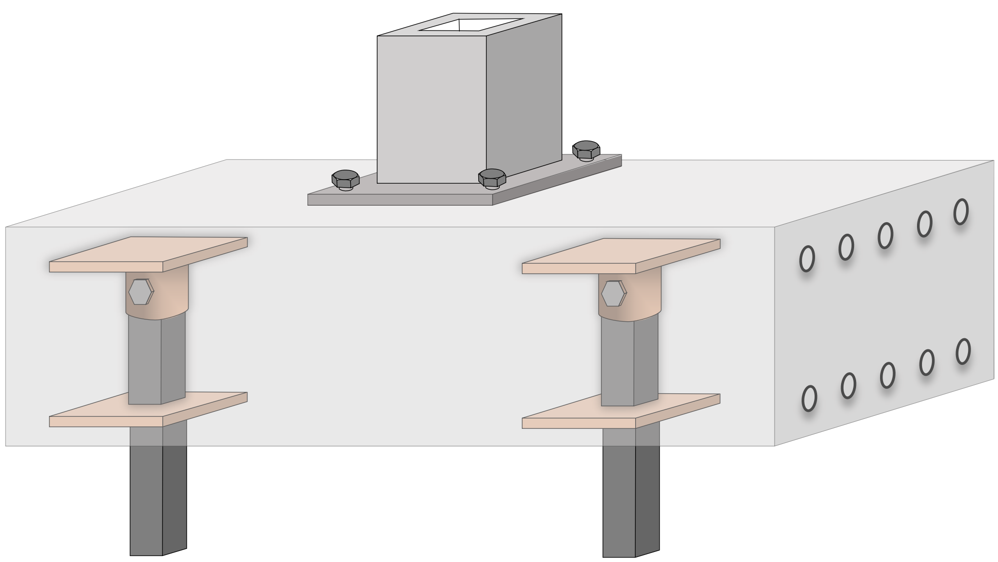

Figure 3-3: Helical pile with double bracket anchorage.

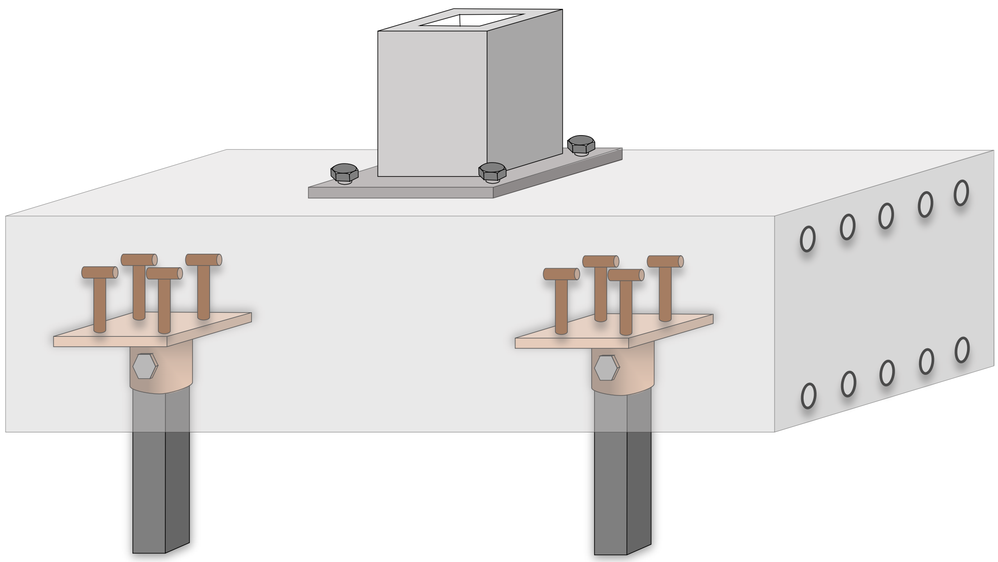

Figure 3-4: Helical pile with studded bracket anchorage.

3.4 Parameters to be investigated

Three influencing parameters, $h_{e,}$ ρ_x percentage, and *a/d* ratio, are to be investigated.

3.4.1 Embedment Depths (h_e)

In the study, h_e is the distance from the bottom of the pile cap to the top of the bracket. The single bracket has three $h_{e:}$ bottom h_e (140 mm {5.5"} up from the bottom of the pile cap), middle h_e (300 mm {11.8"} up from the bottom of the pile cap) and top h_e (460 mm {18.1"} up from the bottom of the pile cap); the studded bracket has two h_e; and the double bracket has one h_e. For unbiased comparisons, the positions of the plates in the studded and double brackets are taken in the same way as in the single bracket for their respective $h_{e,}$ as shown in **Fig 3-5**.

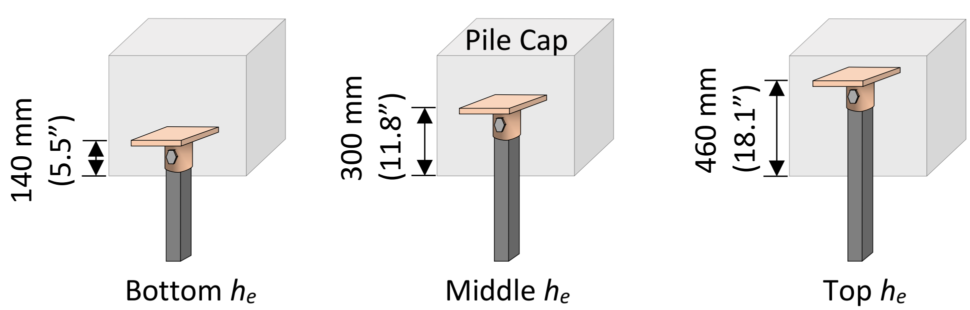

(a)

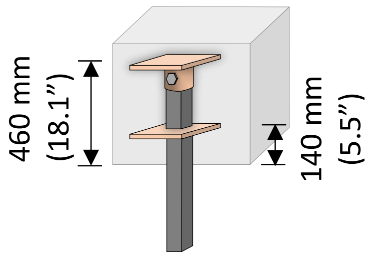

Top h_e

(b)

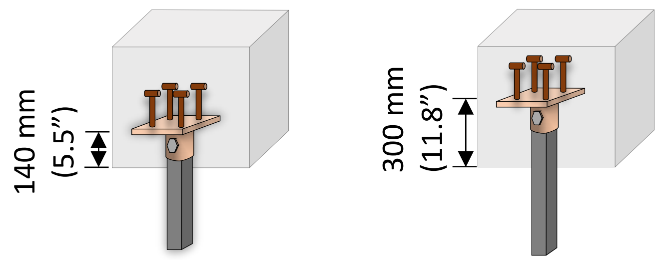

Bottom h_e Middle h_e

(c)

Figure 3-5: Different of the h_e (a) single bracket type; (b) double bracket type; (c) double bracket type.

3.4.2 Longitudinal Reinforcement Ratios (ρ_x)

Three different ρ_x percentages are selected for the investigation: minimum ρ_x percentage and two and three times the minimum ρ_x percentage.

Table 3-4 summarizes the total area of the ρ_x% to be used in the numerical simulations. An equal amount of reinforcement area is used in the compression zone since the pile cap strip will be subjected to reversed-cyclic loads.

Table 3-4: Rebar quantities.

ρ_x %	Bar size	No. of bars	Diameter mm (in)	Total area mm^2 (in^2)
0.2	#5	5	15.88 (0.63)	1000 (1.55)
0.4	#6	7	19.05 (0.75)	2000 (3.10)
0.8	#7	10	22.23 (0.88)	3880 (6.01)

3.4.3 Shear Span to Depth (*a/d*) Ratios

The three *a/d* ratios to be used are 1.68, 1.42, and 1.11 for all the brackets. "*a*" and "d" are the shear span and the effective depth, respectively. Shear spans to be used are 865 (34"), 725 (28.5"), and 565 mm (22.3"), whereas the effective depth of the pile cap is 514 mm, as shown in **Fig 3-6**.

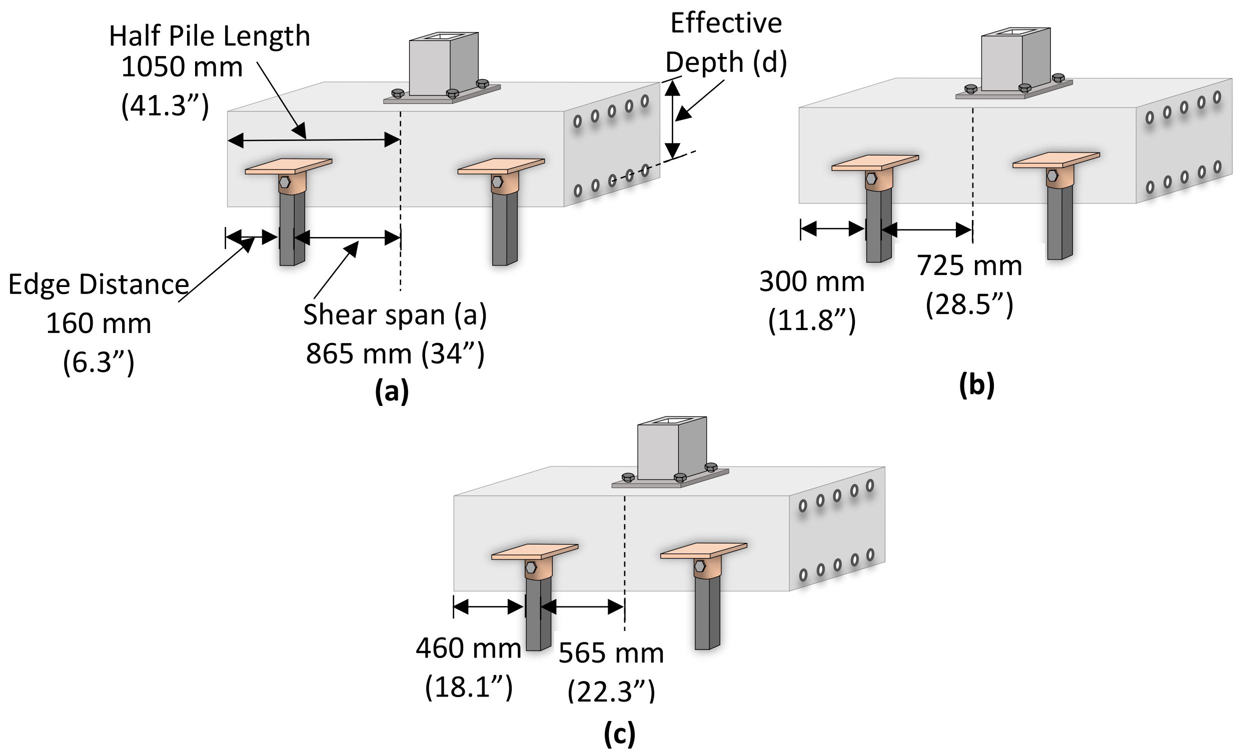

Figure 3-6: Different *a/d* ratios (a) 1.68; (b) 1.42; (c) 1.11.

4. Numerical Simulation Approach

4.1 Introduction

The aim of the research is to develop nonlinear finite element models which can accurately show the behavior of the helical pile foundation and the possible failure modes of the helical pile anchorage. The objective of this chapter is to briefly explain the numerical simulation approach that was taken to perform numerical investigation for the study. Finite element software VecTor2 was delineated in the beginning and followed by material properties and the numerical models of the simulations.

4.2 Selection of Finite Element Program

Most of the finite element programs capture only the linear behavior of the structure (i.e., up to the yielding of the structure). The post-peak responses (i.e., ultimate load-displacement responses, failure modes, crack patterns) are difficult to capture in these programs. However, the anchorage between the helical pile shaft and the concrete pile cap exhibits nonlinear behavior. Along with the nonlinearity, the program should be able to capture the post-peak response of the structure. Therefore, it is necessary to select a program which can accommodate these behaviors. Therefore, unlike other programs, VecTor2 is a 2D nonlinear finite element software packaged with commonly used constitutive models to represent concrete behavior, steel behavior, and the interface between concrete and steel. VecTor2 has options to capture different conditions of concrete structures (i.e., concrete softening, tension softening/stiffening, dowel action, buckling, and confinement) which are necessary for helical pile anchorage.

4.3 Numerical Approach using Finite Element Program VecTor2

Computer program **VecTor2** (VTAG 2019) is an advanced nonlinear finite element analysis platform for modeling concrete elements with disturbed regions and anchorage zones. Consequently, it is one of the most suited simulation platforms for this study. VecTor2 has been continuously developed since the 1990s at the University of Toronto, Canada. The formulation is based on the Disturbed Stress Field Model (Vecchio 2000) which is an extension of the Modified Compression Field Theory (MCFT) (Vecchio and Collins 1986). The MCFT models reinforced concrete as an orthotropic material using a smeared, rotating crack approach within a total-load, secant-stiffness solution algorithm, and allows the consideration of the coupled flexure, axial, and shear effects. The MCFT can consider the interaction of normal and shear stresses and accounts for such influences as aggregate interlock, tension stiffening, compression softening, and dowel action, all of which are important for this study. The MCFT has been validated with over 200 large-scale experimental tests and is currently used in the Canadian Code CSA A23.3 (CSA 2014) and American Code AASHTO LFRD (AASHTO 2014) as the required method for calculating the shear strengths of concrete members.

4.3.1 Element Library

Finite element models constructed for VecTor2 use a fine mesh of low-powered elements. This methodology has advantages of computational efficiency and numerical stability. It is also well suited for reinforced concrete structures, which require a relatively fine mesh to model reinforcement detailing and three local crack patterns. The element library includes a three-node constant strain triangle, a four-node plane stress rectangular element, a four-node quadrilateral element for modeling concrete with smeared reinforcement, a two-node truss-bar for modeling discrete reinforcement, and a two-node link and a four-node contact element for modeling bond-slip mechanisms.

Figure 4-1: Material elements used (a) Plane-stress rectangle; (b) Truss bar.

In this study, the concrete was modelled as a four-node plane stress rectangular element (see **Fig 4-1 (a)**) with a mesh size of 20 mm x 20 mm, without smeared reinforcement due to the absence of transverse reinforcement in the design foundations. The longitudinal reinforcement was modeled as a two-node truss-bar (see **Fig 4-1 (b)**). The bond between the steel and the concrete was assumed to be perfect and bond slip wasn't considered.

4.3.2 Material Models in VecTor2

VecTor2 has several concrete constitutive and behavioral models (Wong et al. 2013, Akkaya et al. 2019) that can capture complex nonlinear behavior of the structure including secondary effects such as compression softening, tension stiffening, tension softening, and tension splitting. VecTor2 can also model the cyclic loading and hysteretic response, concrete expansion and confinement, bond slip, reinforcement buckling, reinforcement dowel action, crack shear slip deformations, and crack allocation processes. **Tables 4-1** and **4-2** show the default models used for the simulations. **Fig 4-2** is the screenshot of the software graphics showing different constitutive models. **Fig 4-3** shows the cyclic response of concrete and steel materials used in this program for the concrete and reinforcement responses respectively.

Table 4-1: Default concrete material models.

Concrete Behaviour	Default Model
Compressive Base Curve	Hognestad
Compression Post-Peak	Modified Park-Kent
Compression Softening	Vecchio 1992-A
Tension Stiffening	Modified Bentz 2003
Tension Softening	Linear
Confined Strength	Kupler/Richart
Concrete Dilation	Variable-Isotropic
Cracking criterion	Mohr-Coulomb (Stress)
Crack Width Check	Agg/5 Max crack width
Crack Slip	Walraven

Table 4-2: Default reinforcement material models.

Reinforcement Behavior	Default Model
Hysteretic Response	Bauchinger Effect (Seckin)
Dowel Action	Tassios (Crack Slip)
Buckling	Akkaya 2012 (Modified Dhakal-Maekawa)

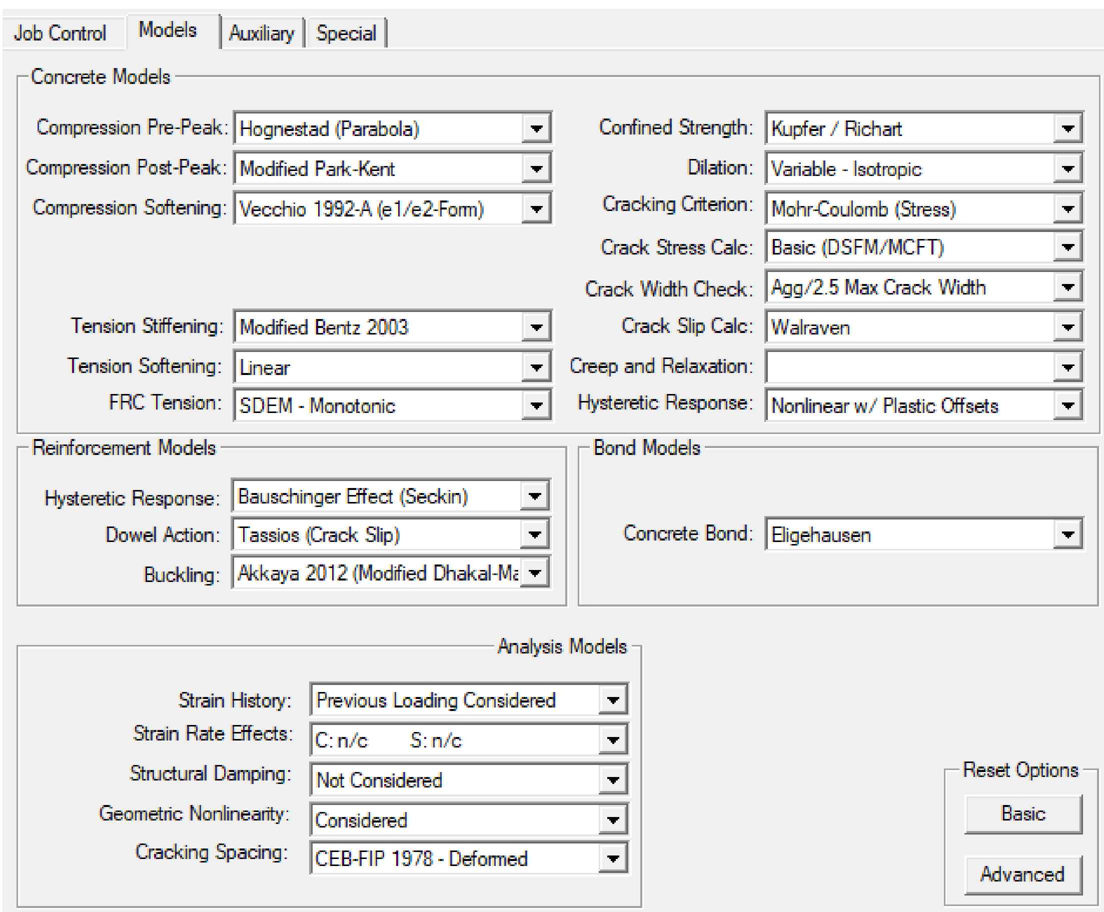

Figure 4-2: Material models simulated in VecTor2.

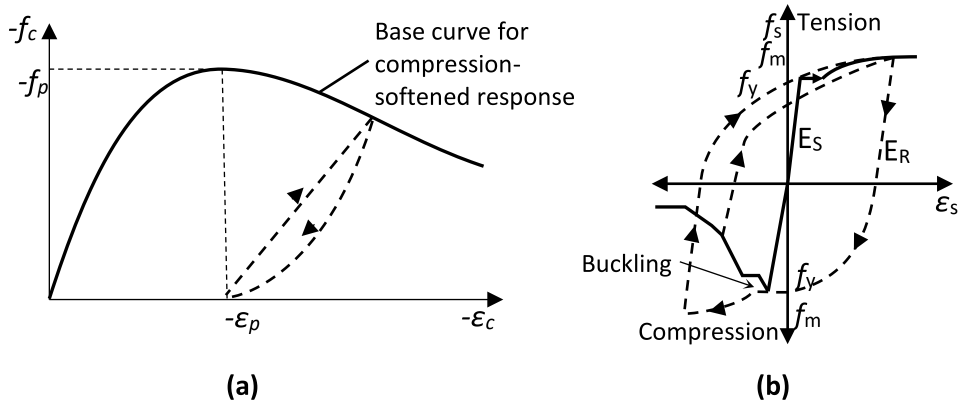

Figure 4-3: (a) Palermo model of cyclic response for concrete; (b) Seckin w/Bauschinger-HP4 model of hysteretic response for ductile steel reinforcement (Wong et al. 2013).

4.3.3 Equivalent Cone Method (ECM)

The helical pile-to-foundation anchorages exhibit three-dimensional cone breakout failures when subjected to tensile and uplift forces. The concrete breakout is a three-dimensional phenomenon that presents a conical shape (see **Fig 4-4a**). However, 2D numerical simulations consider a constant stress distribution along the entire thickness of the foundations, consequently predicting a trapezoidal breakout shape (see **Fig 4-4b**). Therefore, an appropriate thickness must be used in 2D numerical simulations to account for this difference and accurately predict the connection load capacity. The ECM (Almeida Jr 2019, Almeida Jr and Guner 2019) is employed in this study to calculate an equivalent thickness of the concrete foundations to be used in the 2D numerical simulations.

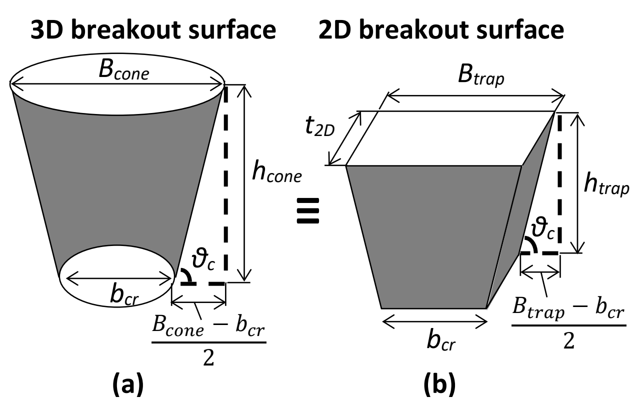

Figure 4-4: Surface area for (a) 3D; (b) 2D concrete breakout shapes.

The first step of the method is to create and run a 2D model with an estimated concrete thickness equal to three times the embedment depth h_{ef} of the bracket type (see **Fig 4-5**). The cracking angle ϑ_{cr} and vertical extent h_{trap} of the crack are determined from the simulation results and used to calculate the concrete cone surface area As_{cone} and the trapezoidal surface area As_{trap}

according to **Equations 4.1** and **4.2**, respectively. The equivalent thickness t_{2D} is calculated using **Equation 4.3** and used in 2D models to accurately estimate the load capacity.

Create and run a 2D FE model with estimated concrete thickness equal to $3h_{ef}$

↓

Obtain the cracking angle (ϑ_{cr}) and vertical extent (h_{trap})

↓

Calculate the concrete cone surface area:

$$As_{cone} = \frac{1}{2}\pi h_{cone}(B_{cone} + b_{cr}) \tag{4.1}$$

↓

Calculate the trapezoidal surface area:

$$As_{trap} = 6h_{ef}\left(\sqrt{\left(\frac{B_{trap}-b_{cr}}{2}\right)^2 + h_{trap}^2}\right) \tag{4.2}$$

↓

Calculate the equivalent concrete thickness:

$$t_{2D} = 3h_{ef}\frac{As_{cone}}{As_{trap}} \tag{4.3}$$

↓

Update the concrete thickness in the 2D FE model to t_{2D} and rerun the analysis

Figure 4-5: Flowchart of the Equivalent Cone Method, EMC (Almeida Jr and Guner 2019).

where:

h_{ef} = Anchor embedment depth

b_{cr} = Base of the cracked trapezoidal and cone shapes

B_{cone} = Base of the cracked cone shape (3D)

B_{trap} = Base of the cracked trapezoidal shape (2D)

h_{trap} = Height of the cracked trapezoidal shape (2D)

As_{cone} = Surface area of the cracked cone shape (3D)

As_{trap} = Surface area of the cracked trapezoidal shape (2D)

t_{2D} = Equivalent concrete/beam thickness

4.4 Experimental Verification of the Numerical Simulation Approach

To verify the modelling approach used in this study, Diab's experimental results (Diab 2015) are used. The specimen configurations are similar to the ones designed in this study. Nine grade beams of different helical pile-to-grade beam anchorages are tested under monotonic tension loading. Diab's foundations consisted of a single bracket embedded into a 500 x 500 x 1600 mm^3 (19.7 x 19.7 x 63 in^3) beam, as shown in **Fig 4-5**. The parameters investigated are h_e, ρ_x, bracket width b_w, shear reinforcement ratio ρ_y, and the concrete compressive strength f'_c. Each configuration is presented in **Table 4-3**; more details can be found at Diab (2015). Using the ECM (Almeida Jr and Guner 2019), the equivalent thickness of the grade beams ranges from 327 mm (12.9”) to 417 mm (16.4”).

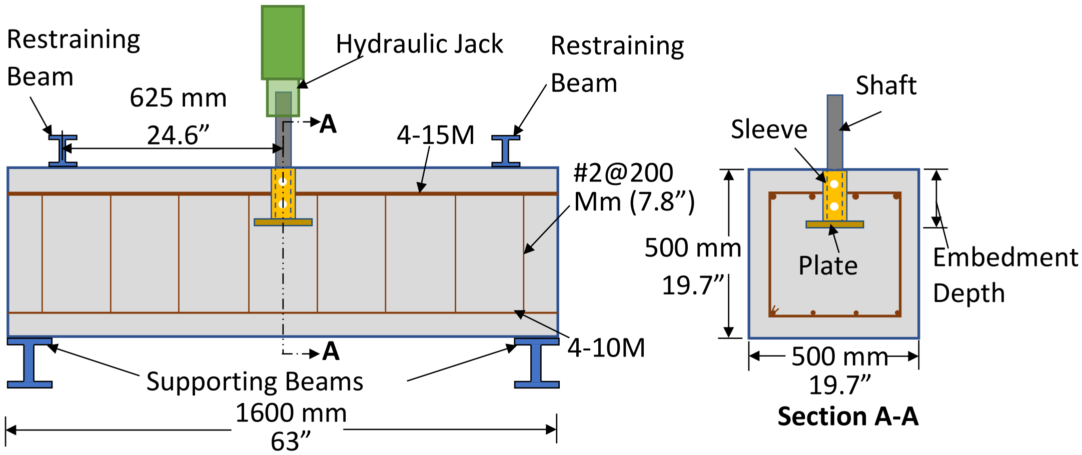

Figure 4-6: Specimen dimensions for T1.

Table 4-3: Diab’s foundation specimen dimensions.

Diab’s Foundation	**Concrete f'_c (MPa)**	**Embedment Depth (h_e) mm (in)**	**Plate Width (mm)**	**Longitudinal Reinforcement**	**Stirrups**
T1	30	152 (5.98)	165 (6.50)	4-15M	2 branches #2@200mm (7.80”)
T2	30	203 (8.00)	165 (6.50)	4-15M	
T3	30	254 (10.00)	165 (6.50)	4-15M	
T4	40	203 (8.00)	190 (7.48)	4-15M	
T5	40	203 (8.00)	229 (9.02)	4-15M	
T6	40	203 (8.00)	165 (6.50)	4-20M	
T7	40	203 (8.00)	165 (6.50)	4-25M	
T8	40	203 (8.00)	165 (6.50)	4-15M	4 branches #2@200mm (7.80”)
T9	40	203 (8.00)	165 (6.50)	4-15M	2 branches #2@200mm (7.80”)

Only half of the foundations are modeled to take advantage of symmetry as shown in **Fig 4-6**. A vertical roller is used at the top of the steel plate while horizontal rollers are added to the right edge of the model to account for the symmetry. The load is applied as an uplift displacement at the top of the bracket in small displacement steps.

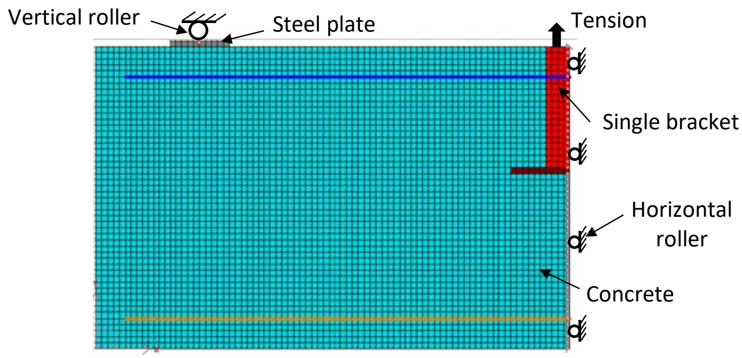

Figure 4-7: Numerical model for Diab's foundation specimen T4.

The load capacities obtained from VecTor2 using equivalent thickness of (t_{eq}) are compared to the experimental load capacities as shown in **Table 4-4**. The load capacities obtained from the developed numerical models ($P_{Simulation}$) are in an excellent agreement with the experimental ($P_{Experimental}$) ones with a very low coefficient of variation 6%.

Table 4-4: Simulated and experimental load capacities.

Grade Beams	**$P_{Experiment}$ kN (kips)**	**$P_{Simulation}$ kN (kips)**	**$P_{Experiment}/P_{Simulation}$**
T1	154 (34.62)	153 (34.4)	1.02
T2	200 (44.96)	190 (42.71)	0.94
T3	235 (52.83)	243 (54.63)	1.02
T4	204 (45.86)	215 (48.33)	1.03
T5	241 (54.18)	222 (49.91)	0.92
T6	223 (50.13)	227 (51.03)	1.03
T7	253 (56.88)	287 (64.52)	1.14
T8	256 (57.55)	265 (59.57)	1.01
T9	256 (57.55)	265 (59.57)	1.01
Average	-	-	1.01
COV	-	-	6%

The load-displacement responses of three specimens, namely, T1, T2, and T3, are shown in **Fig 4-7**. The numerical models provided a good agreement with the experimental results as they were able to simulate the load capacity and overall behavior accurately. The initial stiffnesses are overestimated. This could be attributable to the fact that numerical models are perfectly supported while the experimental specimen supports and loading system are expected to exhibit some flexibility. The experimental specimens may also have some shrinkage cracking which could make their initial stiffnesses softer.

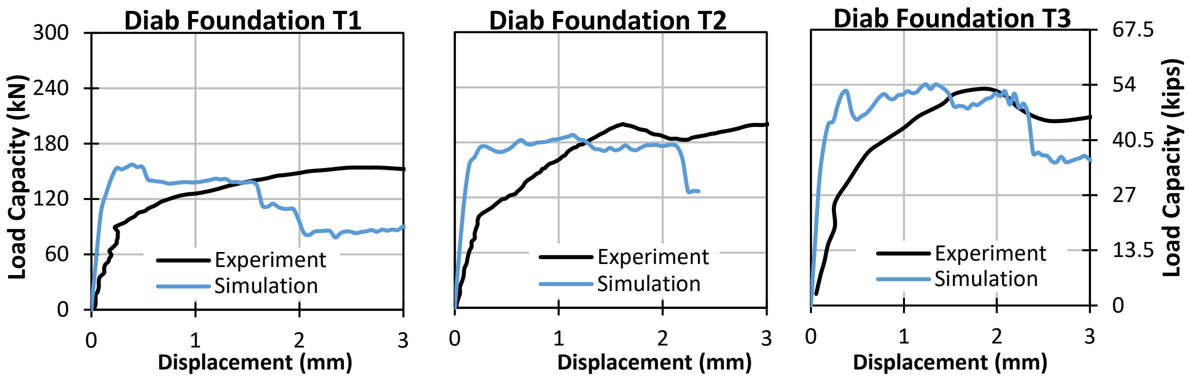

Figure 4-8: Simulated and experimental load-displacement responses.

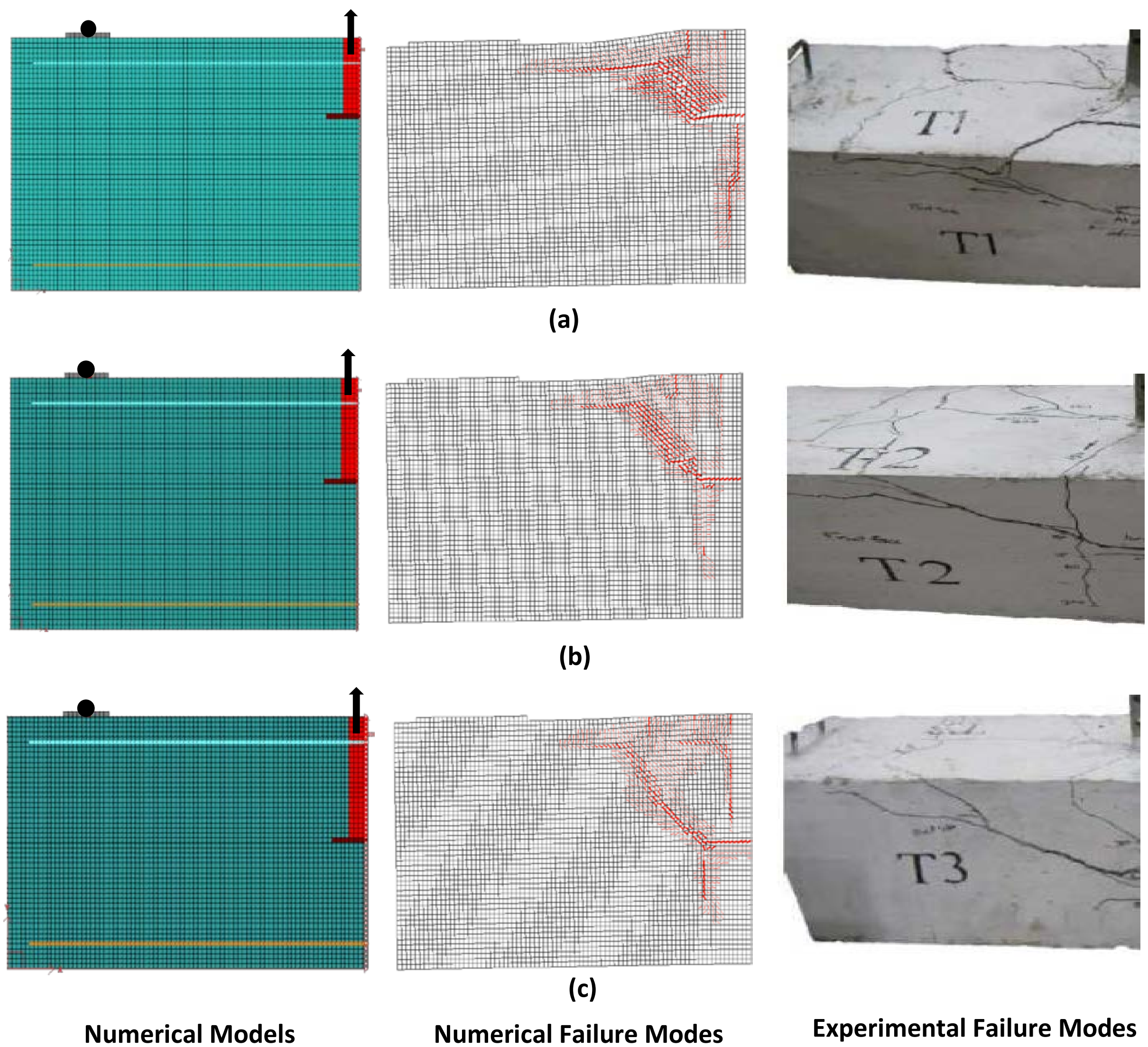

Figure 4-9: Cracking pattern and failure mode comparisons for grade beams (a) T1; (b) T2; (c) T3.

The cracking patterns at the peak load levels obtained from the numerical models developed are compared with those from the experimental testing. As seen in **Fig 4-8**, the cracking pattern and the crack angles match very well.

4.5 Material Modeling of Helical Foundations

The dimensions, types, strength, and components of helical pile system investigated in this study are discussed in Chapter 3. In this section, material modeling is discussed.

4.5.1 Pile Cap

The concrete pile cap has the dimension of 2100 x 800 x 600 mm^3 (82.7 x 31.5 x 23.6 in^3) (see Chapter 3) with a concrete strength of 20.7 MPa (3 ksi). The important properties of concrete are given in **Fig 4-9**.

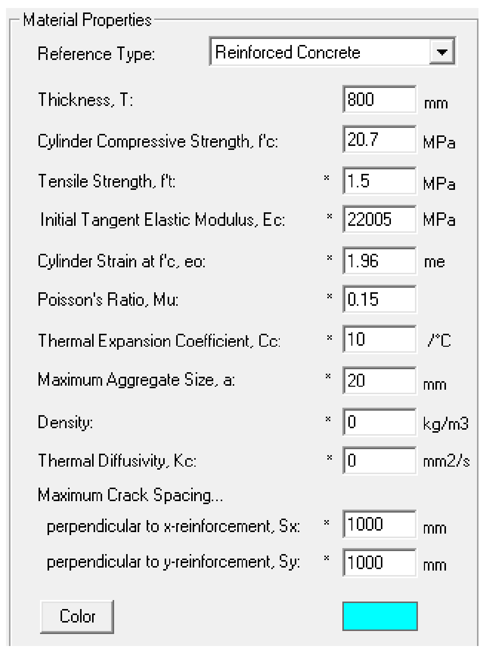

Figure 4-10: Concrete properties.

4.5.2 Helical Pile Shaft

The pile shaft with dimensions of 51 x 51 mm (2” x 2”) is modelled as 60 x 44 mm (2.4” x 1.7”) to match with the meshing size. The total cross section area remains approximately the same. The pile length extending outside the pile cap is taken as 200 mm (7.9”). The ultimate strength of the helical shaft is selected as 552 MPa (80 ksi). The helical shaft properties are shown in **Fig 4-10**.

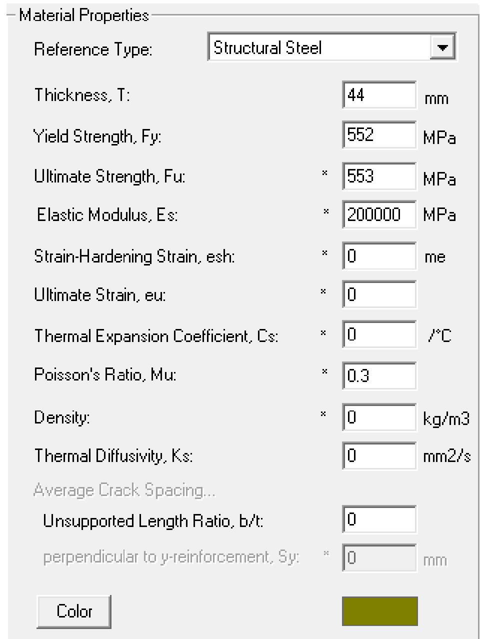

Figure 4-11: Helical shaft properties.

4.5.3 Bracket Types

To fit the finite element mesh of 20 mm x 20 mm (0.79” x 0.79”), a bracket size of 260 mm x 260 mm (10.24” x 10.24”) with a thickness of 20 mm (0.79”) is used. All three bracket types have the same properties. In addition, the studded bracket has four studs. The studs are No.6 rebars and modeled as rectangular with a dimension of 28.5 x 20 mm^2 (1.12 x 0.79 in^2) to match their equivalent cross-sectional areas. Each stud represents two studs because in-plane view of the stud overlaps the out-of-plane position. The length of the stud is 160 mm (6.3”) welded on the top surface of the bracket. The center-to-center spacing between the studs in both directions (i.e., in-plane and out-of-plane) is 160 mm (6.3”). The studs have a termination on the top surface. This termination is modelled as a small element of steel with dimensions of 60 x 20 x 20 mm^3 (2.36 x 0.79 x 0.79 in^3). No.6 studs and the termination steel had same strengths as given in **Fig 4-11**.

4.5.4 Anchor Bolt

The size of the anchor bolt used is 40 x 57 mm^2 (1.6 x 2.2 in^2), which is equivalent to two times the area of the anchor bolt because each anchor bolt in the model represents two anchor bolts (i.e., in-plane and out-of-plane). The length of the anchor bolts is 460 mm (18.11”) and the head of the anchor bolts is modeled with the dimensions of 120 x 20 x 57 mm^3 (4.7 x 0.79 x 2.24 in^3) since each of them is equivalent to two anchor heads. The material properties of the anchor bolts are shown in **Fig 4-12**.

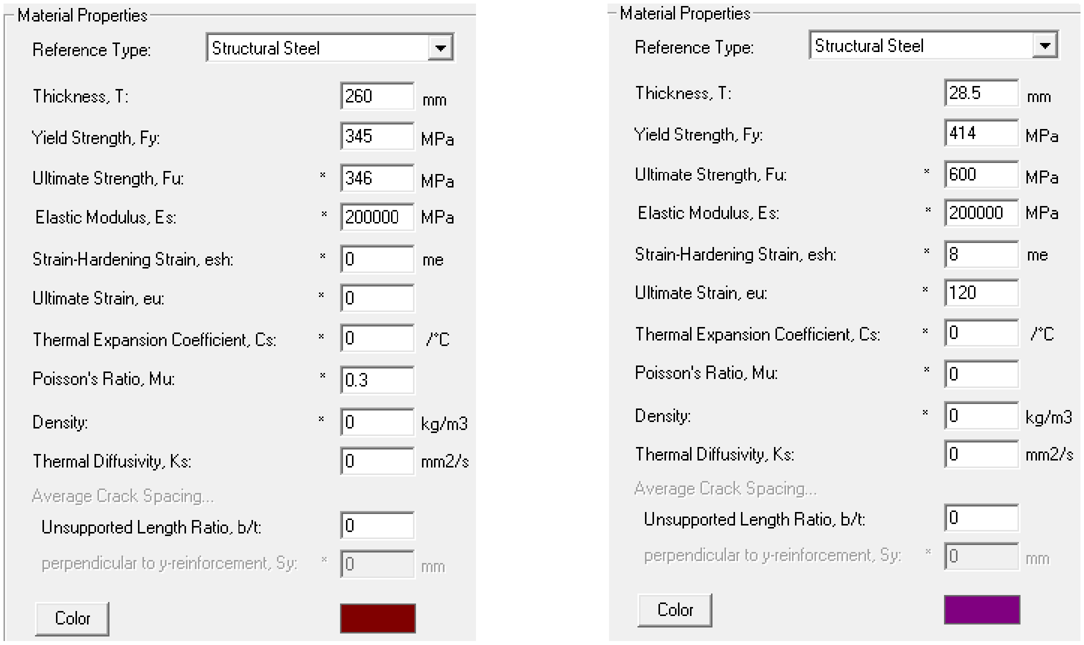

(a) **(b)**

Figure 4-12: Material properties for (a) Bracket type; (b) Stud.

4.5.5 Longitudinal Reinforcement Percentages

The influences of three different longitudinal reinforcement percentage are investigated in this study.

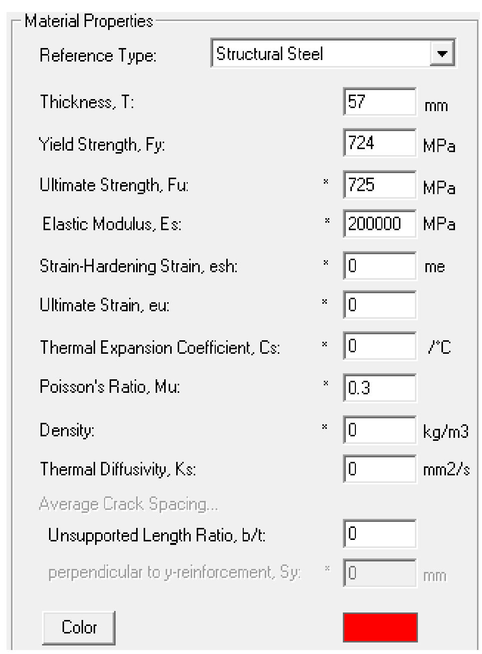

Figure 4-13: Material properties for anchor bolt.

No.5, No.6, and No.7 bars are used to create ρ_x of 0.2%, 0.4%, and 0.8%. All bars are Grade 60 and their properties are given in **Figs 4-13** and **4-14**.

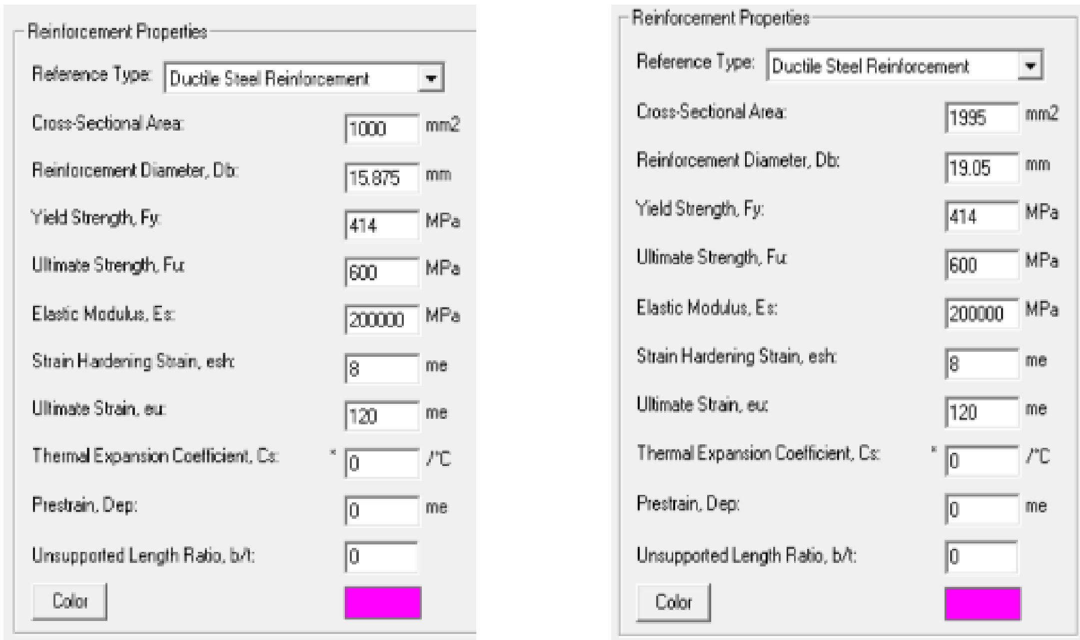

(a) **(b)**

Figure 4-14: Material properties for (a) Rebar No.6; (b) Rebar No.7.

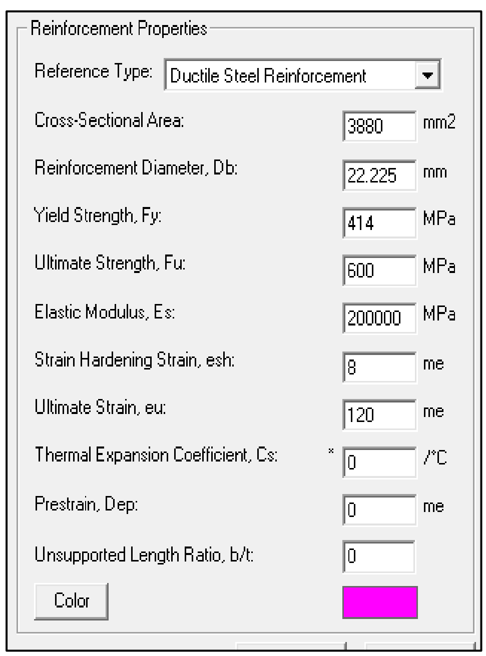

Figure 4-15: Material properties for rebar No.8.

4.6 Finite Element Modeling of the Helical Foundations

The graphical illustrations of the models are presented for each bracket separately.

4.6.1 Single Bracket Type

Fig 4-15 shows three h_e of the single bracket types when the *a/d* ratio is 1.42. **Fig 4-16** shows three *a/d* ratios when the single bracket types h_e is at the middle.

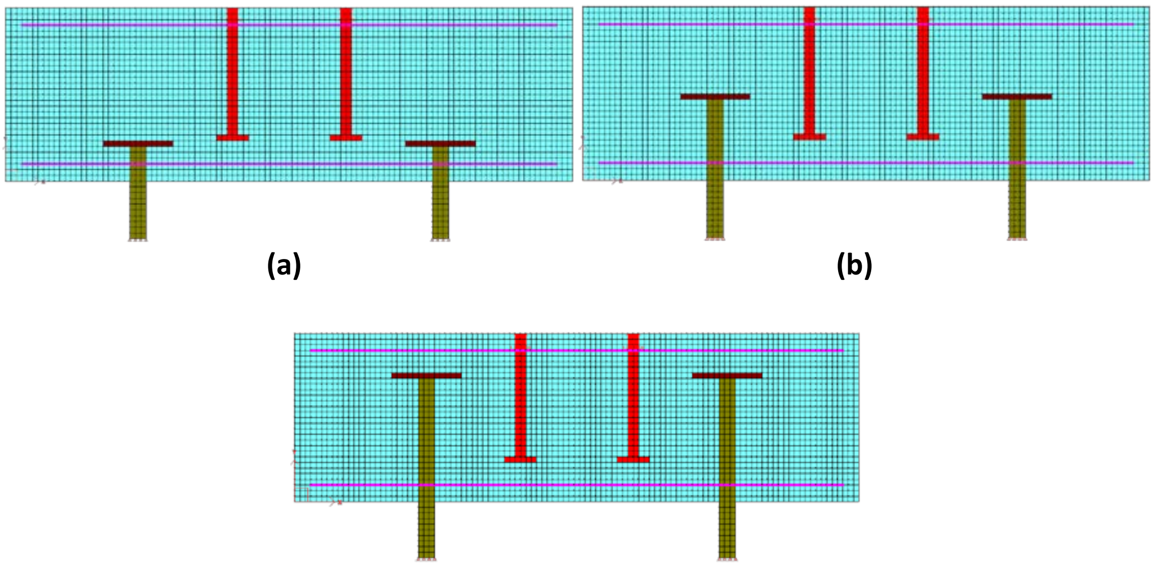

(a) **(b)** **(c)**

Figure 4-16: Numerical models: single bracket type (1.42 *a/d* ratio) - h_e (a) bottom; (b) middle; (c) top.

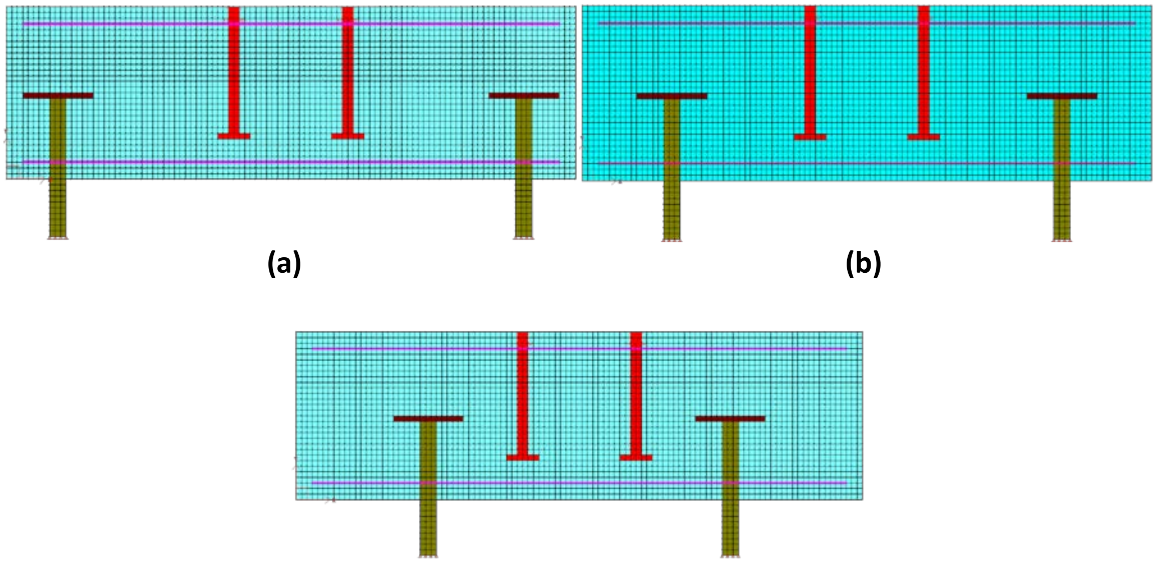

(a) (b) (c)

Figure 4-17: Numerical models: single bracket type (middle h_e) - *a/d* ratios (a) 1.68; (b) 1.42; (c) 1.11.

4.6.2 Double Bracket Type

The graphical illustrations showing the variation of the *a/d* ratios are shown in **Fig 4-17**. The double bracket has only one h_e.

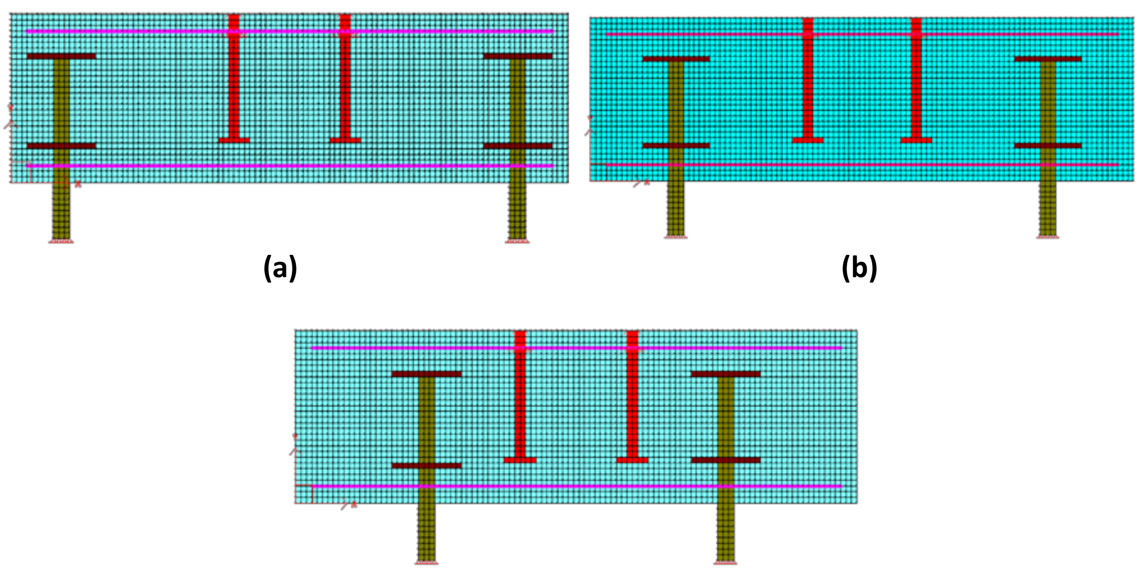

(a) (b) (c)

Figure 4-18: Numerical models: double bracket type - *a/d* ratios (a) 1.68; (b) 1.42; (c) 1.11.

4.6.3 Studded Bracket

The graphical illustrations showing the variation of the h_e and *a/d* ratio are given below. **Fig 4-18** shows the h_e of the bracket type when the *a/d* ratio is 1.42. **Fig 4-19** shows three *a/d* ratios when the bracket type's h_e is at the middle.

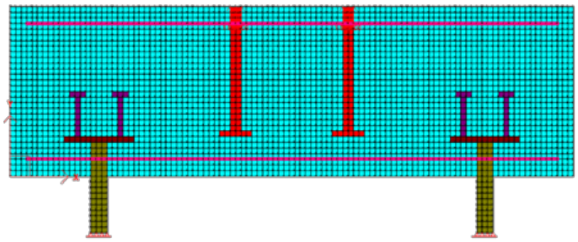

(a)

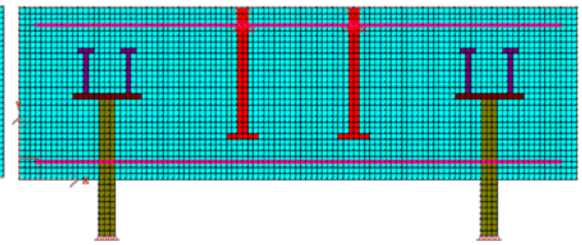

(b)

Figure 4-19: Numerical models: studded bracket type (1.42 *a/d* ratio) - h_e (a) bottom; (b) middle.

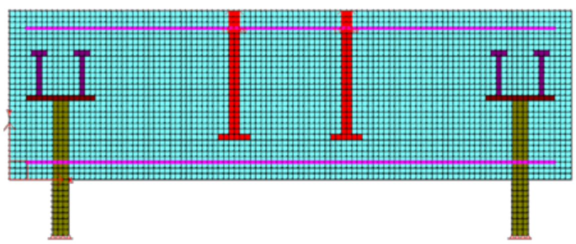

(a)

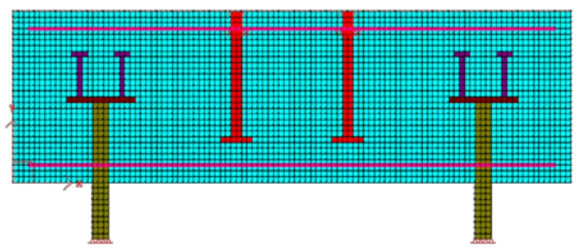

(b)

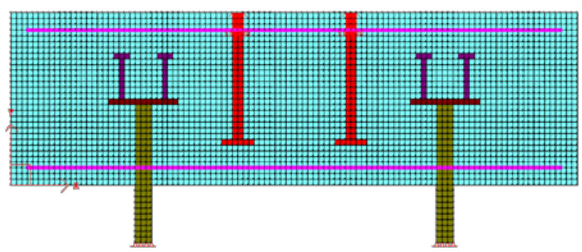

(c)

Figure 4-20: Numerical models: single bracket type (middle h_e) - *a/d* ratios (a) 1.68; (b) 1.42; (c) 1.11.

5. Numerical Simulation Results

5.1 Introduction

The objective of this chapter is to analyze the result of numerical simulations conducted in Chapter 4. The results are analyzed in terms of the bracket types, h_e, *a/d* ratio, and ρ_x%, Their influence on the ultimate load capacities, failure modes, and crack patterns is discussed.

The results of the reversed-cyclic loading were analyzed under 'cyclic compression' and 'cyclic tension,' as shown in **Fig 5-1**, for side-by-side comparison with the monotonic loading. Therefore, *the cyclic tension* represents the part of the reversed-cyclic load where the pile gets the uplift effect and *the cyclic compression* represents the part of the reversed-cyclic load where the pile gets the compressive load effect. Similarly, *the monotonic tension* represents the pure uplift force applied gradually until the failure, whereas *the monotonic compression* represents the pure compressive load applied gradually until the failure. Therefore, three loading types are categorized into four load types (i.e., monotonic tension and compression and cyclic tension and compression). The parameters investigated are the h_e of the brackets, the ρ_x (i.e., 0.2%, 0.4% and 0.8%) of the pile cap, and *a/d* ratios (i.e., 1.68, 1.42 and 1.11).

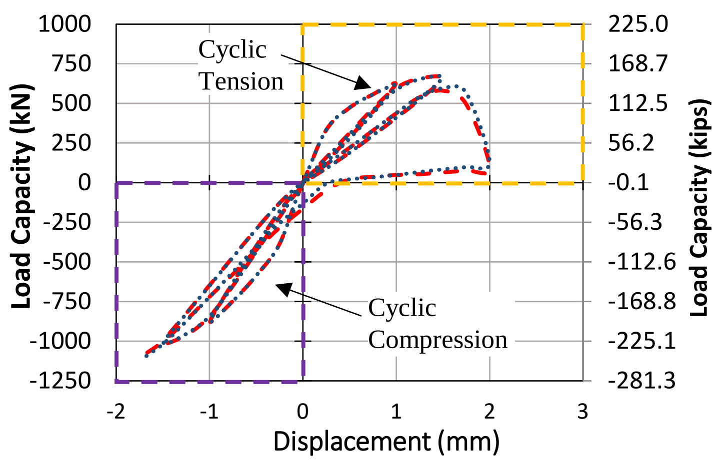

Figure 5-1: One of the sample simulation subjected to reversed-cyclic.

For single bracket type, 81 numerical simulations are performed using three h_e, three ρ_x% and three *a/d* ratios. The details of the single bracket type analyses are given in Appendix A. For the double bracket type, 27 numerical simulations were performed using one h_e, three ρ_x (0.2, 0.4 and 0.8%) and three *a/d* ratios (1.68, 1.42, 1.11). The details of the double bracket type analysis are given in Appendix B. For studded bracket type, 54 numerical simulations were performed using two h_e (bottom and middle), three ρ_x% (0.2, 0.4 and 0.8%) and three *a/d* ratios (1.68, 1.42, 1.11). The details of the studded bracket type are given in Appendix C.

All simulations are performed in a displacement-controlled mode to be able to obtain the post-peak responses. Each simulation takes about ten minutes to complete. The following simulation results are used in the assessments: nonlinear load vs. deflection responses, the peak failure loads, the failure displacement, the initial stiffness, the failure mechanism, and the influence of the bracket zone.

5.2 Effect of h_e on the Load Capacity

5.2.1 Tensile Load Behavior

Figs 5-2a and **5-2c** represent the load capacity of the single bracket type subjected to monotonic and cyclic tension respectively, whereas **Figs 5-2b** and **5-2d** represent the load capacity of the studded bracket type subjected to monotonic and cyclic tension, respectively. The single bracket type in **Figs 5-2a** and **5-2c** has 27 simulations each, and the studded bracket type in **Figs 5-2b** and **5-2d** has 18 simulations each. The single bracket type had three h_e (i.e., bottom, middle, and top) and the studded bracket had two h_e (i.e., bottom and middle). The notations for the bottom and middle h_e of studded bracket type are the same as that for the single bracket type (i.e., 'B' for bottom h_e and 'M' for middle h_e). The red lines, yellow lines, and blue lines represent shear span to depth ratio of 1.11, 1.42, and 1.68, respectively, whereas the dotted lines, dashed lines, and continuous lines represent 0.8, 0.4, and 0.2 ρ_x% respectively.

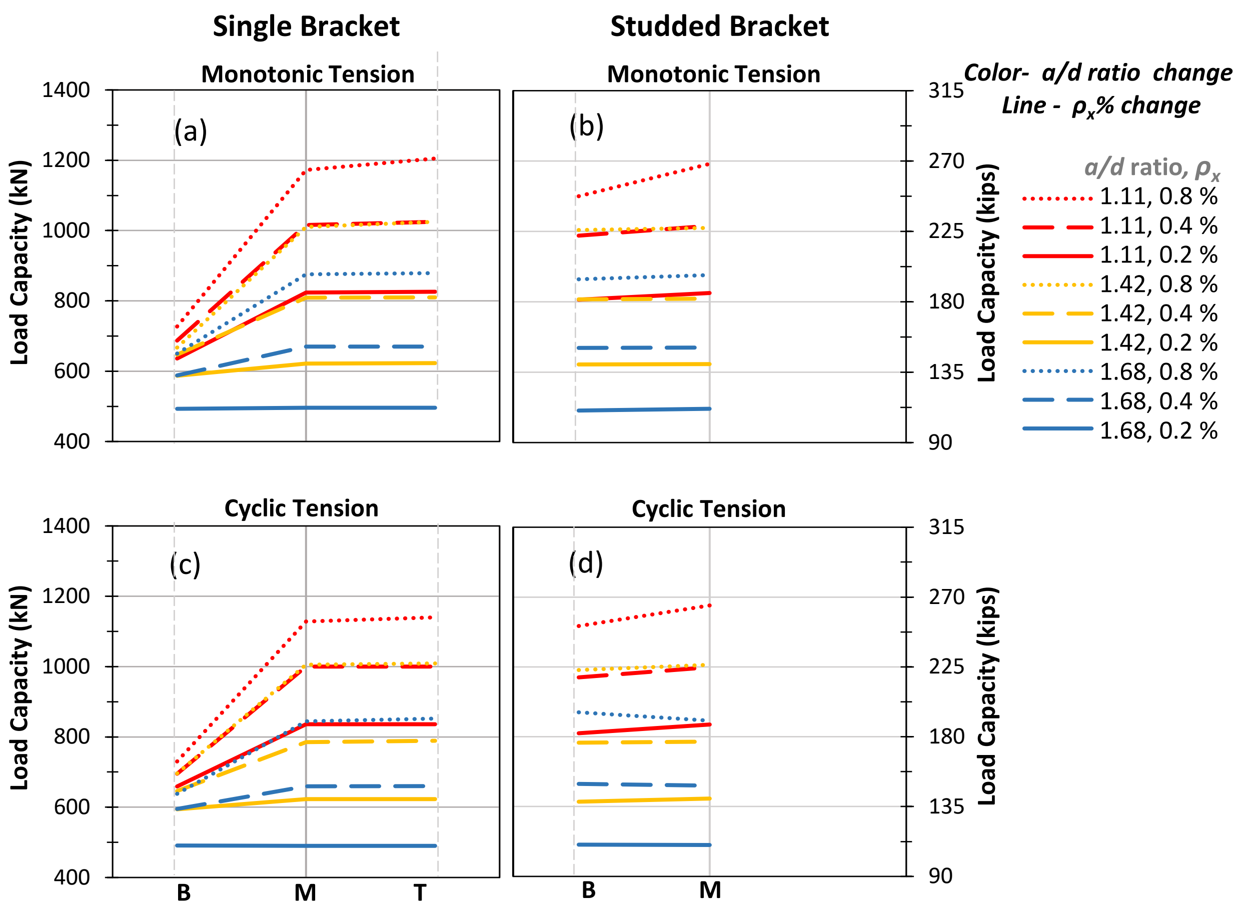

Figure 5-2: Effect of h_e of single and double bracket types on the load capacity subjected to monotonic and cyclic tension.

- For the single bracket type in **Figs 5-2a** and **5-2c**, when changing the h_e from bottom to middle, the load capacity increases by an average of 30% and 28% when subjected to monotonic and cyclic tension, respectively.
- For the single bracket type in **Figs 5-2a** and **5-2c**, all the lines at the middle (M) and top (T) h_e are essentially horizontal, which shows that the load capacity remains very similar for the middle and top h_e when subjected to monotonic and cyclic tension.
- For the studded bracket type in **Figs 5-2b** and **5-2d**, all the lines at the bottom (B) and middle (M) h_e are essentially horizontal, which shows that the load capacity remains very similar for the bottom and middle h_e when subjected to monotonic and cyclic tension, except for the red dotted lines with *a/d* ratio 1.11 and 0.8 ρ_x% reinforcement, in which the load capacity increases by less than 9% when changing the h_e from bottom to middle.

5.2.1.1 Single Bracket Type Subjected to Monotonic and Cyclic Tension

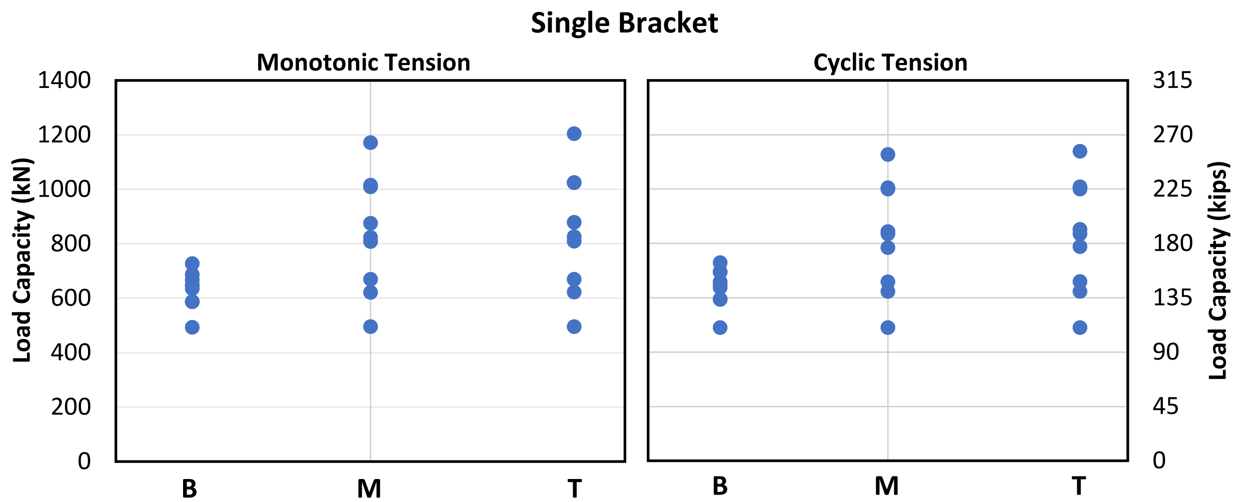

Figure 5-3: Trend for effect of h_e.

Total dotted points ● = 27 simulations for each loading

In **Fig 5-3**, B, M, and T represent the simulations under bottom, middle, and top h_e respectively. The simulation results for the bottom h_e are concentrated as compared to the middle and top h_e for the monotonic tension and the cyclic tension loadings. Therefore, for bottom h_e, increasing ρ_x% and decreasing *a/d* ratio did not increase the capacity significantly. In other words, the load capacity couldn't be efficiently increased when the bottom h_e was subjected to monotonic tension or cyclic tension loadings. It is recommended to use other h_e if a larger load capacity is required.

5.2.2 Compressive Load Behavior

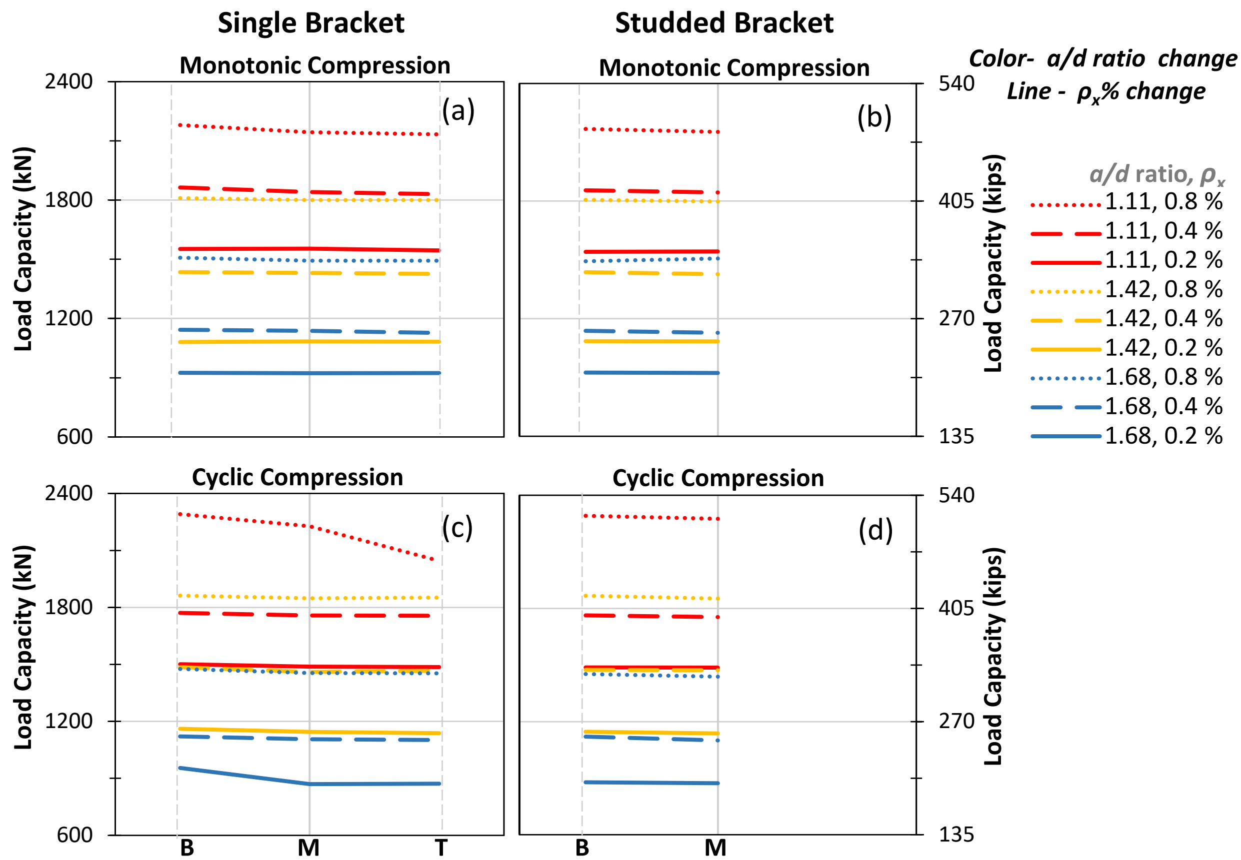

Figure 5-4: Effect of h_e of single and double bracket types on the load capacity subjected to monotonic and cyclic compression.

- For the single bracket type in **Figs 5-4a** and **5-2c**, all the lines at the bottom (B), middle (M), and top (T) h_e are essentially horizontal, which shows that the load capacity remains very similar for all the h_e when subjected to monotonic and cyclic compression. An exception is observed in **Fig 5-4c** for the red dotted line with a/d ratio 1.11 and 0.8% reinforcement, and blue continuous line with a/d ratio 1.68 and 0.8% reinforcement in which the load capacity decreased by 8% and 9% respectively when changing the h_e from middle to top and bottom to middle respectively.
- For the studded bracket type in **Figs 5-4b** and **Figs 5-4d**, all the lines at the bottom (B) and middle (M) h_e are essentially horizontal, which shows that the load capacity remains very similar for the bottom and middle h_e when subjected to monotonic and cyclic compression.

5.3 Effect of ρ_x% on the Load Capacity

5.3.1 Tensile Load Behavior

Figs 5-5a and **5-5d**, **Figs 5-5b** and **5-5e**, and **Figs 5-5c** and **5-5f** represent the load capacity of the single bracket, double bracket, and studded bracket types respectively subjected to monotonic and cyclic tension. The double bracket type has one h_e. The notation for the h_e of the double bracket type is Top (T), which is the same as that of the single bracket type.

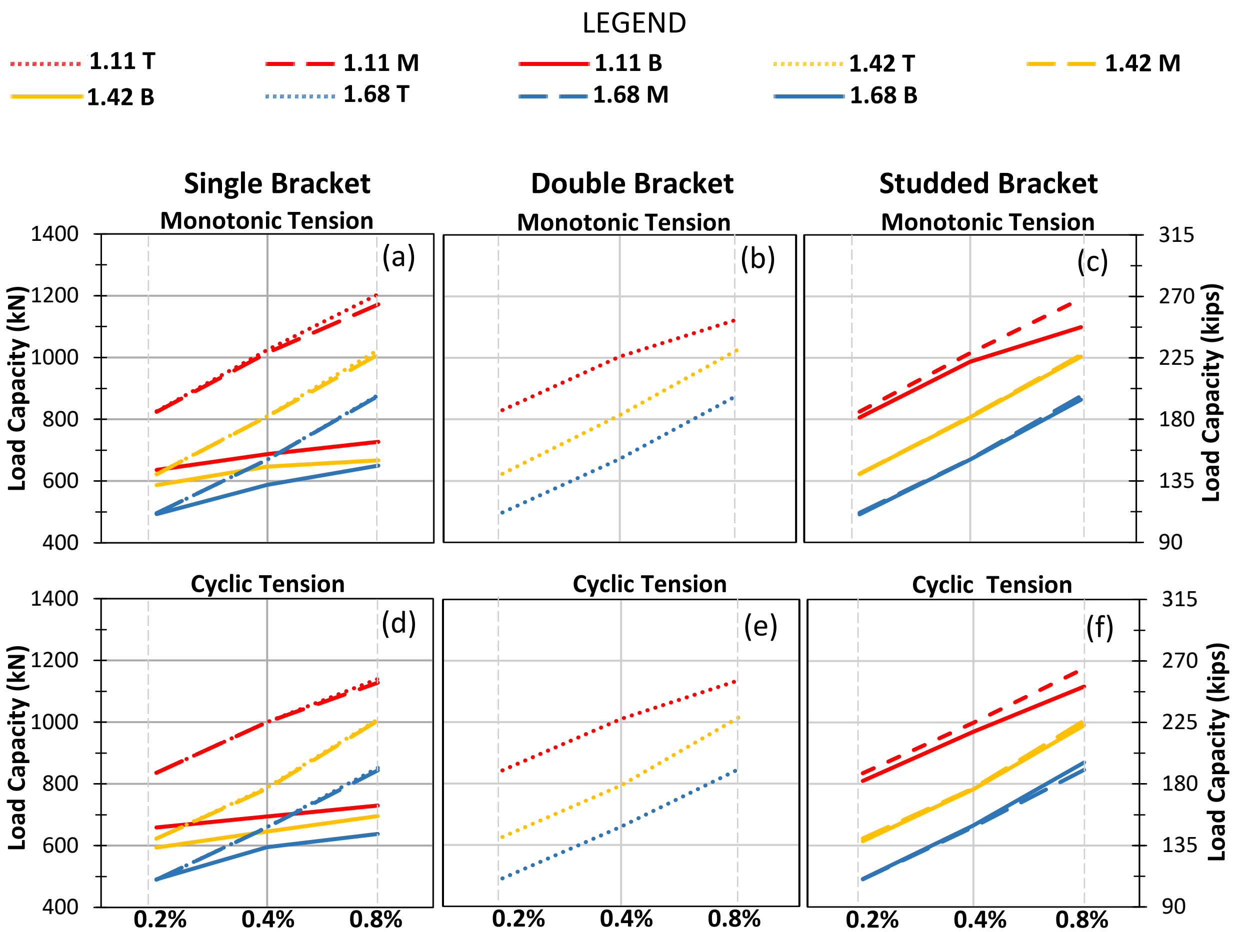

Figure 5-5: Effect of ρ_x% on the load capacity subjected to monotonic and cyclic tension.

- For the single bracket type in **Figs 5-5a** and **5-5d,** increasing the ρ_x% does not significantly affect the load capacity for the bottom h_e (i.e., , , and) when subjected to monotonic and cyclic tension. On the other hand, for the middle and top h_e, represented by dotted and dashed lines, increasing the ρ_x% increases the load capacity significantly.
- For the double bracket type in **Figs 5-5b** and **5-5e,** the load capacity is similar to that of the top h_e of the single bracket type when subjected to monotonic and cyclic compression, except for the red dotted line with 0.8 ρ_x% in which the load capacity decreases by a

negligible 6% when the bracket type is changed from single to double and subjected to monotonic tension.

- For the studded bracket type in **Figs 5-5c** and **5-5f,** the load capacity of the bottom or middle h_e is similar to that of the middle or top h_e of the single bracket type when subjected to monotonic and cyclic compression.
- For the configurations involving bottom h_e, the change of bracket type from single to studded improves the foundation capacity by an average of 22% (compare the blue lines in **Figs 5-5a** and **5-2d** with **Figs 5-5c** and **5-5f**).
- The tensile capacity of all bracket types increases with higher ρ_x% (as shown by the increasing slopes in **Fig 5-5** or the bar graphs in **Fig 5-6**). The loads in **Fig 5-6** represents the average of the loads of all the configurations involving a particular ρ_x%. For the single bracket type, the capacity increases by an average of 24% and 19%; for the double bracket type, by an average of 29% and 24%; and for the studded bracket type, by an average of 28% and 22%, when ρ_x% is increased from 0.2% to 0.4%, and 0.4% to 0.8% respectively. The cyclic tension shows similar gains in the load capacity.

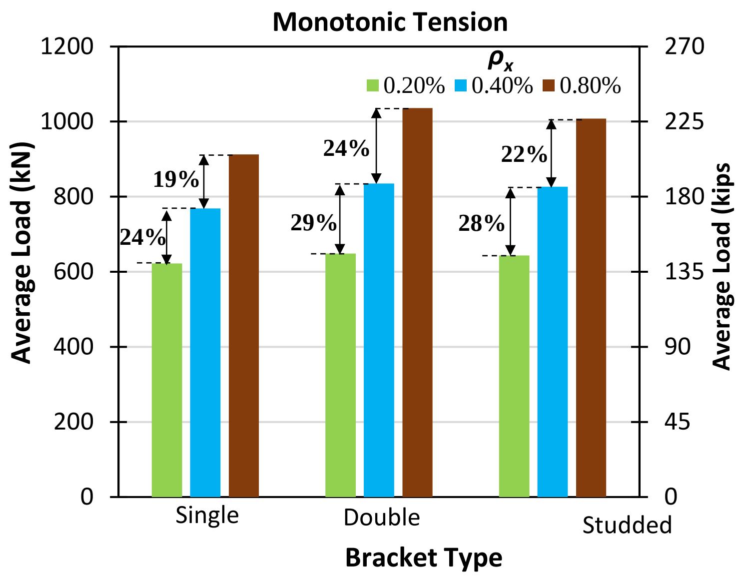

Figure 5-6: Plot of average load capacities for changing ρ_x%.

5.3.2 Compressive Load Behavior

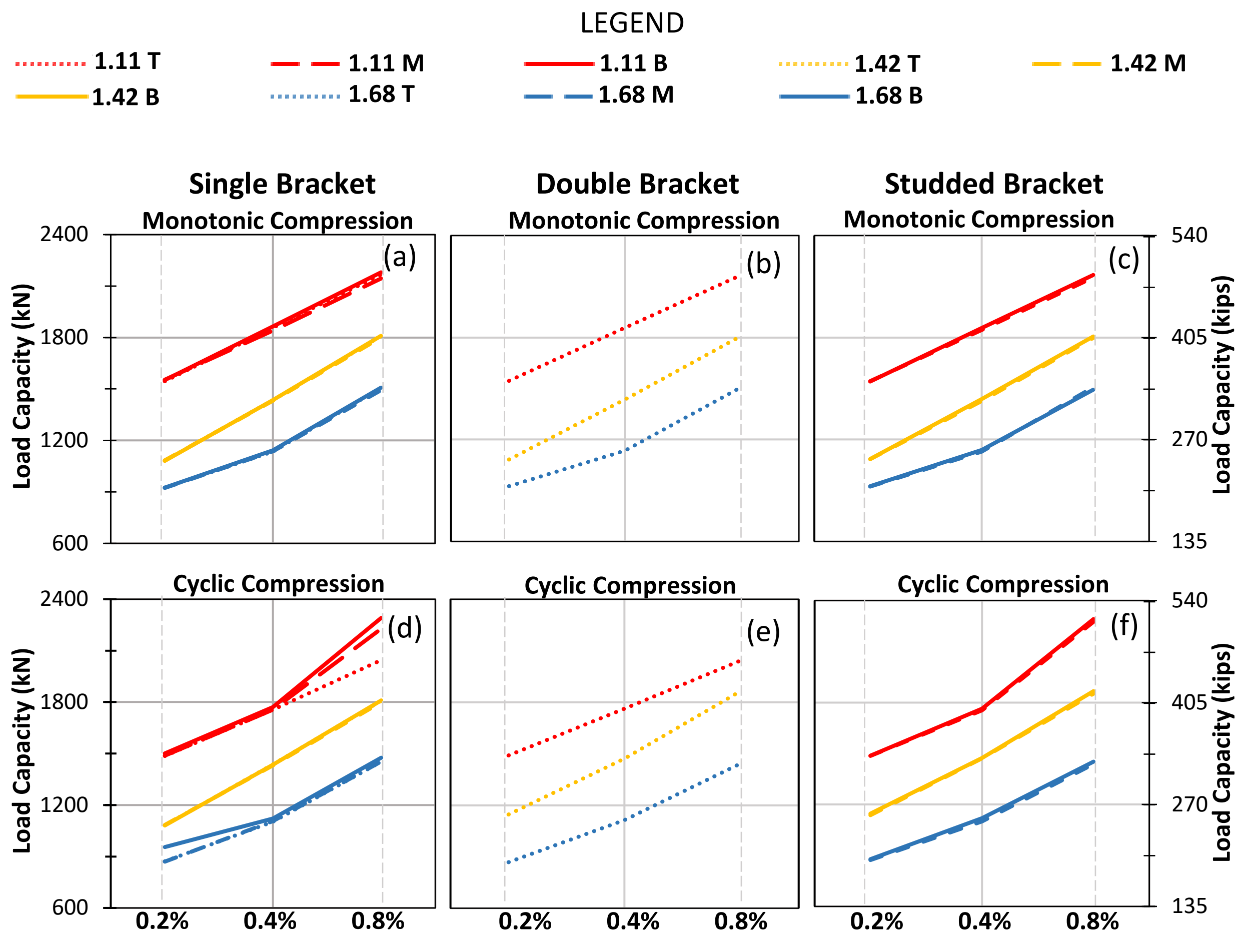

Figure 5-7: Effect of ρ_x% on the load capacity subjected to monotonic and cyclic compression.

- For the double bracket type, the load capacity is similar to that of the top h_e of the single bracket type (compare **Fig 5-7a** with **Fig 5-7b**, and **Fig 5-7d** with **Fig 5-7e**) when subjected to monotonic and cyclic compression.
- For the studded bracket type in **Figs 5-7c and 5-7f**, the load capacity of the bottom or middle h_e is similar to that of the middle or top h_e of the single bracket type when subjected to monotonic and cyclic compression.
- Similar to the tensile capacity, the compression capacity of all bracket types increases with higher ρ_x% (as shown by the increasing slopes in **Fig 5-7**). For the single bracket type, the capacity increases by an average of 24%; for the double bracket type, by an average of 25%; and for the studded bracket type, by an average of 24%, when the ρ_x% is increased from 0.2% to 0.4%, or 0.4% to 0.8% respectively. The cyclic compression shows similar gains in the load capacity.

5.4 Effect of *a/d* ratios on the Load Capacity

5.4.1 Tensile Load Behavior

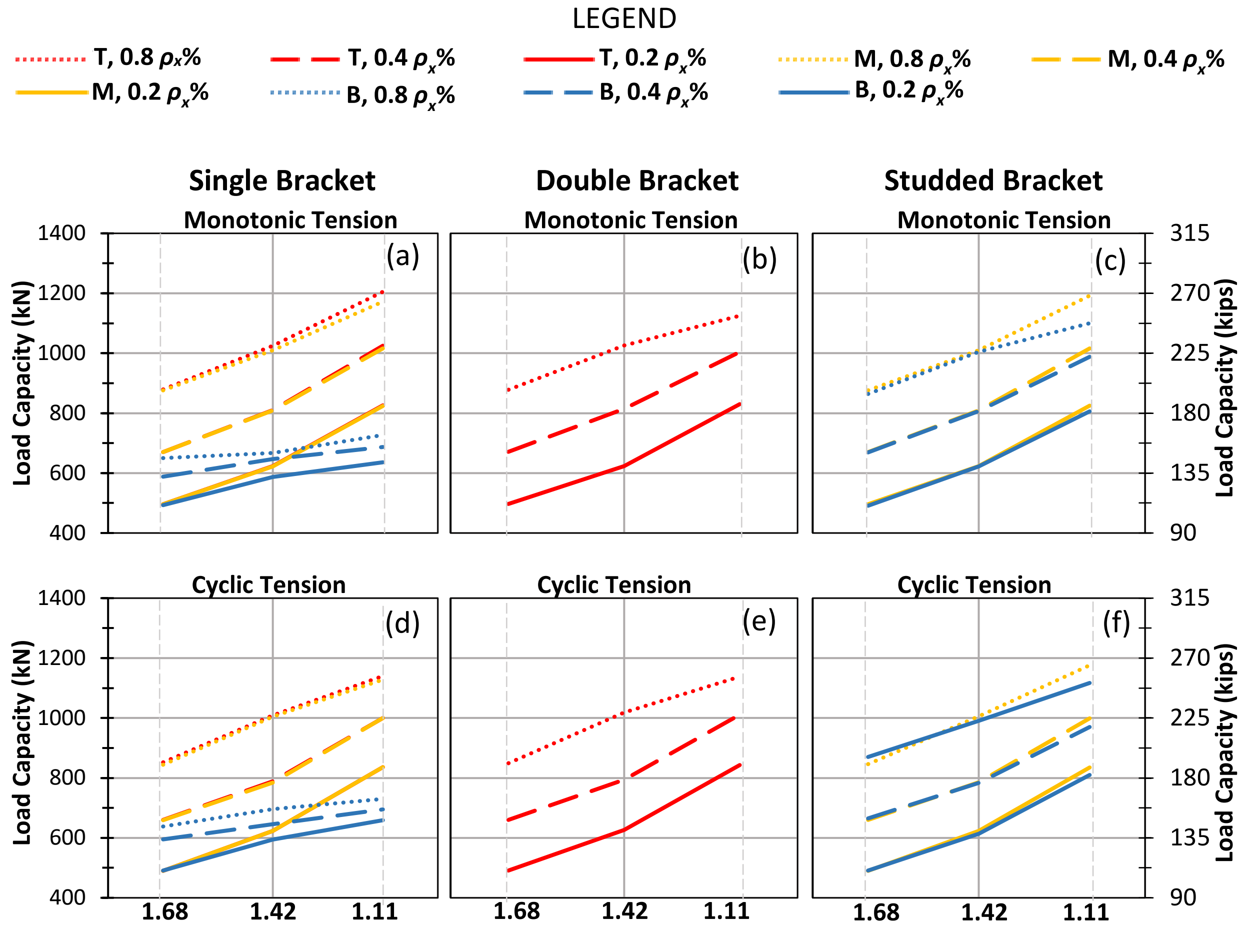

Figure 5-8: Effect of *a/d* ratio on the load capacity subjected to monotonic and cyclic tension.

- For the single bracket type in **Figs 5-8a** and **5-2d**, all three blue lines (i.e., , , and) are almost flat, which shows that the decrease in the *a/d* ratio does not significantly affect the load capacity of the bottom h_e when subjected to monotonic and cyclic tension. On the other hand, for the middle and top h_e, represented by dotted and dashed lines, decreasing the *a/d* ratio increases the load capacity significantly.
- Unlike ρ_x%, the tensile capacity of all bracket types increases with lower *a/d* ratio (as shown by the increasing slopes in **Fig 5-8** or the bar graphs in **Fig 5-9**). The loads in **Fig 5-9** represents the average of the loads of all the configurations involving a particular *a/d* ratio. For the single bracket type, the capacity increases by an average of 17% and 20%; for the double bracket type, by an average of 20% and 24%; and for the studded bracket type, by an average of 20% and 22%, when the *a/d* ratio is decreased from 1.68 to 1.42, and 1.42 to 1.11 respectively. The cyclic tension shows similar gains in the load capacity.

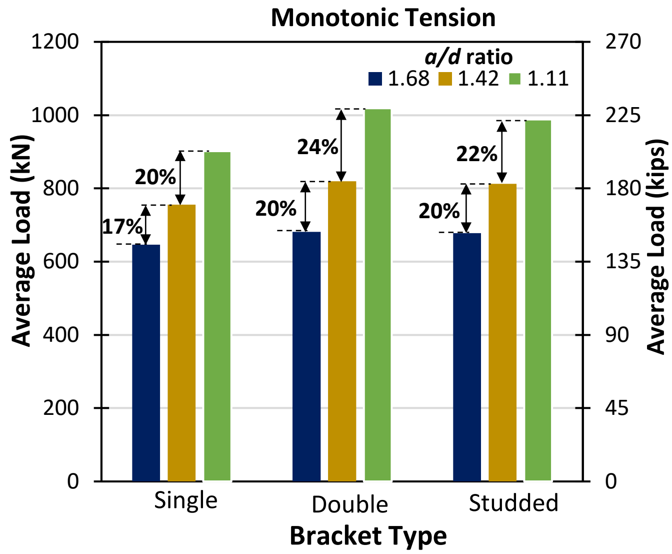

Figure 5-9: Plot of average load capacities for changing *a/d* ratio.

5.4.2 Compressive Load Behavior

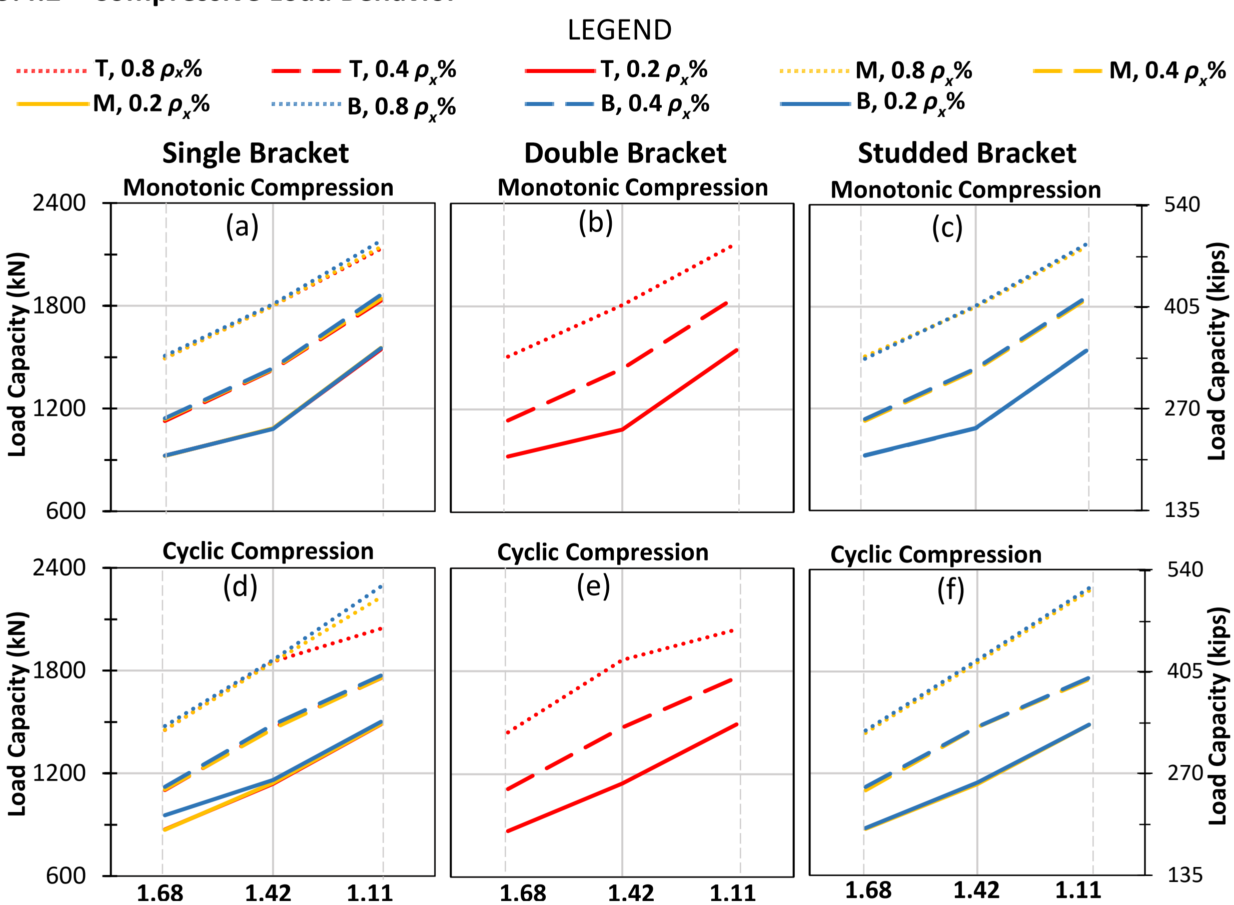

Figure 5-10: Effect of *a/d* ratio on the load capacity subjected to monotonic and cyclic compression.

- The load capacity of all bracket types increases with the increase in ρ_x% and decrease in *a/d* ratios similar to the tensile loading. This increase is more pronounced for the lowest ρ_x% as apparent from the bilinear nature of the solid lines in **Fig 5-10a**, **Fig 5-10b**, and **Fig 5-10c**. When the *a/d* ratio is changed from 1.42 to 1.11, the capacity increases for ρ_x of 0.2, 0.4, and 0.8 percentages are 43%, 29%, and 19% respectively in all three graphs.
- Unlike longitudinal reinforcement, the compressive capacity of all bracket types increases with lower *a/d* ratios (as shown by the increasing slopes in **Fig 5-10**). For all the bracket types, the capacity increases by an average of 21% and 29%, when the *a/d* ratio is decreased from 1.68 to 1.42, and 1.42 to 1.11 respectively. The cyclic compression shows similar gains in the load capacity.

5.5 Effect of h_e on the Displacement Capacity

5.5.1 Tensile Load Behavior

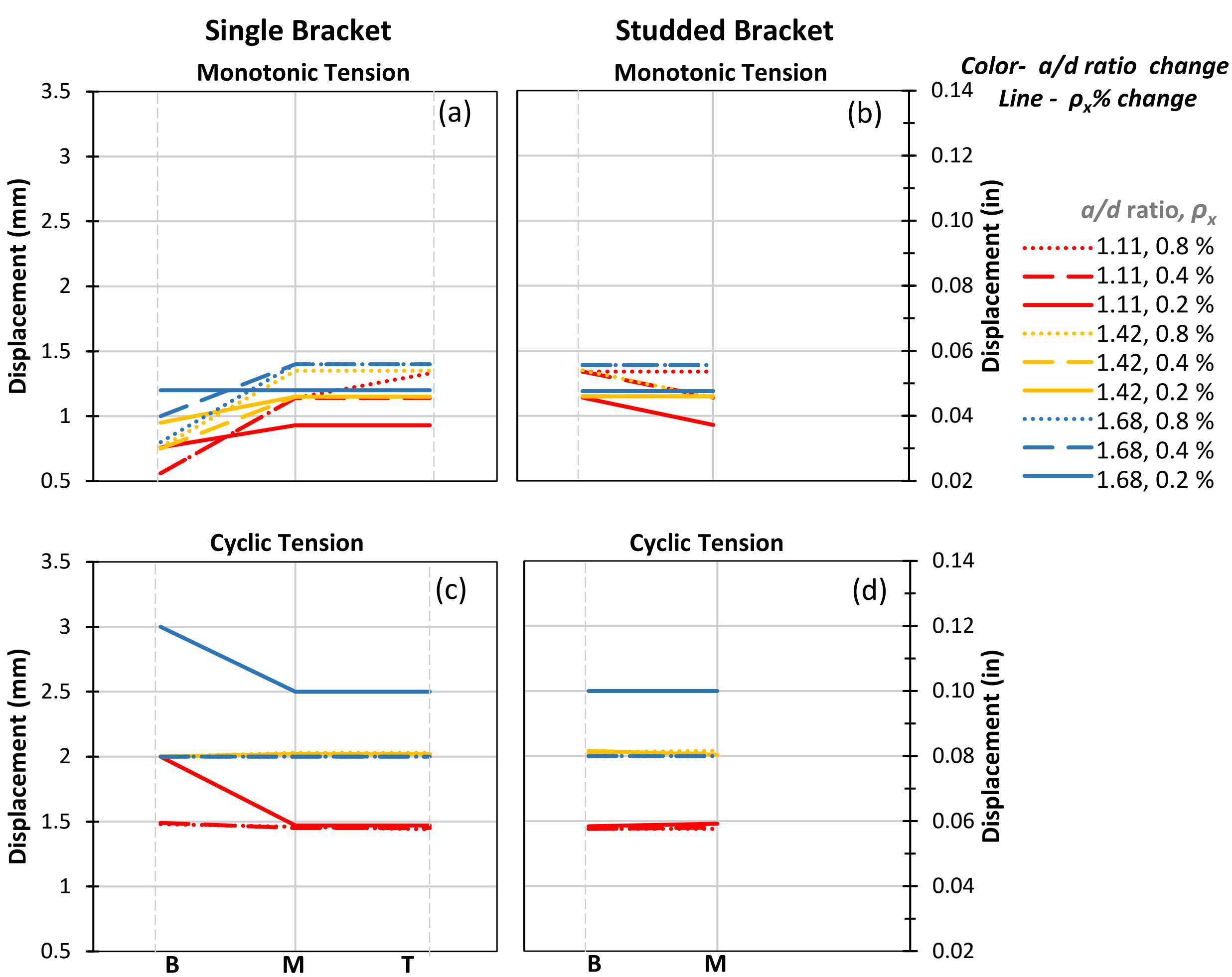

Figure 5-11: Effect of h_e on the displacement capacity subjected to monotonic and cyclic tension.

- One general trend is that, for the single bracket type in **Fig 5-11a**, when changing the h_e from bottom to middle, the displacement capacity increases by an average of 55% when subjected to monotonic tension.
- For the single bracket type in **Figs 5-11a** and **c**, when changing the h_e from middle to top, the displacement capacity remains very similar when subjected to monotonic and compression tension.
- For the studded bracket type in **Figs 5-11b** and **d**, when changing the h_e from middle to top, the displacement capacity remains very similar when subjected to monotonic and compression tension.

5.5.2 Compressive Load Behavior

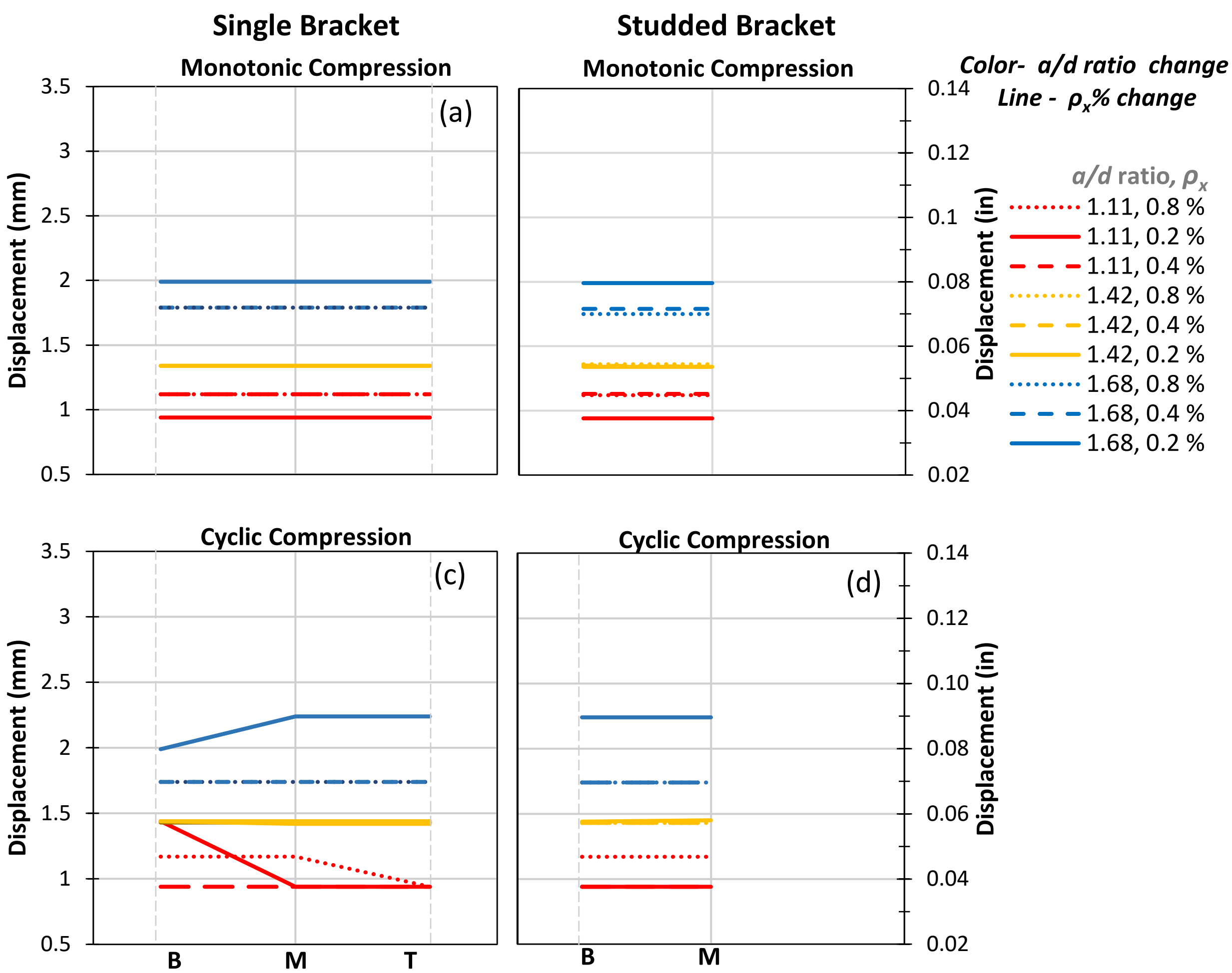

Figure 5-12: Effect of h_e on the displacement capacity subjected to monotonic and cyclic compression.

- For the single bracket type in **Figs 5-12a** and **5-12c**, all the lines are essentially horizontal which shows that the load capacity remains very similar for all the h_e when subjected to monotonic tension.
- For the studded bracket type in **Figs 5-12b** and **5-12d**, all the lines are essentially horizontal which shows that the load capacity remains very similar for all the h_e when subjected to monotonic and cyclic tension.

5.6 Comparison of Loading Types

Concrete is inherently weak in tensile loading. It is expected that helical pile foundations exhibit lower capacity in this type of loading in the absence of any vertical shear reinforcement. The same phenomenon applies to the cyclic components of the reversed-cyclic loading. Each blue and orange bar in **Fig 5-13** presents the average capacity of the 54 combined simulations of all the bracket types in a particular loading type. The helical pile foundation is found to be around 1.85 times stronger in compression than in tension which is similar to that of Diab's experimental specimens (Diab 2015), which were 1.82 times stronger in compression.

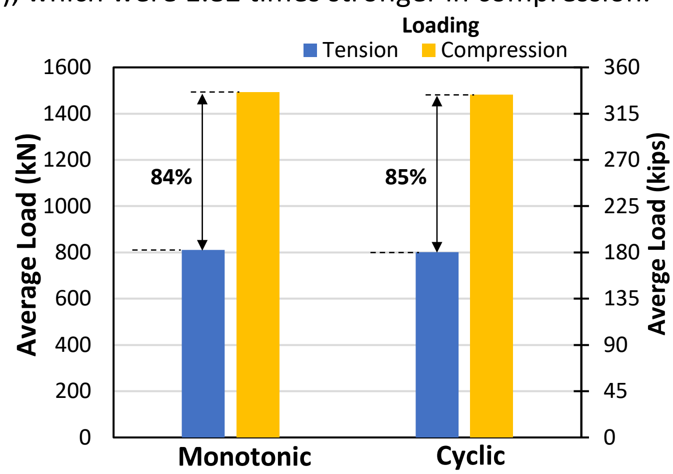

Figure 5-13: Plot of average load capacities subjected to different loading types.

5.7 Failure Modes

For all the brackets, there was no yielding of longitudinal reinforcement. The failure modes were either flexural, or shear failure, or anchorage failure.

5.7.1 Failure Mode Subjected to Monotonic Tension

All h_e exhibited first cracking in similar uplift loads (i.e., less than 5% difference).

5.7.1.1 Failure Mode of Single Bracket Anchorages

- Failure cracks are either flexural around the top longitudinal reinforcement or splitting of the concrete around the bracket zone as shown in **Fig 5-14**.

- The widespread and less-concentrated crack patterns (see **Fig 5-14b**) give higher load capacity as compared to concentrated crack patterns (see **Fig 5-14a**).
- Bottom h_e exhibits splitting of concrete around anchorage zone (see **Fig 5-14a**) where the cracks are concentrated around smaller regions. On the other hand, all top h_e and most middle h_e exhibits flexural cracks around longitudinal reinforcement (i.e., **Fig 5-14b**) where cracks are widespread and less concentrated. In other words, the bottom h_e exhibits the least preferable crack patterns.

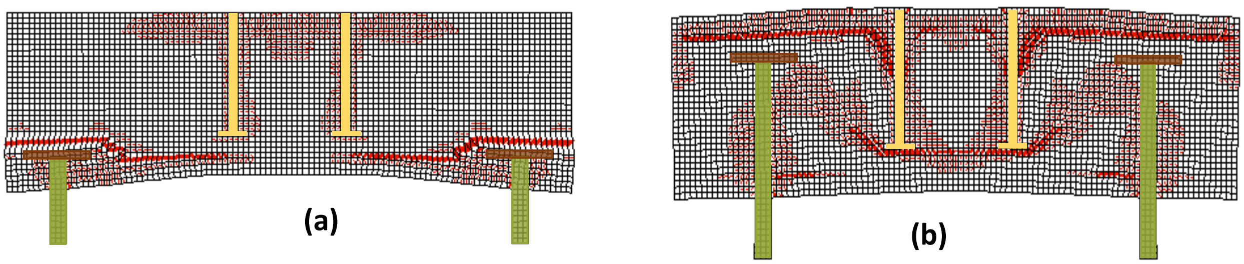

Figure 5-14: Crack Patterns (a) Splitting of concrete around bracket zone; (b) Flexural cracks around top longitudinal reinforcement.

5.7.1.2 Failure Mode of Double Bracket Anchorages

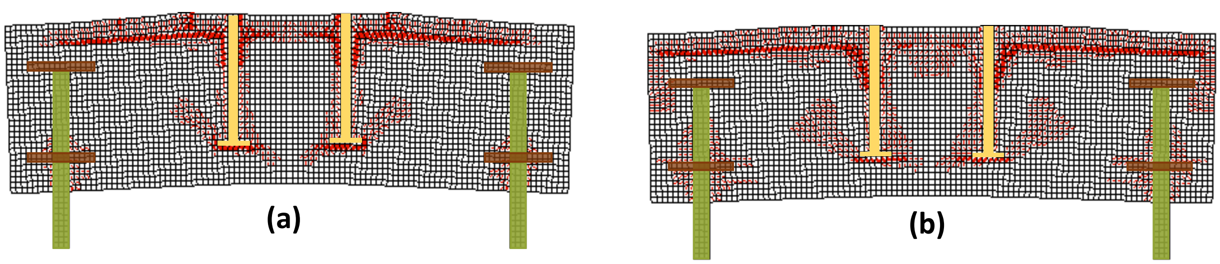

Figure 5-15: (a) Flexural cracks around top longitudinal reinforcement; (b) Flexural cracks around top longitudinal reinforcement with local cracks around the bottom plate.

- The crack patterns are flexural around the top longitudinal reinforcement for lower reinforcement percentage (see **Fig 5-15a**). Addition of local cracks around the bottom plate are predicted for higher reinforcement percentage (see **Fig 5-15b**). However, no premature failure is predicted in any of these simulations.

5.7.1.3 Failure Mode of Studded Bracket Anchorages

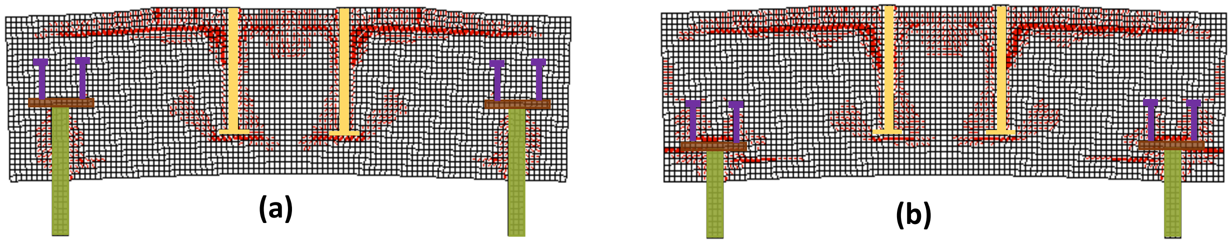

Figure 5-16: (a) Flexural cracks around top longitudinal reinforcement; (b) Flexural cracks around top longitudinal reinforcement with local cracks around the bottom plate.

- The crack patterns are flexural around the top longitudinal reinforcement for lower reinforcement percentage (see **Fig 5-16a**). The addition of local cracks around the bottom plate is predicted for higher reinforcement percentage (see **Fig 5-16b**). However, no anchorage zone failure is predicted for the bottom h_e.

5.7.2 Failure Mode Subjected to Monotonic Compression

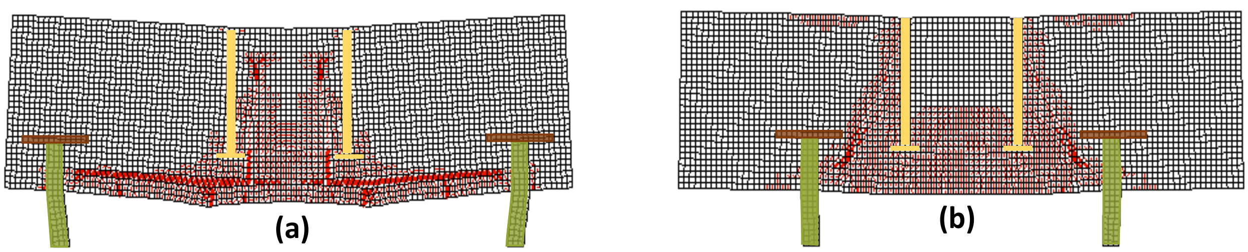

Figure 5-17: (a) Flexural cracks around top longitudinal reinforcement; (b) Shear cracks.

- For all the bracket types, the flexural cracks are predicted around bottom longitudinal reinforcement, where the cracks propagated from the tip of the anchor bolts to the helical pile supports through the concrete around the bottom reinforcement (see **Fig 5-17a**), except for the simulations with an *a/d* ratio of 1.11 and ρ_x% of 0.4 or 0.8 where shear failures occur (see **Fig 5-17b**). With the decreasing shear span, the beams become deeper and the shear failure governs on the condition that sufficient ρ_x% is provided.

5.7.3 Failure Mode Subjected to Reversed-cyclic

5.7.3.1 Failure Mode of Single Bracket Anchorages

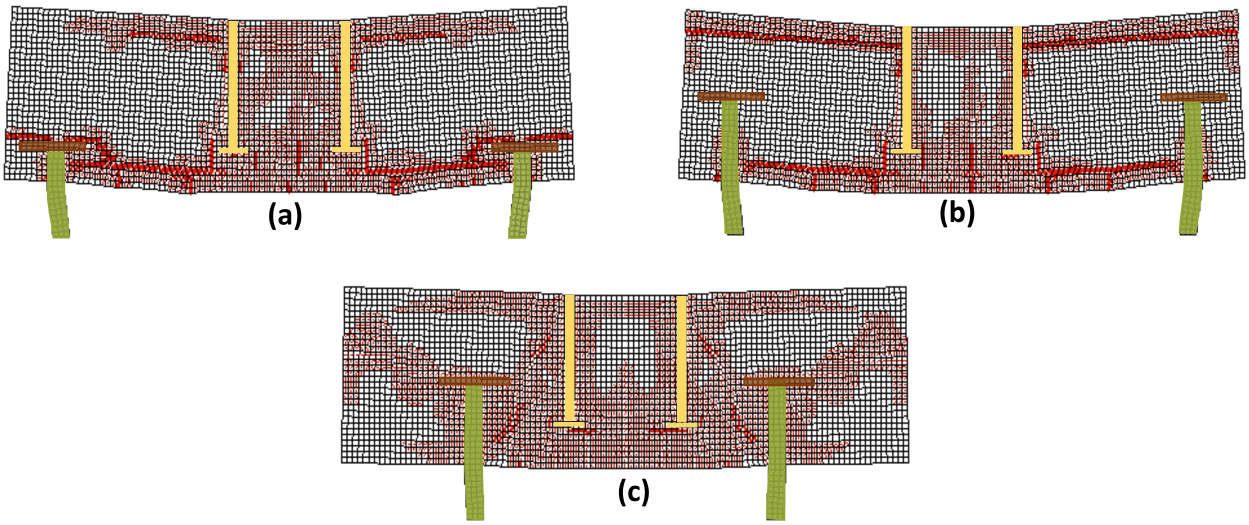

Figure 5-18: (a) Anchorage zone cracks around bracket zone and flexural cracks around longitudinal reinforcement; (b) Flexural cracks around longitudinal reinforcement; (c) Shear failure.

- Failure cracks are either combinations of anchorage zone cracks around bracket zone and flexural cracks around the longitudinal reinforcement (i.e., in **Fig 5-18a**), or flexural cracks around the longitudinal reinforcement (i.e., in **Fig 5-18b**), or shear cracks (i.e., in **Fig 5-18c**).
- Bottom h_e exhibits splitting of concrete around anchorage bracket zone (see **Fig 5-18a**) for which the load capacity is lower than that of the top and middle h_e which exhibit failure cracks as shown in **Fig 5-18b** or **Fig 5-18c**.
- For the simulations with higher ρ_x% and lower *a/d* ratio, shear failure is predicted for the middle and top h_e (see **Fig 5-18c**).

5.7.3.2 Failure Mode of Double Bracket Anchorages

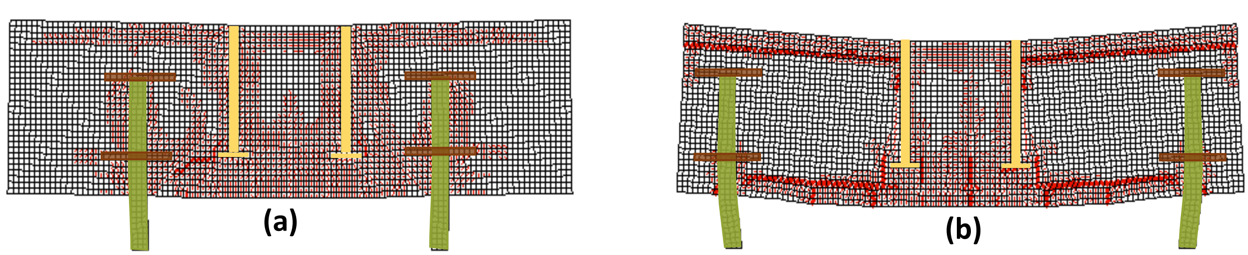

Figure 5-19: (a) Shear cracks; (b) Flexural cracks around longitudinal reinforcement.

- The simulations with an *a/d* ratio of 1.1 and, ρ_x% of 0.4 or 0.8 exhibit shear cracks (see **Fig 5-19a**) whereas all other simulations exhibit splitting of concrete around the longitudinal reinforcement (see **Fig 5-19b**).

5.7.3.3 Failure Mode of Studded Bracket Anchorages

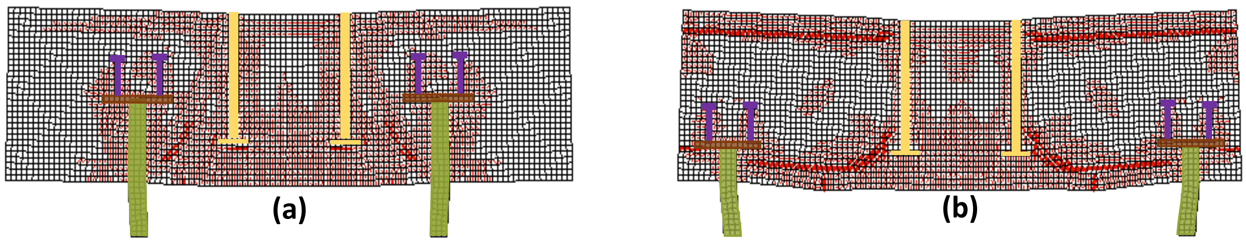

Figure 5-20: (a) Shear cracks; (b) Flexural cracks around longitudinal reinforcement

- The simulations with an *a/d* ratio of 1.1 and, ρ_x% of 0.4 or 0.8 exhibit shear cracks (see **Fig 5-20a**) whereas all other simulations exhibit splitting of concrete around longitudinal reinforcement (see **Fig 5-20b**).

6. Statistical Analysis

6.1 Introduction

The objective of this chapter is to use statistical methods to analyze the influence of the pile anchorage conditions on the global behavior of concrete foundations and to develop conclusions and recommendations for the efficient design of helical piles' anchorage zones. The analysis of variance and factorial design methods were used to study the influence of the different analyzed parameters on the monotonic compressive and tensile load capacity of concrete foundations. Since the response of the helical pile foundation subjected to the reversed-cyclic load was similar to that of the monotonic loading, this analysis holds true for the reversed-cyclic also.

6.2 Statistical Analysis of Experiments

Experimental design methods have found broad application in many disciplines. Much of the research in engineering, science, and industry is empirical and makes extensive use of experimentation. Statistical methods can greatly increase the efficiency of these experiments and often strengthens the conclusions so obtained. Statistical analysis methods are particularly important in cases when it is not obvious that the difference in the experimental result caused by the change of an analyzed parameter level is large enough to imply that the different configurations are different or not (Montgomery 2013). Throughout this chapter, two important concepts of statistical analysis of experiments will be extensively used: the Analysis of Variance (ANOVA) and the factorial design (Fisher 1992).

The analysis of variance relies on the partitioning of the total variability of the collected dataset into its component parts. In statistical analysis, the total sum of squares is used as a measure of the overall variability in the data (see **Equation 6-1**).

$$SS_T = \sum_{i=1}^{a} \sum_{j=1}^{n} \left(y_{ij} - \bar{y}_{..}\right)^2 \tag{6-1}$$

where *i* is the different levels of the parameter *a* being investigated, *n* is the number of replicates for each experiment, y_{ij} is the collected result under level *i* and replicate *j*, and $\bar{y}_{..}$ is the average of all the collected results.

The fundamental ANOVA identity states that the total sum of squares can be decomposed into the sum of squares of the treatments plus the sum of squares of the random error (see **Equation 6-2**).

$$SS_T = SS_{Treatments} + SS_E \tag{6-2}$$

where $SS_{Treatments}$ is the sum of squares of the treatments (which comprise the sum of the individual sum of squares of each parameter being investigated and their respective interactions), and SS_E is the sum of squares of the error.

This identity indicates that the sum of squares of the individual treatments (i.e., the different parameters analyzed in the experiment) can be used to determine if the changes in the experimental result due to the changes in the different parameters are statistically significant or not. The checking of the significance of a parameter is part of a hypothesis test. The most common hypothesis test is that **1)** the means of the results do not change with a change in the parameters levels (also called the null hypothesis) or that **2)** the means of the results do change with a change in the parameter levels (also called the alternative hypothesis). The ANOVA analysis relies on the data to follow a chi-squared distribution (Satterthwaite 1946) and defines the ratio F_0 in order to test if the null hypothesis is true (see **Equation 6-3**). If the calculated F_0 value of a given treatment effect is higher than a given threshold, that treatment effect has statistical significance in the experiment.

$$F_0 = \frac{MS_{Treatments}}{MS_E} \tag{6-3}$$

where $MS_{Treatments}$ is the mean square of the treatments, and MS_E is the mean square of the error.

The factorial design is an efficient type of experiment when two or more parameters are analyzed. In a factorial design, in each complete replicate of the experiment all possible combinations of the levels of the parameters are investigated. For example, if two parameters *A* and *B* are investigated in a fictitious experiment, and each of these parameters have two levels such as low (-) and high (+), a factorial design would have, in each replicate, 2^2 = 4 combinations investigated (i.e., A-B-, A+B-, A+B+, A-B+). This type of design is more efficient than one-factor-at-a-time type of experiments and it is necessary when the interaction between the different parameters may be present to avoid misleading conclusions. The ANOVA analysis can be used in analyzing factorial designed experiments in order to indicate which parameters (or their interaction) are statistically significant.

To allow the use of ANOVA and factorial design concepts, the experimentally collected data is usually assumed to follow a model and a set of pre-determined assumptions. The most commonly used model (and the one used in this study) is given in **Equation 6-4** alongside the assumptions that the errors are normally and independently distributed with mean zero and constant but unknown variance σ^2. These assumptions are the foundations on which the ANOVA and factorial designs are built and they must be appropriately checked to ensure the accuracy of the conclusions.

$$y_{ij} = \mu + \tau_i + \beta_j + (\tau\beta)_{ij} + \epsilon_{ij} \tag{6-4}$$

where μ is the overall mean effect, τ_i is the effect of the i_{th} level of the first parameter, β_j is the effect of the j_{th} level of the second parameter, $(\tau\beta)_{ij}$ is the effect of the interaction between τ_i and β_j, and ϵ_{ij} is the random error component.

6.3 Analysis Set Up

In this study, the four different parameters being investigated are h_e of the bracket, ρ_x %, *a/d* ratio, and different types of helical pile brackets. For each of these parameters there are, in general, three different levels (i.e., 1.11, 1.42, and 1.68 for the *a/d* ratio, 0.2%, 0.4%, and 0.8% for the ρ_x, bottom, middle, and top for the h_e, and single bracket, studded bracket, and double bracket types for the 'bracket'). Thus, this constitutes a 3^4 factorial design. However, some of the foundations do not have three levels for all the parameters, such as the studded bracket type has only two h_e, and the double bracket type has only one h_e. As such, the statistical analysis was performed on a set of three factorial designs, one for each type of brackets. The results of the individual statistical analysis can be considered to perform a single analysis including the bracket types as an investigated parameter.

For each type of bracket analyzed, two response variables were considered: **1)** the peak load capacity under monotonic compressive load and **2)** the peak load capacity under monotonic tensile load. **Fig 6-1** shows how the response variable was collected from the load-displacement curve obtained for each numerical analysis performed.

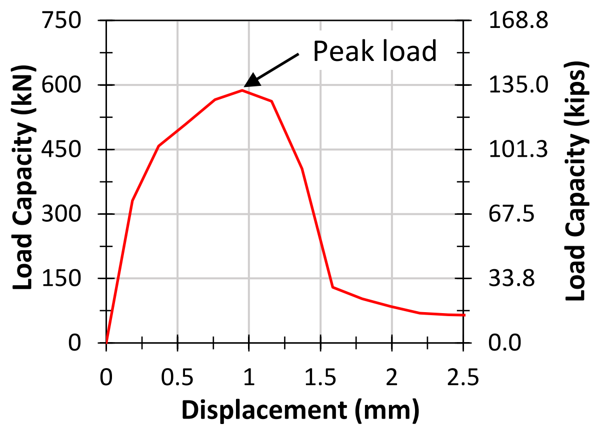

Figure 6-1: Example of a load-displacement curve extracted from one of the numerical analysis.

To enable an easier representation, the three analyzed parameters were categorized in the following way: (***A***) *a/d* ratio; (***B***) ρ_x; (***C***) h_e of the bracket type; and their respective interactions are represented as ***AB***, ***AC***, etc.

6.4 Results under Tension Load

6.4.1 Single Bracket Type

For the single bracket, **Table 6-1** shows the results of the analysis of the sums of squares of each analyzed parameter. The *a/d* ratio, ρ_x, and h_e parameters dominated this process, accounting for 87.8% of the total variability, whereas all of the two- and three-parameter interactions accounted for the remaining 12.2%. This conclusion diverges from the case of compression load, where h_e was found to be insignificant. In addition to the three main effects, the ***AC*** and ***BC*** interactions appear to have some significance, which was statistically studied in an ANOVA analysis.

Table 6-1: Analysis of the sums of squares of single bracket type under tension.

Parameters	Sum of Squares	% Contribution
***a/d* ratio (A)**	296668.13	28.1%
ρ_x% (B)	378332.08	35.8%
h_e (C)	251923.19	23.9%
AB	1143.31	0.1%
AC	51825.61	4.9%
BC	73869.78	7.0%
ABC	1943.85	0.2%
Total	1055705.94	

The ANOVA analysis in **Table 6-2** was used to confirm the magnitude of these effects. The non-significant parameters (and their interactions) were moved to the residual term of the ANOVA table and only the main parameters ***A***, ***B***, ***C***, and the two-parameter interactions ***AC*** and ***BC*** were considered in the final model. The high values of F_0 (and consequently lower values of the p-value), corroborated the conclusions that parameters ***A***, ***B***, ***C*** are statistically significant in this experiment. In addition, the ***AC*** and ***BC*** interactions, although contributing significantly less (see **Table 6-1**), are also statistically significant.

Table 6-2: ANOVA analysis for single bracket type under tension.

Parameters	Sum of Squares	Degrees of Freedom	Mean Squares	F_0	P-val
***a/d* ratio (A)**	296668.13	2	148334.06	576.58	<0.01
ρ_x% (B)	378332.08	2	189166.04	735.30	<0.01
h_e (C)	251923.19	2	125961.59	489.62	<0.01
AC	51825.61	4	12956.40	50.36	<0.01
BC	73869.78	4	18467.44	71.78	<0.01
Residual (LOF)	3087.16	12	257.26		
Total	1055705.94	26			

The ***AB***, ***AC***, and ***BC*** interactions are plotted in **Fig 6-2a**, **Fig 6-2b**, and **Fig 6-2c** to provide a visual investigation of the influence of the calculated significant parameters on the tensile load supported by the helical pile. The similar slopes of the three curves in **Fig 6-2a** verified the conclusion of no interaction between these two main effects. The different slopes in the ***AC*** and ***BC*** plots showed the statistically calculated (see **Table 6-2**) interaction between these parameters. This interaction indicated that as *a/d* ratio increased, the tension load capacity provided by the different embedment depths diminished (see **Fig 6-2b**). Similarly, as the ρ_x% decreased, the tension load capacity provided by the different h_e diminished (see **Fig 6-2c**). In addition, the analyses of **Fig 6-2b** and **Fig 6-2c** showed that there is no difference in tension load capacity when the h_e parameter has a value of mid or top. The combined analysis of **Fig 6-2** can be used to conclude that the combination of low *a/d* ratio, high ρ_x, and either mid or top h_e yields the highest tension load capacity.

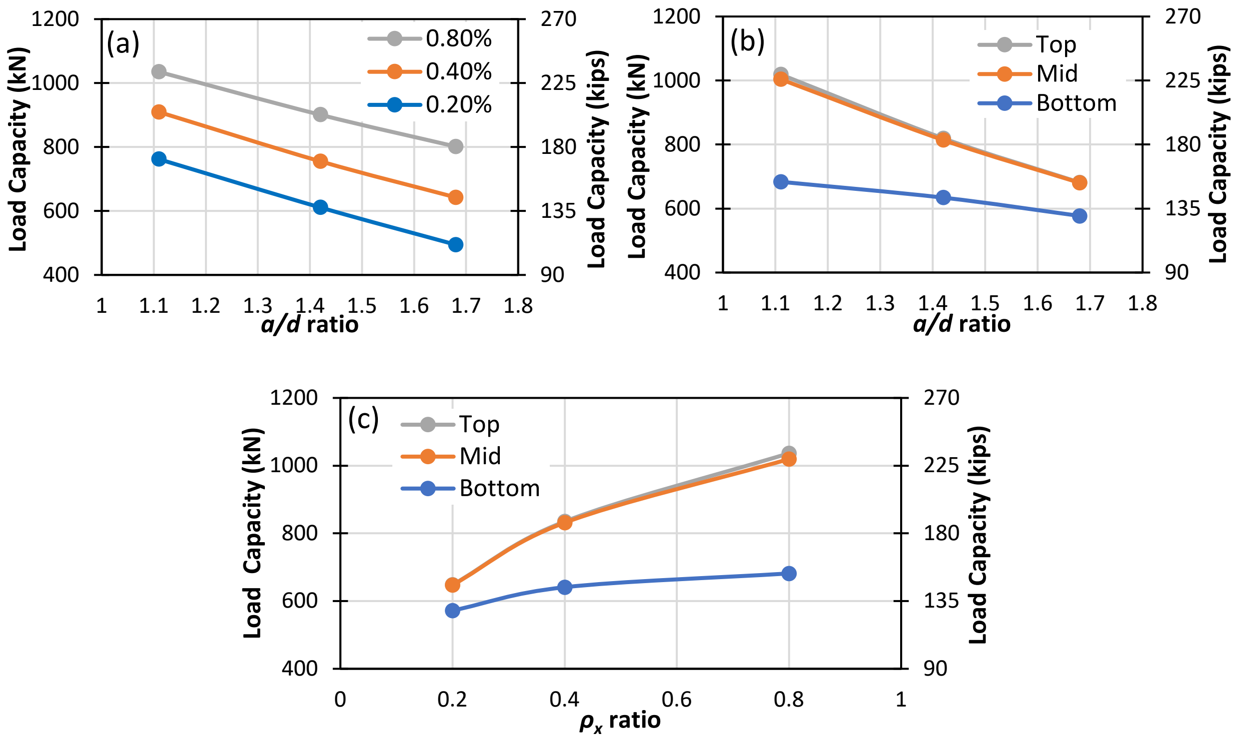

Figure 6-2: Tension load under different (a) *a/d* ratio and ρ_x% combinations, (b) *a/d* ratio and h_e combinations, and (c) ρ_x% and h_e combinations.

6.4.2 Double Bracket Type

For the double bracket, **Table 6-3** shows the results of the analysis of the sums of squares of each analyzed parameter. Note that **Table 6-3** shows the results of only two parameters since the double bracket type studied has only one h_e. Similar to the results calculated for the single bracket type, the *a/d* ratio and ρ_x% parameters dominated this process, accounting for 99.9% of the total variability, whereas the two-parameter interaction accounted for the remaining 0.1%.

Table 6-3: Analysis of the sums of squares of double bracket type under tension.

Parameters	Sum of Squares	Degrees of Freedom	% Contribution
***a/d* ratio (A)**	172254.89	2	43.2%
ρ_x% (B)	225923.56	2	56.7%
AB	438.44	4	0.1%
Total	398616.89	8	

The ANOVA analysis in **Table 6-4** was used to confirm the magnitude of these effects. The two-parameter interaction was moved to the residual term of the ANOVA table and only the main parameters ***A*** and ***B*** were considered in the final model. The high values of F_0 (and consequently lower values of the p-value), corroborated the conclusions that only parameters ***A*** and ***B*** are statistically significant in this experiment.

Table 6-4: ANOVA analysis for double bracket type under tension.

	Sum of Squares	Degrees of Freedom	Mean Squares	F0	P-val
***a/d* ratio (A)**	172254.89	2	86127.44	785.75	<0.01
ρ_x% (B)	225923.56	2	112961.80	1030.57	<0.01
Residual (LOF)	438.44	4	109.61		
Total	398616.89	8			

The ***AB*** interaction is plotted in **Fig 6-3** to provide a visual investigation of the influence of the observed significant parameters on the compressive load supported by the helical pile. The similar slopes of the three curves in **Fig 6-3** verified the conclusion of no interaction between these two main effects. It can also be concluded from **Fig 6-3** that the combination of low *a/d* ratio and high ρ_x% yielded the highest compressive load capacity.

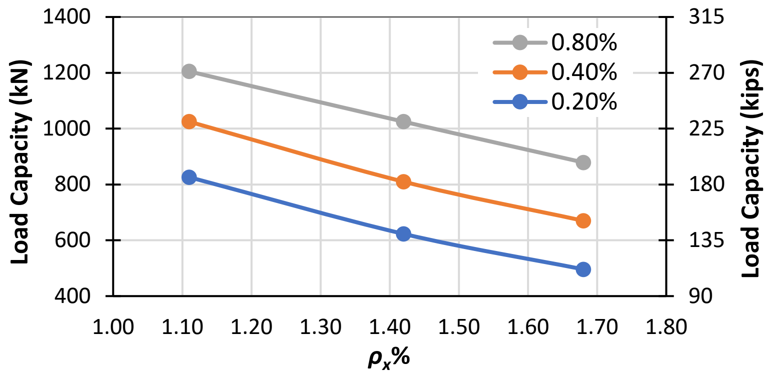

Figure 6-3: Tension load under different *a/d* ratio and ρ_x% combinations.

6.4.3 Studded Bracket Type

For the studded bracket, **Table 6-5** shows the results of the analysis of the sums of squares of each analyzed parameter. The *a/d* ratio and ρ_x% parameters dominated this process, accounting for 89.9% of the total variability, whereas the h_e parameter and all of the two- and three-parameter interactions accounted for the remaining 1.1%.

Table 6-5: Analysis of the sums of squares of studded bracket type under tension.

Parameters	Sum of Squares	% Contribution
***a/d* ratio (A)**	290250.33	41.8%
ρ_x% (B)	397126.33	57.1%
h_e (C)	1530.89	0.2%
AB	2559.33	0.4%
AC	1756.78	0.3%
BC	750.11	0.1%
ABC	872.22	0.1%
Total	694846.00	

The ANOVA analysis in **Table 6-6** was used to confirm the magnitude of these effects. The non-significant parameters (and their interactions) were moved to the residual term of the ANOVA table and only the main parameters ***A*** and ***B*** were considered in the final model. The high values of F_0 (and consequently lower values of the p-value), corroborated the conclusions that only parameters ***A*** and ***B*** are statistically significant in this experiment.

Table 6-6: ANOVA analysis for studded bracket type under tension.

Parameters	Sum of Squares	Degrees of Freedom	Mean Squares	F_0	P-val
A	290250.33	2	145125.17	252.58	<0.01
B	397126.33	2	198563.17	345.59	<0.01
Residual (LOF)	7469.33	13	574.56		
Total	694846.00	17			

The ***AB*** interaction is plotted in **Fig 6-4** to provide a visual investigation of the influence of the observed significant parameters on the compressive load supported by the helical pile. The similar slopes of the three curves in **Fig 6-4** verified the conclusion of no interaction between these two main effects. It can also be concluded from **Fig 6-4** that the combination of low *a/d* ratio and high ρ_x% yielded the highest compressive load capacity.

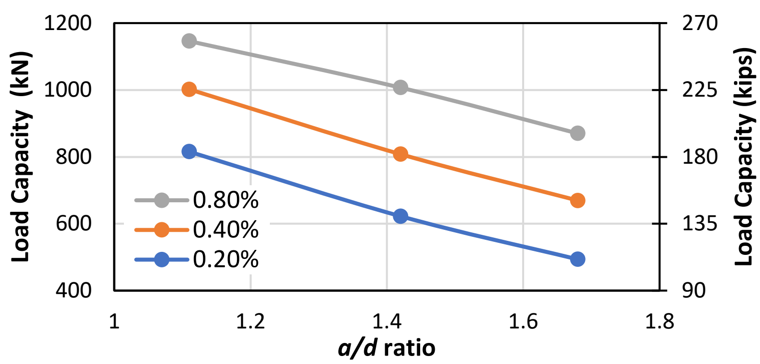

Figure 6-4: Tension load under different *a/d* ratio and ρ_x% combinations.

6.4.4 Comparison of Bracket Types

The analysis of each individual helical pile revealed that the embedment depth was only statistically significant for the single bracket. Thus, to allow a direct comparison of all three-bracket type helical piles, the h_e parameter was removed and an additional 'bracket type' (***C***) parameter was introduced in the statistical analysis. The results corresponding to the optimal h_e alternative for the single bracket type (i.e., the top h_e) was used in this analysis. **Table 6-7** shows the results of the analysis of the sums of squares for the new set of analyzed parameters. Similar to the results calculated for each individual bracket type of helical piles, the *a/d* ratio and ρ_x% parameters dominated the experiment, accounting for 99.9% of the total variability, whereas the 'bracket type' parameter and all of the two- and three-parameter interactions accounted for the remaining 0.1%.

Table 6-7: Analysis of the sums of squares of all types of bracket under tension.

Parameters	Sum of Squares	Degrees of Freedom	% Contribution
***a/d* ratio (A)**	510635.68	2	43.3%
ρ_x% (B)	666456.46	2	56.6%
Bracket Type (C)	131.16	2	0.0%
AB	1101.68	4	0.1%
AC	48.99	4	0.0%
BC	108.17	4	0.0%
ABC	40.98	8	0.0%
Total	1178523.12	26	

The results of the ANOVA analysis considering only parameters ***A*** and ***B*** in the final model are shown in **Table 6-8**. The high values of F_0 (and consequently lower values of the p-value), corroborates the conclusions that parameters ***A*** and ***B*** are statistically significant in this experiment.

Table 6-8: ANOVA analysis for all types of piles under tension.

Parameters	Sum of Squares	Degrees of Freedom	Mean Squares	F_0	P-val
***a/d* ratio (A)**	510635.68	2	255317.84	3925.28	<0.01
ρ_x% (B)	666456.46	2	333228.23	5123.09	<0.01
Residual (LOF)	1430.98	22	65.04		
Total	1178523.12	26			

The ***AB*** interaction is plotted in **Fig 6-5** to provide a visual investigation of the influence of the observed significant parameters on the compressive load supported by the helical pile. The similar slopes of the three curves in **Fig 6-5** verified the conclusion of no interaction between these two main effects. It can also be noted through the investigation of **Fig 6-5** and **Fig 6-2**, **Fig 6-3**, and **Fig 6-4** that the tensile capacity of all the three brackets analyzed have similar magnitudes, which corroborates the conclusion that this parameter has no influence in the compressive capacity. From **Fig 6-5** it can also be concluded that the combination of low *a/d* ratio and high ρ_x% yields the highest compressive load capacity.

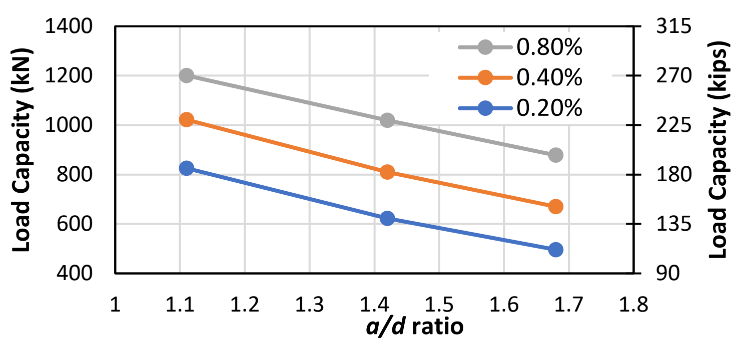

Figure 6-5: Tension load under different *a/d* ratio and ρ_x% combinations.

6.5 Results under Compressive Load

6.5.1 Single Bracket Type

For the single bracket type, **Table 6-9** shows the results of the analysis of the sums of squares of each analyzed parameter. The '% contribution' column measures the contribution of each parameter effect (and their respective interactions) relative to the total sum of squares. This contribution is a rough but effective guide to the relative importance of each parameter effect. The *a/d* ratio and ρ_x% parameters dominated this process, accounting for 99.4% of the total variability, whereas the h_e parameter and all of the two- and three-parameter interactions accounted for the remaining 0.6%.

Table 6-9: Analysis of the sums of squares of single bracket type under compression.

Parameters	Sum of Squares	% Contribution
***a/d* ratio (A)**	2017357.19	52.5%
ρ_x% (B)	1801655.49	46.9%
h_e (C)	1123.74	0.0%
AB	24017.62	0.6%
AC	478.04	0.0%
BC	531.59	0.0%
ABC	160.92	0.0%
Total	3845324.60	

The ANOVA analysis in **Table 6-10** was used to confirm the magnitude of these effects. The non-significant parameters (and their interactions) were moved to the residual term of the ANOVA table and only the main parameters ***A*** and ***B*** were considered in the final model. The high values of F0 (and consequently lower values of the p-value), corroborated the conclusions that only parameters ***A*** and ***B*** are statistically significant in this experiment.

Table 6-10: ANOVA analysis for single bracket type under compression.

Parameters	Sum of Squares	Degrees of Freedom	Mean Squares	F_0	P-val
A	2017357.19	2	1008678.60	843.38	<0.01
B	1801655.49	2	900827.75	753.20	<0.01
Residual (LOF)	26311.91	22	1196.00		
Total	3845324.59	26			

The AB interaction is plotted in **Fig 6-6** to provide a visual investigation of the influence of the observed significant parameters on the compressive load supported by the helical pile. The similar slopes of the three curves in **Fig 6-6** verified the conclusion of no interaction between these two main effects. It can also be concluded from **Fig 6-6** that the combination of low *a/d* ratio and high ρ_x% yielded the highest compressive load capacity.

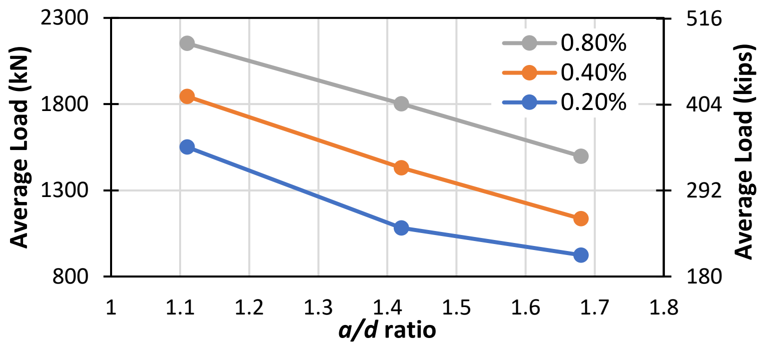

Figure 6-6: Compressive load under different *a/d* ratio and ρ_x% combinations.

6.5.2 Double Bracket Type

For the double bracket type, **Table 6-11** shows the results of the analysis of the sums of squares of each analyzed parameter. Note that **Table 6-11** shows the results of only two parameters since the double bracket type studied has only one h_e. Similar to the results calculated for the single bracket type, the *a/d* ratio and ρ_x% parameters dominated this process, accounting for 99.4% of the total variability, whereas two-parameter interaction accounted for the remaining 0.6%.

Table 6-11: Analysis of the sums of squares of double bracket type under compression.

Parameters	Sum of Squares	% Contribution
***a/d* ratio (A)**	681014.89	51.9%
ρ_x% (B)	622576.89	47.5%
AB	8193.78	0.6%
Total	1311785.56	

The ANOVA analysis in **Table 6-12** was used to confirm the magnitude of these effects. The two-parameters interaction was moved to the residual term of the ANOVA table and only the main parameters ***A*** and ***B*** were considered in the final model. The high values of F_0 (and consequently lower values of the p-value), corroborated the conclusions that only parameters ***A*** and ***B*** are statistically significant in this experiment.

Table 6-12: ANOVA analysis for double bracket type under compression.

Parameters	Sum of Squares	Degrees of Freedom	Mean Squares	F_0	P-val
***a/d* ratio (A)**	681014.89	2	340507.40	166.23	<0.01
ρ_x% (B)	622576.89	2	311288.40	151.96	<0.01
Residual (LOF)	8193.78	4	2048.44		
Total	1311785.56	8			

The ***AB*** interaction is plotted in **Fig 6-7** to provide a visual investigation of the influence of the observed significant parameters on the compressive load supported by the helical pile. The similar slopes of the three curves in **Fig 6-7** verified the conclusion of no interaction between these two main effects. It can also be concluded from **Fig 6-7** that the combination of low *a/d* ratio and high ρ_x% yielded the highest compressive load capacity.

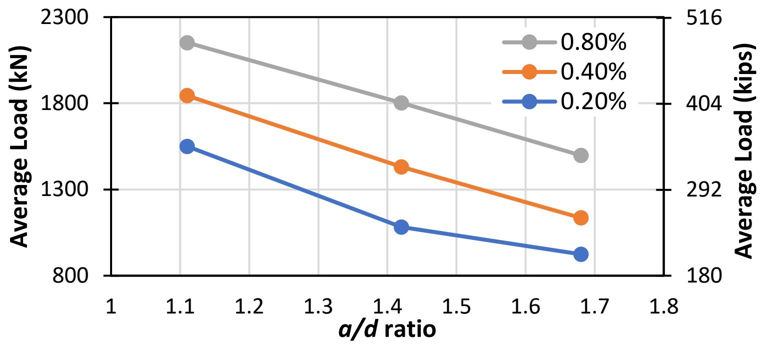

Figure 6-7: Compressive load under different *a/d* ratio and ρ_x% combinations.

6.5.3 Studded Bracket Type

For the studded bracket type, **Table 6-13** shows the results of the analysis of the sums of squares of each analyzed parameter. Similar to the results calculated for the single bracket type, the *a/d* ratio and ρ_x% parameters dominated this process, accounting for 99.4% of the total variability, whereas the h_e parameter and all of the two- and three-parameter interactions accounted for the remaining 0.6%.

Table 6-13: Analysis of the sums of squares of studded bracket type under compression.

Parameters	Sum of Squares	% Contribution
***a/d* ratio (A)**	1351428.78	52.2%
ρ_x% (B)	1222343.11	47.2%
h_e (C)	93.39	0.0%
AB	15275.56	0.6%
AC	63.44	0.0%
BC	80.44	0.0%
ABC	170.22	0.0%
Total	2589454.94	

The ANOVA analysis in **Table 6-14** was used to confirm the magnitude of these effects. The non-significant parameters (and their interactions) were moved to the residual term of the ANOVA table and only the main parameters ***A*** and ***B*** were considered in the final model. The high values of F_0 (and consequently lower values of the p-value), corroborated the conclusions that only parameters ***A*** and ***B*** are statistically significant in this experiment.

Table 6-14: ANOVA analysis for studded bracket type under compression.

Parameters	Sum of Squares	Degrees of Freedom	Mean Squares	F_0	P-val
A	1351428.78	2	675714.39	560.11	<0.01
B	1222343.11	2	611171.56	506.61	<0.01
Residual (LOF)	15683.06	13	1206.39		
Total	2589454.94	17			

The AB interaction is plotted in **Fig 6-8** to provide a visual investigation of the influence of the observed significant parameters on the compressive load supported by the helical pile. The similar slopes of the three curves in **Fig 6-8** verified the conclusion of no interaction between these two main effects. It can also be concluded from **Fig 6-8** that the combination of low *a/d* ratio and high ρ_x% yielded the highest compressive load capacity.

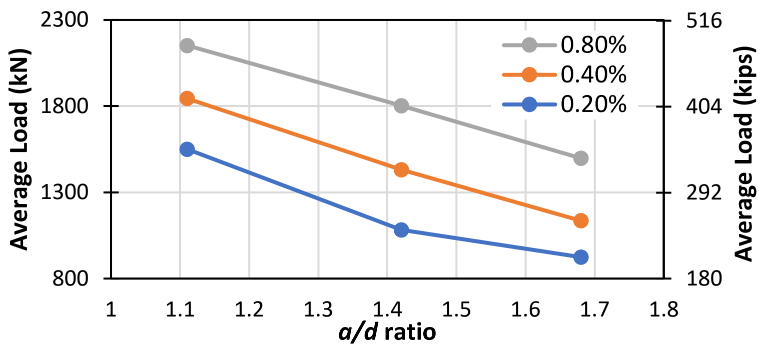

Figure 6-8: Compressive load under different *a/d* ratio and ρ_x% combinations.

6.5.4 Comparison of Bracket Types

The analysis of each individual helical pile revealed that the h_e was not statistically significant for the compression load capacity of the piles. Thus, this parameter was removed and an additional 'bracket type' (***C***) parameter was introduced in the statistical analysis to enable a direct comparison of all three-bracket type helical piles. **Table 6-15** shows the results of the analysis of the sums of squares for the new set of analyzed parameters. Similar to the results calculated for each individual bracket type of helical piles, the *a/d* ratio and ρ_x% parameters dominated the experiment, accounting for 89.9% of the total variability, whereas the 'bracket type' parameter and all of the two- and three-parameter interactions accounted for the remaining 1.1%.

Table 6-15: Analysis of the sums of squares of all types of brackets under compression.

Parameters	Sum of Squares	Degrees of Freedom	% Contribution
***a/d* ratio (A)**	2017216.81	2	51.9%
ρ_x% (B)	1830286.80	2	47.0%
Bracket Type (C)	824.30	2	0.0%
AB	29304.43	4	0.8%
BC	2233.90	4	0.1%
AC	2392.19	4	0.1%
ABC	4585.65	8	0.1%
Total	3886844.07	26	

The ***AB*** interaction is plotted in **Fig 6-9** to provide a visual investigation of the influence of the observed significant parameters on the compressive load supported by the helical pile. The similar slopes of the three curves in **Fig 6-9** verified the conclusion of no interaction between these two main effects. It can also be noted through the investigation of **Fig 6-9** and **Fig 6-7**, **Fig 6-8**, and **Fig 6-9**, that the compressive capacity of all the three bracket type analyzed have similar magnitudes, which corroborates the conclusion that this parameter has no influence in the compressive capacity. From **Fig 6-9** it can also be concluded that the combination of low *a/d* ratio and high ρ_x% yields the highest compressive load capacity.

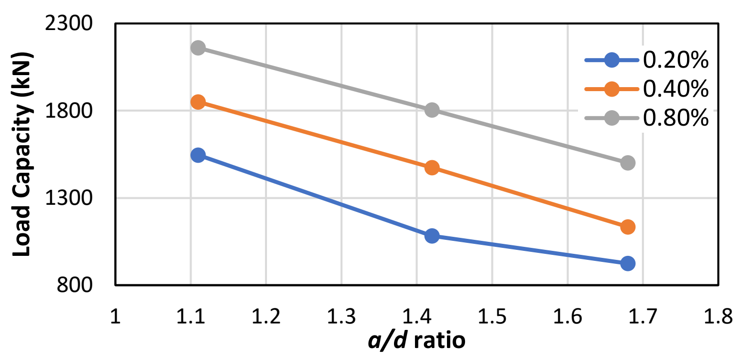

Figure 6-9: Compressive load under different *a/d* ratio and ρ_x% combinations.

6.6 Model Adequacy Checking

In this section, the three assumptions made in order to make use of the ANOVA analysis and factorial designs (see Section 6.1 for details on the assumptions made) were checked.

6.6.1 The Normality Assumption

A useful procedure to test this assumption is to construct a normal probability plot of the residuals of the experiment. The residuals can be calculated from the difference of the predicted result (i.e., the value calculated using a regression curve fitted to the analyzed data) and the actual collected response for each individual parameter combination. If the underlying error distribution is normal, this plot will resemble a straight line. In addition, when using such a plot to check the normality, more emphasis should be put on the central values than on the extremes.

Fig 6-10, which shows the normal probability plots for the analyses performed on this study, indicates that, in general, all the analyses' data follow a normal probability distribution. For a few analyses (such as in **Fig 6-10a**, **Fig 6-10c**, **Fig 6-10d**, and **Fig 6-10e**), some residual points might be visually characterized as outliers. To check if these points characterize real outliers, the standardized residual equation (see **Equation 6-2**) was used. **Equation 6-2** assists in analyzing outlier residuals because a residual bigger than 3 or 4 standard deviations from zero is a potential outlier.

$$d_{ij} = \frac{e_{ij}}{\sqrt{MS_E}} \tag{6-2}$$

where e_{ij} is the residual for the level i of the first parameter and level j of the second parameter, MS_E is the mean square of the error. The residual e_{ij} is calculated using **Equation 6-3**.

$$e_{ij} = y_{ij} - \hat{y}_{ij} \tag{6-3}$$

where y_{ij} is the observation under the i_{th} level of parameter A and j_{th} level of parameter B; and $\hat{y}_{ij}$ is the estimate of the corresponding observation. In this study, a linear regression model of the data was fitted in order to obtain the estimate of the observations.
Using **Equation 6-2** to analyze the possible outlier residuals mentioned above, the standardized residual values fell between 2.5 and 3.3 standard deviations from zero. Although some of them are within the range of 3 or 4 standard deviations from zero, they only exceed this threshold by a slight margin. Thus, in this study, these points were not considered outliers.

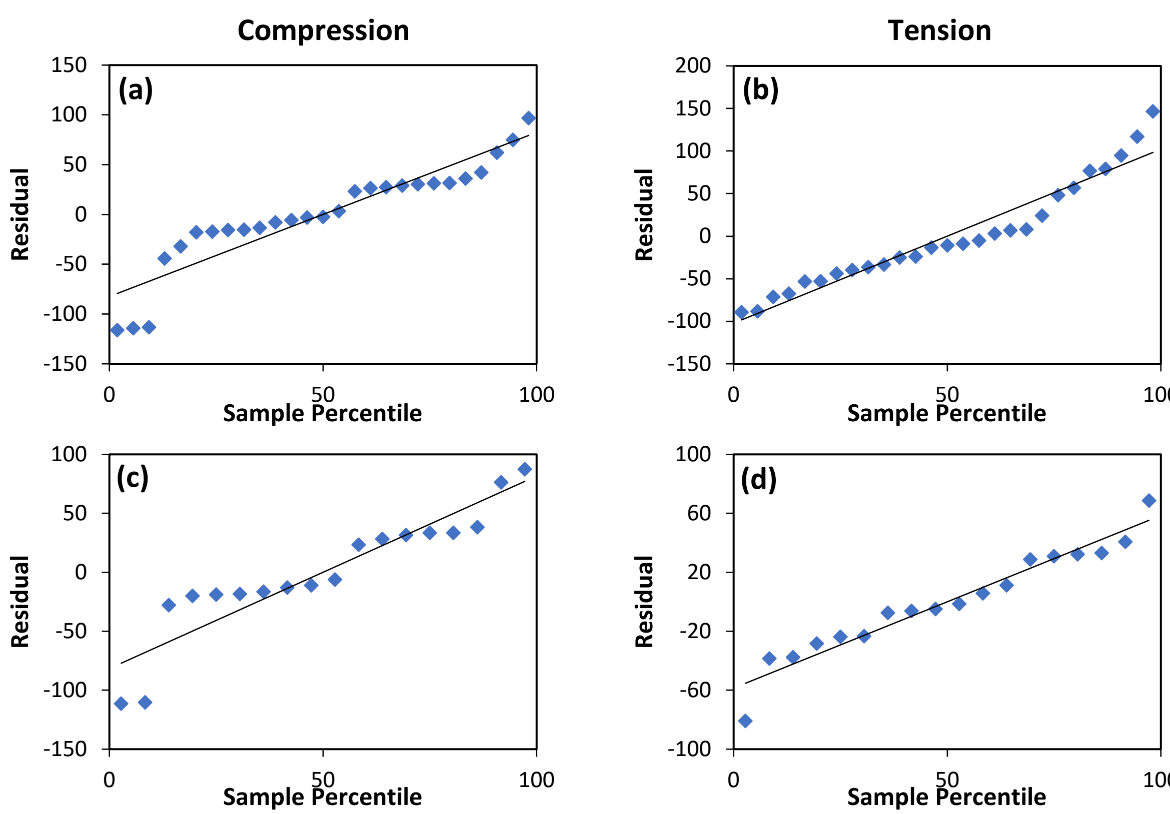

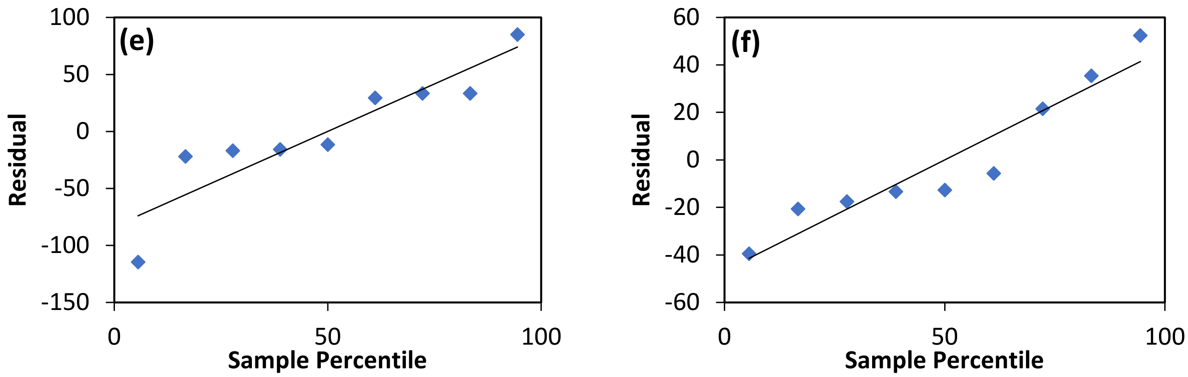

Figure 6-2: Normal probability plots of the residuals of the single bracket types under (a)compression and (b) tension analyses; studded bracket types under (c) compression and (d) tension analyses; and double bracket types under (e) compression and (f) tension analyses.

6.6.2 The Independence and Constant Variance Assumption

To test the independence of the variance's assumption, a plot of the residuals of each analysis in time order of data collection can be used to detect if any strong correlation between the residuals exists. A clear visual pattern between the residuals in this plot indicates a correlation and, thus, non-independence of the residuals. Since the data collected in this study resulted from computational analyses, the data collection order is not as significant as it is when physical experimentation is employed. For this reason, the checking of this assumption was not considered in this study.

To test the independence and constant variance assumption, several residual plots can be constructed. A clear visual pattern between the residuals in these plots indicates a correlation and, thus, non-independence of the residuals. Similarly, the range of the residuals (i.e., the range between the minimum and maximum values) can be used to check the constant variance assumption. In this study, for each analysis performed, the residuals were plotted against the main factor levels and the predicted results (see Section 6.3.1 for a definition of 'predicted results'). The plots for each analysis are shown in **Fig 6-11** to **Fig 6-16**. From these plots, for all of the analyses, even though the variance of the residuals changed slightly, they were not drastically different to constitute a clear violation of the constant variance assumption. On the other hand, the residuals plotted against the ρ_x% parameter indicated a clear pattern for all the analyses (except for single bracketed piles under tension). The presence of this clear pattern may indicate a non-independence of the residuals when the ρ_x% parameter is considered. In addition, the exhibited pattern (i.e., negative values for low ρ_x%, positive values for medium ρ_x%, and negative values for high ρ_x%) may indicate interaction between ρ_x% and *a/d* ratio, as confirmed in the analysis of the parameter effects in the sections 6.1 and 6.2. In those sections, some of these interactions were smaller (and, thus, removed from the final model) and some were more significant, which explains how the observed residual patterns were more evident than others in some plots. Data transformation can be used to eliminate or minimize this interaction; however, no transformation used in this study could entirely prevent the observed pattern without affecting the other two assumptions of the model. Thus, since this clear pattern only occurred when considering the ρ_x% factor, no transformation or treatment of this non-independent variance assumption was further performed in this study.

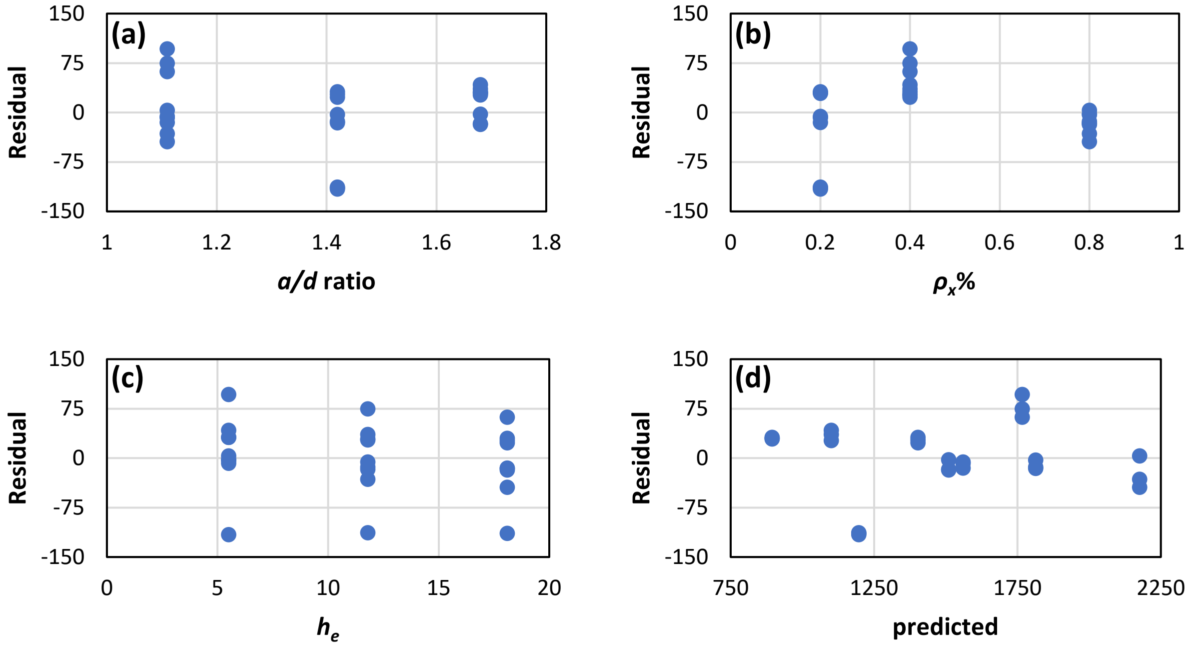

Figure 6-3: Analysis of residuals and (a) a/d ratio; (b) ρ_x%; (c) h_e; (d) predicted values for the single bracket type under compression.

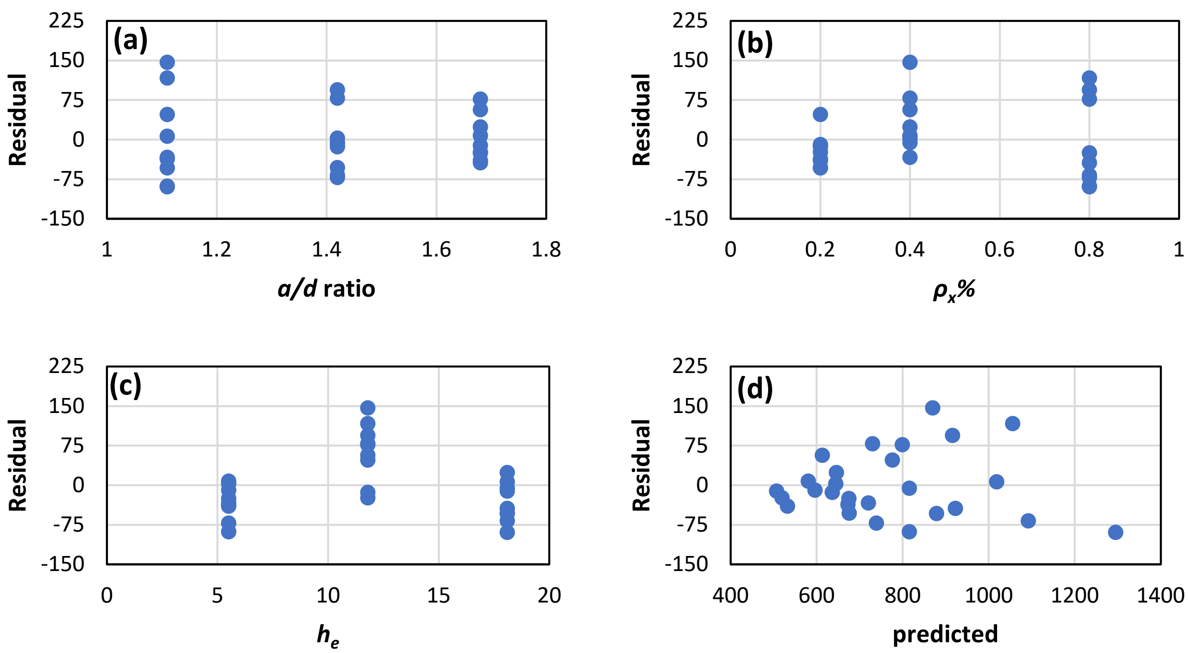

Figure 6-4: Analysis of residuals and (a) a/d ratio; (b) ρ_x%; (c) h_e; (d) predicted values for the single bracket type under tension.

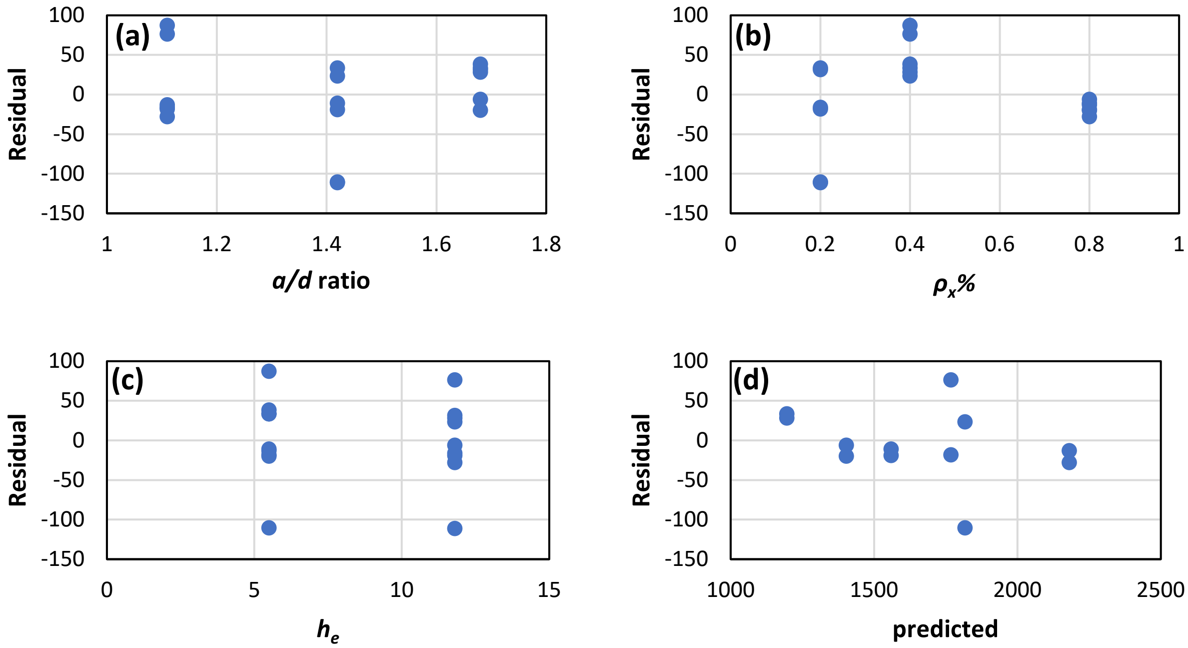

Figure 6-5: Analysis of residuals and (a) *a/d* ratio; (b) ρ_x%; (c) h_e; (d) predicted values for the studded bracket type under compression.

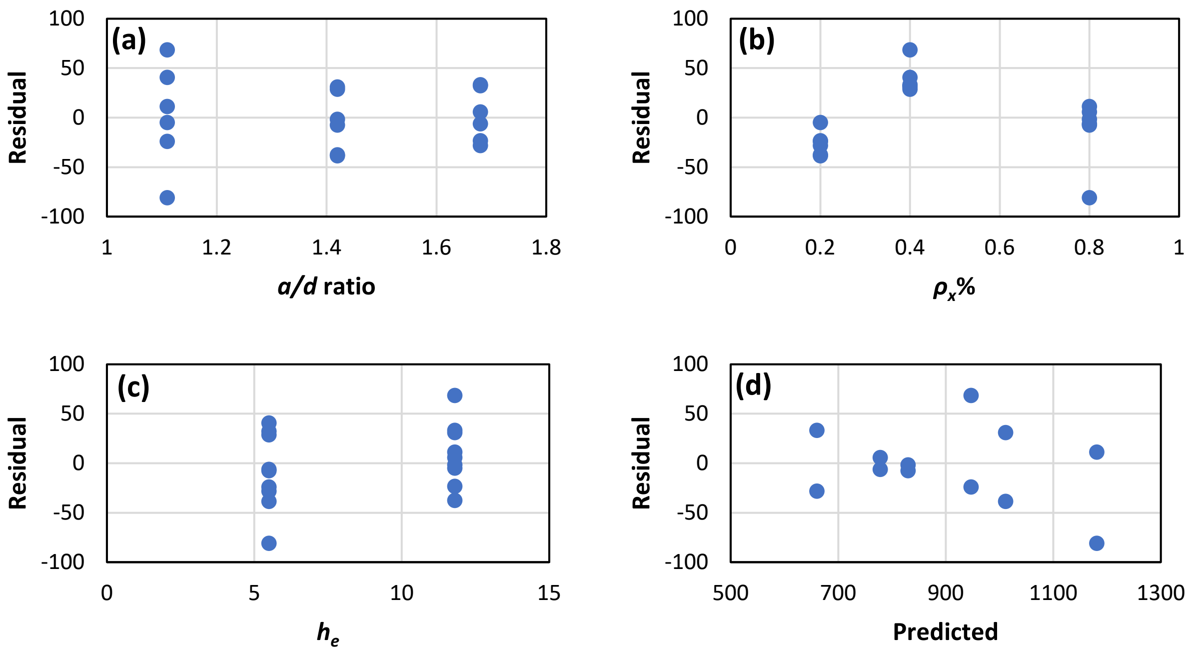

Figure 6-6: Analysis of residuals and (a) *a/d* ratio; (b) ρ_x%; (c) h_e; (d) predicted values for the studded bracket type under tension.

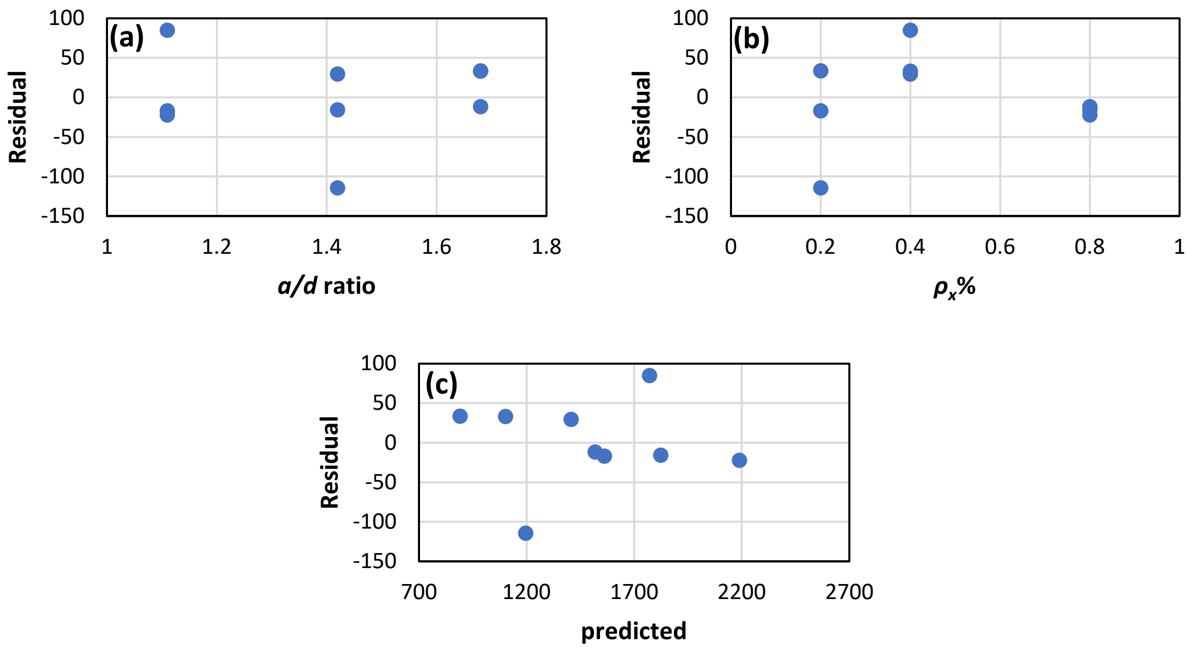

Figure 6-7: Analysis of residuals and (a) *a/d* ratio; (b) ρ_x%; (c) h_e; and (d) predicted values for the double bracket type under compression.

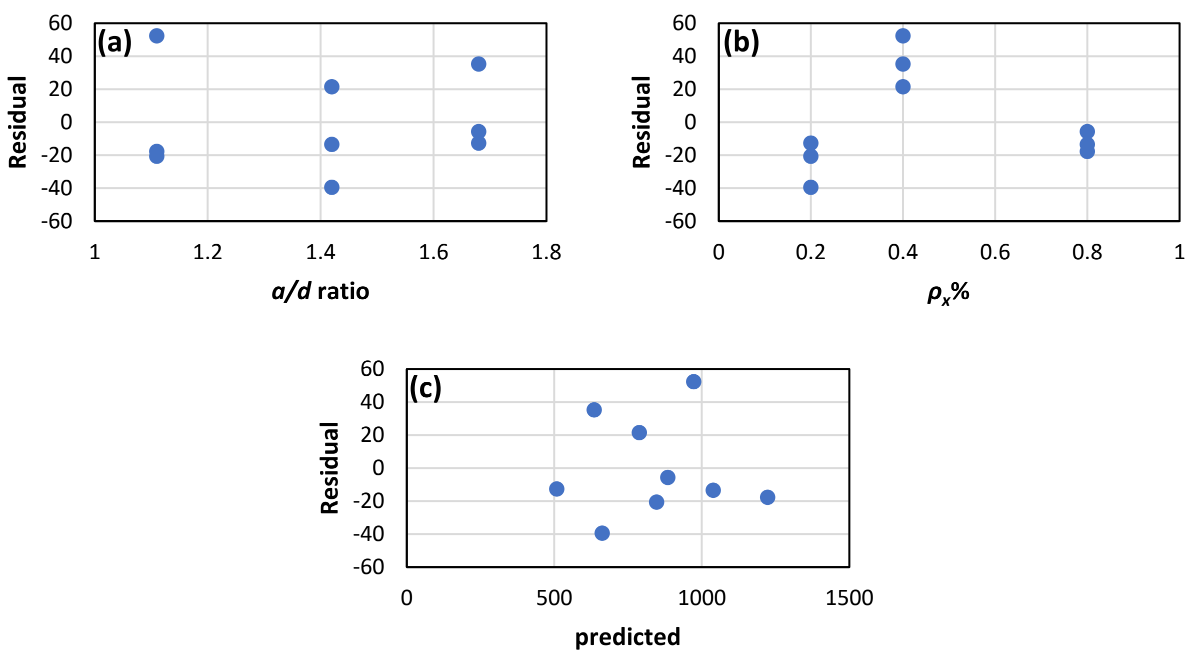

Figure 6-8: Analysis of residuals and (a) *a/d* ratio; (b) ρ_x%; (c) h_e; (d) predicted values for the double bracket type under tension.

7. Global Concrete Foundation Checks

7.1 Introduction

The objective of this chapter is to assess the significance of considering/neglecting the anchorage zone behavior. The numerical & experimental results which incorporate the influence and failure modes of the helical pile-to-foundation connections are compared with the global foundation checks (i.e., sectional flexure and shear checks) which calculate the global strength of the concrete foundations while neglecting the influence of the anchorage conditions.

7.2 Global Checks for the Concrete Foundation

7.2.1 Methods

The global sectional strengths of the experimental specimens (in Diab's foundations – see Section 4.4) and and the pile caps (investigated in this study) are calculated to compare with the obtained nonlinear simulation results. The global capacities are calculated based on three different methods; sectional flexure, sectional shear and Strut and Tie Method (STM). If the concrete foundations fail in flexure due to the yielding of reinforcement, sectional flexure (ACI 318-19) governs; if the beams fail in shear, sectional shear (ACI 318-19) dominates. Sectional prediction methods can predict the global capacities of the slender beams. For the deep concrete foundations (e.g., Diab's foundations and pile caps investigated in this study), STM prediction (ACI 318-19, CSA A23.3-2014) provide more accurate results provided the foundations include sufficient amounts of longitudinal reinforcements with proper anchorage. In this section, all three predictions will be compared with the nonlinear simulation results to assess the consequences of using each method.

7.3 Global Checks for Diab's Experimental Foundation Specimens

7.3.1 Monotonic Tension

The experimental capacities (indicated by black bars in **Fig 7-1**) are much smaller than those predicted by the global analysis method. This result confirms that the anchorage capacity governs the entire foundation response and that the use of the global foundation checks (which neglect the anchorage capacity) can be dangerously unsafe (i.e., overestimates the foundation system capacity on average by 2.2 times.)

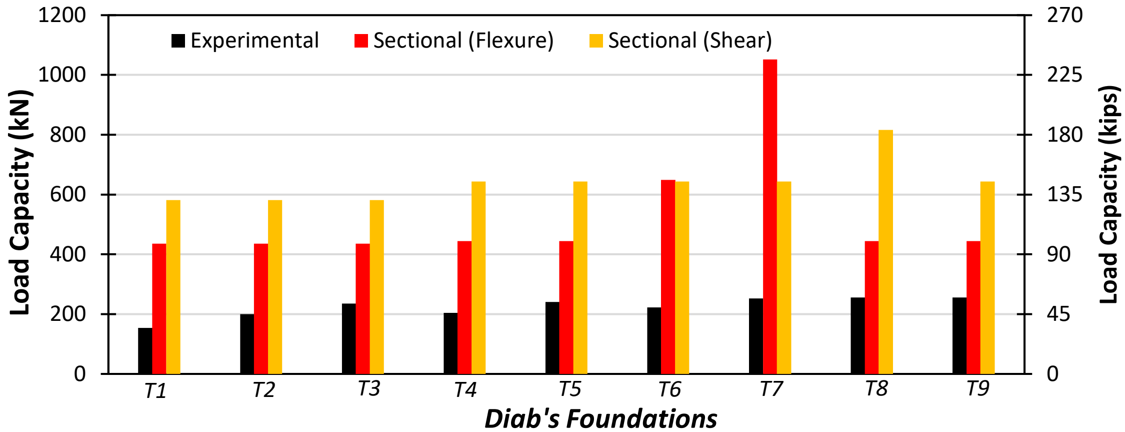

Figure 7-1: Comparison among experimental and predicted capacities subjected to monotonic tension for Diab's foundations.

7.3.2 Monotonic Compression

The experimental capacities (indicated by black bars in **Fig 7-2**) are smaller than those predicted by the global analysis method. This result confirms that the anchorage capacity may govern the entire foundation response and that the use of the global foundation checks (which neglect the anchorage capacity) may be unsafe (i.e., overestimates the foundation system capacity on average by 1.44 times.)

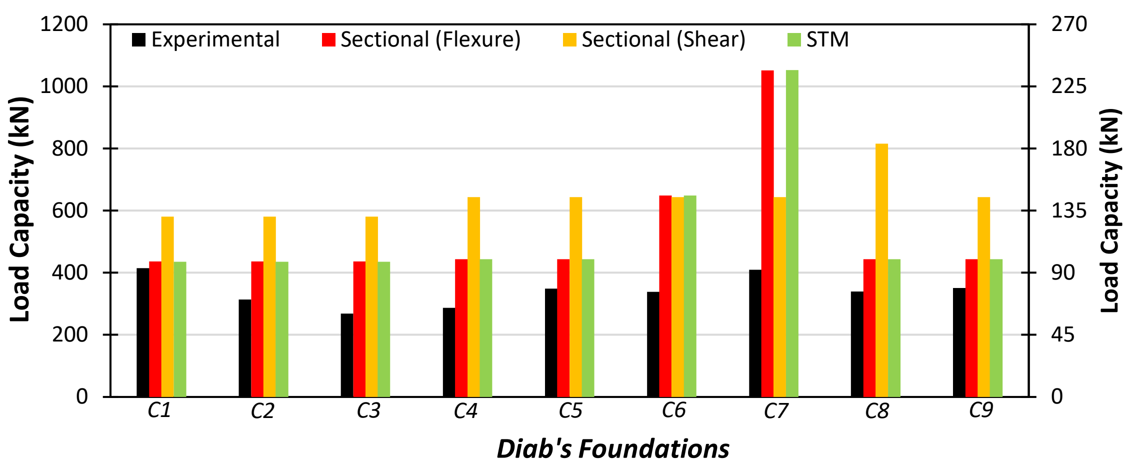

Figure 7-2: Comparison among experimental and predicted capacities subjected to monotonic compression for Diab's foundations.

7.4 Global Checks for the Helical Foundations Examined in this Study

The global strengths of the pile caps are calculated and compared with the results obtained from the nonlinear simulations (which include the anchorage response). Due to large volume of data obtained from 162 simulations, only some significant results will be shown.

7.4.1 Monotonic Tension

The anchorage capacity governs the holistic behavior of the helical foundations in most of the cases for ρ_x of 0.2% (see **Fig 7-3**) since the nonlinear FE simulation results are smaller than any of the global foundation prediction results except for a few cases (e.g., top and middle h_e in a/d ratio of 1.11).

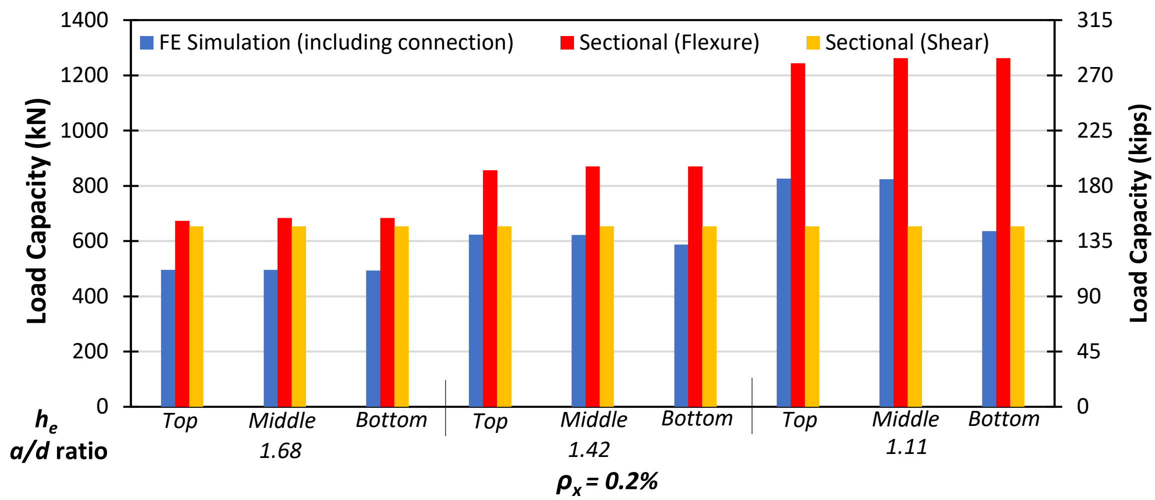

Figure 7-3: Comparison among simulation and predicted capacities for single bracket type subjected to monotonic tension in ρ_x of 0.2%.

The sectional method shear prediction values are known to be overly conservative (i.e., very low) for deep beams (e.g., all the foundations considered in this study) as clearly demonstrated by many studies (e.g., Baniya and Guner 2019). Considering the deep beam effects, the correct shear prediction results would have been higher than the simulated results in **Figs 7-4** and **7-5** and the anchorage capacity would have still governed. Note that the STM is not applicable here due to its negligence of the tensile stresses in concrete.

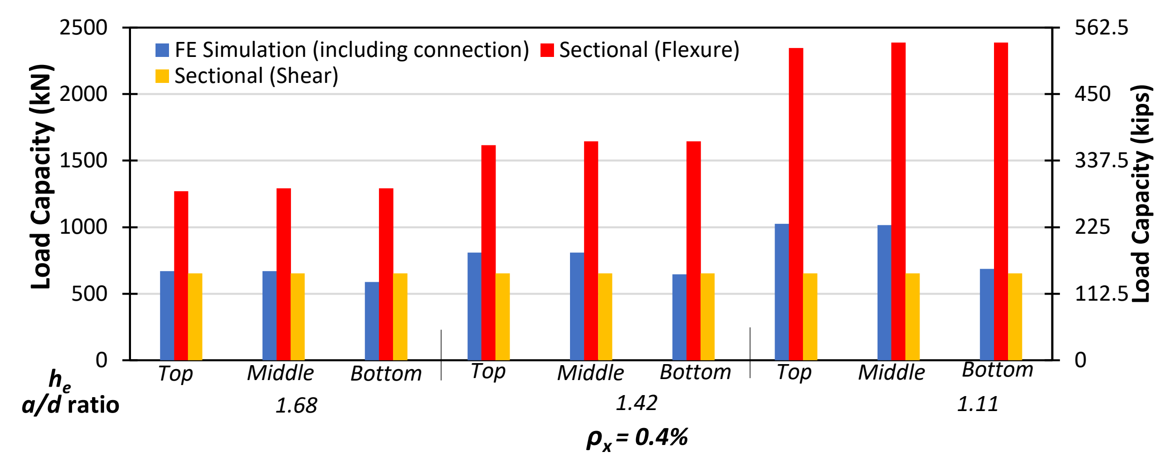

Figure 7-4: Comparison among simulation and predicted capacities for single bracket type subjected to monotonic tension in ρ_x of 0.4%.

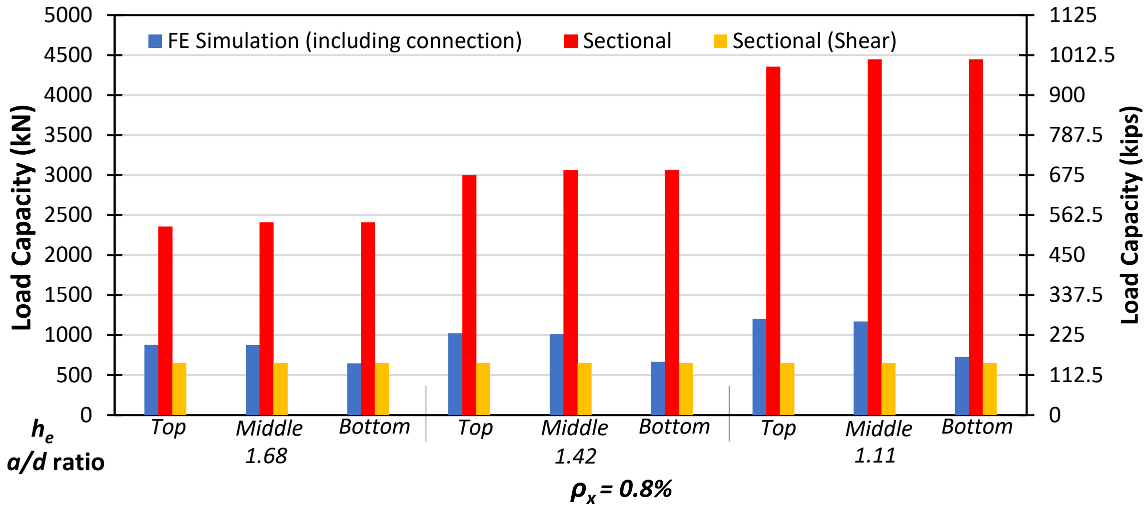

Figure 7-5: Comparison among simulation and predicted capacities for single bracket type subjected to monotonic tension in ρ_x of 0.8%.

7.4.2 Monotonic and Cyclic Compression

For the illustration purpose, the comparison of the obtained results with the global pile cap strengths is shown (see **Fig 7-6**) for the single bracket type subjected to monotonic tension. For the ρ_x of 0.2%, the simulated results are higher than any of the global strength prediction methods which shows that the anchorage zone does not govern the response of the foundations.

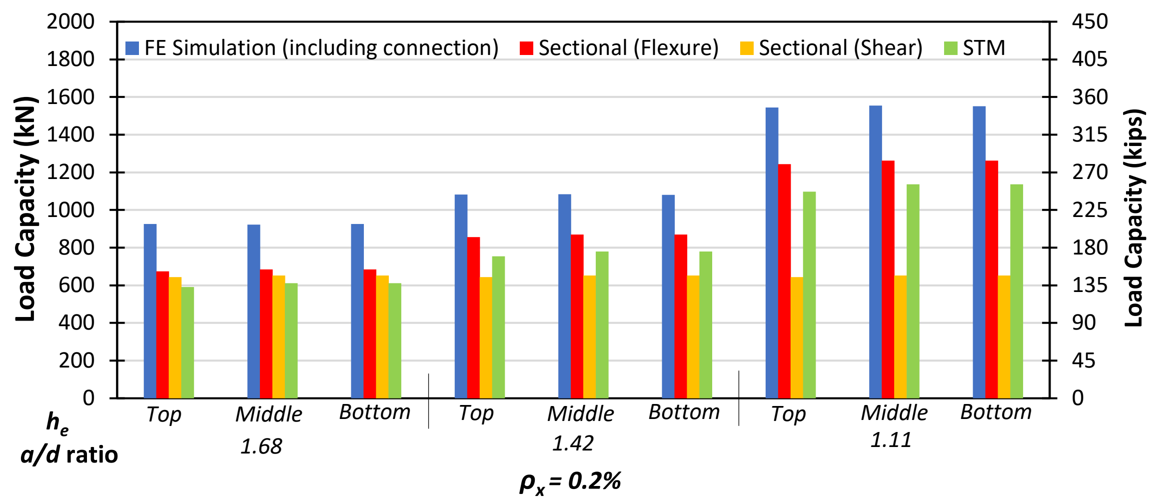

Figure 7-6: Comparison among simulation and predicted capacities for single bracket type subjected to monotonic compression in ρ_x of 0.2%.

Figures 7-7 and **7-8** show the results for the well-reinforced helical foundations with a ρ_x of 0.4% and 0.8% respectively. These higher reinforcement percentages make the deep beam action more effective, thereby increasing their shear strengths. As such the STM becomes applicable and provide similarly accurate results to the FE simulations. The sectional shear predictions become excessively overly-conservative (i.e., very low) due to the inability of this method to consider the deep beam action (Baniya and Guner 2019). The sectional flexure capacities are much higher (due to high ρ_x%) and thus do not govern the responses. Based on these results, for the monotonic and cyclic compression, the connection capacity does not govern in any of the bracket types since the FE simulation results are either higher or similar to those from other methods.

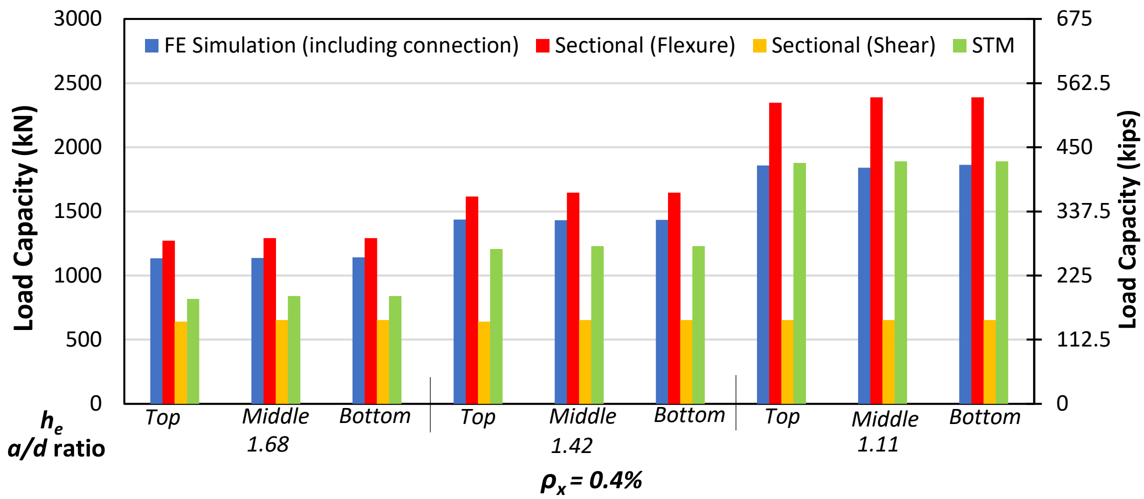

Figure 7-7: Comparison among simulation and predicted capacities for single bracket type subjected to monotonic compression in ρ_x of 0.4%.

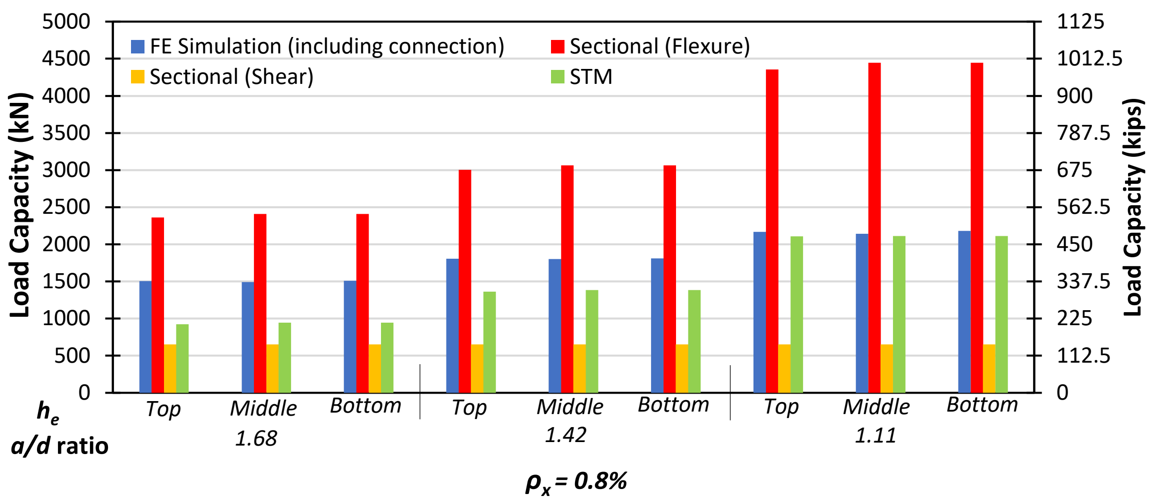

Figure 7-8: Comparison among simulation and predicted capacities for single bracket type subjected to monotonic compression in ρ_x of 0.8%.

8. Conclusions and Recommendations

Three bracket types (i.e., ***single, double** and **studded***) are numerically investigated using the experimentally-verified nonlinear finite element models. The parameters investigated are ***the embedment depths h_e of the brackets*** (i.e., bottom, middle and top for the single bracket; top for the double bracket; and middle and top for the studded bracket) ***longitudinal reinforcement percentages ρ_x*** (i.e., 0.2%, 0.4% and 0.8%) of the pile caps, and ***the shear span to depth ratios a/d*** (i.e., 1.68, 1.42 and 1.11) subjected to ***three types of loadings*** (i.e., monotonic tension, monotonic compression and reversed-cyclic). The results of the reversed-cyclic loading are divided into *'cyclic compression'* and *'cyclic tension'* to allow for a consistent comparison with the monotonic compression and monotonic tension loads. **Fig 7-1** illustrates the variables.

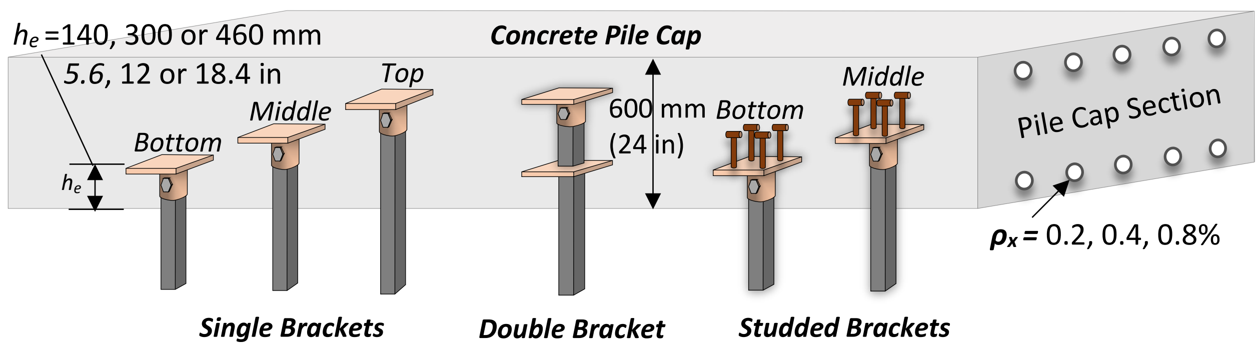

Figure 8-1: Three bracket types examined in the study, illustrated in the same pile cap for comparison purposes.

The results of the investigations demonstrate that the helical pile-to-foundation anchorages ***may govern the entire system capacity*** for the load conditions involving uplift and reversed-cyclic forces. ***The traditional global analysis methods***, which neglect the influence of the anchorage zones, are found to significantly overestimate the capacity of the helical foundations (***up to 2.2 times*** in this study). ***These results justify the recommendation*** of performing an explicit capacity check of the anchorage zones in addition to the structural and geotechnical checks for the global foundation and helical pile capacities. The findings of this study are ***also applicable to micro piles*** which incorporate similar termination bracket details. Detailed conclusions and recommendations are provided below.

Monotonic and Cyclic Tension (subjected to uplift forces)

- The helical pile-to-foundation ***anchorage zone detailing*** significantly influences the global tensile capacity of the helical pile cap foundations.
- ***The tensile load capacities*** of the foundation systems (all of which are doubly and symmetrically reinforced) are found to be ***only 54%*** of their compression load capacities. If analyzed with the traditional sectional analysis methods, which neglect the influence of the anchorage zones, their load capacities in tension (i.e., a point load applied upwards) and compression (i.e., a point load applied downwards) would be incorrectly calculated as equal.

- Anchorage zone failure is predicted for ***the bottom h_e of the single bracket type***, with a decrease in the global load capacity by 25% on average. It is recommended that the middle h_e be used if the single bracket termination is to be used.
- The statistical analysis of the results indicates that the combination of ***low a/d ratios, high ρ_x, and the middle h_e*** yields the highest tension load capacity for the single bracket. These analyses also indicate that h_e dictates the effectiveness of ρ_x and *a/d* ratio. In other words, if larger tensile load capacities are desired, h_e should be changed from bottom to middle, as opposed to using the bottom h_e and increasing the ρ_x percentage or reducing the *a/d* ratio with hopes to increase the load capacity (which is not effective).
- **The double bracket type** has only one embedment depth which provides satisfactory responses with no anchorage zone failure in all simulations contained in this study.
- **The studded bracket type** has two h_e positions. While no anchorage zone failure is predicted, major anchorage zone cracking is observed for the bottom h_e. For the configurations involving the bottom h_e, the change of the bracket type from single to studded improves the foundation capacity by an average of 22%; consequently, the studded bracket may be preferred over the single bracket for the bottom h_e. For the most optimum results, however, the middle h_e is recommended for both the single and studded bracket types.
- Although ***the bottom h_e of the single bracket type*** demonstrated the least-favorable behavior, it can still be successfully used for resisting uplift forces if a special anchorage zone detailing is developed (e.g., sufficient amounts of vertical ties or stirrups in the anchorage zone). This recommendation is also applicable to the ***bottom h_e of the studded bracket type***.
- When designing the helical pile-to-foundation connections, special attention should be given to ***light and tall structures*** where one of the foundation load cases may be tensile in nature.

Monotonic and Cyclic Compression

- The helical pile-to-foundation anchorages are found to ***not influence the monotonic compression load capacity*** of the helical pile foundations in any of the bracket types examined; no anchorage failures are predicted.
- The statistical analyses show that ***the h_e parameter*** has no significant contribution on the monotonic compression capacity of the helical foundations.
- To maximize the load capacity, ***high ρ_x*** and ***low a/d ratios*** should be used for all bracket types.
- The compression capacity of the foundations examined are found, on average, to be ***1.85 times higher*** than their tension capacity. Consequently, particular attention should be paid to the connection design when there is a load case involving ***net uplift forces***.
- For the ***cyclic compression loading***, anchorage zone cracks and reduced load capacities (up to 10%) are predicted for ***the top h_e of the single bracket*** in some design configurations. It is recommended to ***follow the tension load recommendations (above)*** for the load cases involving cyclic load reversals.

9. References

AASHTO, 2014. LRFD bride design specifications. Washington, DC, USA: *American Association of State Highway and Transportation Officials.*

ACI Committee 318, 2019. Building code requirements for structural concrete and commentary (ACI 318R-19), American Concrete Institute, Farmington Hills, MI, USA, 623 p.

Adebar, P., Kuchma, D., and Collins, M.P., 1990. Strut-and-tie models for the design of pile caps: an experimental study. *ACI Structural Journal,* 87(1): 81-92. Retrieved from https://trid.trb.org/view/307069

Akkaya, Y., Guner, S., and Vecchio, F.J., 2019. A constitutive model for the inelastic buckling behavior of reinforcing bars. *ACI Structural Journal,* 116(3): 195-204. Retrieved from http://www.utoledo.edu/engineering/faculty/serhan-guner/docs/JP11_Akkaya_et_al_2019.pdf

Almeida Jr, S. A., 2019. Modeling of concrete anchors supporting non-structural components subjected to strong wind and adverse environmental conditions. M.S. Thesis. The University of Toledo, Ohio, U.S., 90 pp. Retrieved from https://www.utoledo.edu/engineering/faculty/serhan-guner/docs/T6_Almeida_MS_2019.pdf

Almeida Jr, S. A., and Guner, S., 2019. A practical methodology for the analysis of adhesive anchors in adverse environments for hurricane resilience. *Engineering Structures* (submitted).

Baniya, P., and Guner, S., 2019. A specialized strut-and-tie method for predicting shear capacities of bridge pier caps," *Engineering Structures*, V. 198, pp. 1-9. http://www.utoledo.edu/engineering/faculty/serhan-guner/docs/JP13_Baniya_Guner_2019.pdf

Cao, J., 2009. The shear behaviour of the reinforced concrete four-pile caps. Ph.D. Thesis, School of Civil Engineering and the Environment, University of Southampton, Southampton, UK, 2009, 287 p. Retrieved from https://eprints.soton.ac.uk/73699/

Cerato, A., and Victor, R., 2009. Effects of long-term dynamic loading and fluctuating water table on helical anchor performance for small wind tower foundations. *Journal of Performance of Constructed Facilities,* 23(4): 251-61. https://doi.org/10.1061/(ASCE)CF.1943-5509.0000013

Chan, T. K., and Poh, C. K., 2000. Behavior of precast reinforced concrete pile caps. *Construction and Building Materials*, 14(2): 73-78. https://doi.org/10.1016/S0950-0618(00)00006-4

CRSI., 2015. Design guide for pile caps (1st ed.). Concrete Reinforcing Steel Institute, Schaumburg, IL, 156 p. Retrieved from http://resources.crsi.org/resources/design-guide-for-pile-caps

CSA A23.3., 2014. Design of concrete structures. Canadian Standards Association, Mississauga, ON, Canada., 668 p.

Diab, M.A.M., 2015. Behavior of helical pile connectors for new foundations. Ph.D. Thesis, School of Civil and Environment Engineering, University of Western Ontario, London, Ontario, Canada, 638 p. Retrieved from https://ir.lib.uwo.ca/cgi/viewcontent.cgi?article=4736&context=etd

DFI, 2014. University presentation on helical piles and anchors (powerpoint slides). Helical Piles and Tiebacks Committee, Deep Foundation Institute. Retrived from http://www.dfi.org/update/HPTUniv01notes.pdf

El Naggar, M. H., Youssef, M. A., and Ahmed, M., 2007. Monotonic and cyclic lateral behaviour of helical pile specialized connectors. *Engineering Structures, 29(10):* 2635–2640. https://doi.org/10.1016/j.engstruct.2007.01.018

El Sharnouby, M. M., and El Naggar, M. H., 2010. Numerical investigation of the response of expansion anchors used to attach helical pile connectors to concrete foundations. *Canadian Journal of Civil Engineering*, 37(6): 866–877. https://doi.org/10.1139/L10-025

El Sharnouby, M. M., and El Naggar, M. H., 2012. Axial monotonic and cyclic performance of fibre-reinforced polymer (FRP) – steel fibre–reinforced helical pulldown micropiles (FRP-RHPM). *Canadian Geotechnical Journal*, 49(12), 1378–1392. https://doi.org/10.1139/cgj-2012-0009

Eligehausen, R., and Sawade, G., 1985. Verhalten von Beton auf Zug. (Behaviour of concrete under tension). Betnwerk. Fertigteil-Technik, 5, 315–322.

Elkasabgy, M., and El Naggar, M.H., 2013. Dynamic response of vertically loaded helical and driven steel piles. *Canadian Geotechnical Journal*, 50(5): 521–535. https://doi.org/10.1139/cgj-2011-0126

Elsherbiny, Z.H., and El Naggar, M.H., 2013. Axial compressive capacity of helical piles from field tests and numerical study. *Canadian Geotechnical Journal*, 50(12): 1191–1203. https://doi.org/10.1139/cgj-2012-0487

Fisher, R. A., 1992. Statistical methods for research workers. In: Kotz S., Johnson N.L. (Ed.) Breakthroughs in Statistics. Springer Series in Statistics (Perspectives in Statistics), Springer, New York, NY, 360 p.

Guner, S., and Carrière, J., 2016. Analysis and strengthening of caisson foundations for uplift loads. *Canadian Journal of Civil Engineering*, 43(5): 411–419. Retrieved from http://www.utoledo.edu/engineering/faculty/serhan-guner/docs

IBC., 2018. International Building Code. International Code Council, Inc, New Jersey.

Kani G.N.J., 1967. How safe are our large reinforced concrete beams? *ACI Journal Proceedings*, 11(13): 128–141. https://doi.org/10.14359/7549

Labuda, T., Corley, G.W., and Murphy, M., 2013. Failure investigation of a helical anchor tie-down system supporting an olympic size swimming pool. Proceedings of the Seventh International Conference on Case Histories in Geotechnical Engineering, Chicago, April 29-May 4, Scholoars' Mine, Missouri University of Science and Technology, 7 p. Retrieved from http://scholarsmine.mst.edu/cgi/viewcontent.cgi?article=3223&context=icchge

Livneh, B., and El Naggar, M.H., 2008. Axial testing and numerical modeling of square shaft helical piles under compressive and tensile loading. *Canadian Geotechnical Journal*, 45(8): 1142-1155. https://doi.org/10.1139/T08-044

MacGregor, J.G., and James W.K., 2012. Reinforced concrete: mechanics and design (6th ed). Pearson Education, Inc., Upper Saddle River, New Jersey, 1177 p.

Montgomery, D. C., 2013. Design and analysis of experiments (8th ed). John Wiley & Sons, Inc, Hoboken, NJ, 724 p.

Nilsson, M., Ohlsson, U., and Elfgren, L., 2011. Effects of surface reinforcement on bearing capacity of concrete with anchor bolts. *Cement and Concrete Research*, 44(11): 161-174. Retrieved from https://nordicconcrete.net/wp-content/uploads/2011/01/Vol-43-Proceedings-Finland-2011.pdf

Otsuki, K., and Suzuki, K., 1996. Experimental study on bending ultimate strength of four-pile caps. *Transactions of the Japan Concrete Institute*, 482: 93-102. Retrieved from https://ci.nii.ac.jp/naid/110004303171

Pack, J.S., 2009. Design and inspection guide for helical piles and helical tension anchors (4th ed.). Intermountainhelicalpiers Inc, Denver, CO, 194 p. Retrieved from http://www.intermountainhelicalpiers.com/downloads/DesignGuide4Rev2.pdf

Richards, P.W., Rollins, K.M., and Stenlund, T.E., 2011. Experimental testing of pile-to-cap connections for embedded pipe piles. *Journal of Bridge Engineering* 2011, 16(2): 286-94. https://doi.org/10.1061/(ASCE)BE.1943-5592.0000144

Sakr, M., Naggar, M. H. El, and Nehdi, M., 2004. Load transfer of fibre-reinforced polymer (FRP) composite tapered piles in dense sand. *Canadian Geotechnical Journal*, 41(1): 70–88. https://doi.org/10.1139/t03-067

Satterthwaite, F. E., 1946. An approximate distribution of estimates of variance components. Biometrics Bulletin, 2(6), 110-114.

Supportworks, 2018. Retrieved from https://commercial.supportworks.com/case-study/case-studies.html

Suzuki, K., Otsuki, K., and Tsubata, T., 1998. Influence of bar arrangement on ultimate strength of four-pile caps. *Transactions of the Japan Concrete Institute*, 20, 195–202.

Suzuki, K., Otsuki, K., and Tsubata, T., 2000. Influence of edge distance on failure mechanism of pile caps. *Transactions of the Japan Concrete Institute*, 22: 361-67. Retrieved from https://ci.nii.ac.jp/naid/10007467724/

Suzuki, K., and Otsuki, K., 2002. Experimental study on corner shear failure of pile caps. *Transactions of the Japan Concrete Institute*, 23: 303-10. Retrieved from https://ci.nii.ac.jp/naid/10007251043/

Tortola, L.M., Pallares, L., and Miguel, P.F, 2018. Punching shear failure in three-pile caps: Influence of the shear span-depth ratio and secondary reinforcement. *Engineering Structures*, 155: 127-143. https://doi.org/10.1016/j.engstruct.2017.10.077

Vecchio, F.J., and Collins, M.P., 1986. The modified compression field theory for reinforced concrete elements subject to shear. *ACI Journal*, 83(2): 219–231. https://doi.org/10.14359/10416

Vecchio, F.J., 2000. Disturbed stress field model for reinforced concrete: formulation. *Journal of Structural Engineering*, 126(8): 1070–1077. https://doi.org/10.1061/(asce)0733-9445(2000)126:9(1070)

VTAG, 2019. VecTor2: Nonlinear finite element analysis software for reinforced concrete structures. VecTor Analysis Group (VTAG) Version 2.9 (Online), Retrieved from http://vectoranalysisgroup.com

Vickars, R. A., and Clemence, S. P., 2000. Performance of helical piles with grouted shafts. Proceedings of the new technological and design developments in deep foundations, american society of civil engineers, denver, co, 327–341. https://doi.org/10.1061/40511(288)2

Wong P.S., Vecchio F.J., and Trommels H., 2013. VecTor2 and formworks user's manual. Technical Report, Department of Civil Engineering, University of Toronto, ON, Canada, 347 p. Retrieved from http://www.vectoranalysisgroup.com/user_manuals/manual1.pdf

Xiao, Y., and Chen, L., 2013. Behavior of model steel H-pile-to-pile-cap connections. *Journal of Constructional Steel Research*, 80: 153-162. https://doi.org/10.1016/j.jcsr.2012.09.008

Youssef, M.A., El Naggar, M.H., and Ahmed, M., 2006. Monotonic and cyclic load behaviour of helical pile connectors in the vertical direction. *Canadian Journal of Civil Engineering*, 18(1996): 10–18. https://doi.org/10.1139/l05-074

Appendix A   Nonlinear Finite Element Analysis of Single Bracket Anchorages

In this appendix, the following simulation results are presented: the nonlinear load vs. deflection responses, the peak loads, the failure displacement, the initial stiffnesses, the failure mechanisms and the influence of the bracket zone.

Subjected to Monotonic Tension

***a/d* ratio = 1.68, ρ_x = 0.2%**

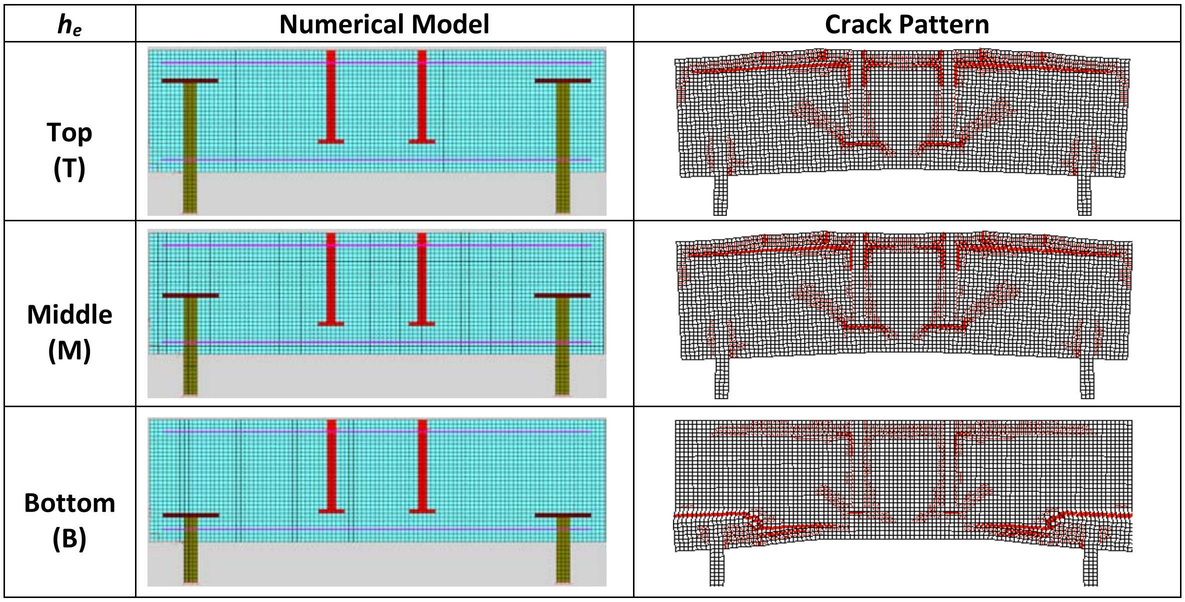

Figure A-1: Numerical model and crack pattern-single bracket type-monotonic tension - *a/d* ratio = 1.68, ρ_x = 0.2%.

Table A-1: Comparison of numerical simulation-single bracket type-monotonic tension - *a/d* ratio = 1.68, ρ_x = 0.2%.

h_e	*a/d* ratio	P_u (kN)	$P_{u\text{-}T/B}$	$P_{u\text{-}M/B}$	δ_u (mm)	$\delta_{u\text{-}T/B}$	$\delta_{u\text{-}M/B}$	Stiff (kN/mm)	Failure Mode	Bracket Infl.
T	1.68	496	1.01	1.01	1.19	1.00	1.00	1350	Flexural	None
M		496			1.19			1350	Flexural	None
B		493			1.19			1350	Splt-brkt	High

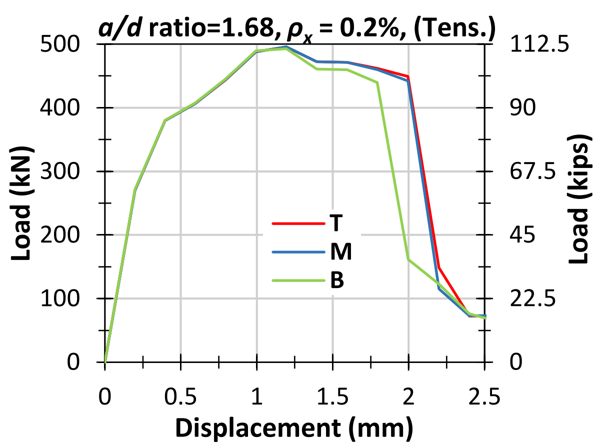

Figure A-2: Load-displacement response-single bracket type-monotonic tension - *a/d* ratio = 1.68, ρ_x = 0.2%.

- The load capacities for all h_e are the same.
- The displacement capacities for all h_e are the same.
- Dominant anchorage cracks are seen for the bottom h_e.

***a/d* ratio = 1.68, ρ_x = 0.4%**

h_e	**Numerical Model**	**Crack Pattern**
Top (T)	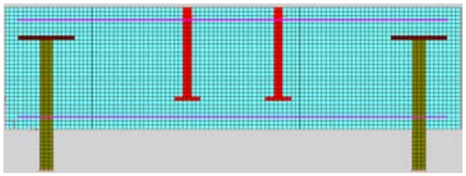	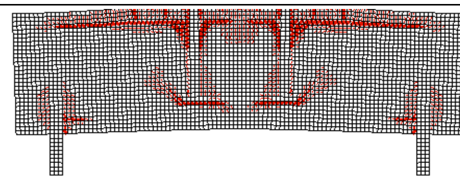
Middle (M)	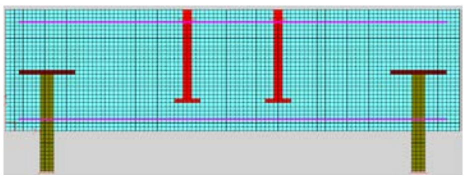	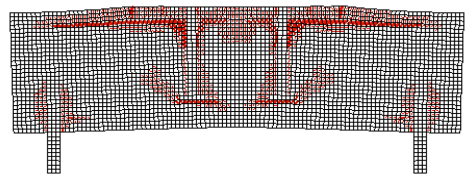
Bottom (B)	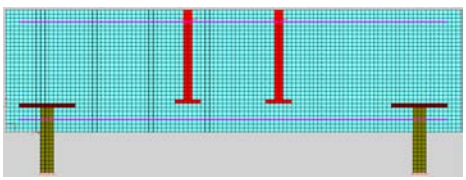	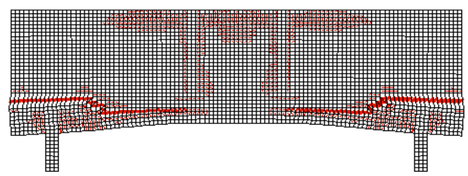

Figure A-3: Numerical model and crack pattern-single bracket type-monotonic tension - *a/d* ratio = 1.68, ρ_x = 0.4%.

Table A-2: Comparison of numerical simulation-single bracket type-monotonic tension - *a/d* =1.68, ρ_x = 0.4%.

h_e	***a/d* ratio**	**P_u (KN)**	**$P_{u\text{-}T/B}$**	**$P_{u\text{-}M/B}$**	**δ_u (mm)**	**$\delta_{u\text{-}T/B}$**	**$\delta_{u\text{-}M/B}$**	**Stiff (KN/mm)**	**Failure Mode**	**Bracket Infl.**
T		670	1.14		1.40	1.40		1420	Flexural	None
M	1.68	670		1.14	1.40		1.40	1420	Flexural	None
B		588			1.00			1420	Splt-brkt	**High**

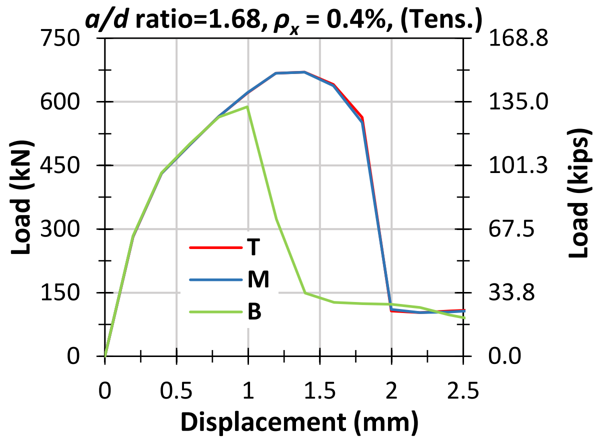

Figure A-4: Load-displacement response-single bracket type-monotonic tension - *a/d* ratio = 1.68, ρ_x = 0.4%.

- The load capacities increase by 14% when the h_e is changed from bottom to middle.
- The displacement capacities increase by 40% when the h_e is changed from bottom to middle.
- Dominant anchorage cracks are seen for the bottom h_e.

***a/d* ratio = 1.68, ρ_x = 0.8%**

h_e	Numerical Model	Crack Pattern
Top (T)	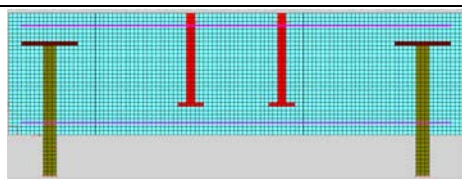	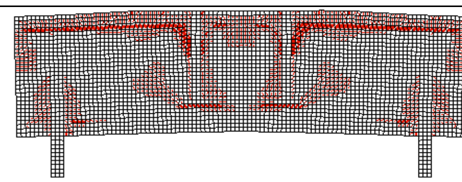
Middle (M)	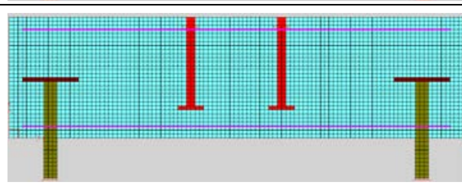	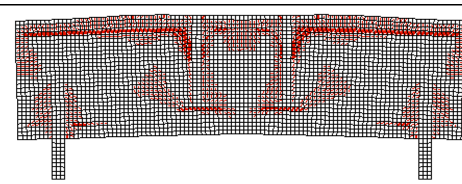
Bottom (B)	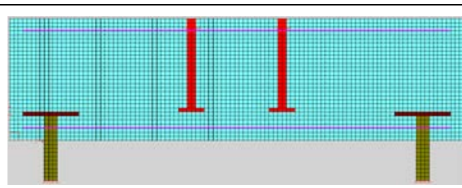	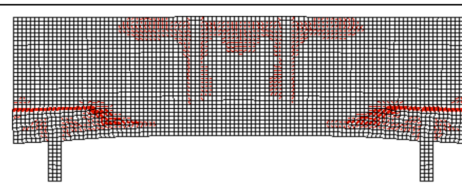

Figure A-5: Numerical model and crack pattern-single bracket type-monotonic tension - *a/d* ratio = 1.68, ρ_x = 0.8%.

Table A-3: Comparison of numerical simulation-single bracket type-monotonic tension - *a/d* ratio = 1.68, ρ_x = 0.8%.

h_e	*a/d* ratio	P_u (KN)	$P_{u\text{-}T/B}$	$P_{u\text{-}M/B}$	δ_u (mm)	$\delta_{u\text{-}T/B}$	$\delta_{u\text{-}M/B}$	Stiff (KN/mm)	Failure Mode	Bracket Infl.
T		879	1.35		1.40	1.75		1505	Flexural	None
M	1.68	876		1.35	1.40		1.75	1505	Flexural	None
B		650			0.80			1505	Splt-brkt	**High**

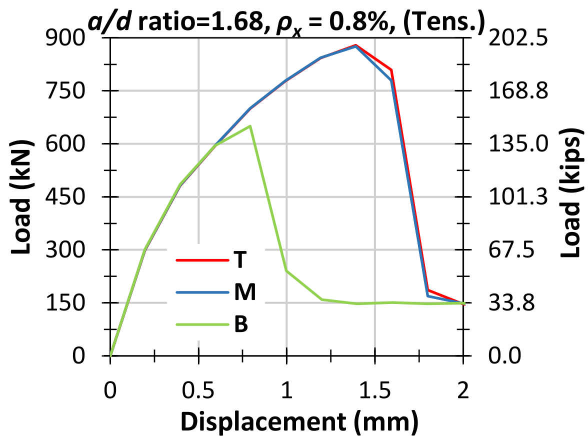

Figure A-6: Load-displacement response-single bracket type-monotonic tension - *a/d* ratio = 1.68, ρ_x = 0.8%.

- The load capacities increase by 35% when the h_e is changed from bottom to middle.
- The displacement capacities increase by 75% when the h_e is changed from bottom to middle.
- Dominant anchorage cracks are seen for the bottom h_e.

***a/d* ratio = 1.42, ρ_x = 0.2%**

h_e	Numerical Model	Crack Pattern
Top (T)	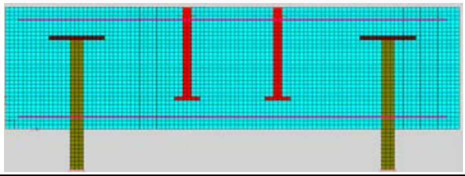	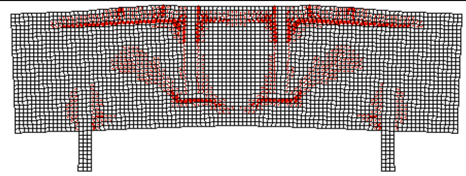
Middle (M)	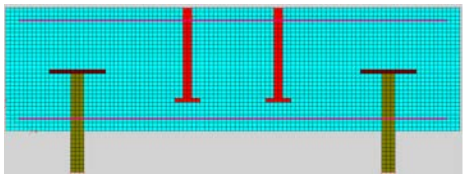	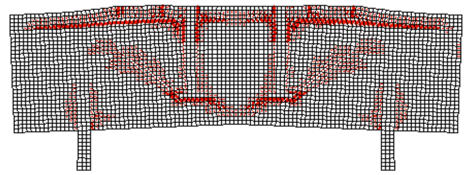
Bottom (B)	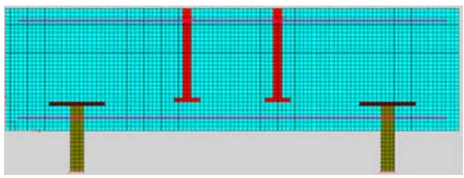	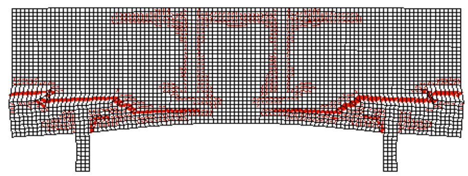

Figure A-7: Numerical model and crack pattern-single bracket type-monotonic tension - *a/d* ratio=1.42, ρ_x = 0.2%.

Table A-4: Comparison of numerical simulation-single bracket type-monotonic tension - *a/d* ratio = 1.42, ρ_x = 0.2%.

h_e	*a/d* ratio	P_u (KN)	$P_{u\text{-}T/B}$	$P_{u\text{-}M/B}$	δ_u (mm)	$\delta_{u\text{-}T/B}$	$\delta_{u\text{-}M/B}$	Stiff (KN/mm)	Failure Mode	Bracket Infl.
T		623	1.06		1.15	1.21		1650	Flexural	None
M	1.42	622		1.06	1.15		1.21	1650	Flexural	None
B		587			0.95			1650	Splt-brkt	High

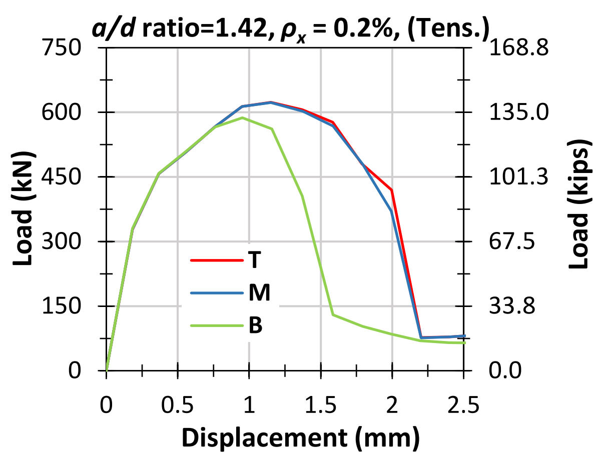

Figure A-8: Load-displacement response-single bracket type- monotonic tension - *a/d* ratio = 1.42, ρ_x = 0.2%.

- The load capacities increase slightly by 6% when the h_e is changed from bottom to middle.

- The displacement capacities increase by 21% when the h_e is changed from bottom to middle.
- Dominant anchorage cracks are seen for the bottom h_e.

a/d ratio = 1.42, ρ_x = 0.4%

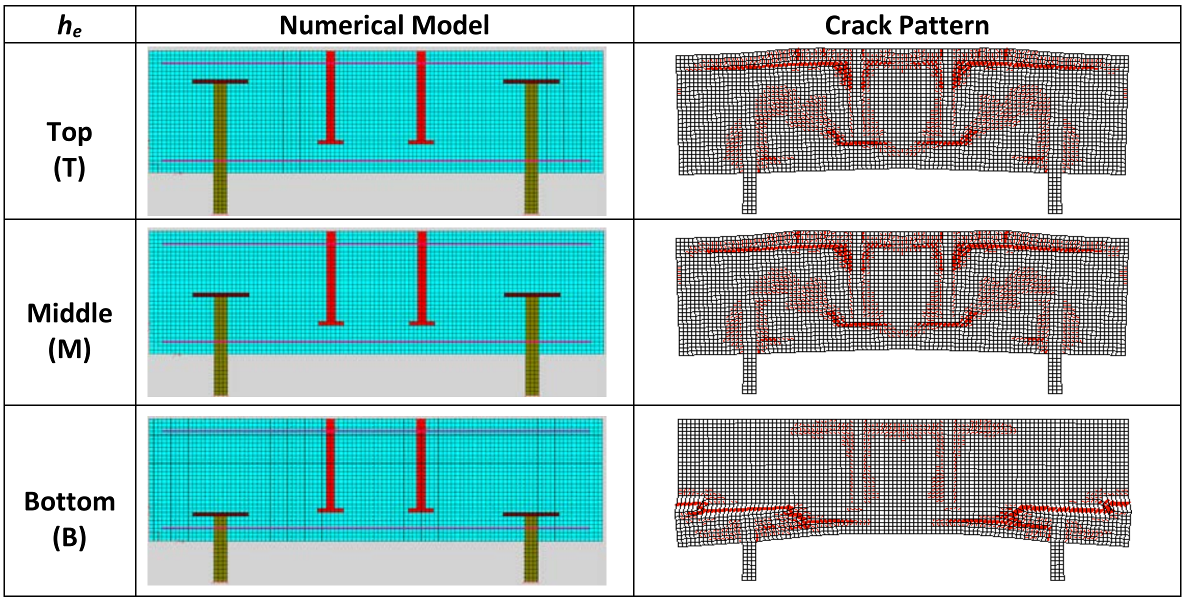

Figure A-9: Numerical model and crack pattern-single bracket type-monotonic tension - a/d ratio = 1.42, ρ_x = 0.4%.

Table A-5: Comparison of numerical simulation-single bracket type-monotonic tension - a/d ratio = 1.42, ρ_x = 0.4%.

h_e	a/d ratio	P_u (KN)	$P_{u\text{-}T/B}$	$P_{u\text{-}M/B}$	δ_u (mm)	$\delta_{u\text{-}T/B}$	$\delta_{u\text{-}M/B}$	Stiff (KN/mm)	Failure Mode	Bracket Infl.
T		810	1.25		1.15	1.53		1720	Flexural	Low
M	1.42	809		1.25	1.15		1.53	1720	Flexural	Low
B		647			0.75			1720	Splt-brkt	High

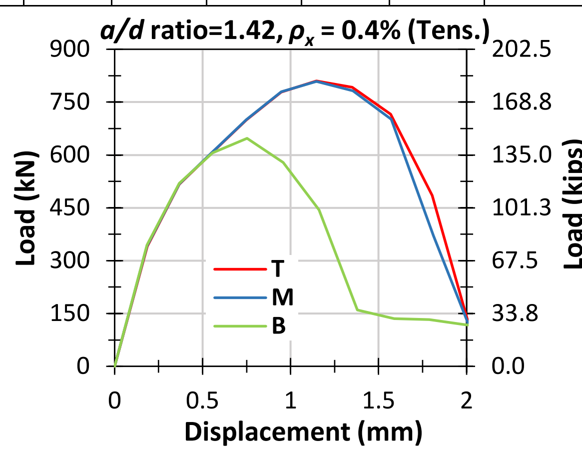

Figure A-10: Load-displacement response-single bracket type-monotonic tension - a/d ratio = 1.42, ρ_x = 0.4%.

- The load capacities increase by 25% when the h_e is changed from bottom to middle.
- The displacement capacities increase by 53% when the h_e is changed from bottom to middle.
- Dominant anchorage cracks are seen for the bottom h_e.

***a/d* ratio = 1.42, ρ_x = 0.8%**

h_e	Numerical Model	Crack Pattern
Top (T)	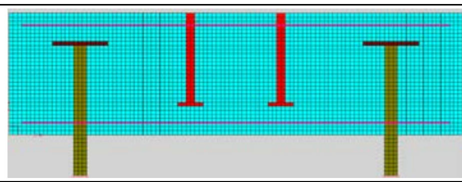	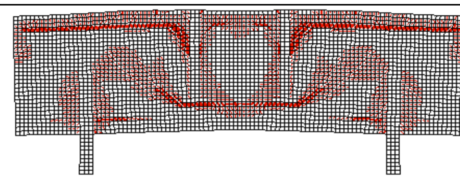
Middle (M)	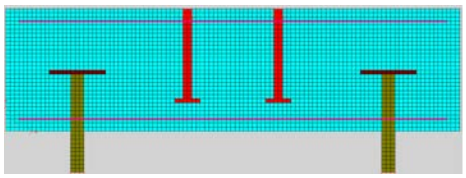	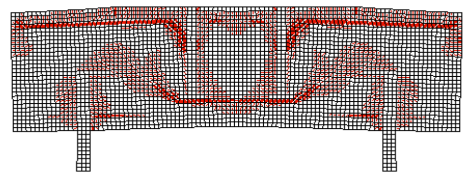
Bottom (B)	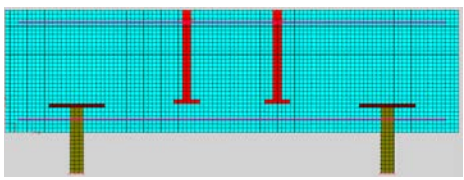	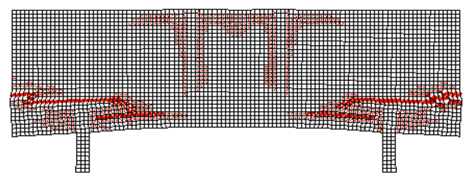

Figure A-11: Numerical model and crack pattern-single bracket type-monotonic tension - *a/d* ratio = 1.42, ρ_x = 0.8%.

Table A-6: Comparison of numerical simulation-single bracket type-monotonic tension - *a/d* ratio = 1.42, ρ_x = 0.8%.

h_e	*a/d* ratio	P_u (KN)	$P_{u\text{-}T/B}$	$P_{u\text{-}M/B}$	δ_u (mm)	$\delta_{u\text{-}T/B}$	$\delta_{u\text{-}M/B}$	Stiff (KN/mm)	Failure Mode	Bracket Infl.
T		1025	1.54		1.35	1.78		1805	Flexural	Low
M	1.42	1010		1.52	1.35		1.78	1805	Flexural	Low
B		667			0.76			1805	Splt-brkt	**High**

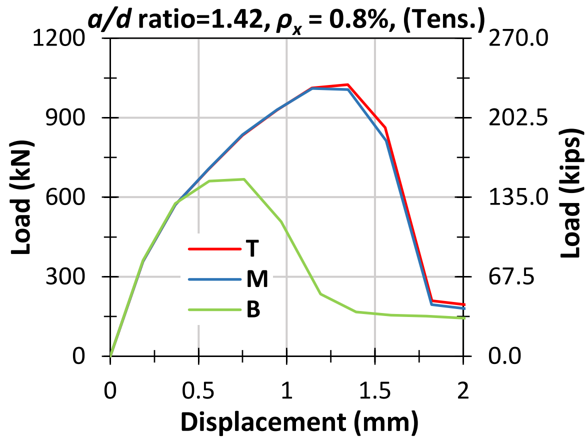

Figure A-12: Load-displacement response-single bracket type-monotonic tension - *a/d* ratio = 1.42, ρ_x = 0.8%.

- The load capacities increase by 52% when the h_e is changed from bottom to middle.
- The displacement capacities increase by 78% when the h_e is changed from bottom to middle.
- Dominant anchorage cracks are seen for the bottom h_e.

_a/d_ ratio = 1.11, ρ_x = 0.2%

h_e	Numerical Model	Crack Pattern
Top (T)	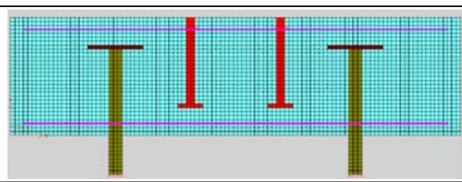	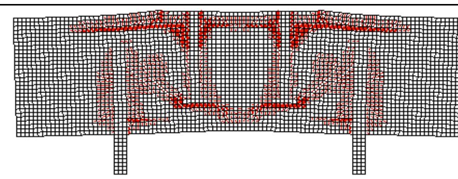
Middle (M)	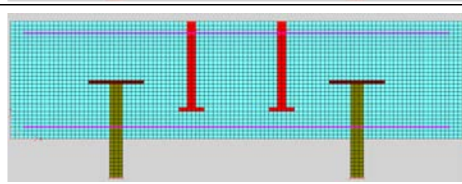	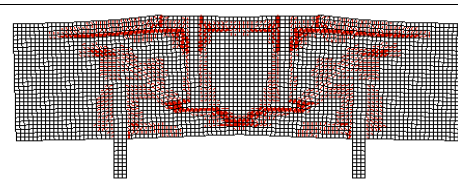
Bottom (B)	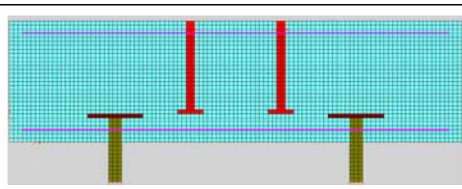	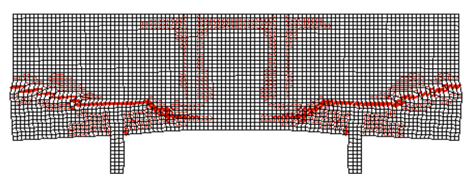

Figure A-13: Numerical model and crack pattern-single bracket type-monotonic tension -*a/d* ratio = 1.11, ρ_x = 0.2%.

Table A-7: Comparison of numerical simulation-single bracket type-monotonic tension - *a/d* ratio = 1.11, ρ_x = 0.2%.

h_e	*a/d* ratio	P_u (KN)	$P_{u\text{-}T/B}$	$P_{u\text{-}M/B}$	δ_u (mm)	$\delta_{u\text{-}T/B}$	$\delta_{u\text{-}M/B}$	Stiff (KN/mm)	Failure Mode	Bracket Infl.
T		826	1.30		0.93	1.22		2040	Flexural	Low
M	1.11	824		1.30	0.93		1.22	2040	Flexural	Low
B		636			0.76			2040	Splt-brkt	**High**

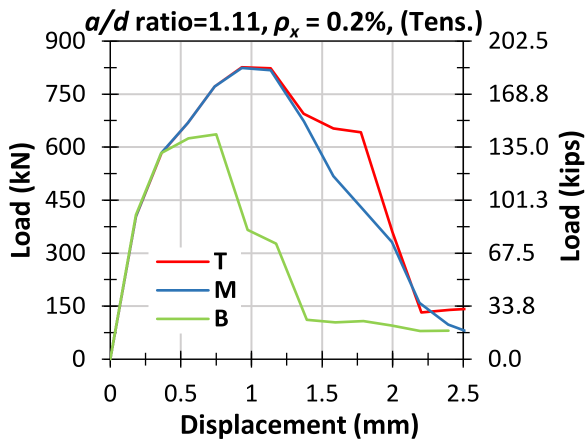

Figure A-14: Load-displacement response-single bracket-monotonic tension- *a/d* ratio = 1.11, ρ_x = 0.2%.

- The load capacities increase by 30% when the h_e is changed from bottom to middle.
- The displacement capacities increase by 22% when the h_e is changed from bottom to middle.
- Dominant anchorage cracks are seen for the bottom h_e.

***a/d* ratio = 1.11, ρ_x = 0.4%**

h_e	Numerical Model	Crack Pattern
Top (T)	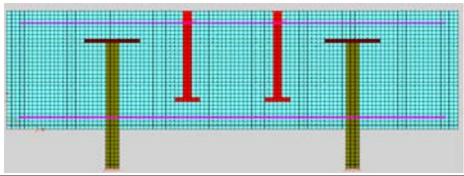	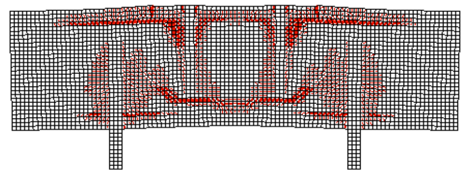
Middle (M)	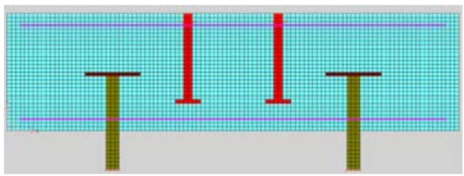	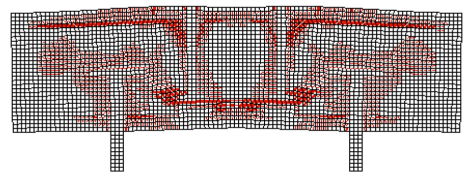
Bottom (B)	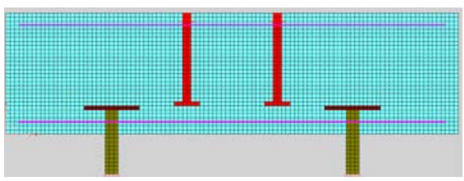	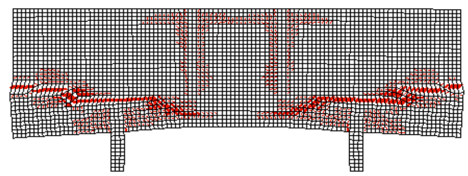

Figure A-15: Numerical model and crack pattern-single bracket type-monotonic tension - *a/d* ratio = 1.11, ρ_x = 0.4%.

Table A-8: Comparison of numerical simulation-single bracket type-monotonic tension -*a/d* ratio = 1.11, ρ_x = 0.4%.

h_e	*a/d* ratio	P_u (KN)	$P_{u\text{-}T/B}$	$P_{u\text{-}M/B}$	δ_u (mm)	$\delta_{u\text{-}T/B}$	$\delta_{u\text{-}M/B}$	Stiff (KN/mm)	Failure Mode	Bracket Infl.
T	1.11	1025	1.49	1.48	1.14	2.38	2.04	2095	Flexural	Low
M		1016			1.14			2095	Flexural	Low
B		687			0.56			2095	Splt-brkt	High

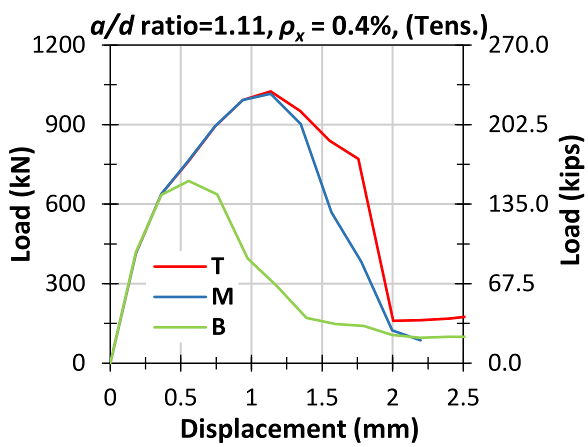

Figure A-16: Load-displacement response-single bracket type-monotonic tension - *a/d* ratio = 1.11, ρ_x = 0.4%.

- The load capacities increase by 48% when the h_e is changed from bottom to middle.

- The displacement capacities increase by 104% when the h_e is changed from bottom to middle.
- Dominant anchorage cracks are seen for the bottom and middle h_e.

***a/d* ratio = 1.11, ρ_x = 0.8%**

h_e	Numerical Model	Crack Pattern
Top (T)	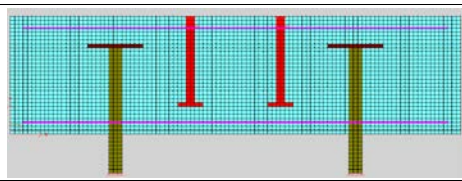	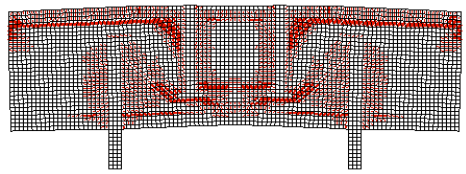
Middle (M)	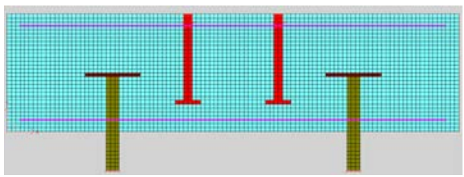	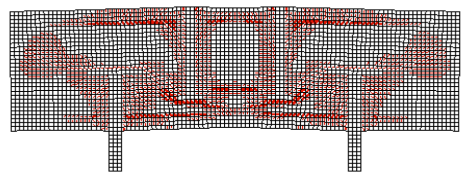
Bottom (B)	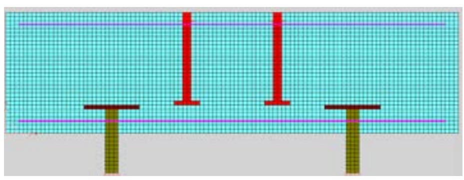	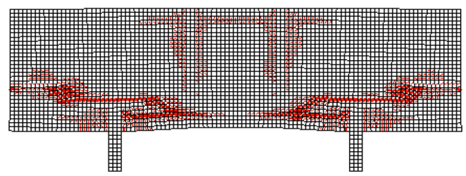

Figure A-17: Numerical model and crack pattern-single bracket type-monotonic tension - *a/d* ratio = 1.11, ρ_x = 0.8%.

Table A-9: Comparison of numerical simulation-single bracket type-monotonic tension - *a/d* ratio = 1.11, ρ_x = 0.8%.

h_e	*a/d* ratio	P_u (KN)	$P_{u\text{-}T/B}$	$P_{u\text{-}M/B}$	δ_u (mm)	$\delta_{u\text{-}T/B}$	$\delta_{u\text{-}M/B}$	Stiff (KN/mm)	Failure Mode	Bracket Infl.
T		1205	1.66		1.33	2.38		2160	Flexural	Low
M	1.11	1172		1.61	1.14		2.04	2160	Flexural	Low
B		727			0.56			2160	Splt-brkt	High

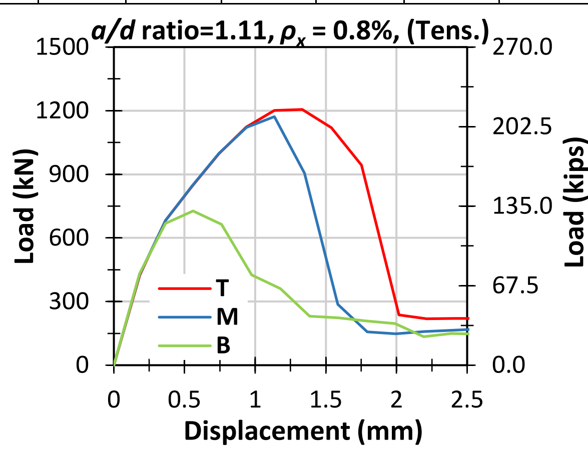

Figure A-18: Load-displacement response-single bracket type-monotonic tension -*a/d* = 1.11, ρ_x = 0.8%.

- The load capacities increase by 61% when the h_e is changed from bottom to middle.
- The displacement capacities increase by 104% when the h_e is changed from bottom to middle.
- Dominant anchorage cracks are seen for the bottom and middle h_e.

Subjected to Monotonic Compression

***a/d* ratio = 1.68, ρ_x = 0.2%**

h_e	Numerical Model	Crack Pattern
Top (T)	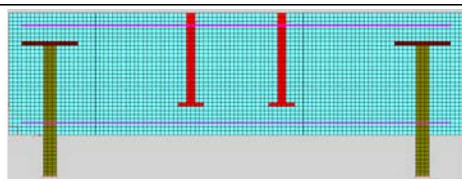	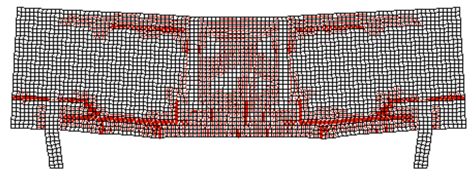
Middle (M)	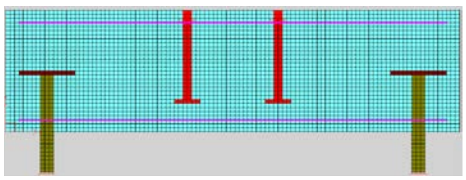	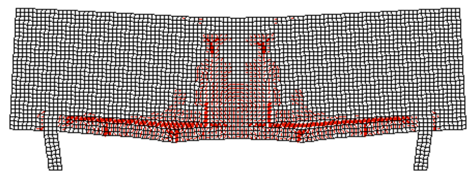
Bottom (B)	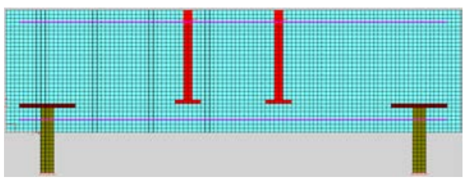	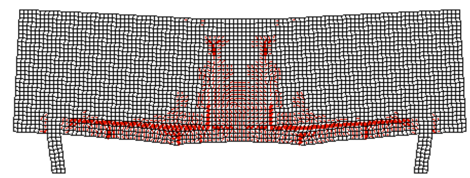

Figure A-19: Numerical model and crack pattern-single bracket type-monotonic compression - *a/d* ratio = 1.68, ρ_x = 0.2%.

Table A-10: Comparison of numerical simulation-single bracket type-monotonic compression - *a/d* ratio = 1.68, ρ_x = 0.2%.

h_e	*a/d* ratio	P_u (KN)	$P_{u\text{-}T/B}$	$P_{u\text{-}M/B}$	δ_u (mm)	$\delta_{u\text{-}T/B}$	$\delta_{u\text{-}M/B}$	Stiff (KN/mm)	Failure Mode	Bracket Infl.
T		924	1.00		1.99	1.00		1595	Flexural	None
M	1.68	923		1.00	1.99		1.00	1595	Flexural	None
B		925			1.99			1595	Flexural	None

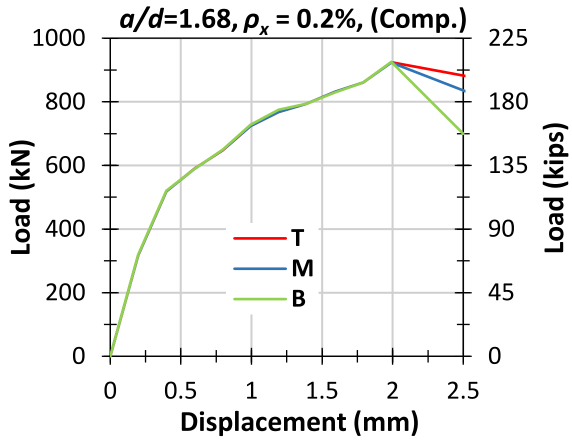

Figure A-20: Load-displacement response-single bracket type-monotonic compression - *a/d* ratio = 1.68, ρ_x = 0.2%.

- The load capacities for all h_e are the same.
- The displacement capacities for all h_e are the same.
- No dominant anchorage cracks are seen for all h_e.

_a/d_ ratio = 1.68, ρ_x = 0.4%

h_e	Numerical Model	Crack Pattern
Top (T)	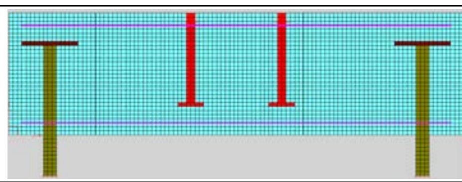	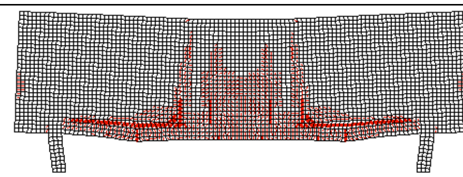
Middle (M)	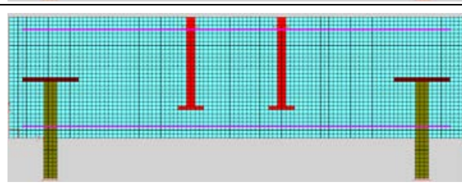	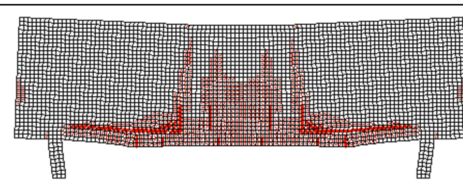
Bottom (B)	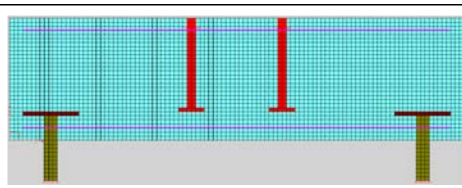	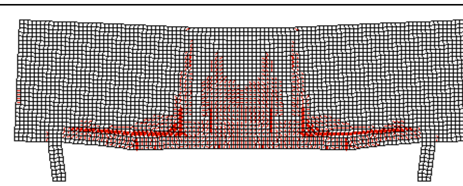

Figure A-21: Numerical model and crack pattern-single bracket type-monotonic compression - *a/d* ratio = 1.68, ρ_x = 0.4%.

Table A-11: Comparison of numerical simulation-single bracket type-monotonic compression - *a/d* ratio = 1.68, ρ_x = 0.4%.

h_e	*a/d* ratio	P_u (KN)	$P_{u\text{-}T/B}$	$P_{u\text{-}M/B}$	δ_u (mm)	$\delta_{u\text{-}T/B}$	$\delta_{u\text{-}M/B}$	Stiff (KN/mm)	Failure Mode	Bracket Infl.
T	1.68	1127	0.99	0.99	1.79	1.00	1.00	1650	Flexural	None
M		1137			1.79			1650	Flexural	None
B		1143			1.79			1650	Flexural	None

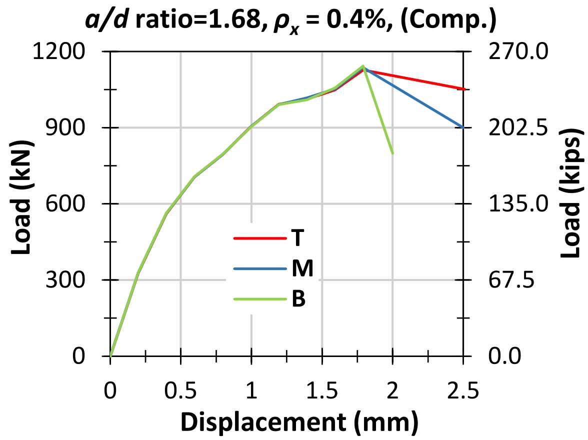

Figure A-22: Load-displacement response-single bracket type-monotonic compression -*a/d* ratio = 1.68, ρ_x = 0.4%.

- The load capacities for all h_e are the same.
- The displacement capacities for all h_e are the same.
- No dominant anchorage cracks are seen for all h_e.

a/d ratio = 1.68, ρ_x = 0.8%

h_e	Numerical Model	Crack Pattern
Top (T)	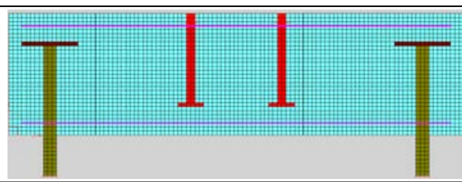	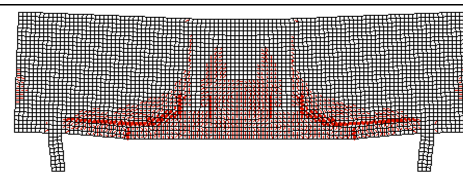
Middle (M)	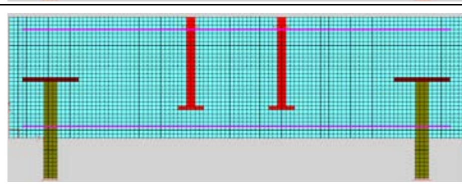	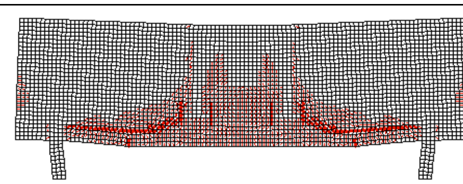
Bottom (B)	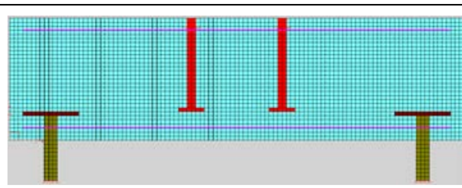	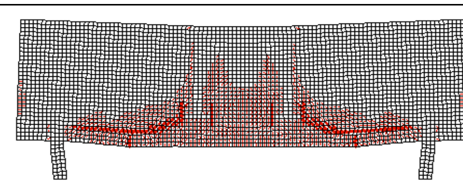

Figure A-23: Numerical model and crack pattern-single bracket type-monotonic compression - *a/d* ratio = 1.68, ρ_x = 0.8%.

Table A-12: Comparison of numerical simulation-single bracket type-monotonic compression - *a/d* ratio = 1.68, ρ_x = 0.8%.

h_e	*a/d* ratio	P_u (KN)	$P_{u\text{-}T/B}$	$P_{u\text{-}M/B}$	δ_u (mm)	$\delta_{u\text{-}T/B}$	$\delta_{u\text{-}M/B}$	Stiff (KN/mm)	Failure Mode	Bracket Infl.
T		1493	0.99		1.79	1.00		1715	Flexural	None
M	1.68	1493		0.99	1.79		1.00	1715	Flexural	None
B		1508			1.79			1715	Flexural	None

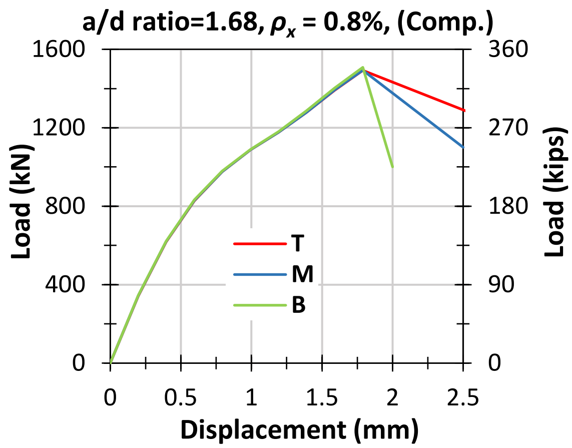

Figure A-24: Load-displacement response-single bracket type-monotonic compression - *a/d* ratio = 1.68, ρ_x = 0.8%.

- The load capacities for all h_e are the same.
- The displacement capacities for all h_e are the same.
- No dominant anchorage cracks are seen for all h_e.

***a/d* ratio = 1.42, ρ_x = 0.2%**

h_e	Numerical Model	Crack Pattern
Top (T)	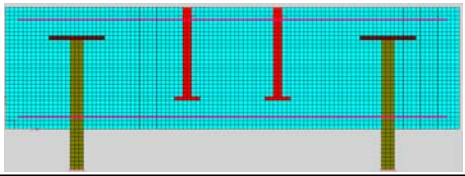	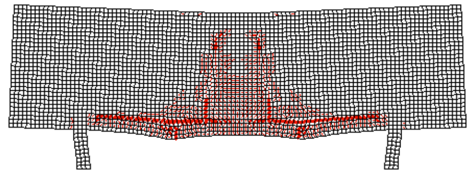
Middle (M)	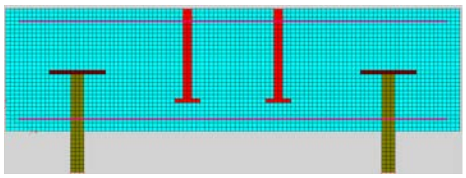	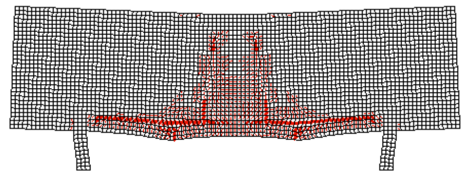
Bottom (B)	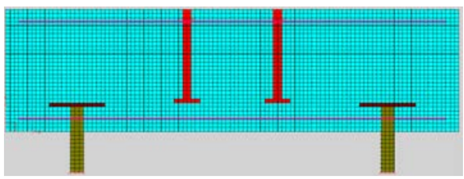	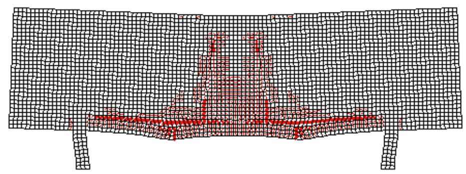

Figure A-25: Numerical model and crack pattern-single bracket type-monotonic compression - *a/d* ratio = 1.42, ρ_x = 0.2%.

Table A-13: Comparison of numerical simulation-single bracket type-monotonic compression - *a/d* ratio = 1.42, ρ_x = 0.2%.

h_e	*a/d* ratio	P_u (KN)	$P_{u\text{-}T/B}$	$P_{u\text{-}M/B}$	δ_u (mm)	$\delta_{u\text{-}T/B}$	$\delta_{u\text{-}M/B}$	Stiff (KN/mm)	Failure Mode	Bracket Infl.
T		1083	1.00		1.34	1.00		2030	Flexural	None
M	1.42	1084		1.00	1.34		1.00	2030	Flexural	None
B		1081			1.34			2030	Flexural	None

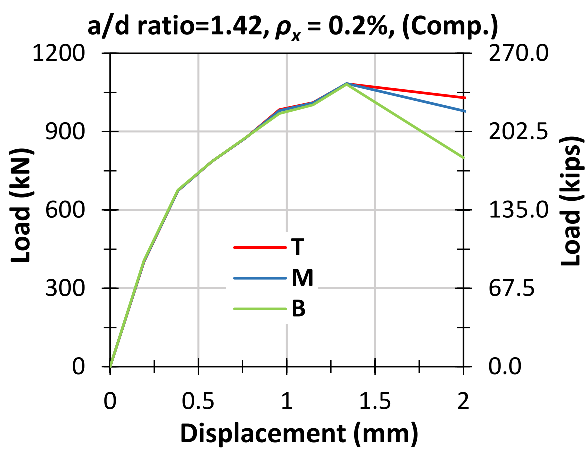

Figure A-26: Load-displacement response-single bracket type-monotonic compression - *a/d* ratio = 1.42, ρ_x = 0.2%.

- The load capacities for all h_e are the same.

- The displacement capacities for all h_e are the same.
- No dominant anchorage cracks are seen for all h_e.

***a/d* ratio = 1.42, ρ_x = 0.4%**

h_e	Numerical Model	Crack Pattern
Top (T)	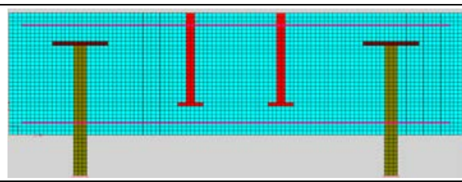	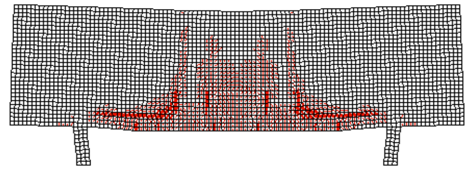
Middle (M)	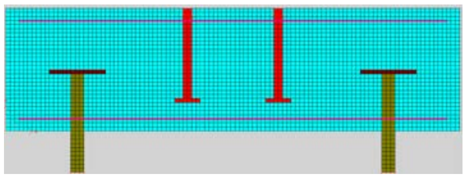	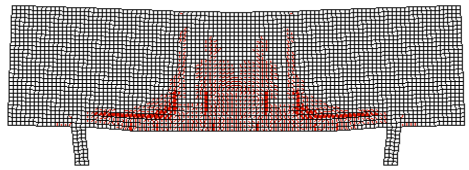
Bottom (B)	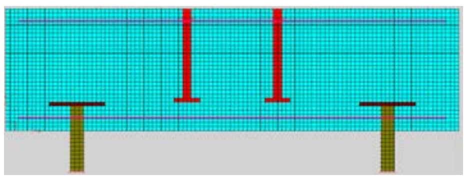	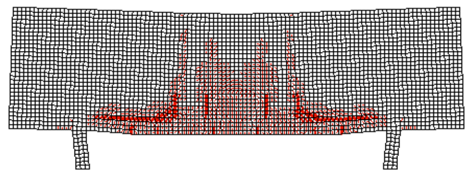

Figure A-27: Numerical model and crack pattern-single bracket type-monotonic compression - *a/d* ratio = 1.42, ρ_x = 0.4%.

Table A-14: Comparison of numerical simulation-single bracket type-monotonic compression - *a/d* ratio = 1.42, ρ_x = 0.4%.

h_e	*a/d* ratio	P_u (KN)	$P_{u\text{-}T/B}$	$P_{u\text{-}M/B}$	δ_u (mm)	$\delta_{u\text{-}T/B}$	$\delta_{u\text{-}M/B}$	Stiff (KN/mm)	Failure Mode	Bracket Infl.
T	1.42	1426	0.99	1.00	1.34	1.00	1.00	2080	Flexural	None
M		1431			1.34			2080	Flexural	None
B		1435			1.34			2080	Flexural	None

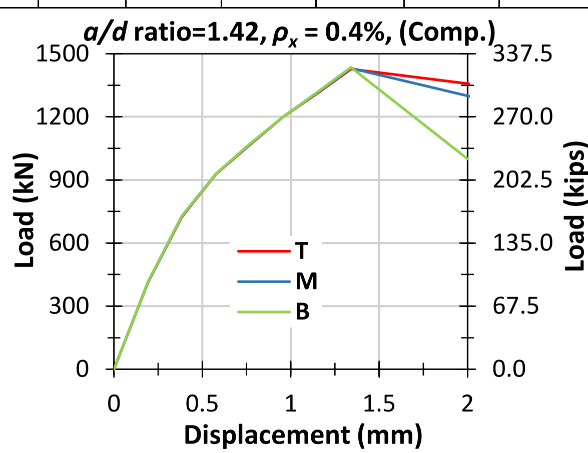

Figure A-28: Load-displacement response-single bracket type-monotonic compression - *a/d* ratio = 1.42, ρ_x = 0.4%.

- The load capacities for all h_e are the same.
- The displacement capacities for all h_e are the same.
- No dominant anchorage cracks are seen for all h_e.

***a/d* ratio = 1.42, ρ_x = 0.8%**

h_e	Numerical Model	Crack Pattern
Top (T)	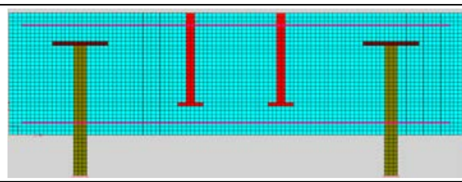	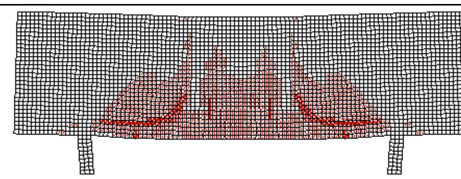
Middle (M)	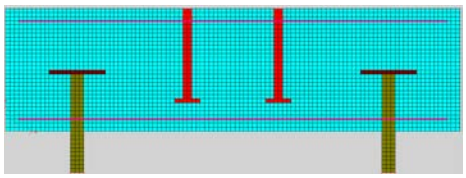	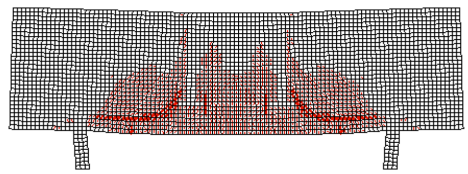
Bottom (B)	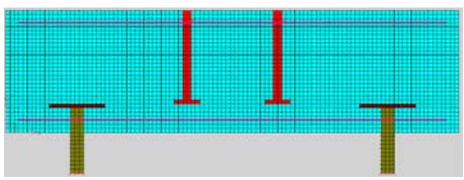	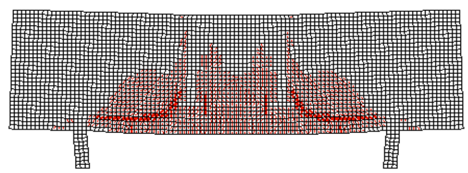

Figure A-29: Numerical model and crack pattern-single bracket type-monotonic compression - *a/d* ratio = 1.42, ρ_x = 0.8%.

Table A-15: Comparison of numerical simulation-single bracket type-monotonic compression - *a/d* ratio = 1.42, ρ_x = 0.8%.

h_e	*a/d* ratio	P_u (KN)	$P_{u\text{-}T/B}$	$P_{u\text{-}M/B}$	δ_u (mm)	$\delta_{u\text{-}T/B}$	$\delta_{u\text{-}M/B}$	Stiff (KN/mm)	Failure Mode	Bracket Infl.
T		1800	0.99		1.34	1.00		2155	Flexural	None
M	1.42	1800		0.99	1.34		1.00	2155	Flexural	None
B		1810			1.34			2155	Flexural	None

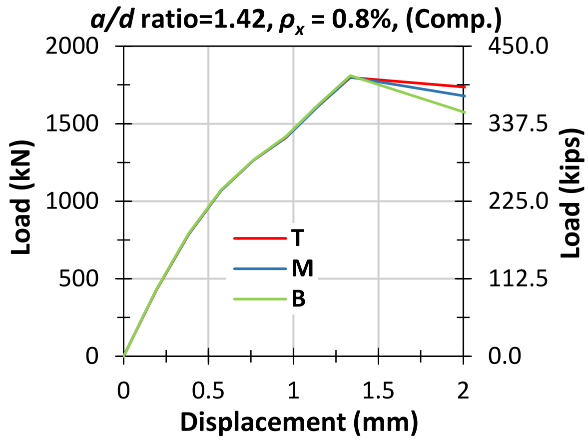

Figure A-30: Load- displacement response-single bracket type-monotonic compression - *a/d* ratio = 1.42, ρ_x = 0.8%.

- The load capacities for all h_e are the same.
- The displacement capacities for all h_e are the same.
- No dominant anchorage cracks are seen for all h_e.

***a/d* ratio = 1.11, ρ_x = 0.2%**

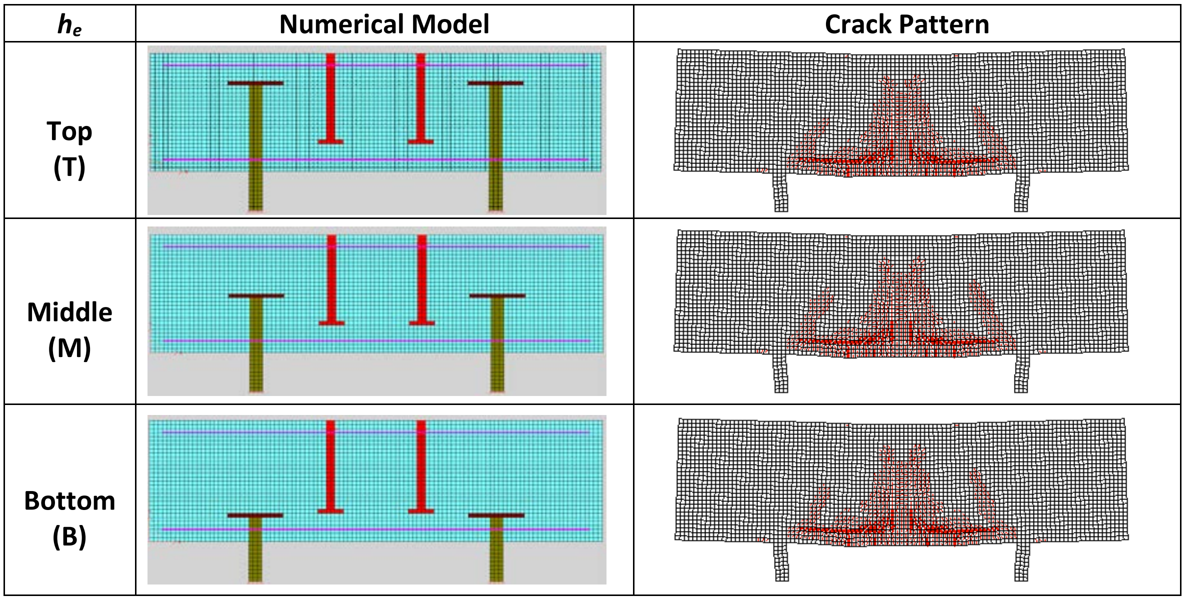

Figure A-31: Numerical model and crack pattern-single bracket type-monotonic compression - *a/d* ratio = 1.11, ρ_x = 0.2%.

Table A-16: Comparison of numerical simulation-single bracket type-monotonic compression - *a/d* ratio = 1.11, ρ_x = 0.2%.

h_e	*a/d* ratio	P_u (KN)	$P_{u\text{-}T/B}$	$P_{u\text{-}M/B}$	δ_u (mm)	$\delta_{u\text{-}T/B}$	$\delta_{u\text{-}M/B}$	Stiff (KN/mm)	Failure Mode	Bracket Infl.
T	1.11	1545	0.99	1.00	0.94	1.00	1.00	2595	Flexural	None
M		1554			0.94			2595	Flexural	None
B		1552			0.94			2595	Flexural	None

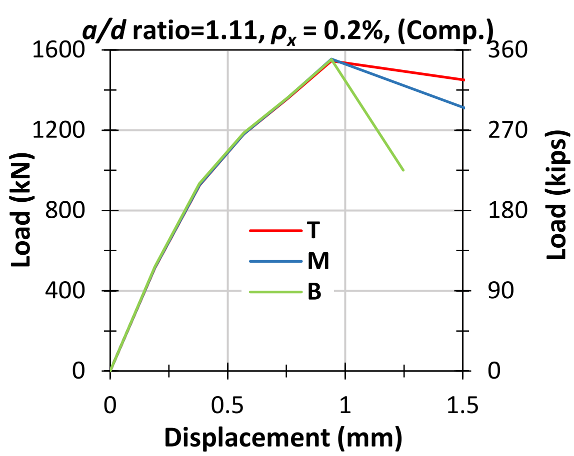

Figure A-32: Load-displacement response-single bracket type-monotonic compression - *a/d* ratio = 1.11, ρ_x = 0.2%.

- The load capacities for all h_e are the same.

- The displacement capacities for all h_e are the same.
- No dominant anchorage cracks are seen for all h_e.

***a/d* ratio = 1.11, ρ_x = 0.4%**

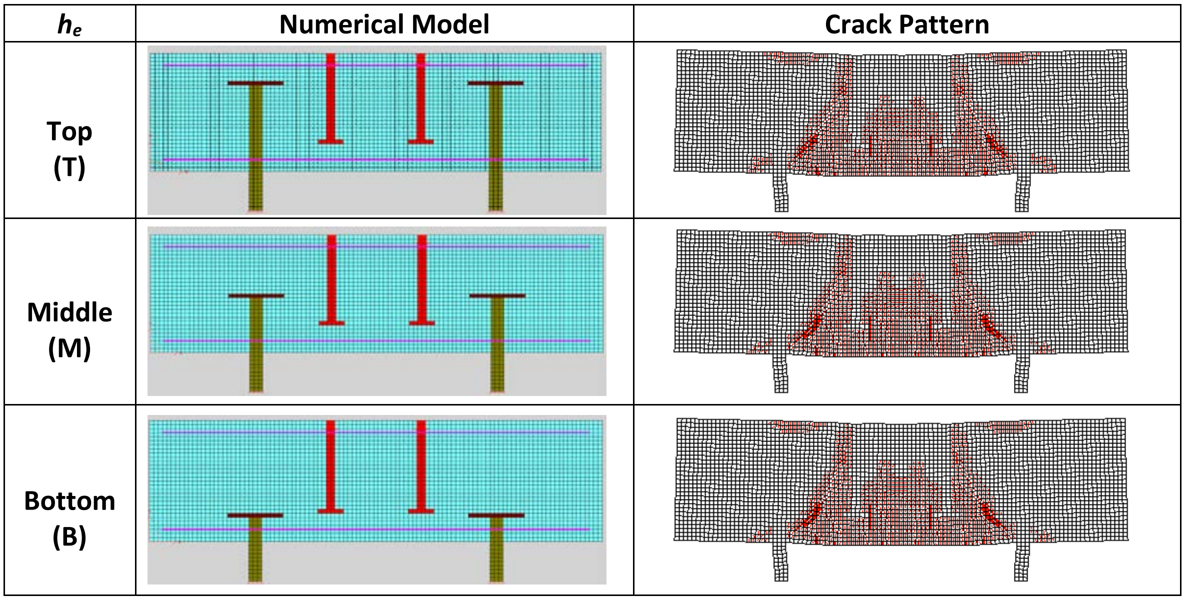

Figure A-33: Numerical model and crack pattern-single bracket type-monotonic compression - *a/d* ratio = 1.11, ρ_x = 0.4%.

Table A-17: Comparison of numerical simulation-single bracket type-monotonic compression - *a/d* ratio = 1.11, ρ_x = 0.4%.

h_e	*a/d* ratio	P_u (KN)	$P_{u\text{-}T/B}$	$P_{u\text{-}M/B}$	δ_u (mm)	$\delta_{u\text{-}T/B}$	$\delta_{u\text{-}M/B}$	Stiff (KN/mm)	Failure Mode	Bracket Infl.
T		1830	0.98		1.12	1.00		2630	Shear	None
M	1.11	1841		0.99	1.12		1.00	2630	Shear	None
B		1864			1.12			2630	Shear	None

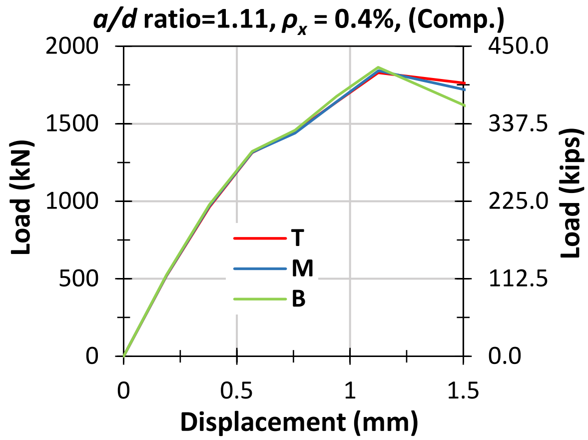

Figure A-34: Load-displacement response-single bracket type-monotonic compression - *a/d* ratio = 1.11, ρ_x = 0.4%.

- The load capacities for all h_e are the same.
- The displacement capacities for all h_e are the same.
- No dominant anchorage cracks are seen for all h_e.

***a/d* ratio = 1.11, ρ_x = 0.8%**

h_e	Numerical Model	Crack Pattern
Top (T)	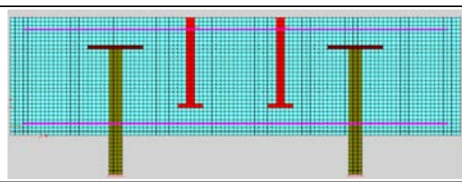	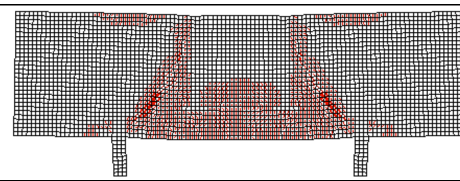
Middle (M)	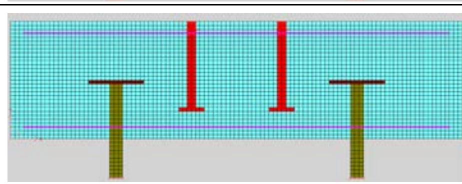	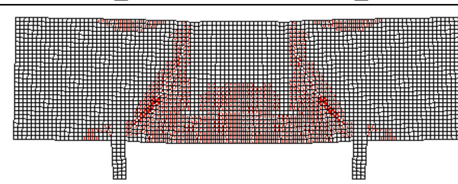
Bottom (B)	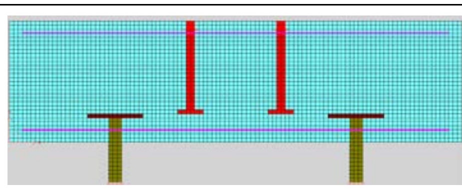	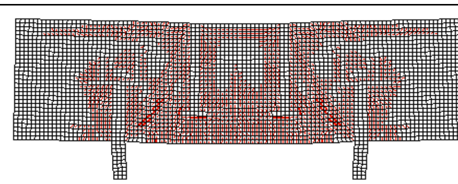

Figure A-35: Numerical model and crack pattern-single bracket type-monotonic compression - *a/d* ratio = 1.11, ρ_x = 0.8%.

Table A-18: Comparison of numerical simulation-single bracket type-monotonic compression - *a/d* ratio = 1.11, ρ_x = 0.8%.

h_e	*a/d* ratio	P_u (KN)	$P_{u\text{-}T/B}$	$P_{u\text{-}M/B}$	δ_u (mm)	$\delta_{u\text{-}T/B}$	$\delta_{u\text{-}M/B}$	Stiff (KN/mm)	Failure Mode	Bracket Infl.
T	1.11	2133	0.98	0.98	1.12	1.00	1.00	2675	Shear	None
M		2144			1.12			2675	Shear	None
B		2180			1.12			2675	Shear	None

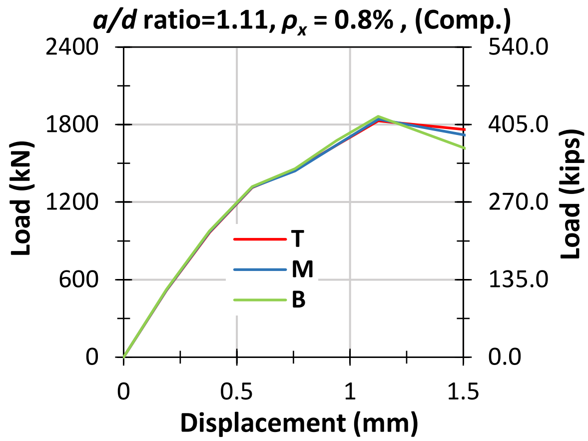

Figure A-36: Load-displacement curve-single bracket type-monotonic compression - *a/d* ratio = 1.11, ρ_x = 0.8%.

- The load capacities for all h_e are the same.
- The displacement capacities for all h_e are the same.
- No dominant anchorage cracks are seen for all h_e.

Subjected to Reversed-Cyclic Loads

a/d ratio = 1.68, ρ_x = 0.2%

h_e	Numerical Model	Crack Pattern
Top (T)	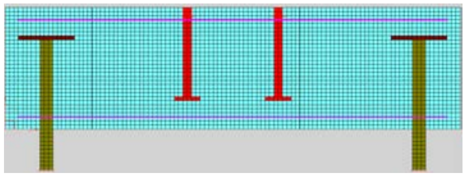	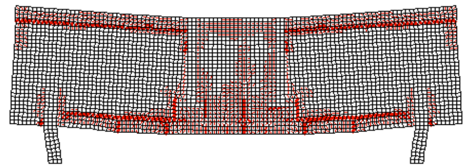
Middle (M)	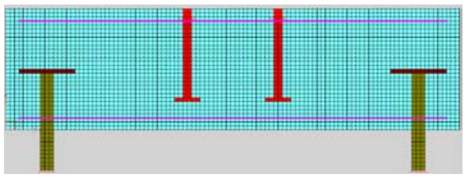	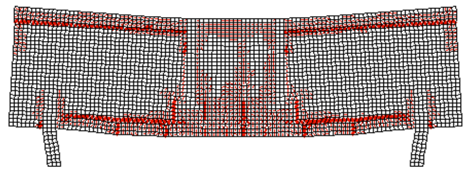
Bottom (B)	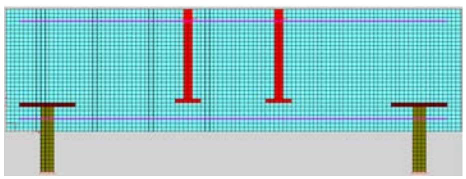	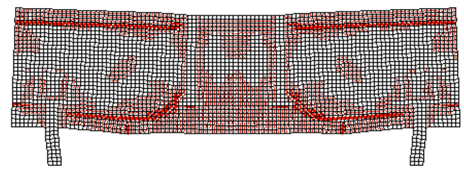

Figure A-37: Numerical model and crack pattern-single bracket type-reversed-cyclic - *a/d* ratio = 1.68, ρ_x = 0.2%.

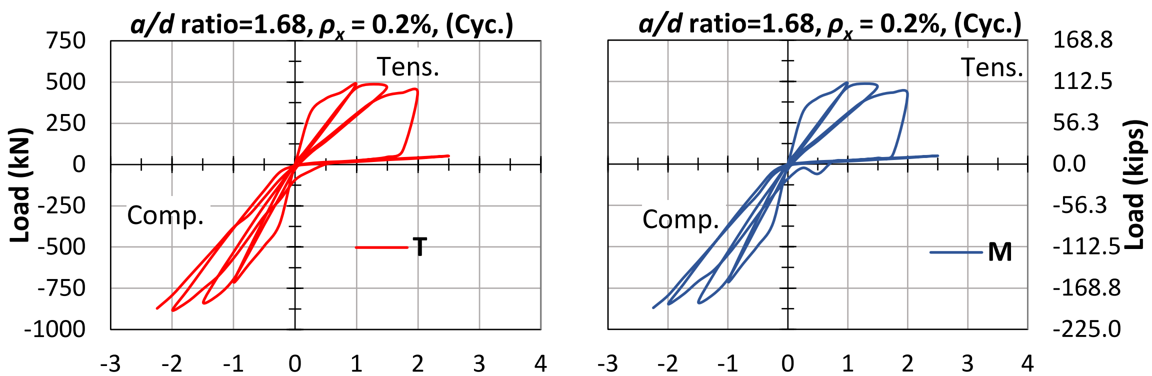

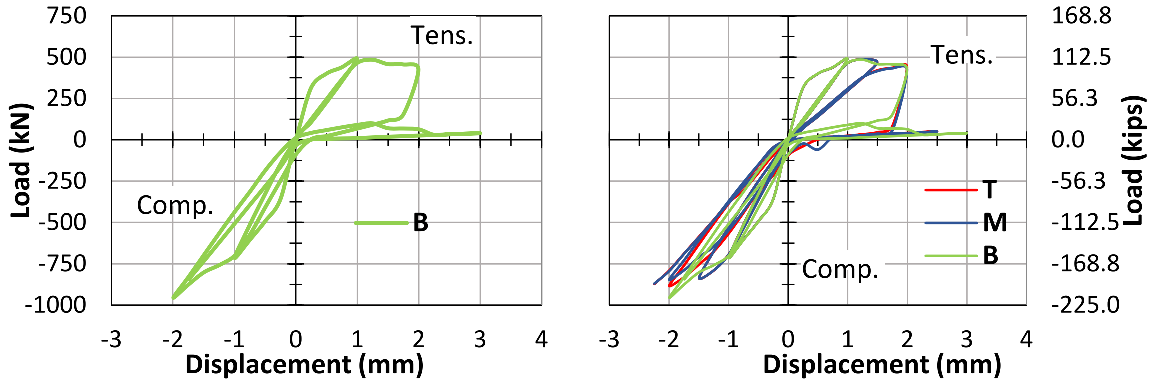

Figure A-38: Load-displacement response-single bracket type-reversed-cyclic - *a/d* ratio = 1.68, ρ_x = 0.2%.

Table A-19: Comparison of numerical simulation-single bracket type-reversed-cyclic - *a/d* ratio = 1.68, ρ_x = 0.2%.

h_e	*a/d* ratio	Tensile Component						Compression Component						Failure Mode	Bracket Infl.
		P_t (KN)	$P_{t\text{-}T/B}$	$P_{t\text{-}M/B}$	δ_t (mm)	$\delta_{t\text{-}T/B}$	$\delta_{t\text{-}M/B}$	P_t (KN)	$P_{c\text{-}T/B}$	$P_{c\text{-}M/B}$	δ_c (mm)	$\delta_{c\text{-}T/B}$	$\delta_{c\text{-}M/B}$		
T		490	1.00		2.50	0.83		872	0.91		2.24	1.13		Flexural	None
M	1.68	490		1.00	2.50		0.83	870		0.91	2.24		1.13	Flexural	None
B		491			3.00			955			1.99			Splt-brkt	High

Tensile component's result

- The load capacities for all h_e are the same.

Compression component's result

- The load capacities decreased slightly by 9% when the h_e is changed from bottom to middle.

Bracket influence

- Bottom h_e gives splitting of concrete around anchorage bracket zone.

***a/d* ratio = 1.68, ρ_x = 0.4%**

h_e	Numerical Model	Crack Pattern
Top (T)	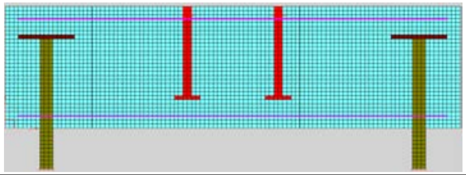	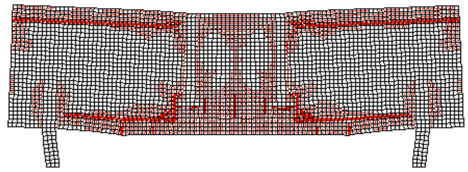
Middle (M)	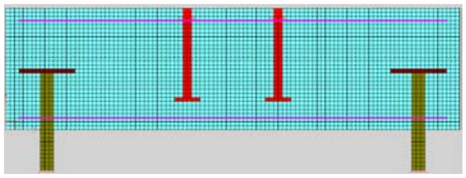	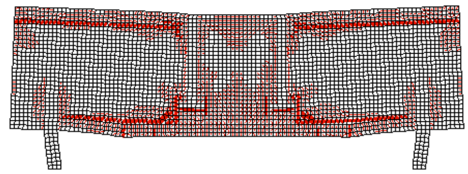
Bottom (B)	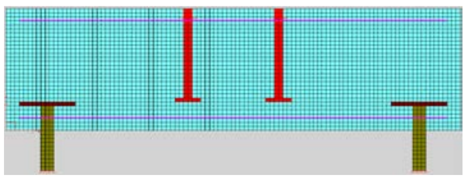	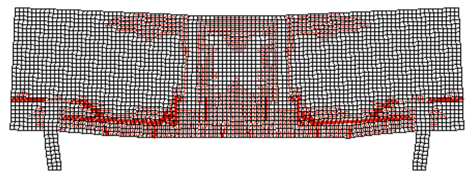

Figure A-39: Numerical model and crack pattern-single bracket type-reversed-cyclic - *a/d* ratio = 1.68, 0.4 ρ_x%.

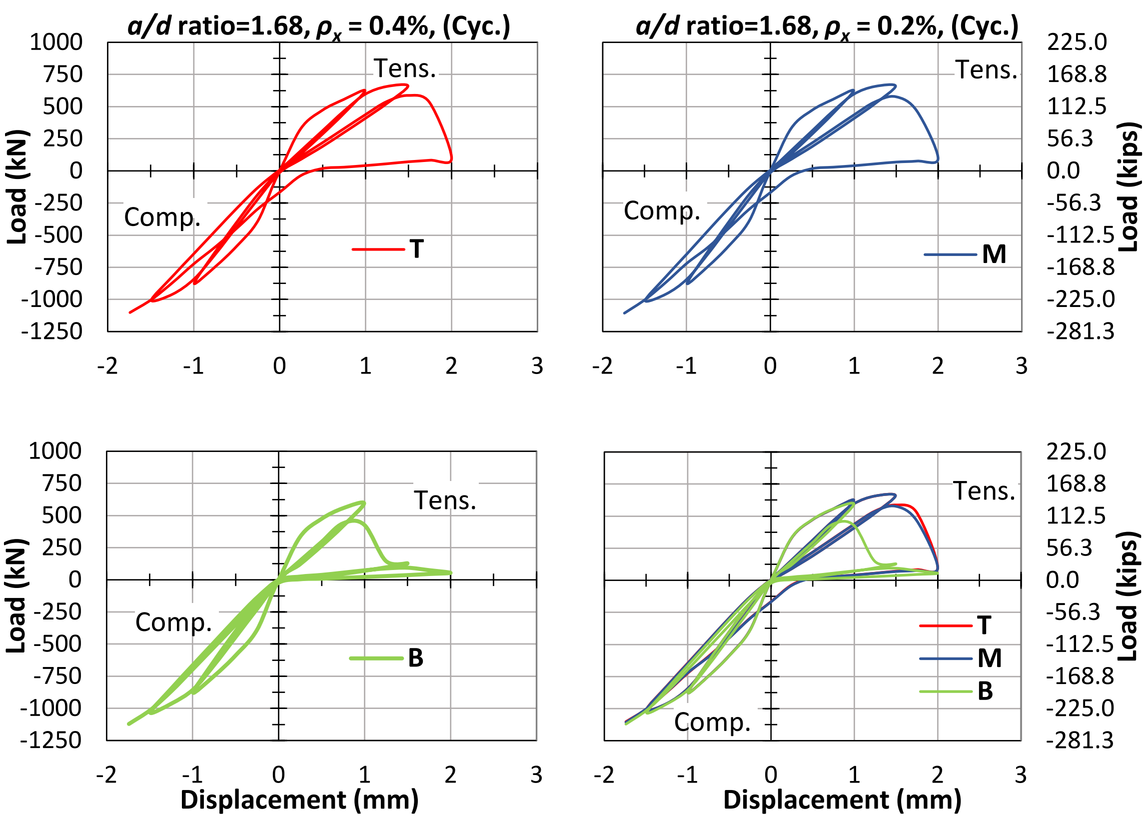

Figure A-40: Load-displacement response-single bracket type-reversed-cyclic - *a/d* ratio = 1.68, ρ_x = 0.4%.

Table A-20: Comparison of numerical simulation-single bracket type-reversed-cyclic - *a/d* ratio = 1.68, ρ_x = 0.4%.

h_e	*a/d* ratio	Tensile Component						Compression Component						Failure Mode	Bracket Infl.
		P_t (KN)	$P_{t\text{-}T/B}$	$P_{t\text{-}M/B}$	δ_t (mm)	$\delta_{t\text{-}T/B}$	$\delta_{t\text{-}M/B}$	P_t (KN)	$P_{c\text{-}T/B}$	$P_{c\text{-}M/B}$	δ_c (mm)	$\delta_{c\text{-}T/B}$	$\delta_{c\text{-}M/B}$		
T		660	1.11		2.00	1.00		1102	0.98		1.74	1.00		Flexural	None
M	1.68	659		1.11	2.00		1.00	1106		0.99	1.74		1.00	Flexural	None
B		595			2.00			1121			1.74			Splt-brkt	High

Tensile component's result

- The load capacities increase slightly by 11% when the h_e is changed from bottom to middle.
- The displacement capacities for all h_e are the same.

Compression component's result

- The load capacities for all h_e are the same.
- The displacement capacities for all h_e are the same.

Bracket influence

- Bottom h_e gives splitting of concrete around anchorage bracket zone.

***a/d* ratio = 1.68, ρ_x = 0.8%**

h_e	Numerical Model	Crack Pattern
Top (T)	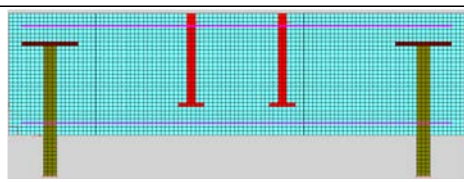	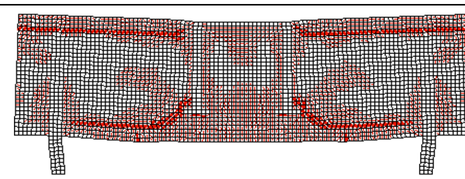
Middle (M)	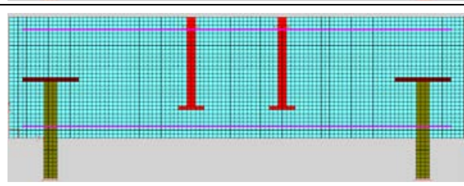	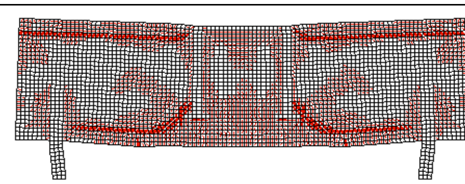
Bottom (B)	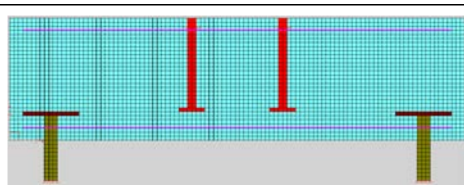	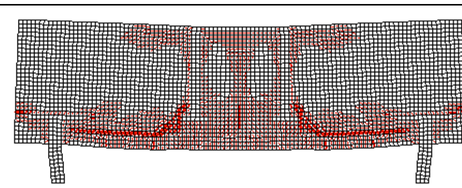

Figure A-41: Numerical model and crack pattern-single bracket type-reversed-cyclic - *a/d* ratio = 1.68, ρ_x = 0.8%.

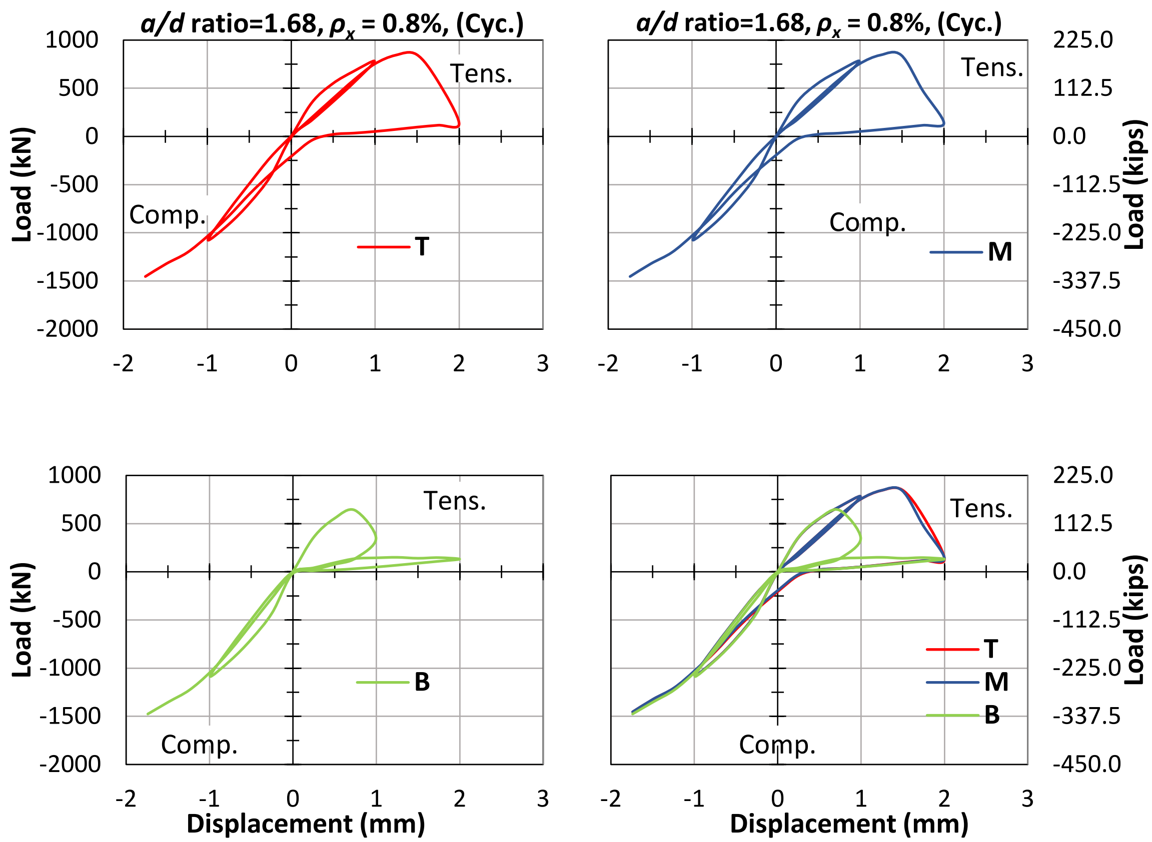

Figure A-42: Load-displacement response-single bracket type-reversed-cyclic - *a/d* ratio = 1.68, ρ_x = 0.8%.

Table A-21: Comparison of numerical simulation-single bracket type-reversed-cyclic - *a/d* ratio = 1.68, ρ_x = 0.8%.

h_e	*a/d* ratio	Tensile Component						Compression Component						Failure Mode	Bracket Infl.
		P_t (KN)	$P_{t\text{-}T/B}$	$P_{t\text{-}M/B}$	δ_t (mm)	$\delta_{t\text{-}T/B}$	$\delta_{t\text{-}M/B}$	P_t (KN)	$P_{c\text{-}T/B}$	$P_{c\text{-}M/B}$	δ_c (mm)	$\delta_{c\text{-}T/B}$	$\delta_{c\text{-}M/B}$		
T		852	1.34		2.00	1.00		1453	0.98		1.74	1.00		Flexural	None
M	1.68	844		1.32	2.00		1.00	1454		0.99	1.74		1.00	Flexural	None
B		638			2.00			1476			1.74			Splt-brkt	High

Tensile component's result

- The load capacities increase by 34% when the h_e is changed from bottom to middle.
- The displacement capacities for all embedment depths are the same.

Compression component's result

- The load capacities decreased slightly by 9% when the h_e is changed from bottom to middle.

Bracket influence

- Bottom h_e gives splitting of concrete around anchorage bracket zone.

***a/d* ratio = 1.42, ρ_x = 0.2%**

h_e	Numerical Model	Crack Pattern
Top (T)	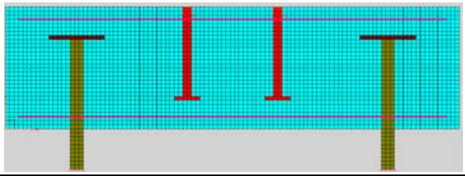	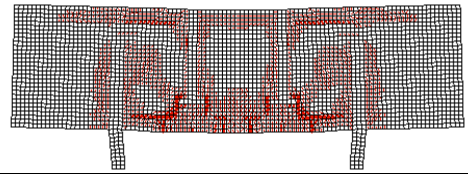
Middle (M)	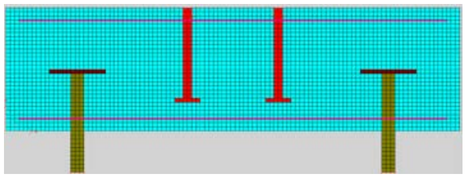	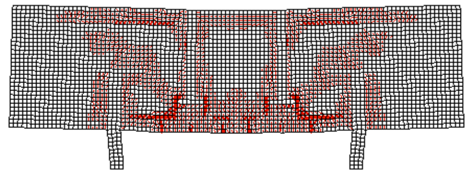
Bottom (B)	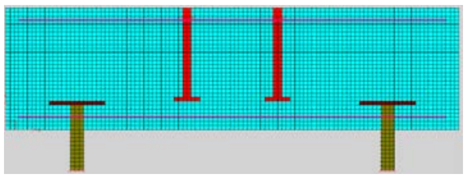	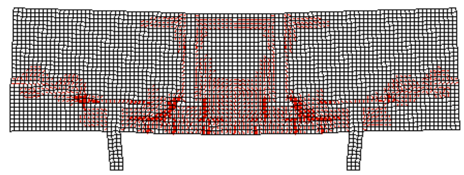

Figure A-43: Numerical model and crack pattern-single bracket type-reversed-cyclic - *a/d* ratio = 1.42, ρ_x = 0.2%.

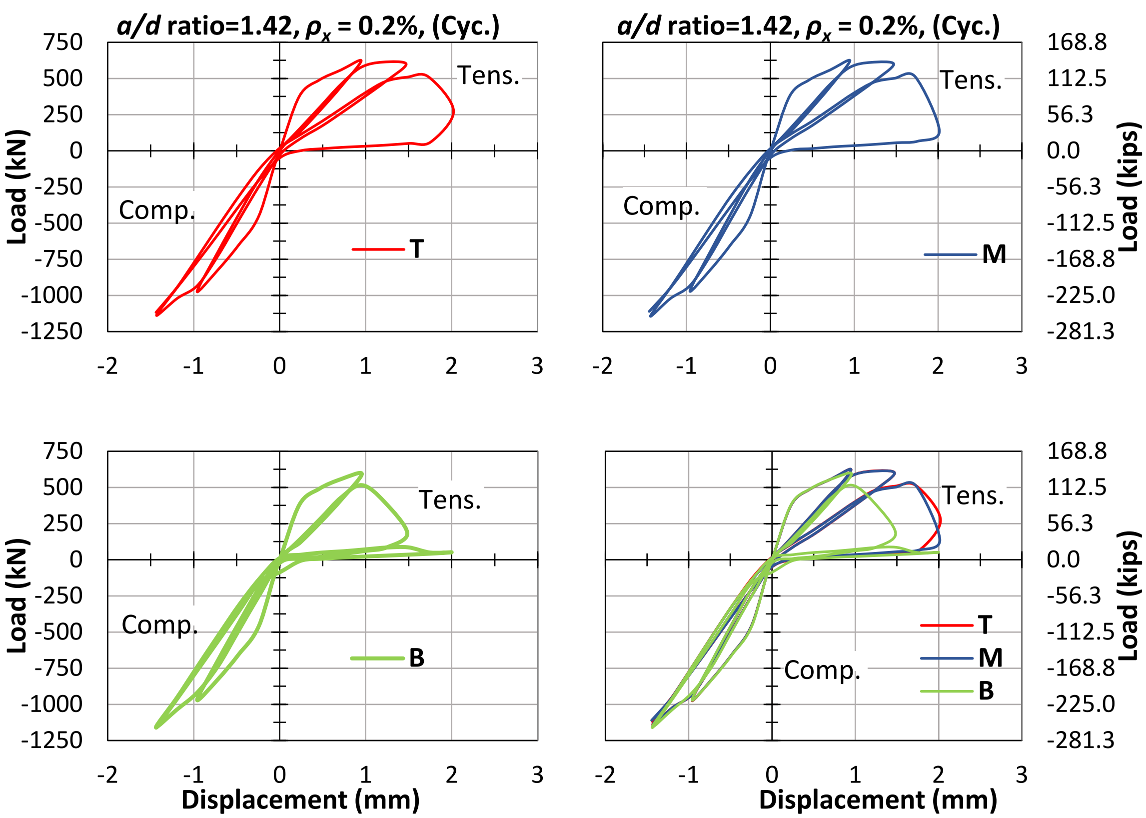

Figure A-44: Load-displacement response-single bracket type-reversed-cyclic - *a/d* ratio = 1.42, ρ_x = 0.2%.

Table A-22: Comparison of numerical simulation-single bracket type-reversed-cyclic - *a/d* ratio = 1.42, ρ_x = 0.2%.

h_e	*a/d* ratio	Tensile Component						Compression Component						Failure Mode	Bracket Infl.
		P_t (KN)	$P_{t\text{-}T/B}$	$P_{t\text{-}M/B}$	δ_t (mm)	$\delta_{t\text{-}T/B}$	$\delta_{t\text{-}M/B}$	P_t (KN)	$P_{c\text{-}T/B}$	$P_{c\text{-}M/B}$	δ_c (mm)	$\delta_{c\text{-}T/B}$	$\delta_{c\text{-}M/B}$		
T		623	1.05		2.02	1.01		1138	0.98		1.44	1.00		Flexural	None
M	1.42	623		1.05	2.02		1.01	1144		0.99	1.44		1.00	Flexural	None
B		594			2.00			1161			1.44			Splt-brkt	None

Tensile component's result

- The load capacities for all h_e are similar.
- The displacement capacities for all embedment depths are the same.

Compression component's result

- The load capacities for all h_e are similar.
- The displacement capacities for all h_e are the same.

Bracket influence

- Bottom h_e gives splitting of concrete around anchorage bracket zone.

***a/d* ratio = 1.42, ρ_x = 0.4%**

h_e	Numerical Model	Crack Pattern
Top (T)	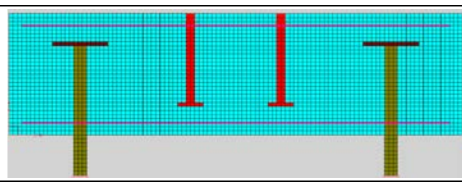	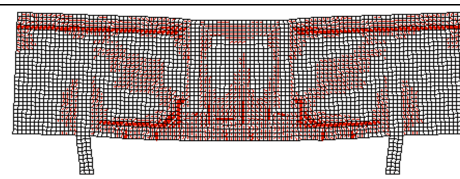
Middle (M)	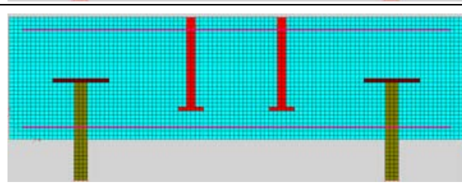	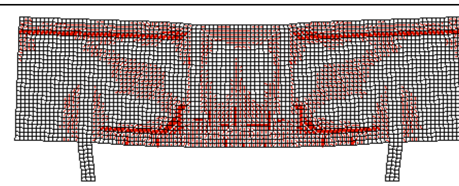
Bottom (B)	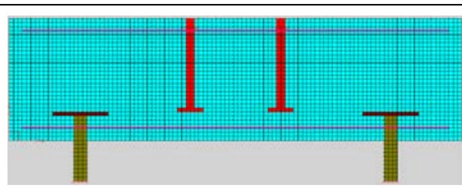	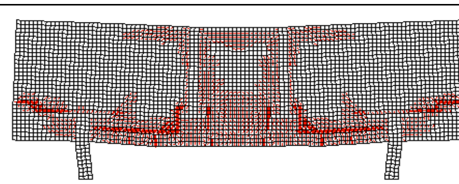

Figure A-45: Numerical model and crack pattern-single bracket type-reversed-cyclic - *a/d* ratio = 1.42, ρ_x = 0.4%.

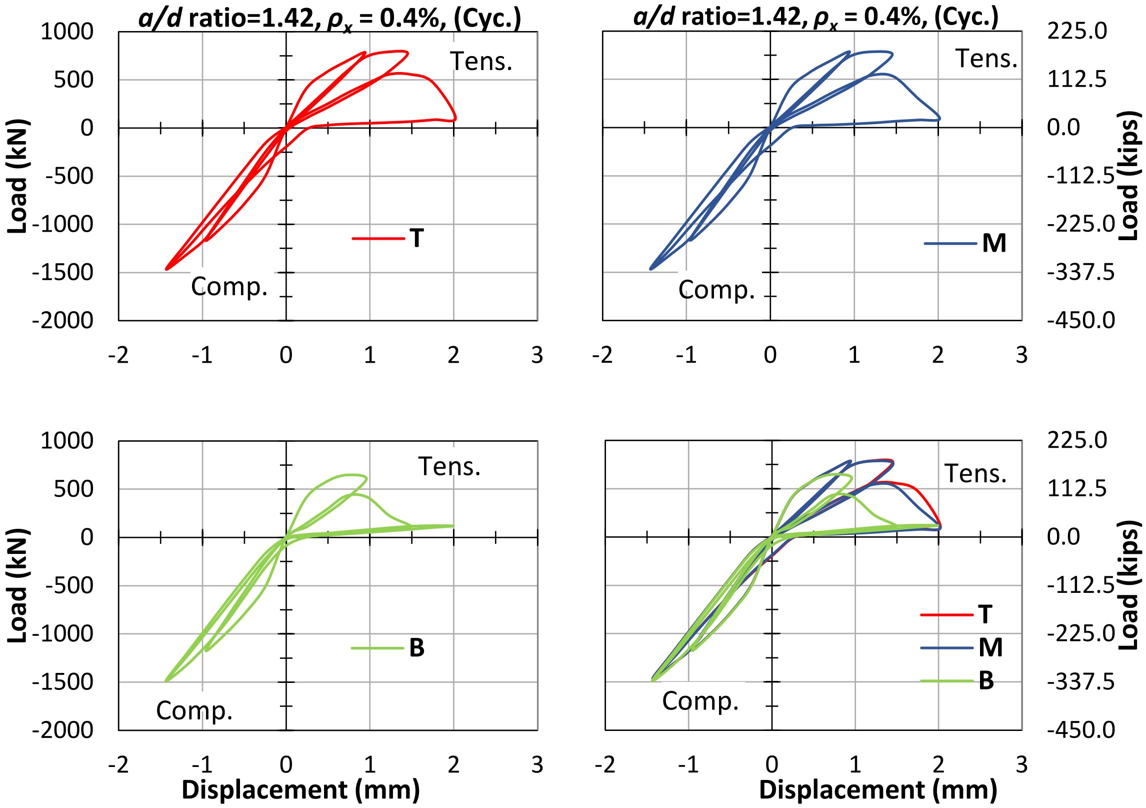

Figure A-46: Load-displacement response-single bracket type-reversed-cyclic - *a/d* ratio = 1.42, ρ_x = 0.4%.

Table A-23: Comparison of numerical simulation-single bracket type-reversed-cyclic - *a/d* ratio = 1.42, ρ_x = 0.4%.

h_e	*a/d* ratio	Tensile Component						Compression Component						Failure Mode	Bracket Infl.
		P_t (KN)	$P_{t\text{-}T/B}$	$P_{t\text{-}M/B}$	δ_t (mm)	$\delta_{t\text{-}T/B}$	$\delta_{t\text{-}M/B}$	P_t (KN)	$P_{c\text{-}T/B}$	$P_{c\text{-}M/B}$	δ_c (mm)	$\delta_{c\text{-}T/B}$	$\delta_{c\text{-}M/B}$		
T		789	1.22		2.02	1.01		1466	0.99		1.42	0.99		Flexural	None
M	1.42	785		1.22	2.02		1.01	1460		0.98	1.42		0.99	Flexural	None
B		646			2.00			1485			1.44			Splt-brkt	High

Tensile component's result

- The load capacities increase by 22% when the h_e is changed from bottom to middle.
- The displacement capacities for all h_e are the same.

Compression component's result

- The load capacities for all h_e are similar.
- The displacement capacities for all h_e are the same.

Bracket influence

- Bottom h_e gives splitting of concrete around anchorage bracket zone.

***a/d* ratio = 1.42, ρ_x = 0.8%**

h_e	Numerical Model	Crack Pattern
Top (T)	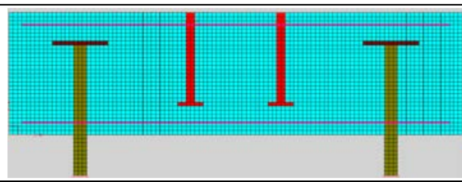	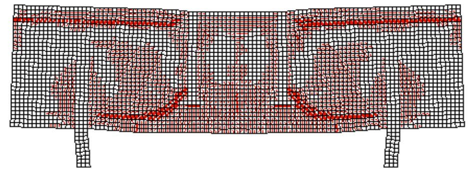
Middle (M)	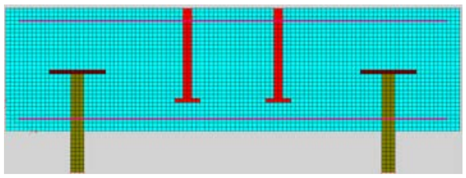	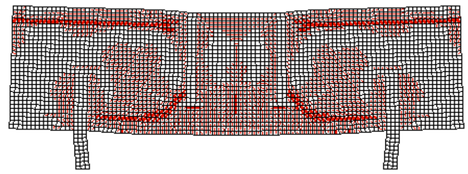
Bottom (B)	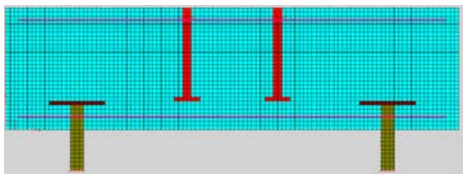	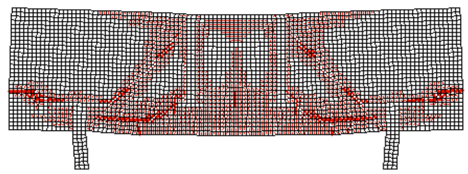

Figure A-47: Numerical model and crack pattern-single bracket type-reversed-cyclic - *a/d* ratio = 1.42, ρ_x = 0.8%.

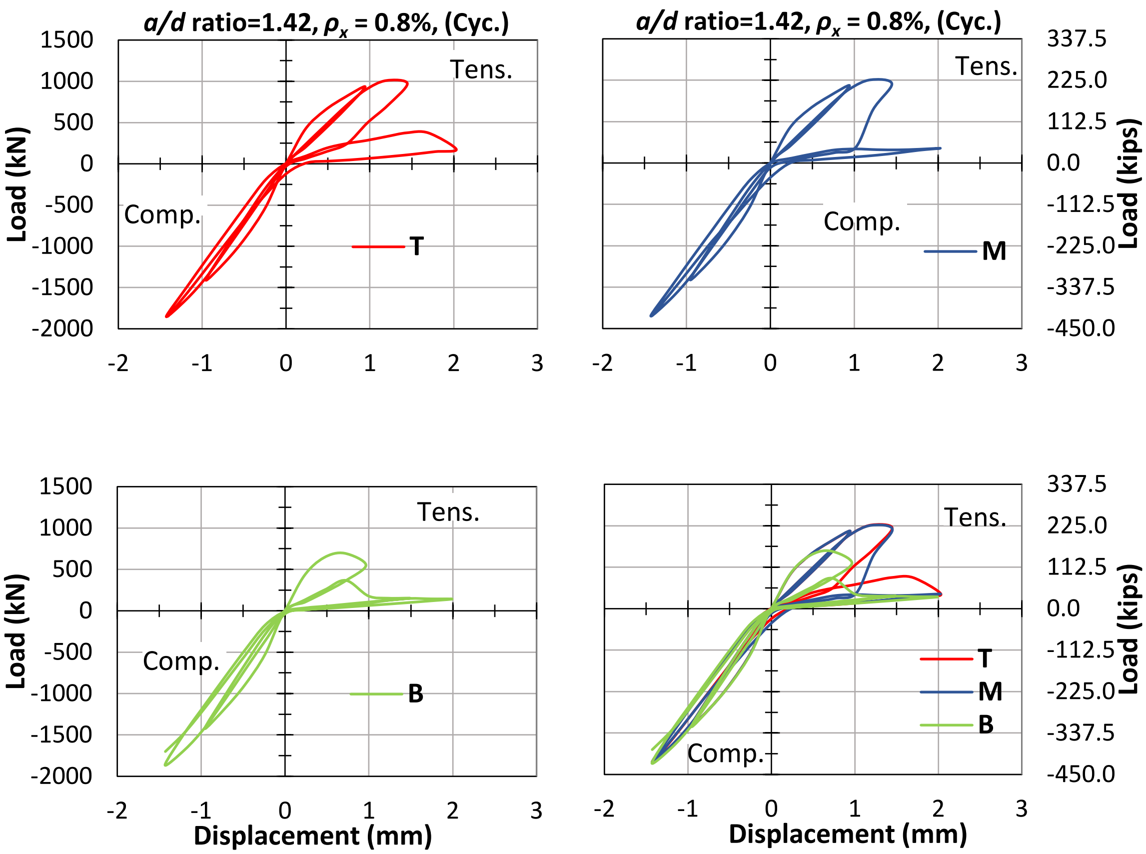

Figure A-48: Load-displacement response-single bracket type-reversed-cyclic - *a/d* ratio = 1.42, ρ_x = 0.8%.

Table A-24: Comparison of numerical simulation-single bracket type-reversed-cyclic - *a/d* ratio = 1.42, ρ_x = 0.8%.

h_e	*a/d* ratio	Tensile Component						Compression Component						Failure Mode	Bracket Infl.
		P_t (KN)	$P_{t\text{-}T/B}$	$P_{t\text{-}M/B}$	δ_t (mm)	$\delta_{t\text{-}T/B}$	$\delta_{t\text{-}M/B}$	P_t (KN)	$P_{c\text{-}T/B}$	$P_{c\text{-}M/B}$	δ_c (mm)	$\delta_{c\text{-}T/B}$	$\delta_{c\text{-}M/B}$		
T		1009	1.45		2.03	1.02		1852	0.99		1.43	1.00		Flexural	None
M	1.42	1005		1.44	2.03		1.02	1848		0.99	1.43		1.00	Flexural	Low
B		696			2.00			1862			1.43			Splt-brkt	High

Tensile component's result

- The load capacities increase by 44% when the h_e is changed from bottom to middle.
- The displacement capacities for all h_e are the same.

Compression component's result

- The load capacities for all h_e are similar.
- The displacement capacities for all h_e are the same.

Bracket influence

- Bottom h_e gives splitting of concrete around anchorage bracket zone.

a/d **ratio = 1.11,** ρ_x **= 0.2%**

h_e	Numerical Model	Crack Pattern
Top (T)	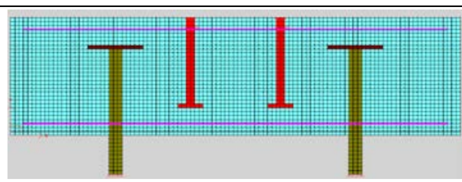	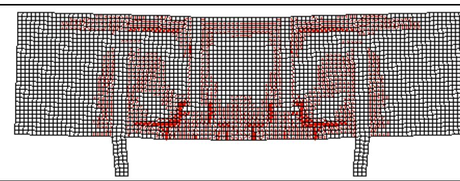
Middle (M)	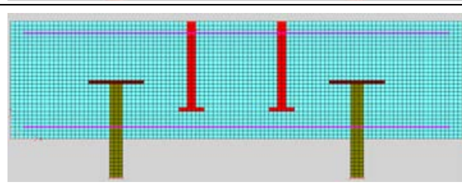	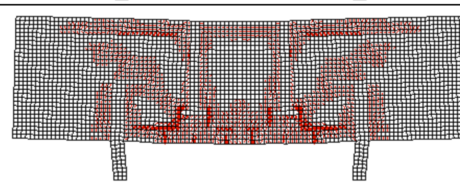
Bottom (B)	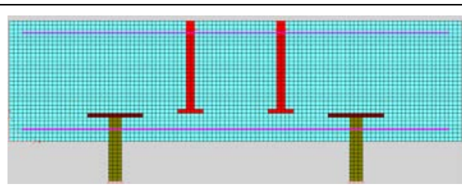	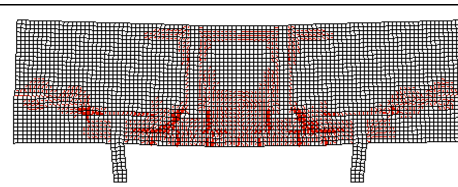

Figure A-49: Numerical model and crack pattern-single bracket type-reversed-cyclic - *a/d* ratio = 1.11, ρ_x = 0.2%.

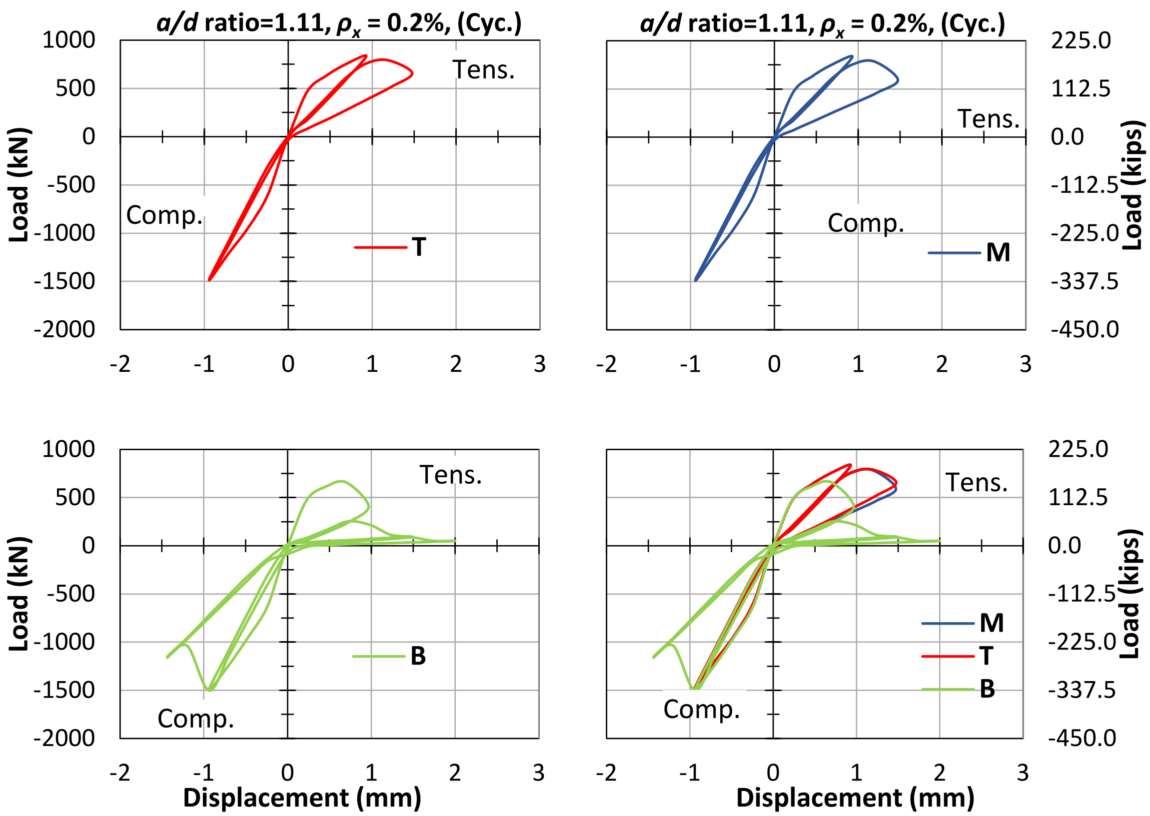

Figure A-50: Load-displacement response-single bracket type-reversed-cyclic - *a/d* ratio = 1.11, ρ_x = 0.2%.

Table A-25: Comparison of numerical simulation-single bracket type-reversed-cyclic - *a/d* ratio = 1.11, ρ_x = 0.2%.

h_e	*a/d* ratio	Tensile Component						Compression Component						Failure Mode	Bracket Infl.
		P_t (KN)	$P_{t\text{-}T/B}$	$P_{t\text{-}M/B}$	δ_t (mm)	$\delta_{t\text{-}T/B}$	$\delta_{t\text{-}M/B}$	P_t (KN)	$P_{c\text{-}T/B}$	$P_{c\text{-}M/B}$	δ_c (mm)	$\delta_{c\text{-}T/B}$	$\delta_{c\text{-}M/B}$		
T		836	1.27		1.47	0.74		1486	0.99		0.94	0.65		Flexural	Low
M	1.11	836		1.27	1.47		0.74	1488		0.99	0.94		0.65	Flexural	Low
B		659			2.00			1501			1.44			Splt-brkt	High

Tensile component's result

- The load capacities increase by 27% when the h_e is changed from bottom to middle.

Compression component's result

- The load capacities for all h_e are similar.

Bracket influence

- Bottom h_e gives splitting of concrete around anchorage bracket zone.

***a/d* ratio = 1.11, ρ_x = 0.4%**

h_e	Numerical Model	Crack Pattern
Top (T)	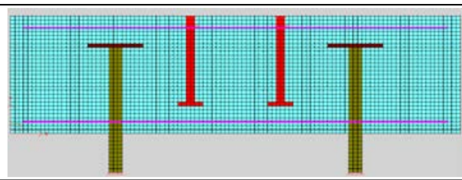	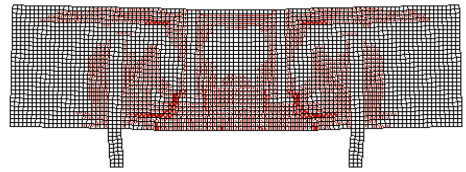
Middle (M)	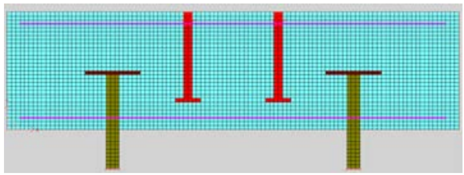	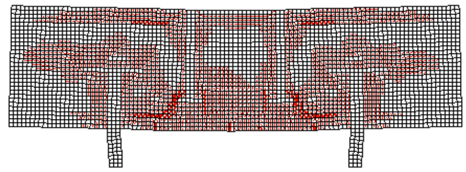
Bottom (B)	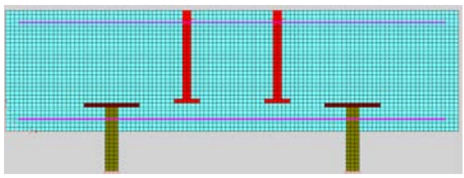	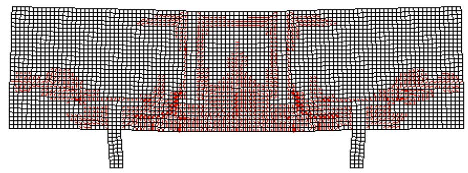

Figure A-51: Numerical model and crack pattern-single bracket type-reversed-cyclic -*a/d* ratio = 1.11, ρ_x = 0.4%.

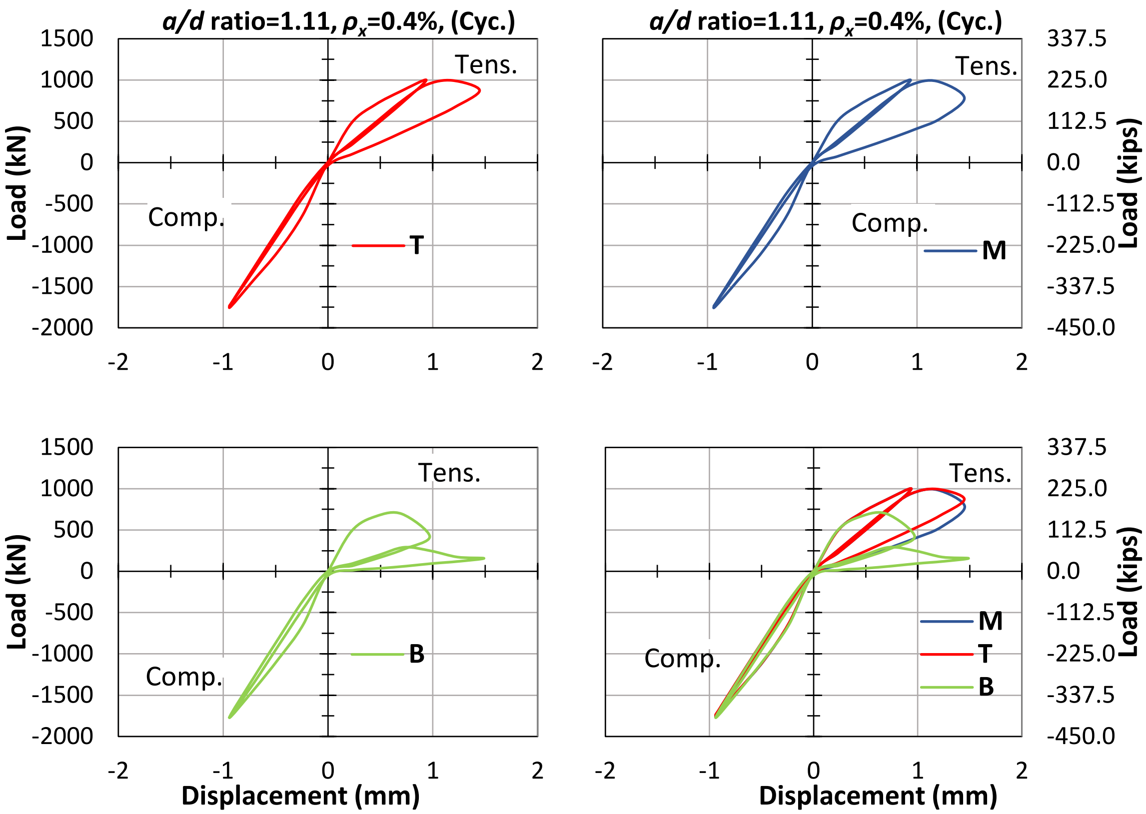

Figure A-52: Load- displacement response-single bracket type-reversed-cyclic -*a/d* ratio = 1.11, ρ_x = 0.4%.

Table A-26: Comparison of numerical simulation-single bracket type-reversed-cyclic -*a/d* ratio = 1.11, ρ_x = 0.4%.

h_e	*a/d* ratio	Tensile Component						Compression Component						Failure Mode	Bracket Infl.
		P_t (KN)	$P_{t\text{-}T/B}$	$P_{t\text{-}M/B}$	δ_t (mm)	$\delta_{t\text{-}T/B}$	$\delta_{t\text{-}M/B}$	P_t (KN)	$P_{c\text{-}T/B}$	$P_{c\text{-}M/B}$	δ_c (mm)	$\delta_{c\text{-}T/B}$	$\delta_{c\text{-}M/B}$		
T		1000	1.44		1.45	0.97		1756	0.99		0.94	1.00		Flexural	Low
M	1.11	1000		1.44	1.45		0.97	1757		0.99	0.94		1.00	Flexural	Low
B		695			1.49			1771			0.94			Splt-brkt	High

Tensile component's result

- The load capacities increase by 44% when the h_e is changed from bottom to middle.
- The displacement capacities for all h_e are the same.

Compression component's result

- The load capacities for all h_e are similar.
- The displacement capacities for all h_e are the same.

Bracket influence

- Bottom h_e gives splitting of concrete around anchorage bracket zone.

***a/d* ratio= 1.11, ρ_x = 0.8%**

h_e	Numerical Model	Crack Pattern
Top (T)	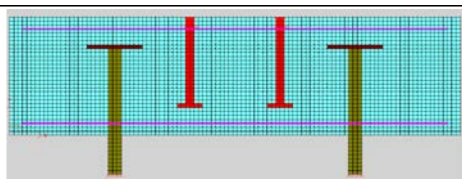	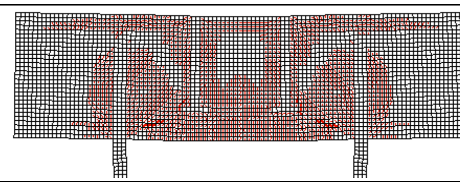
Middle (M)	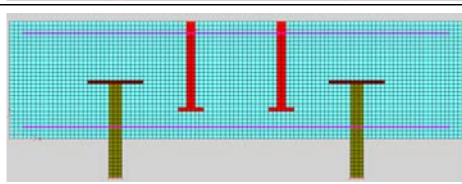	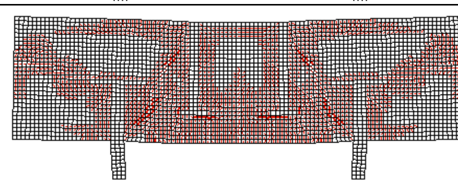
Bottom (B)	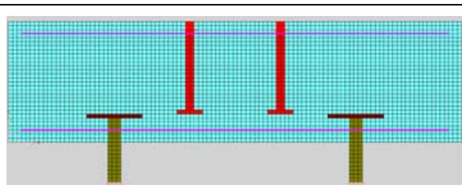	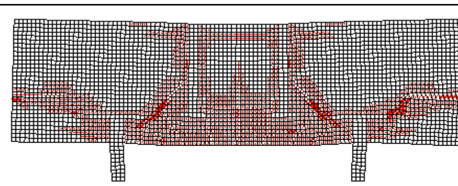

Figure A-53: Numerical model and crack pattern-single bracket type-reversed-cyclic -*a/d* ratio = 1.11, ρ_x = 0.8%.

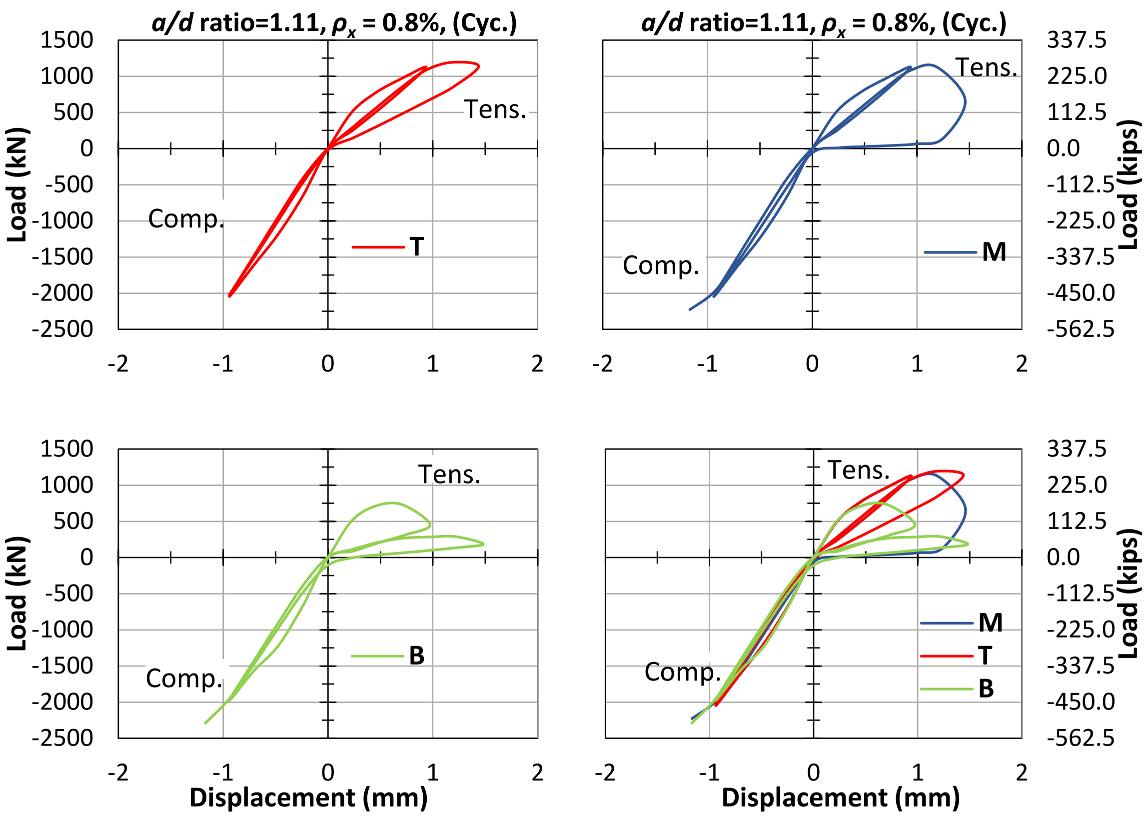

Figure A-54: Load-displacement response-single bracket type-reversed-cyclic -*a/d* ratio = 1.11, ρ_x = 0.8%.

Table A-27: Comparison of numerical simulation-single bracket type-reversed-cyclic -*a/d* ratio = 1.11, ρ_x = 0.8%.

h_e	*a/d* ratio	Tensile Component						Compression Component						Failure Mode	Bracket Infl.
		P_t (KN)	$P_{t\text{-}T/B}$	$P_{t\text{-}M/B}$	δ_t (mm)	$\delta_{t\text{-}T/B}$	$\delta_{t\text{-}M/B}$	P_t (KN)	$P_{c\text{-}T/B}$	$P_{c\text{-}M/B}$	δ_c (mm)	$\delta_{c\text{-}T/B}$	$\delta_{c\text{-}M/B}$		
T		1140	1.56		1.44	0.97		2045	0.89		0.94	0.80		Shear	Low
M	1.11	1128		1.55	1.46		0.99	2228		0.97	1.17		1.00	Shear	Low
B		730			1.48			2291			1.17			Splt-brkt	High

Tensile component's result

- The load capacities increase by 55% when the h_e is changed from bottom to middle.
- The displacement capacities for all h_e are the same.

Compression component's result

- The load capacities decrease slightly by 8% when the h_e is changed from middle to top.

Bracket influence

- Bottom h_e gives splitting of concrete around anchorage bracket zone.

Appendix B Nonlinear Finite Element Analysis of Double Bracket Anchorages

In this appendix, the following simulation results are presented: the nonlinear load vs. deflection responses, the peak loads, the failure displacements, the initial stiffnesses, the failure mechanisms and the influence of the bracket zone.

Subjected to Monotonic Tension

***a/d* ratio = 1.68**

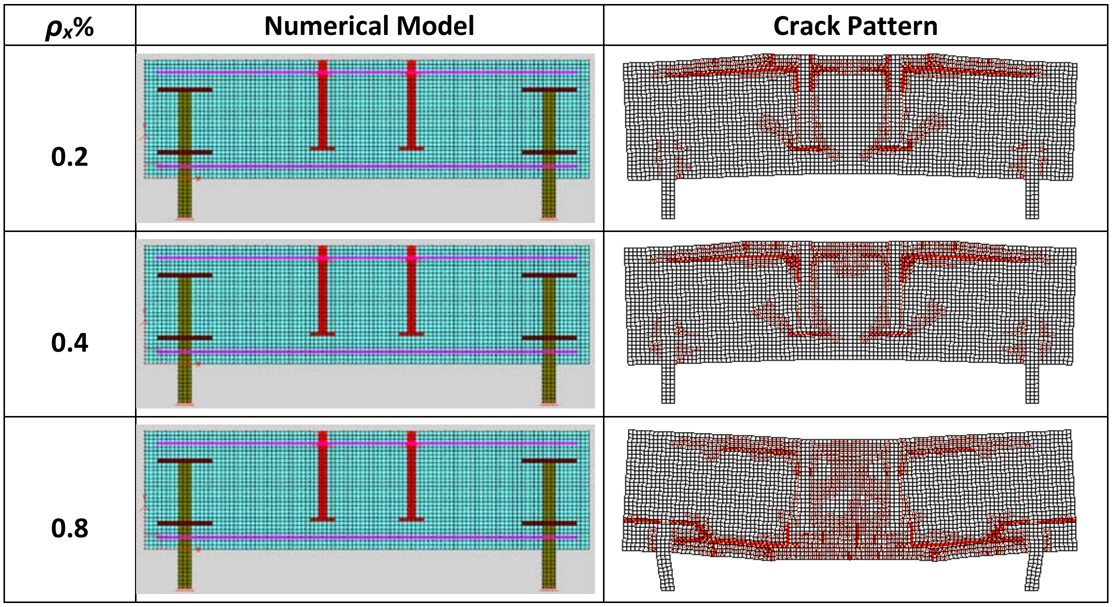

Figure B-1: Numerical model and crack pattern-double bracket type-monotonic tension - *a/d* ratio = 1.68.

Table B-1: Comparison of numerical simulation-double bracket type-monotonic tension - *a/d* ratio = 1.68.

ρ_x%	*a/d* ratio	P_u (KN)	δ_u (mm)	Stiff (KN/mm)	Failure Mode	Bracket Infl.
0.2	1.68	497	1.19	1369	Flexural	None
0.4		671	1.39	1437	Flexural	None
0.8		878	1.39	1523	Flexural	None

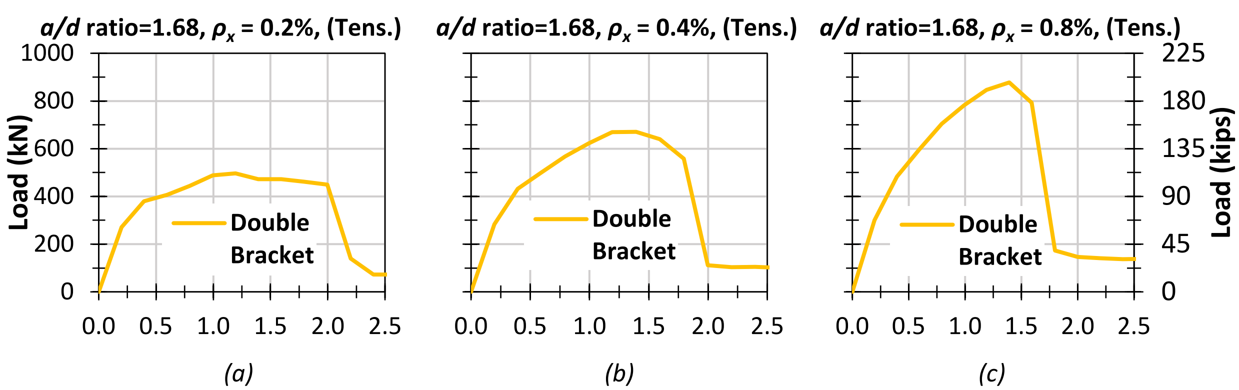

Figure B-2: Load-displacement response-double bracket type-monotonic tension - *a/d* ratio = 1.68: (a) ρ_x = 0.2%, (b) ρ_x = 0.4% & (c) ρ_x = 0.8%.

- The load capacities increase by 35% and 31% when the ρ_x is increased from 0.2 to 0.4% and 0.4 to 0.8% respectively.

***a/d* ratio = 1.42**

ρ_x%	Numerical Model	Crack Pattern
0.2	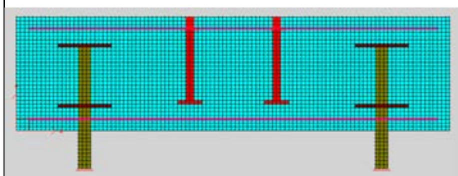	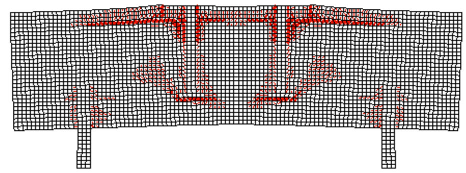
0.4	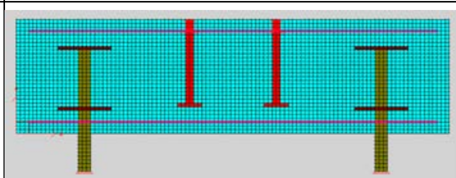	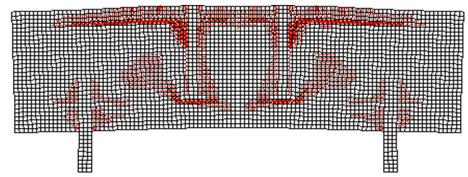
0.8	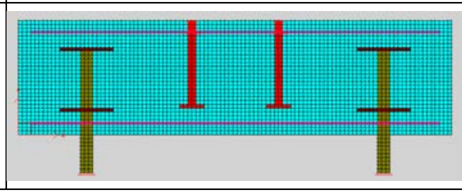	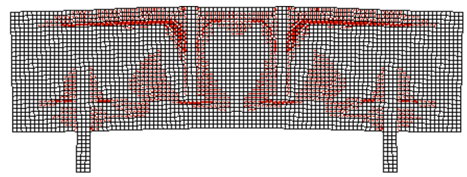

Figure B-3: Numerical model and crack pattern-double bracket type-monotonic tension - *a/d* ratio = 1.42.

Table B-2: Comparison of numerical simulation-double bracket type-monotonic tension - *a/d* ratio = 1.42.

ρ_x%	*a/d* ratio	P_u (KN)	δ_u (mm)	Stiff (KN/mm)	Failure Mode	Bracket Infl.
0.2	1.42	623	1.15	1788	Flexural	None
0.4		814	1.15	1864	Flexural	None
0.8		1026	1.35	1941	Flexural	None

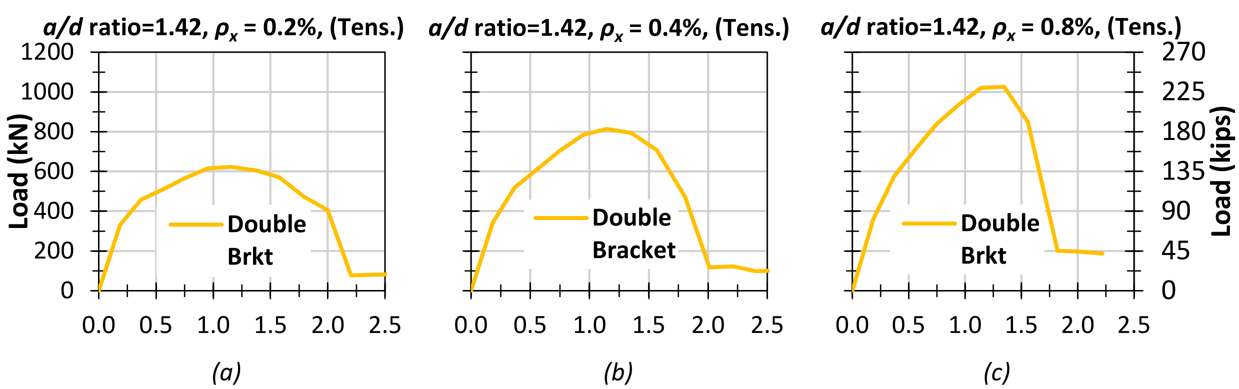

Figure B-4: Load-displacement response-double bracket type-monotonic tension - *a/d* ratio = 1.42: (a) ρ_x = 0.2%, (b) ρ_x = 0.4% & (c) ρ_x = 0.8%.

- The load capacities increase by 31% and 26% when the ρ_x is increased from 0.2 to 0.4% and 0.4 to 0.8% respectively.

_a/d_ ratio = 1.11

ρ_x%	Numerical Model	Crack Pattern
0.2	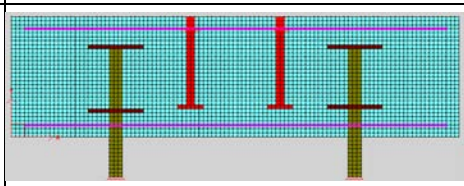	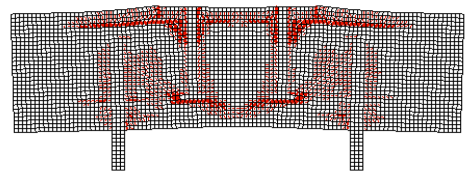
0.4	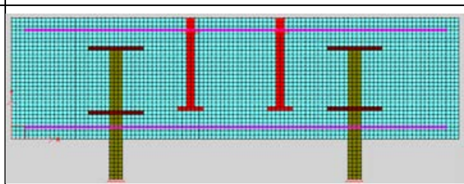	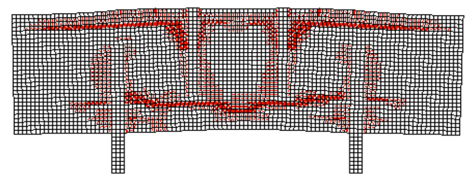
0.8	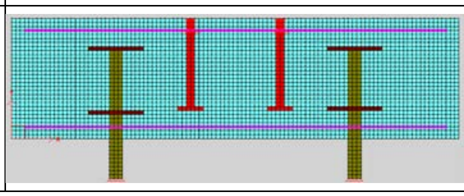	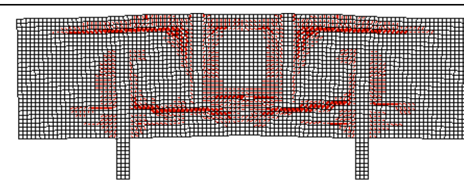

Figure B-5: Numerical model and crack pattern-double bracket type-monotonic tension - *a/d* = 1.11.

Table B-3: Comparison of numerical simulation-double bracket type-monotonic tension - *a/d* ratio = 1.11.

ρ_x%	*a/d* ratio	P_u (KN)	δ_u (mm)	Stiff (KN/mm)	Failure Mode	Bracket Infl.
0.2	1.11	830	0.93	2238	Flexural	None
0.4		1004	0.93	2286	Flexural	None
0.8		1125	1.34	2357	Flexural	None

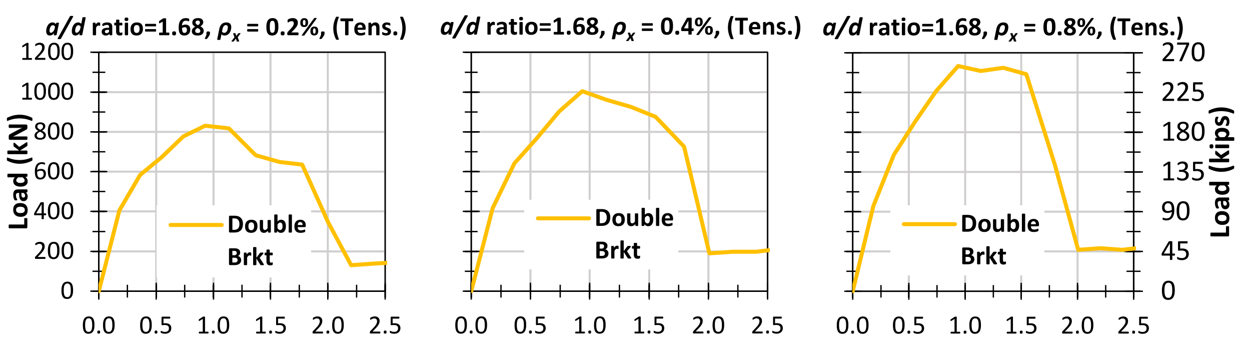

(a) *(b)* *(c)*

Figure B-6: Load-displacement response-double bracket-monotonic tension - *a/d* ratio = 1.42: (a) ρ_x = 0.2%, (b) ρ_x = 0.4% & (c) ρ_x = 0.8%.

- The load capacities increase by 21% and 12% when the ρ_x is increased from 0.2 to 0.4% and 0.4 to 0.8% respectively.

Subjected to Monotonic Compression

***a/d* ratio = 1.68**

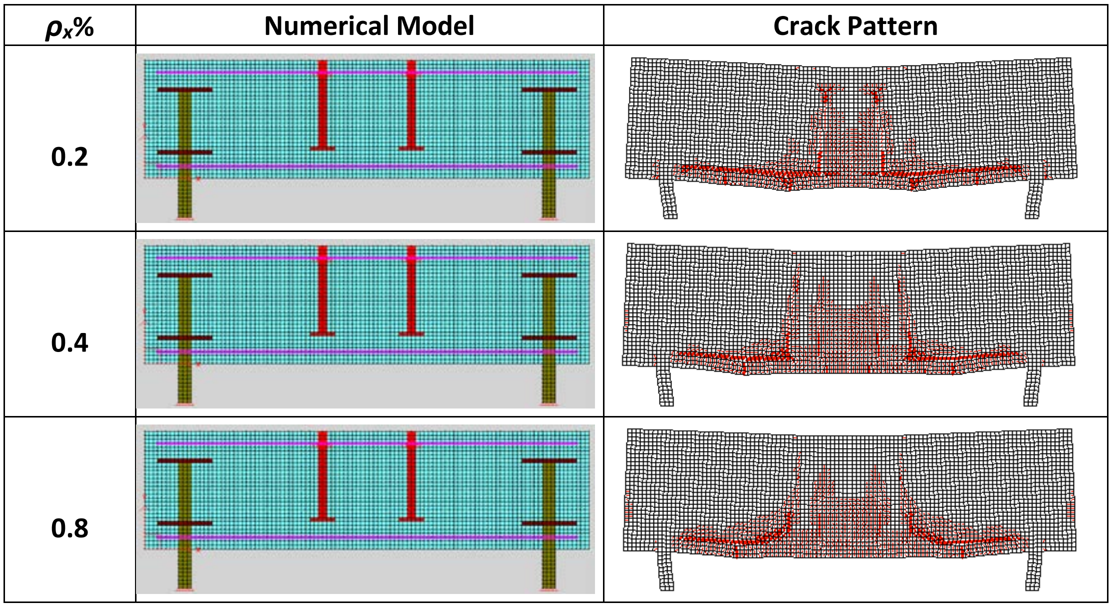

Figure B-7: Numerical model and crack pattern-double bracket type-monotonic compression - *a/d* ratio = 1.68.

Table B-4: Comparison of numerical simulation- double bracket type-monotonic compression - *a/d* ratio = 1.68.

ρ_x%	*a/d* ratio	P_u (KN)	δ_u (mm)	Stiff (KN/mm)	Failure Mode	Bracket Infl.
0.2	1.68	925	1.99	1610	Flexural	None
0.4		1135	1.79	1662	Flexural	None
0.8		1507	1.79	1742	Flexural	None

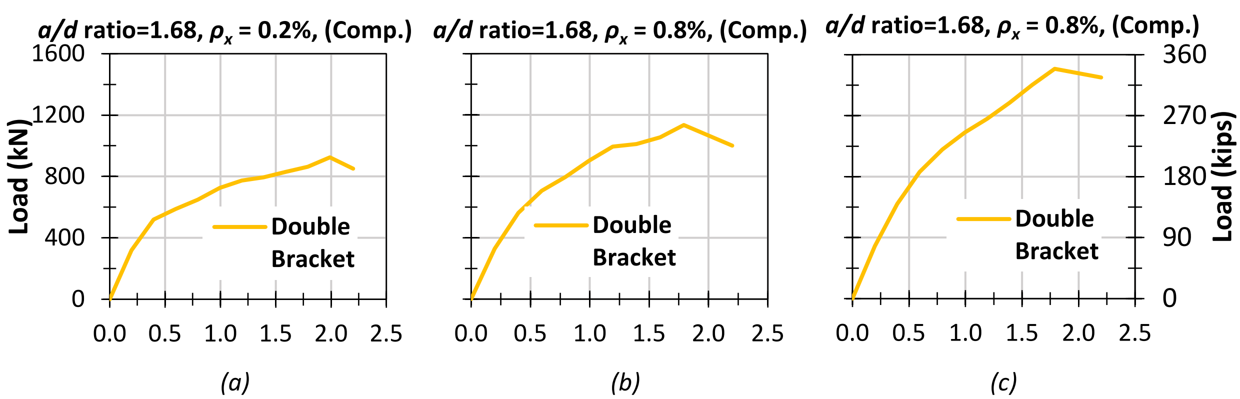

Figure B-8: Load-displacement response-double bracket type-monotonic compression - *a/d* ratio = 1.68: (a) ρ_x = 0.2%, (b) ρ_x = 0.4% & (c) ρ_x = 0.8%.

- The load capacities increase by 23% and 33% when the ρ_x is increased from 0.2 to 0.4% and 0.4 to 0.8% respectively.

***a/d* ratio = 1.42**

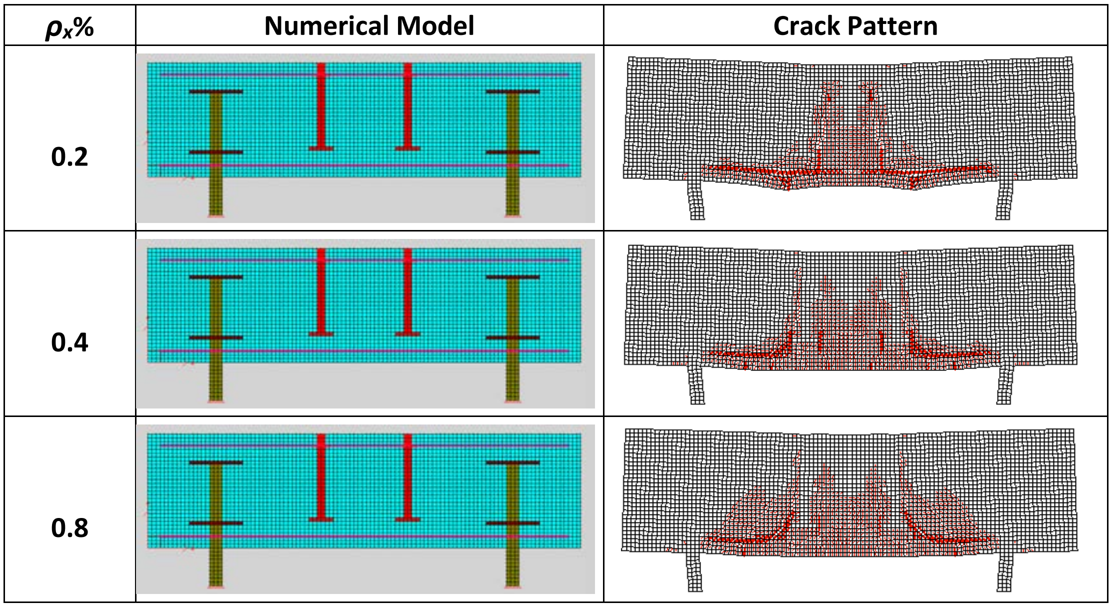

Figure B-9: Numerical model and crack pattern-double bracket type-monotonic compression - *a/d* ratio = 1.42.

Table B-5: Comparison of numerical simulation-double bracket type-monotonic compression - *a/d* ratio = 1.42.

ρ_x%	*a/d* ratio	P_u (KN)	δ_u (mm)	Stiff (KN/mm)	Failure Mode	Bracket Infl.
0.2	1.42	1082	1.34	2110	Flexural	None
0.4		1436	1.34	2162	Flexural	None
0.8		1808	1.34	2235	Flexural	None

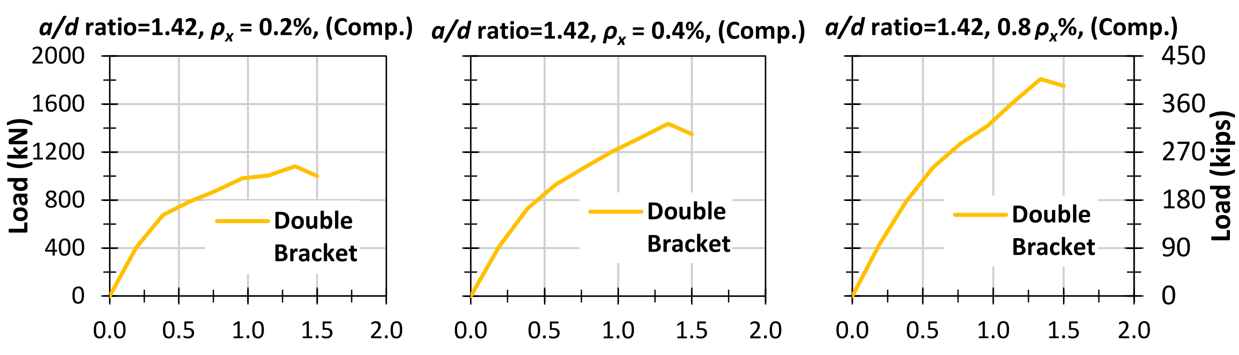

Figure B-10: Load-displacement response-double bracket type-monotonic compression - *a/d* ratio = 1.42: (a) ρ_x = 0.2%, (b) ρ_x = 0.4% & (c) ρ_x = 0.8%.

- The load capacities increase by 33% and 26% when the ρ_x is increased from 0.2 to 0.4% and 0.4 to 0.8% respectively.

***a/d* ratio = 1.11**

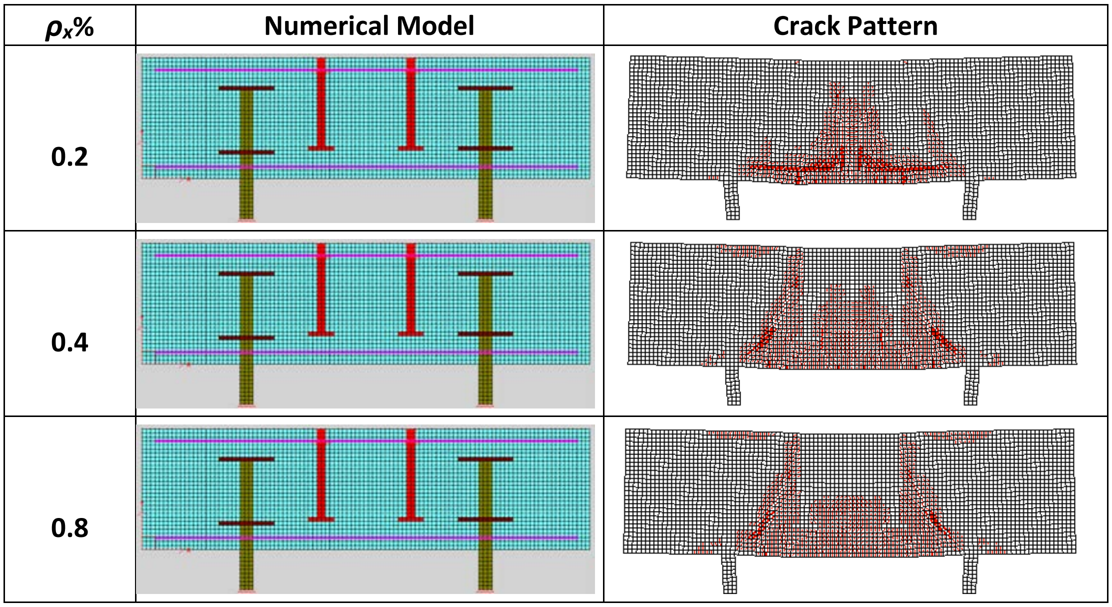

Figure B-11: Numerical model and crack pattern-double bracket type-monotonic compression - *a/d* ratio = 1.11.

Table B-6: Comparison of numerical simulation-double bracket type-monotonic compression - *a/d* ratio = 1.11.

ρ_x%	***a/d* ratio**	**P_u (KN)**	**δ_u (mm)**	**Stiff (KN/mm)**	**Failure Mode**	**Bracket Infl.**
0.2	1.11	1545	0.94	2715	Flexural	None
0.4		1857	1.12	2747	Shear	None
0.8		2167	1.12	2795	Shear	None

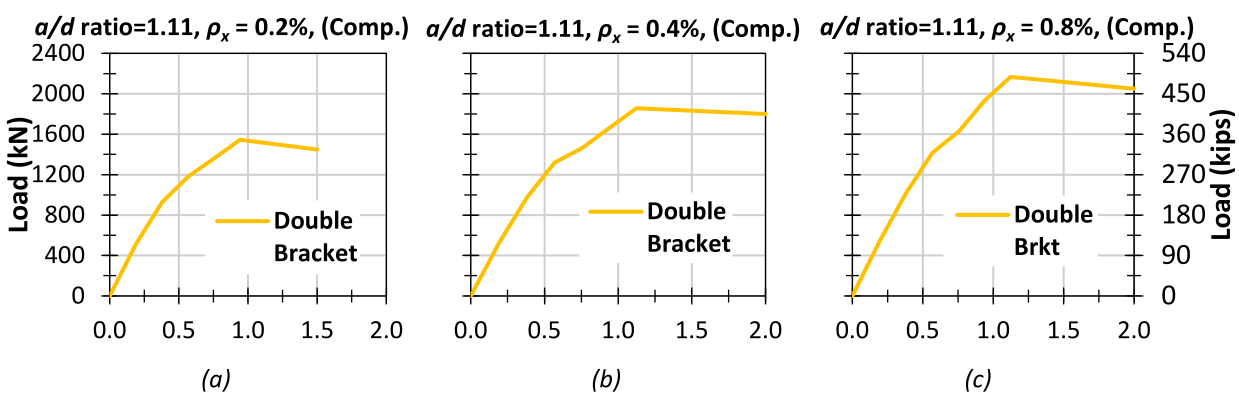

Figure B-12: Load-displacement response-double bracket type-monotonic compression - *a/d* ratio = 1.11: (a) ρ_x = 0.2%, (b) ρ_x = 0.4% & (c) ρ_x = 0.8%.

- The load capacities increase by 20% and 17% when the ρ_x is increased from 0.2 to 0.4% and 0.4 to 0.8% respectively.

Subjected to Reversed-Cyclic Loads

***a/d* ratio = 1.68**

ρ_x%	**Numerical Model**	**Crack Pattern**
0.2	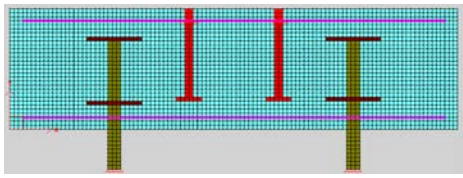	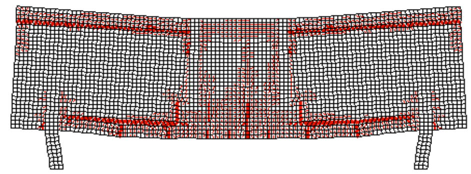
0.4	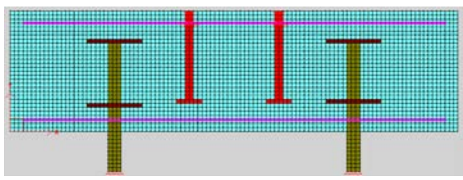	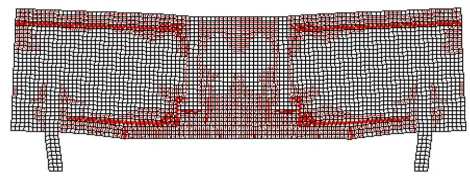
0.8	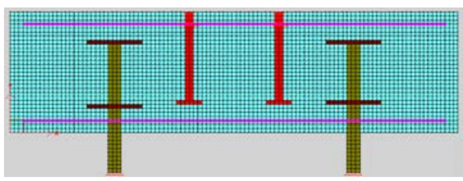	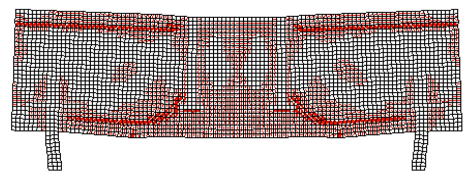

Figure B-13: Numerical model and crack pattern-double bracket type-reversed-cyclic - *a/d* ratio = 1.68.

Table B-7: Comparison of numerical simulation-double bracket type-reversed-cyclic - *a/d* ratio = 1.68.

ρ_x%	***a/d* ratio**	**Tensile Component**		**Compression Component**		**Failure Mode**	**Bracket Infl.**
		P_t (KN)	**δ_t (mm)**	**P_t (KN)**	**δ_c (mm)**		
0.2	1.68	491	2.50	868	2.24	Flexural	None
0.4		660	2.00	1113	1.74	Flexural	None
0.8		849	2.00	1443	1.74	Flexural	None

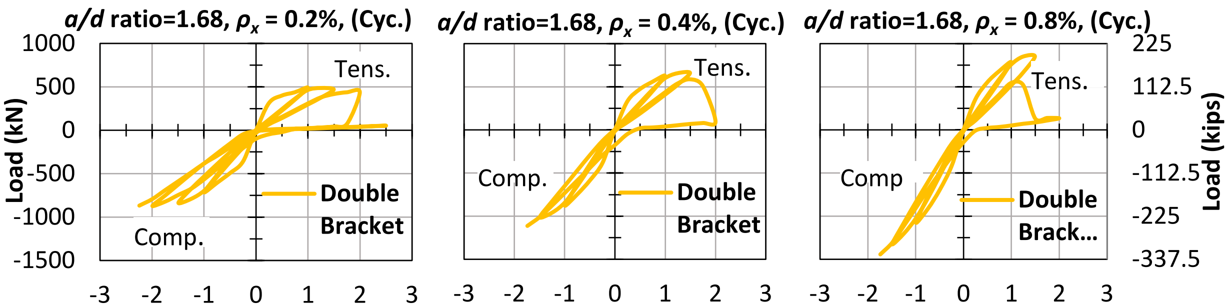

(a) *(b)* *(c)*

Figure B-14: Load-displacement response-double bracket type-monotonic compression - *a/d* ratio = 1.68: (a) ρ_x = 0.2%, (b) ρ_x = 0.4% & (c) ρ_x = 0.8%.

- The load capacities increase by 34% and 29% when the ρ_x is increased from 0.2 to 0.4% and 0.4 to 0.8% respectively subjected to cyclic tension.
- The load capacities increase by 28% and 30% when the ρ_x is increased from 0.2 to 0.4% and 0.4 to 0.8% respectively subjected to cyclic compression.

a/d ratio = 1.42

ρ_x%	Numerical Model	Crack Pattern
0.2	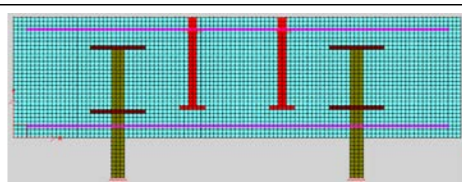	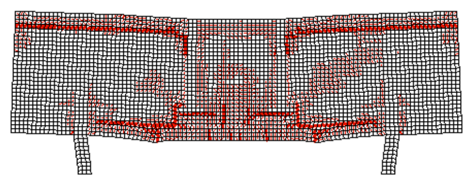
0.4	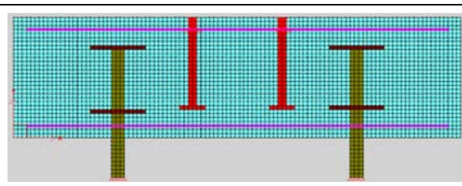	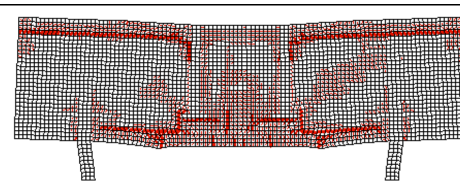
0.8	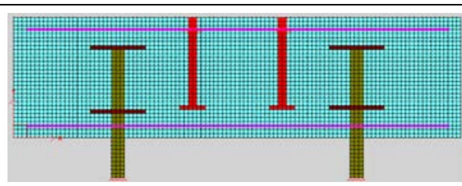	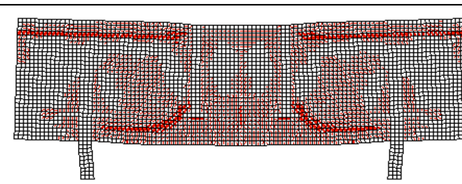

Figure B-15: Numerical model and crack pattern-double bracket type-reversed-cyclic - *a/d* ratio = 1.42.

Table B-8: Comparison of numerical simulation- double bracket type-reversed-cyclic - *a/d* ratio = 1.42.

ρ_x%	*a/d* ratio	Tensile Component		Compression Component		Failure Mode	Bracket Infl.
		P_t (KN)	δ_t (mm)	P_t (KN)	δ_c (mm)		
0.2	1.42	626	2.01	1146	1.44	Flexural	None
0.4		794	2.02	1472	1.42	Flexural	None
0.8		1018	2.03	1865	1.43	Flexural	None

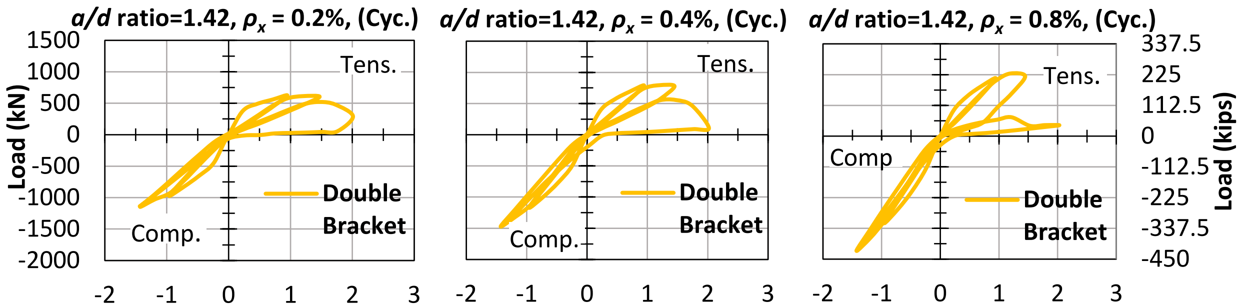

(a) (b) (c)

Figure B-16: Load-displacement response-double bracket type-monotonic compression - *a/d* ratio = 1.42: (a) ρ_x = 0.2%, (b) ρ_x = 0.4% & (c) ρ_x = 0.8%.

- The load capacities increase by 27% and 28% when the ρ_x is increased from 0.2 to 0.4% and 0.4 to 0.8% respectively subjected to cyclic tension.
- The load capacities increase by 28% and 27% when the ρ_x is increased from 0.2 to 0.4% and 0.4 to 0.8% respectively subjected to cyclic compression.

***a/d* ratio = 1.11**

ρ_x%	Numerical Model	Crack Pattern
0.2	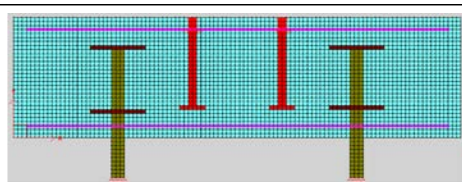	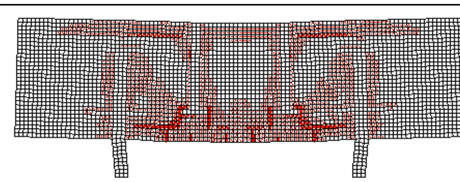
0.4	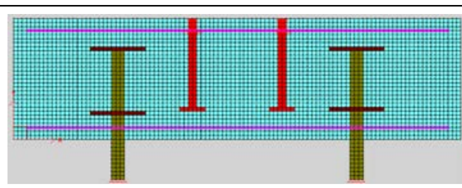	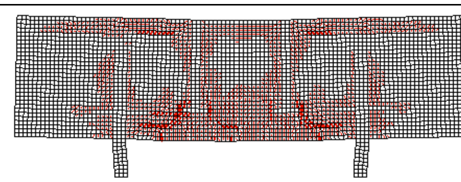
0.8	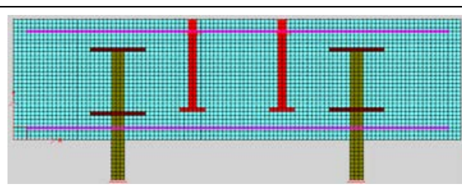	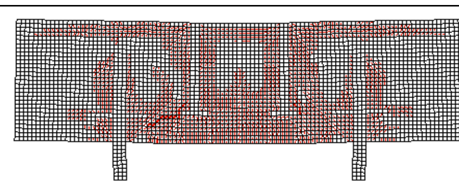

Figure B-17: Numerical model and crack pattern-double bracket type-reversed-cyclic - *a/d* ratio = 1.11.

Table B-9: Comparison of numerical simulation- double bracket type-reversed-cyclic - *a/d* ratio = 1.11.

ρ_x%	***a/d* ratio**	**Tensile Component**		**Compression Component**		**Failure Mode**	**Bracket Infl.**
		P_t (KN)	**δ_t (mm)**	**P_t (KN)**	**δ_c (mm)**		
0.2	1.11	843	1.48	1490	0.94	Flexural	None
0.4		1011	1.45	1763	0.94	Flexural	None
0.8		1138	1.44	2043	0.94	Shear	None

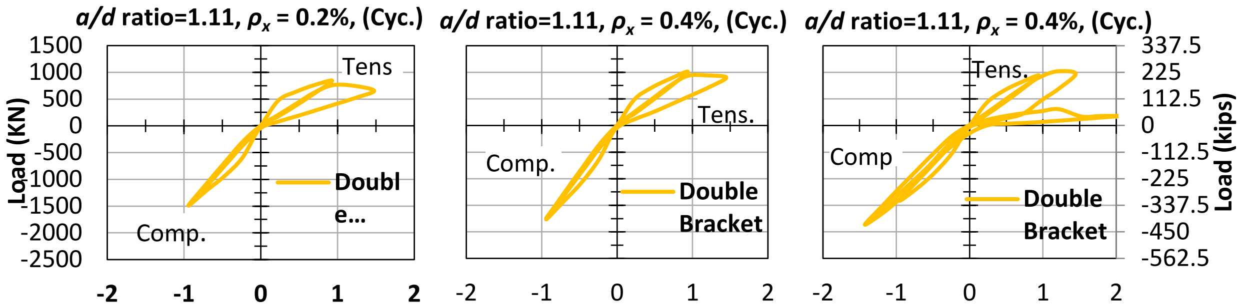

(a) *(b)* *(c)*

Figure B-18: Load-displacement response-double bracket type-monotonic compression - *a/d* ratio = 1.11: (a) ρ_x = 0.2%, (b) ρ_x = 0.4% & (c) ρ_x = 0.8%.

- The load capacities increase by 20% and 13% when the ρ_x is increased from 0.2 to 0.4% and 0.4 to 0.8% respectively subjected to cyclic tension.
- The load capacities increase by 18% and 16% when the ρ_x is increased from 0.2 to 0.4% and 0.4 to 0.8% respectively subjected to cyclic compression.

Appendix C Nonlinear Finite Element Analysis of Studded Bracket Anchorages

In this appendix, the following simulation results are presented: the nonlinear load vs. deflection responses, the peak loads, the failure displacements, the initial stiffnesses, the failure mechanisms and the influence of the bracket zone.

Subjected to Monotonic Tension

***a/d* ratio = 1.68, ρ_x = 0.2%**

h_e	Numerical Model	Crack Pattern
Middle (M)	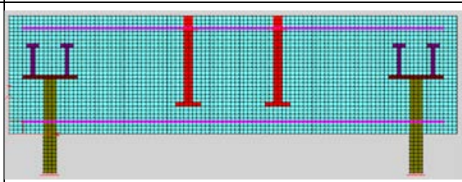	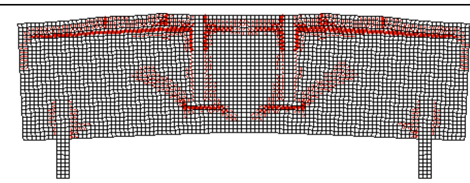
Bottom (B)	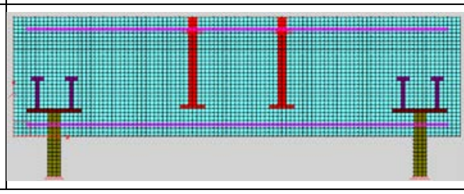	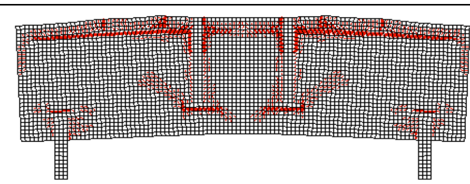

Figure C-1: Numerical model and crack pattern-studded bracket type-monotonic tension - *a/d* ratio = 1.68, ρ_x = 0.2%.

Table C-1: Comparison of numerical simulation-studded bracket type-monotonic tension - *a/d* ratio = 1.68, ρ_x = 0.2%.

h_e	*a/d* ratio	P_u (KN)	δ_u (mm)	Stiff (KN/mm)	Failure Mode	Bracket Infl.
M	1.68	496	1.19	1363	Flexural	None
B		491	1.19	1369	Flexural	None

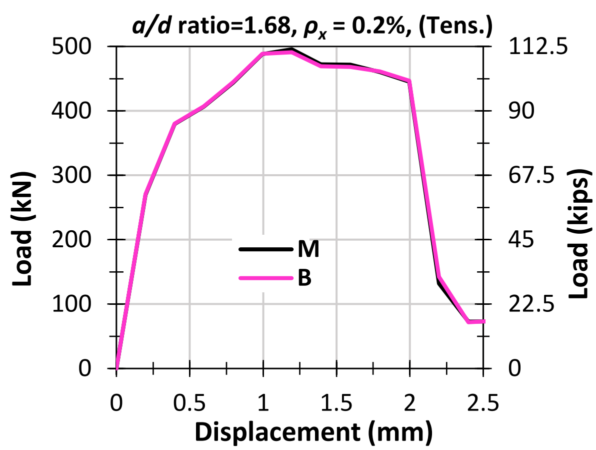

Figure C-2: Load-displacement response-studded bracket type-monotonic tension - *a/d* ratio = 1.68, ρ_x = 0.2%.

- The load and the displacement capacities remain the same for all the h_e.

***a/d* ratio = 1.68, ρ_x = 0.4%**

h_e	Numerical Model	Crack Pattern
Top (T)	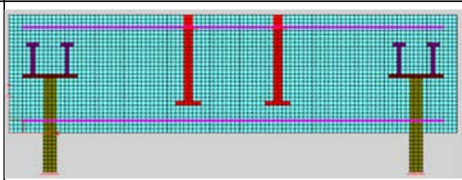	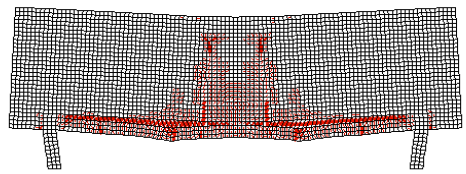
Bottom (B)	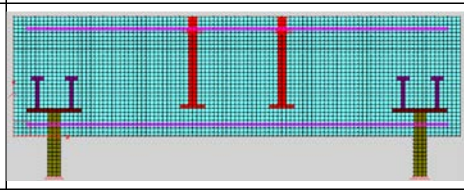	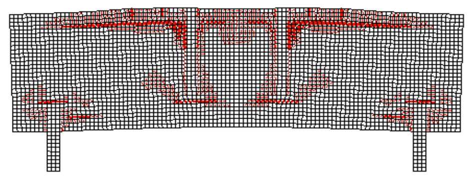

Figure C-3: Numerical model and crack pattern-studded bracket type-monotonic tension -*a/d* ratio = 1.68, ρ_x = 0.4%.

Table C-2: Comparison of numerical simulation-studded bracket type-monotonic tension -*a/d* ratio = 1.68, ρ_x = 0.4%.

h_e	*a/d* ratio	P_u (KN)	δ_u (mm)	Stiff (KN/mm)	Failure Mode	Bracket Infl.
T	1.68	670	1.39	1432	Flexural	None
B		669	1.39	1437	Flexural	None

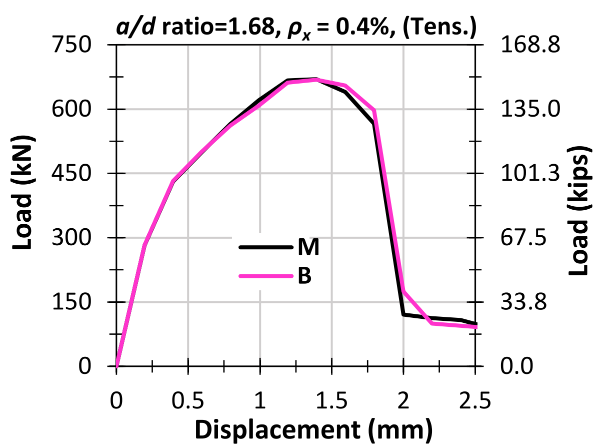

Figure C-4: Load-displacement response-studded bracket type-monotonic tension -*a/d* ratio = 1.68, ρ_x = 0.4%.

- The load and the displacement capacities remain the same for all the h_e.

***a/d* ratio = 1.68, ρ_x = 0.8%**

h_e	Numerical Model	Crack Pattern
Top (T)	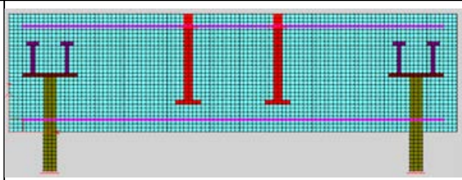	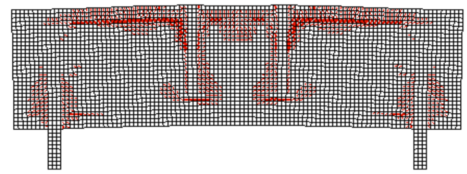
Bottom (B)	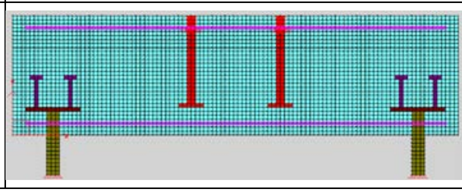	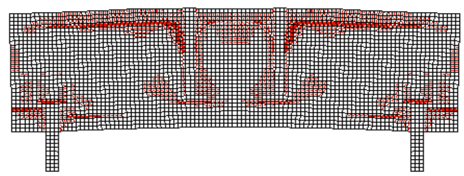

Figure C-5: Numerical model and crack pattern-studded bracket type-monotonic tension - *a/d* ratio = 1.68, ρ_x = 0.8%.

Table C-3: Comparison of numerical simulation-studded bracket type-monotonic tension - *a/d* ratio = 1.68, ρ_x = 0.8%.

h_e	*a/d* ratio	P_u (KN)	δ_u (mm)	Stiff (KN/mm)	Failure Mode	Bracket Infl.
T	1.68	876	1.39	1518	Flexural	None
B		864	1.39	1523	Flexural	None

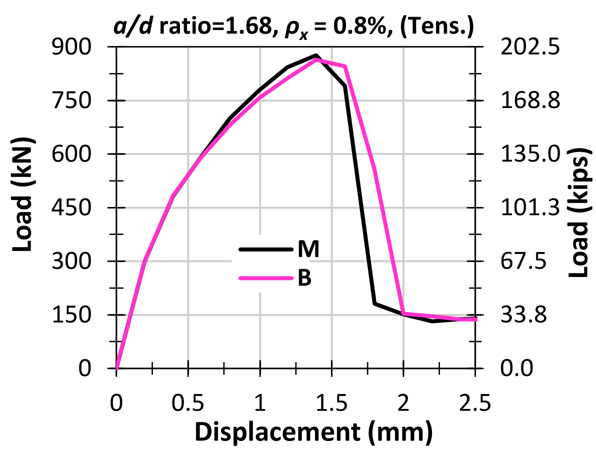

Figure C-6: Load-displacement response-studded bracket type-monotonic tension - *a/d* ratio = 1.68, ρ_x = 0.8%.

- The load and the displacement capacities remain the same for all the h_e.

***a/d* ratio = 1.42, ρ_x = 0.2%**

h_e	Numerical Model	Crack Pattern
Top (T)	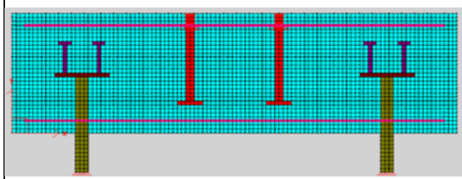	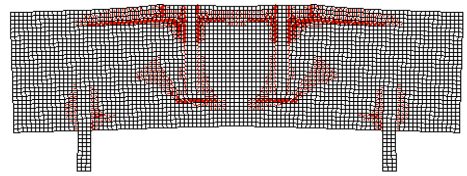
Bottom (B)	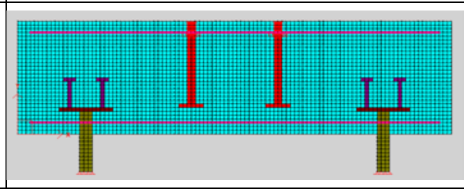	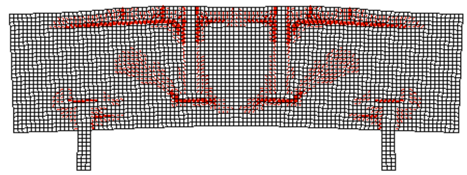

Figure C-7: Numerical model and crack pattern-studded bracket type-monotonic tension - *a/d* ratio = 1.42, ρ_x = 0.2%.

Table C-4: Comparison of numerical simulation- studded bracket type-monotonic tension - *a/d* ratio = 1.42, ρ_x = 0.2%.

h_e	*a/d* ratio	P_u (KN)	δ_u (mm)	Stiff (KN/mm)	Failure Mode	Bracket Infl.
T	1.42	623	1.15	1783	Flexural	None
B		622	1.15	1788	Flexural	None

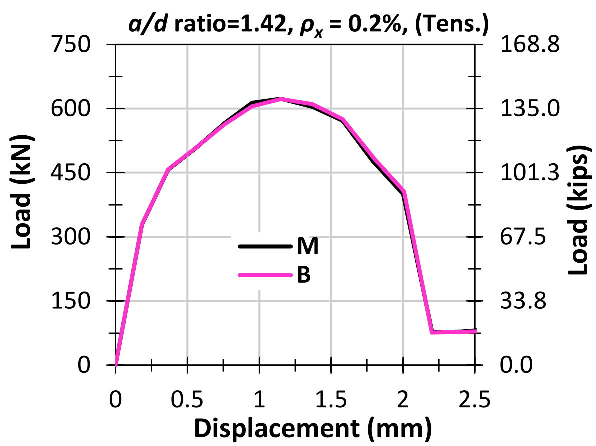

Figure C-8: Load-displacement response-studded bracket type-monotonic tension - *a/d* ratio = 1.42, ρ_x = 0.2%.

- The load and the displacement capacities remain the same for all the h_e.

***a/d* ratio = 1.42, ρ_x = 0.4%**

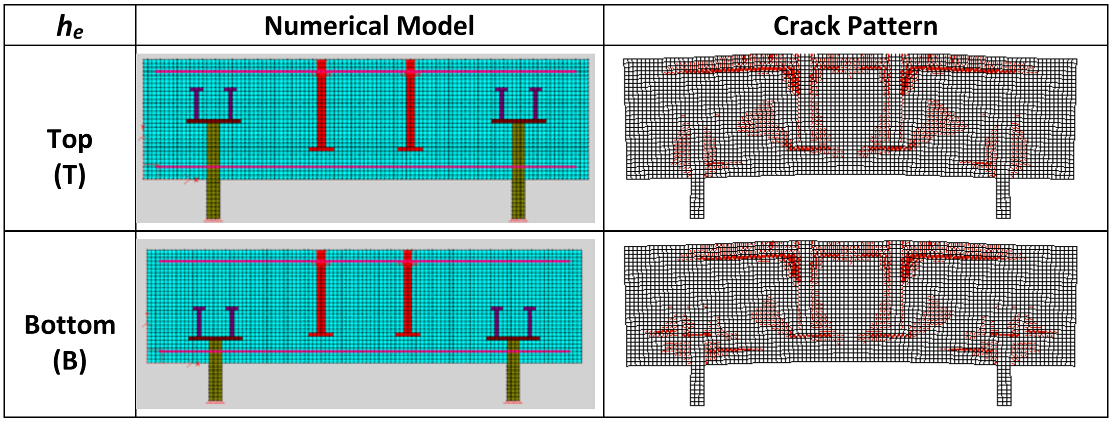

Figure C-9: Numerical model and crack pattern-studded bracket type-monotonic tension - *a/d* ratio = 1.42, ρ_x = 0.4%.

Table C-5: Comparison of numerical simulation-studded bracket type-monotonic tension - *a/d* ratio = 1.42, ρ_x = 0.4%.

h_e	*a/d* ratio	P_u (KN)	δ_u (mm)	Stiff (KN/mm)	Failure Mode	Bracket Infl.
T	1.42	809	1.15	1843	Flexural	None
B		807	1.15	1864	Flexural	None

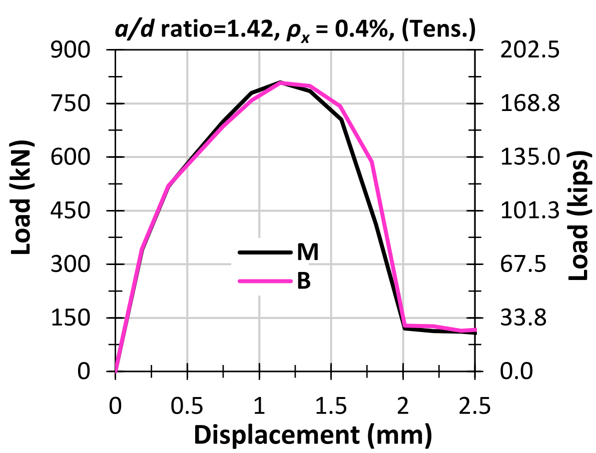

Figure C-10: Load-displacement response-studded bracket type-monotonic tension - *a/d* ratio = 1.42, ρ_x = 0.4%.

- The load and the displacement capacities remain the same for all the h_e.

***a/d* ratio = 1.42, ρ_x = 0.8%**

h_e	Numerical Model	Crack Pattern
Top (T)	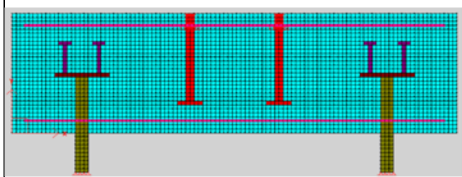	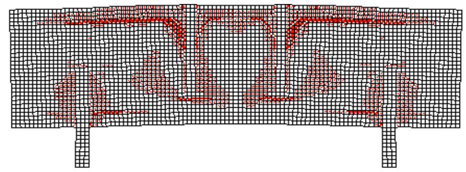
Bottom (B)	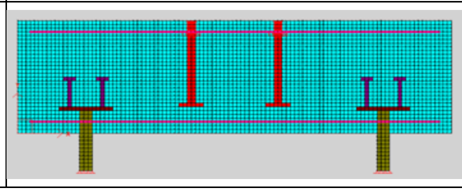	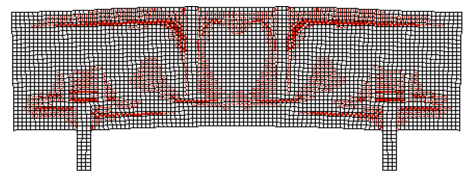

Figure C-11: Numerical model and crack pattern-studded bracket type-monotonic tension - *a/d* ratio = 1.42, ρ_x = 0.8%.

Table C-6: Comparison of numerical simulation-studded bracket type-monotonic tension - *a/d* ratio = 1.42, ρ_x = 0.8%.

h_e	(*a/d*) ratio	P_u (KN)	δ_u (mm)	Stiff (KN/mm)	Failure Mode	Bracket Infl.
T	1.42	1010	1.14	1935	Flexural	None
B		1004	1.35	1941	Flexural	None

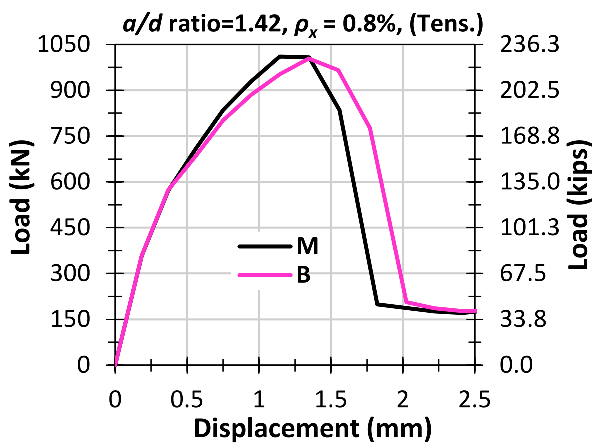

Figure C-12: Load-displacement response-studded bracket type-monotonic tension - *a/d* ratio = 1.42, ρ_x = 0.8%.

- The load and the displacement capacities remain the same for all the h_e.

***a/d* ratio = 1.11, ρ_x = 0.2%**

h_e	Numerical Model	Crack Pattern
Top (T)	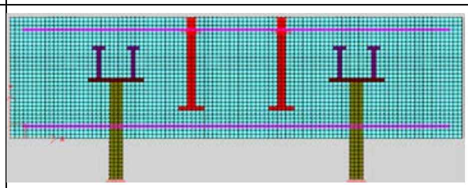	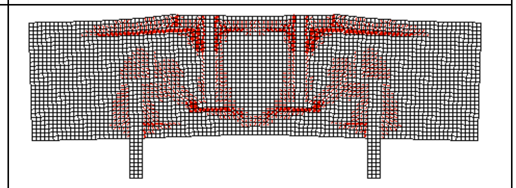
Bottom (B)	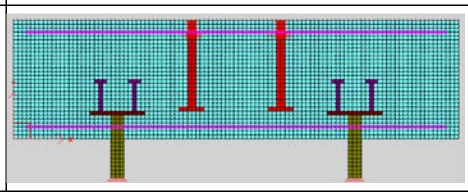	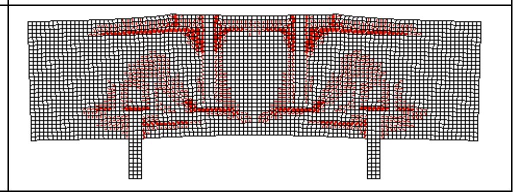

Figure C-13: Numerical model and crack pattern-studded bracket type-monotonic tension - *a/d* ratio = 1.11, ρ_x = 0.2%.

Table C-7: Comparison of numerical simulation-studded bracket type-monotonic tension - *a/d* ratio = 1.11, ρ_x = 0.2%.

h_e	*a/d* ratio	P_u (KN)	δ_u (mm)	Stiff (KN/mm)	Failure Mode	Bracket Infl.
T	1.11	825	0.93	2232	Flexural	None
B		806	1.14	2243	Flexural	None

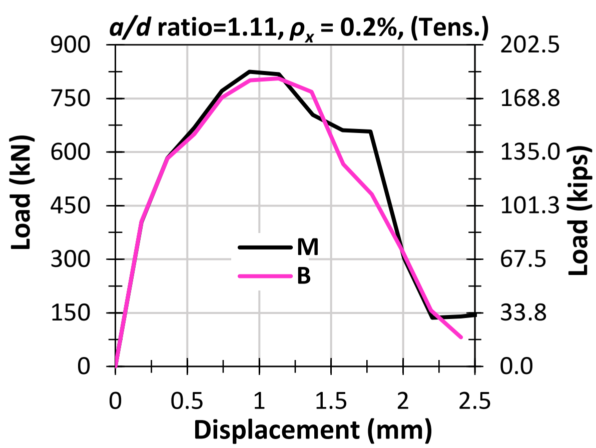

Figure C-14: Load-displacement response- studded bracket type-monotonic tension - *a/d* ratio = 1.11, ρ_x = 0.2%.

- The load and the displacement capacities remain the same for all the h_e.

***a/d* ratio = 1.11, ρ_x = 0.4%**

h_e	Numerical Model	Crack Pattern
Top (T)	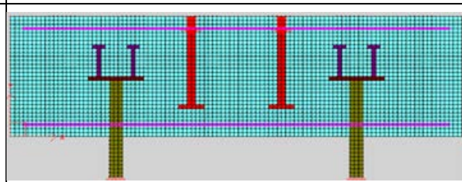	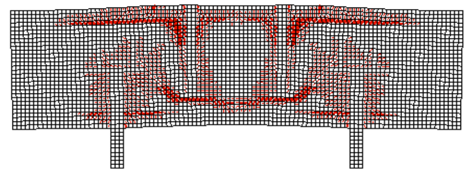
Bottom (B)	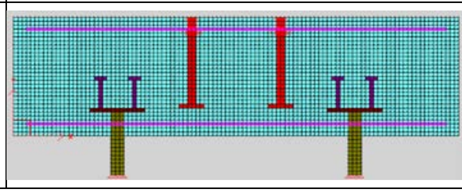	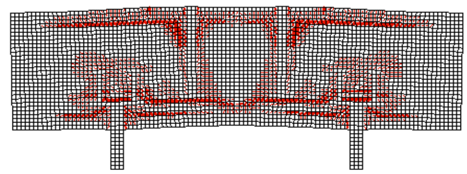

Figure C-15: Numerical model and crack pattern-studded bracket type-monotonic tension - *a/d* ratio = 1.11, ρ_x = 0.4%.

Table C-8: Comparison of numerical simulation-studded bracket-monotonic tension-*a/d*=1.11, ρ_x = 0.4%.

h_e	*a/d* ratio	P_u (KN)	δ_u (mm)	Stiff (KN/mm)	Failure Mode	Bracket Infl.
T	1.11	1016	1.14	2275	Flexural	None
B		988	1.34	2291	Flexural	None

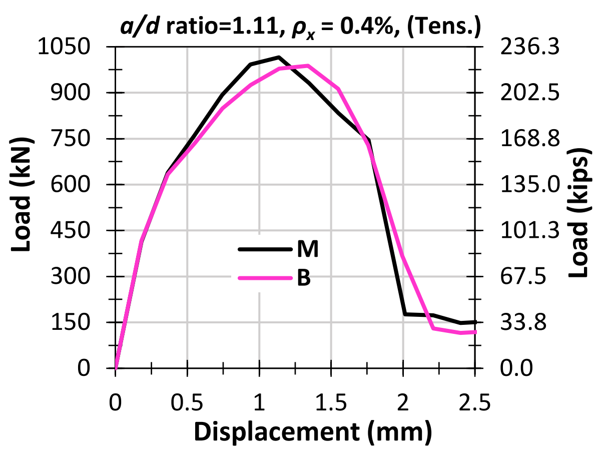

Figure C-16: Load-displacement response-studded bracket type-monotonic tension - *a/d* ratio = 1.11, ρ_x = 0.4%.

- The load and the displacement capacities remain the same for all the h_e.

***a/d* ratio = 1.11, ρ_x = 0.8%**

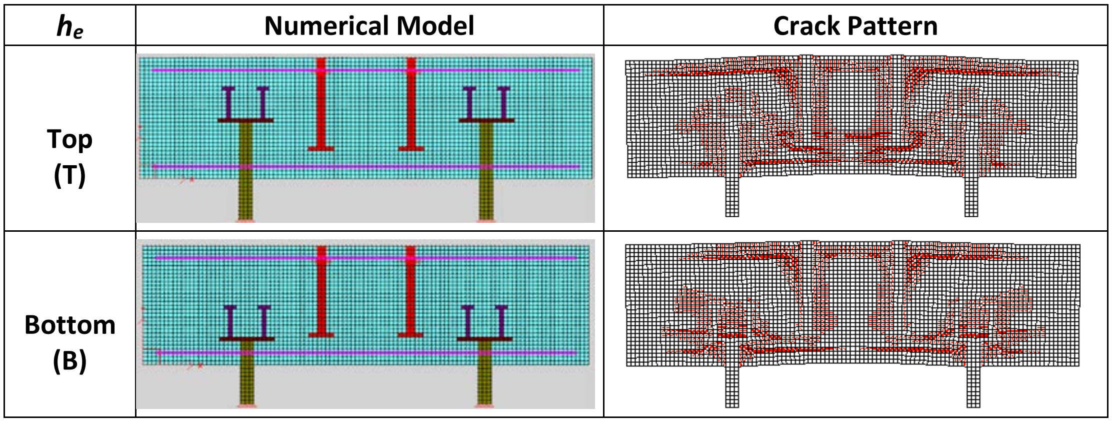

Figure C-17: Numerical model and crack pattern-studded bracket type-monotonic tension - *a/d* ratio = 1.11, ρ_x = 0.8%.

Table C-9: Comparison of numerical simulation- studded bracket type-monotonic tension - *a/d* ratio = 1.11, ρ_x = 0.8%.

h_e	*a/d* ratio	P_u (KN)	δ_u (mm)	Stiff (KN/mm)	Failure Mode	Bracket Infl.
T	1.11	1192	1.34	2333	Flexural	None
B		1100	1.34	2357	Flexural	None

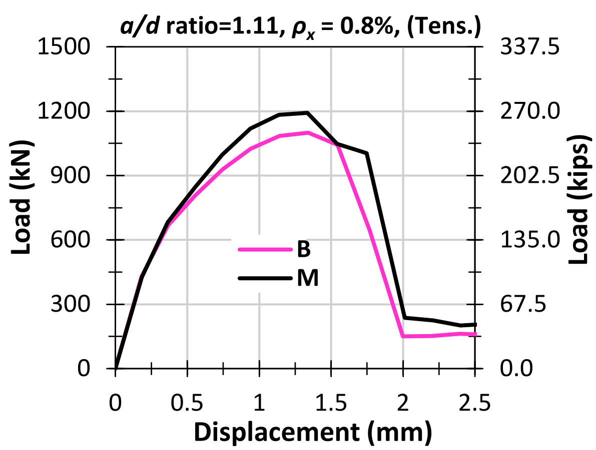

Figure C-18: Load-displacement response-studded bracket-monotonic compression-*a/d*=1.11, ρ_x = 0.8%.

- The load and the displacement capacities remain the same for all the h_e.

Subjected to Monotonic Compression

***a/d* ratio = 1.68, ρ_x = 0.2%**

h_e	Numerical Model	Crack Pattern
Middle (M)	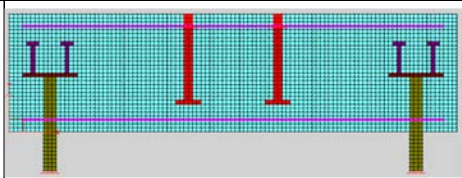	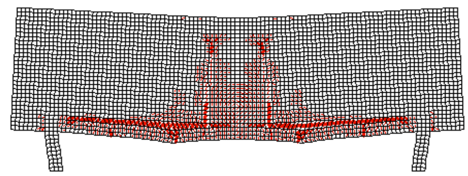
Bottom (B)	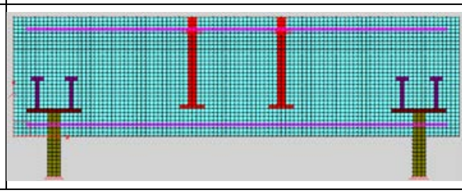	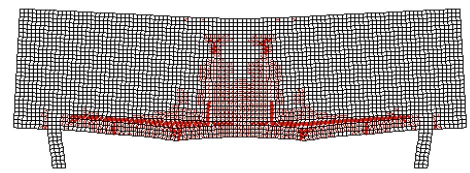

Figure C-19: Numerical model and crack pattern-studded bracket type-monotonic tension - *a/d* ratio = 1.68, ρ_x = 0.2%.

Table C-10: Comparison of numerical simulation-studded bracket type-monotonic tension - *a/d* ratio = 1.68, ρ_x = 0.2%.

h_e	*a/d* ratio	P_u (KN)	δ_u (mm)	Stiff (KN/mm)	Failure Mode	Bracket Infl.
M	1.68	923	1.99	1601	Flexural	None
B		925	1.99	1606	Flexural	None

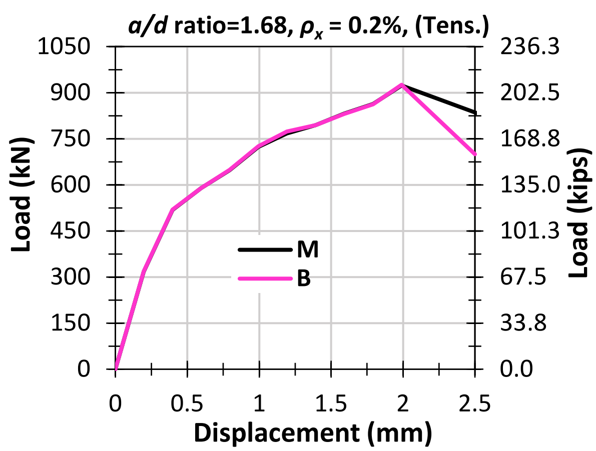

Figure C-20: Load-displacement response-studded bracket type-monotonic tension - *a/d* ratio = 1.11, ρ_x = 0.2%.

- The load and the displacement capacities remain the same for all the h_e.

***a/d* ratio = 1.68, ρ_x = 0.4%**

h_e	Numerical Model	Crack Pattern
Middle (M)	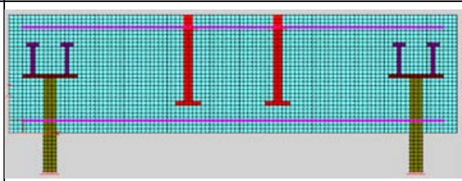	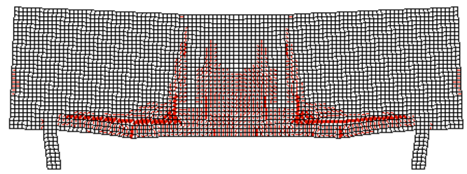
Bottom (B)	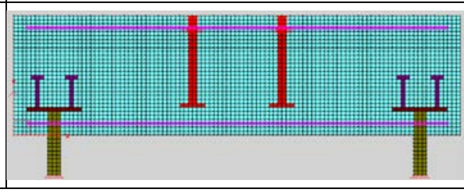	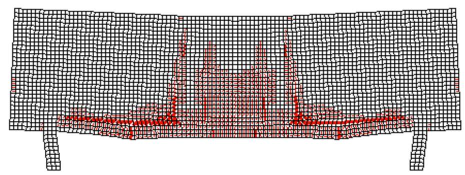

Figure C-21: Numerical model and crack pattern-studded bracket type-monotonic tension - *a/d* ratio = 1.68, ρ_x = 0.4%.

Table C-11: Comparison of numerical simulation-studded bracket type-monotonic tension - *a/d* ratio = 1.68, ρ_x = 0.4%.

h_e	*a/d* ratio	P_u (KN)	δ_u (mm)	Stiff (KN/mm)	Failure Mode	Bracket Infl.
M	1.68	1128	1.79	1652	Flexural	None
B		1138	1.79	1657	Flexural	None

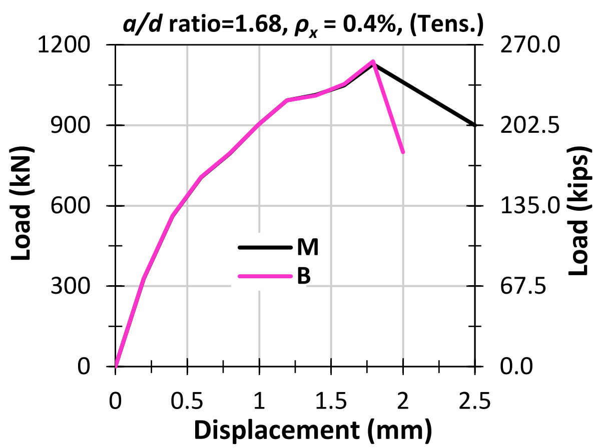

Figure C-22: Load-displacement response-studded bracket type-monotonic tension - *a/d* ratio = 1.68, ρ_x = 0.4%.

- The load and the displacement capacities remain the same for all the h_e.

***a/d* ratio = 1.68, ρ_x = 0.8%**

h_e	Numerical Model	Crack Pattern
Middle (M)	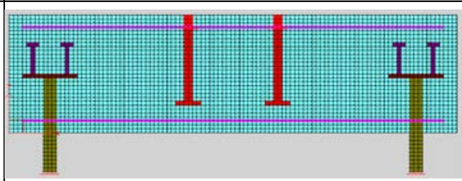	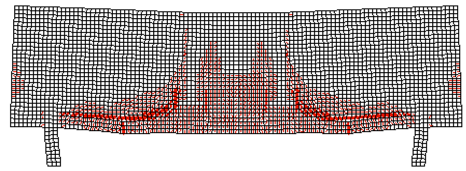
Bottom (B)	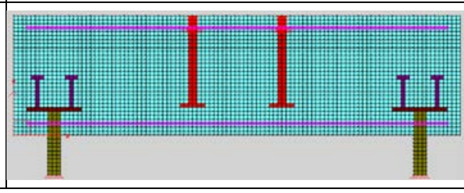	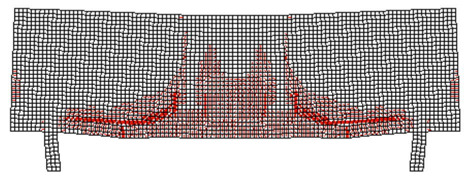

Figure C-23: Numerical model and crack pattern-studded bracket type-monotonic tension - *a/d* ratio = 1.68, ρ_x = 0.8%.

Table C-12: Comparison of numerical simulation-studded bracket type-monotonic tension - *a/d* ratio = 1.68, ρ_x = 0.8%.

h_e	*a/d* ratio	P_u (KN)	δ_u (mm)	Stiff (KN/mm)	Failure Mode	Bracket Infl.
M	1.68	1493	1.79	1733	Flexural	None
B		1507	1.79	1742	Flexural	None

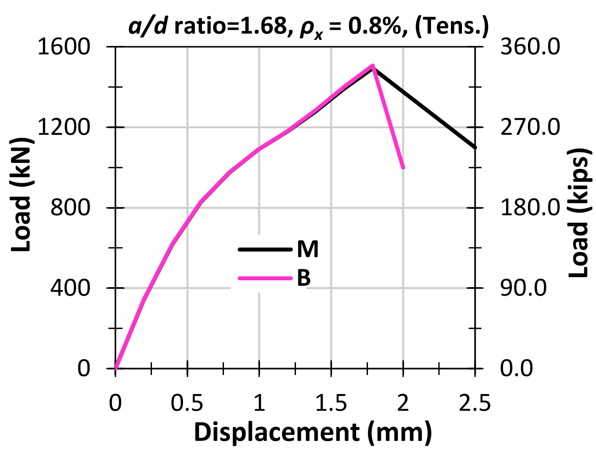

Figure C-24: Load-displacement response-studded bracket type-monotonic tension - *a/d* ratio = 1.68, ρ_x = 0.8%.

- The load and the displacement capacities remain the same for all the h_e.

***a/d* ratio = 1.42, ρ_x = 0.2%**

h_e	Numerical Model	Crack Pattern
Middle (M)	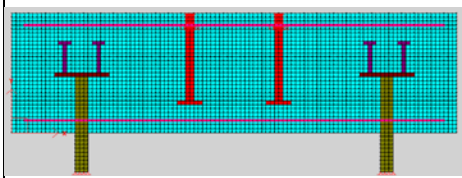	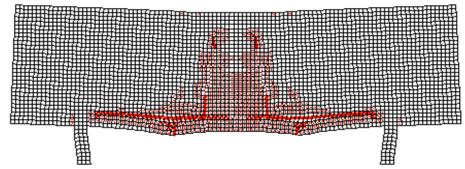
Bottom (B)	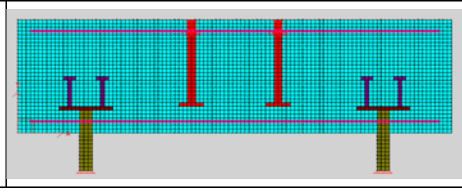	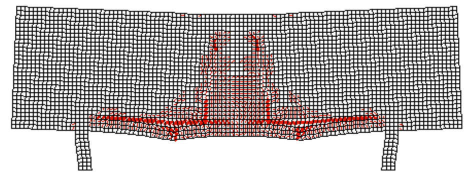

Figure C-25: Numerical model and crack pattern-studded bracket type-monotonic tension - *a/d* ratio = 1.42, ρ_x = 0.2%.

Table C-13: Comparison of numerical simulation-studded bracket type-monotonic tension - *a/d* ratio = 1.42, ρ_x = 0.2%.

h_e	*a/d* ratio	P_u (KN)	δ_u (mm)	Stiff (KN/mm)	Failure Mode	Bracket Infl.
M	1.42	1084	1.34	2099	Flexural	None
B		1085	1.34	2104	Flexural	None

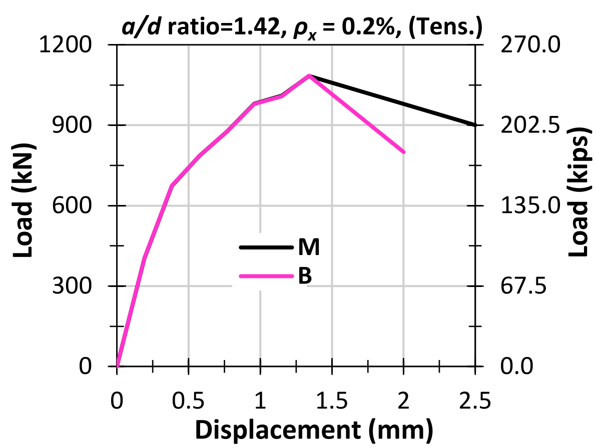

Figure C-14: Load-displacement response-studded bracket type-monotonic tension - *a/d* ratio = 1.42, ρ_x = 0.2%.

- The load and the displacement capacities remain the same for all the h_e.

***a/d* ratio = 1.42, ρ_x = 0.4%**

h_e	Numerical Model	Crack Pattern
Middle (M)	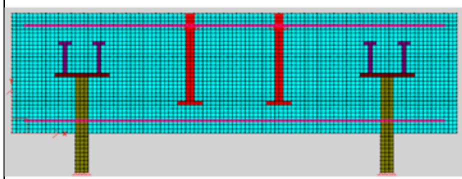	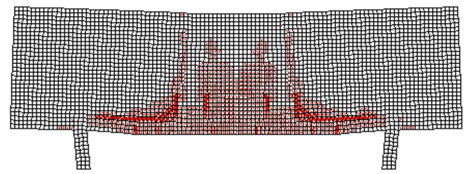
Bottom (B)	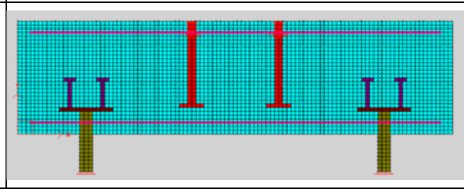	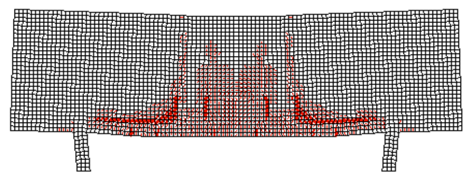

Figure C-27: Numerical model and crack pattern-studded bracket type-monotonic tension - *a/d* ratio = 1.42, ρ_x = 0.4%.

Table C-14: Comparison of numerical simulation-studded bracket type-monotonic tension - *a/d* ratio = 1.42, ρ_x = 0.4%.

h_e	*a/d* ratio	P_u (KN)	δ_u (mm)	Stiff (KN/mm)	Failure Mode	Bracket Infl.
M	1.42	1427	1.34	2147	Flexural	None
B		1437	1.34	2156	Flexural	None

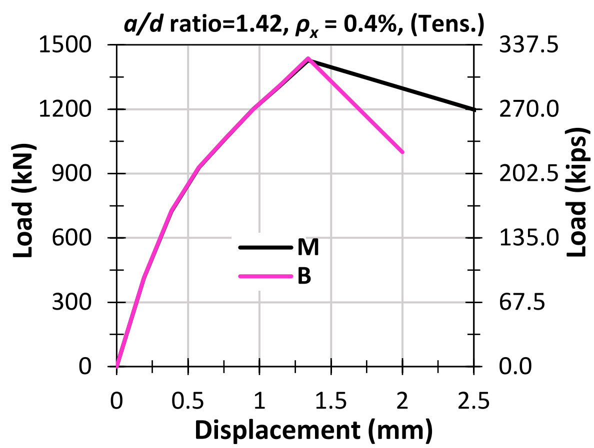

Figure C-28: Load-displacement response-studded bracket type-monotonic tension - *a/d* ratio = 1.42, ρ_x = 0.4%.

- The load and the displacement capacities remain the same for all the h_e.

_a/d_ ratio = 1.42, ρ_x = 0.8%

h_e	Numerical Model	Crack Pattern
Middle (M)	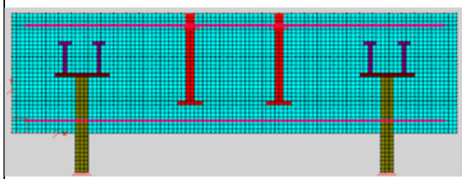	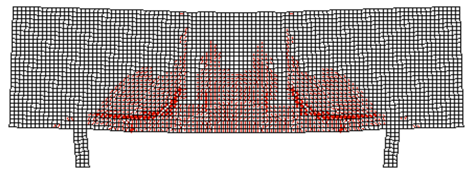
Bottom (B)	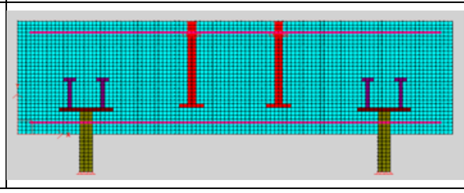	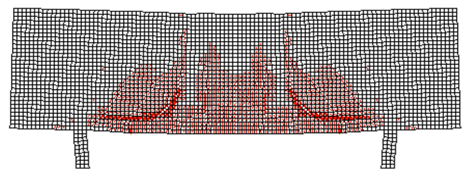

Figure C-29: Numerical model and crack pattern-studded bracket type-monotonic tension - *a/d* ratio = 1.42, ρ_x = 0.8%.

Table C-15: Comparison of numerical simulation-studded bracket type-monotonic tension - *a/d* ratio = 1.42, ρ_x = 0.8%.

h_e	*a/d* ratio	P_u (KN)	δ_u (mm)	Stiff (KN/mm)	Failure Mode	Bracket Infl.
M	1.42	1798	1.34	2224	Flexural	None
B		1806	1.34	2234	Flexural	None

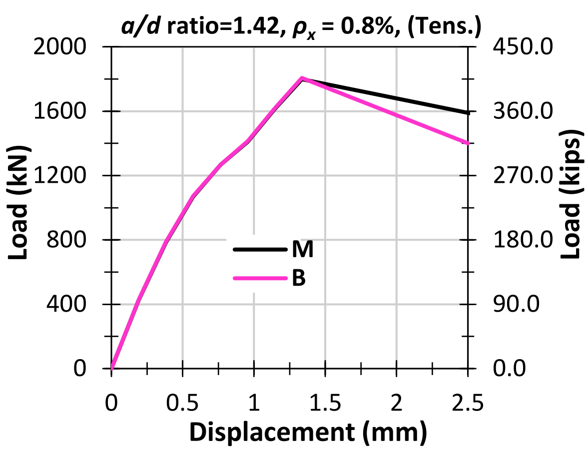

Figure C-30: Load-displacement response-studded bracket-monotonic compression-*a/d ratio* = 1.42, ρ_x = 0.8%.

- The load and the displacement capacities remain the same for all the h_e.

***a/d* ratio = 1.11, ρ_x = 0.2%**

h_e	Numerical Model	Crack Pattern
Middle (M)	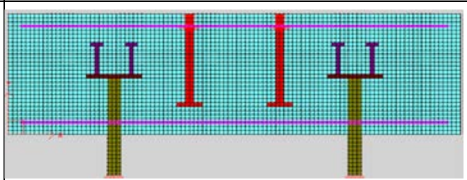	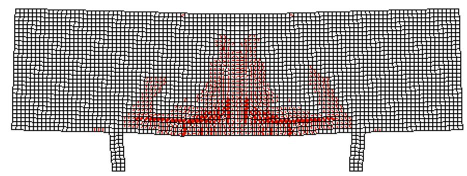
Bottom (B)	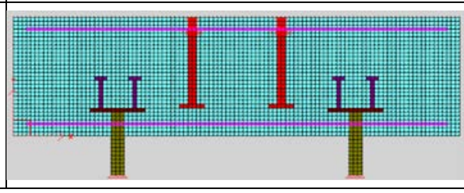	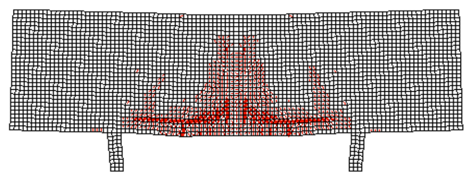

Figure C-31: Numerical model and crack pattern-studded bracket type-monotonic tension - *a/d* ratio = 1.11, ρ_x = 0.2%.

Table C-16: Comparison of numerical simulation-studded bracket type-monotonic tension - *a/d* ratio = 1.11, ρ_x = 0.2%.

h_e	*a/d* ratio	P_u (KN)	δ_u (mm)	Stiff (KN/mm)	Failure Mode	Bracket Infl.
M	1.11	1543	0.94	2700	Flexural	None
B		1541	0.94	2716	Flexural	None

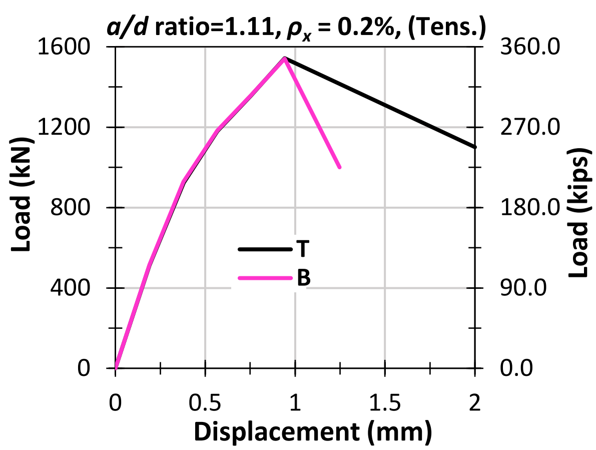

Figure C-32: Load-displacement response-studded bracket type-monotonic tension - *a/d* ratio = 1.11, ρ_x = 0.2%.

- The load and the displacement capacities remain the same for all the h_e.

***a/d* ratio = 1.11, ρ_x = 0.4%**

h_e	Numerical Model	Crack Pattern
Top (T)	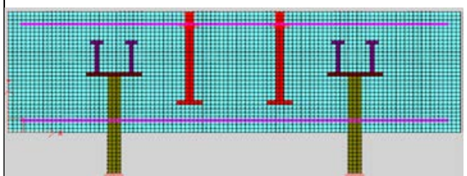	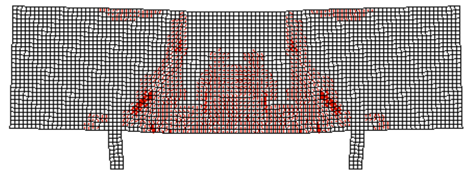
Bottom (B)	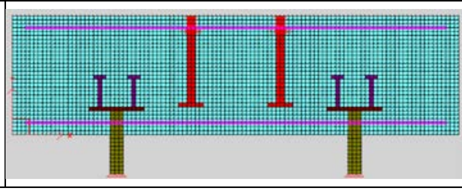	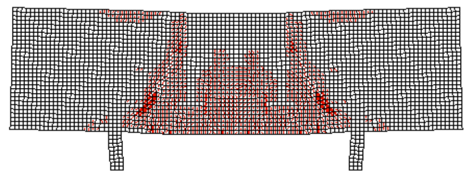

Figure C-33: Numerical model and crack pattern-studded bracket type-monotonic tension - *a/d* ratio = 1.11, ρ_x = 0.4%.

Table C-17: Comparison of numerical simulation-studded bracket type-monotonic tension - *a/d* ratio = 1.11, ρ_x = 0.4%.

h_e	*a/d* ratio	P_u (KN)	δ_u (mm)	Stiff (KN/mm)	Failure Mode	Bracket Infl.
T	1.11	1844	1.13	2726	Shear	None
B		1855	1.13	2748	Shear	None

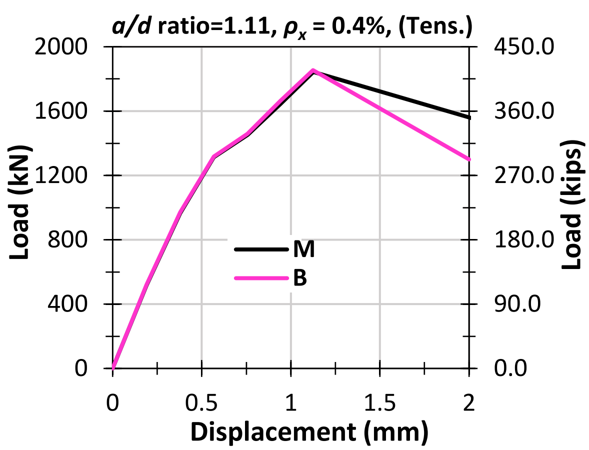

Figure C-34: Load-displacement response-studded bracket type-monotonic tension - *a/d* ratio = 1.11, ρ_x = 0.4%.

- The load and the displacement capacities remain the same for all the h_e.

***a/d* ratio = 1.11, ρ_x = 0.8%**

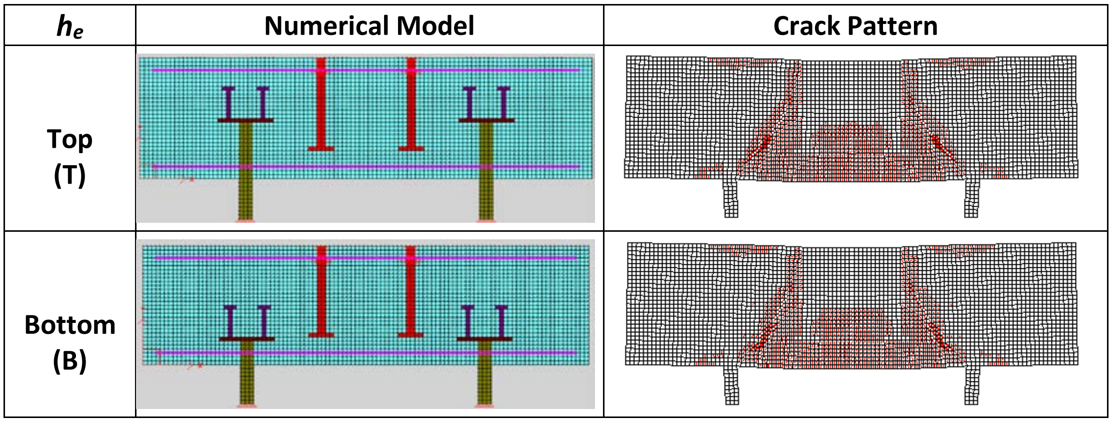

Figure C-35: Numerical model and crack pattern-studded bracket type-monotonic tension - *a/d* ratio = 1.11, ρ_x = 0.8%.

Table C-18: Comparison of numerical simulation-studded bracket type-monotonic tension - *a/d* ratio = 1.11, ρ_x = 0.8%.

h_e	*a/d* ratio	P_u (KN)	δ_u (mm)	Stiff (KN/mm)	Failure Mode	Bracket Infl.
T	1.11	2153	1.12	2779	Shear	None
B		2168	1.12	2795	Shear	None

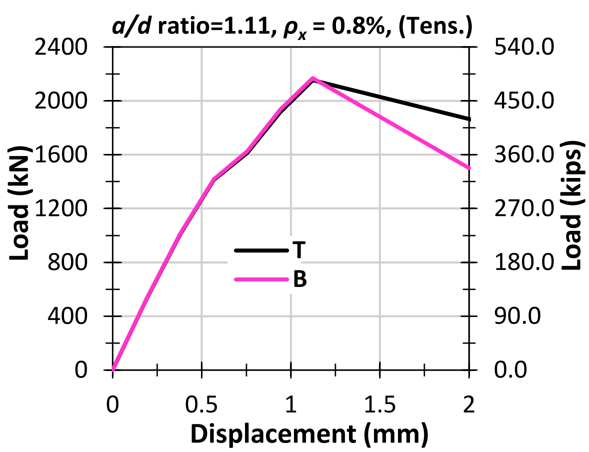

Figure C-36: Load-displacement response-studded bracket type-monotonic tension - *a/d* ratio = 1.11, ρ_x = 0.8%.

- The load and the displacement capacities remain the same for all the h_e.

Subjected to Reversed-Cyclic Loads

***a/d* ratio = 1.68, ρ_x = 0.2%**

h_e	Numerical Model	Crack Pattern
Top (T)	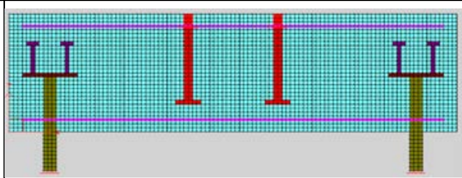	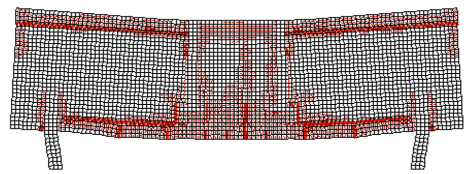
Bottom (B)	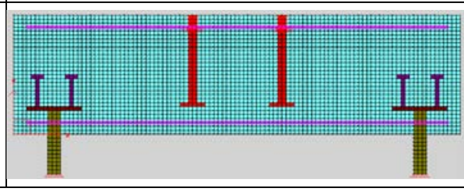	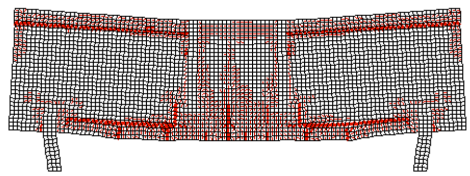

Figure C-37: Numerical model and crack pattern-studded bracket type-monotonic tension - *a/d* ratio = 1.68, ρ_x = 0.2%.

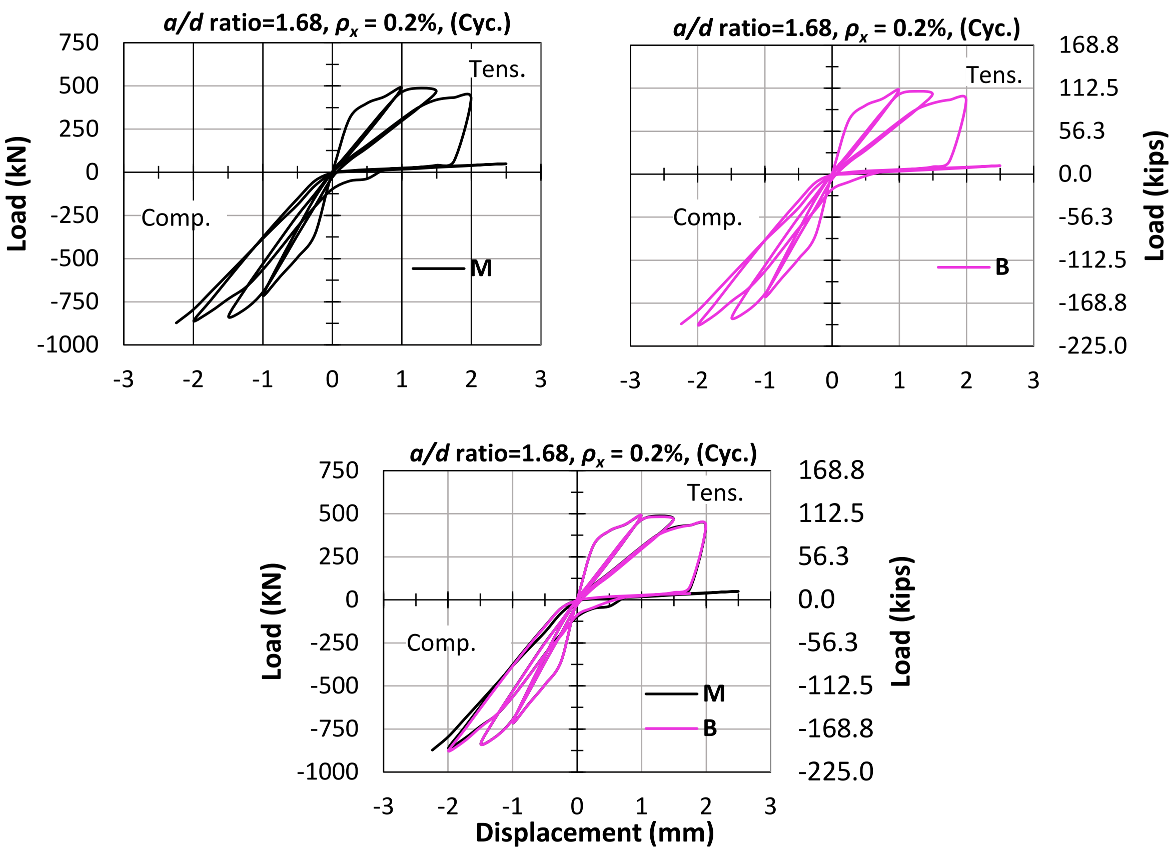

Figure C-38: Load-displacement response-studded bracket type-monotonic tension - *a/d* ratio = 1.68, ρ_x = 0.2%.

Table C-19: Comparison of numerical simulation-studded bracket type-monotonic tension - *a/d* ratio = 1.68, ρ_x = 0.2%.

h_e	*a/d* ratio	Tensile Component				Compression Component				Failure Mode	Bracket Inf.
		P_t (KN)	$P_{t\text{-}M/B}$	δ_t (mm)	$\delta_{t\text{-}M/B}$	P_t (KN)	$P_{c\text{-}M/B}$	δ_c (mm)	$\delta_{c\text{-}M/B}$		
T	1.68	490	1.00	2.50	1.00	873	0.99	2.24	1.00	Flexural	None
B		491		2.50		878		2.24		Flexural	None

Tensile component's result

- The load and the displacement capacities remain the same for all the h_e.

Compression component's result

- The load and the displacement capacities remain the same for all the h_e.

***a/d* ratio = 1.68, ρ_x = 0.4%**

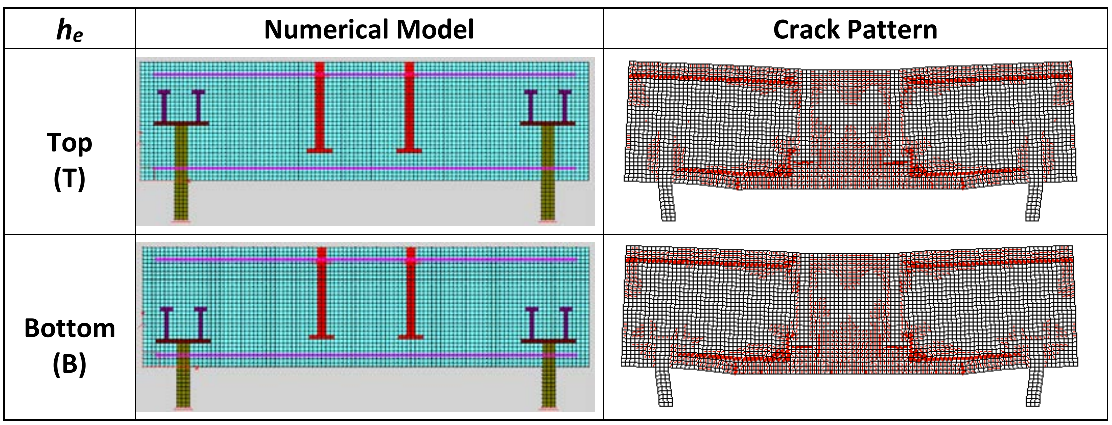

Figure C-39: Numerical model and crack pattern-studded bracket type-monotonic tension - *a/d* ratio = 1.68, ρ_x = 0.4%.

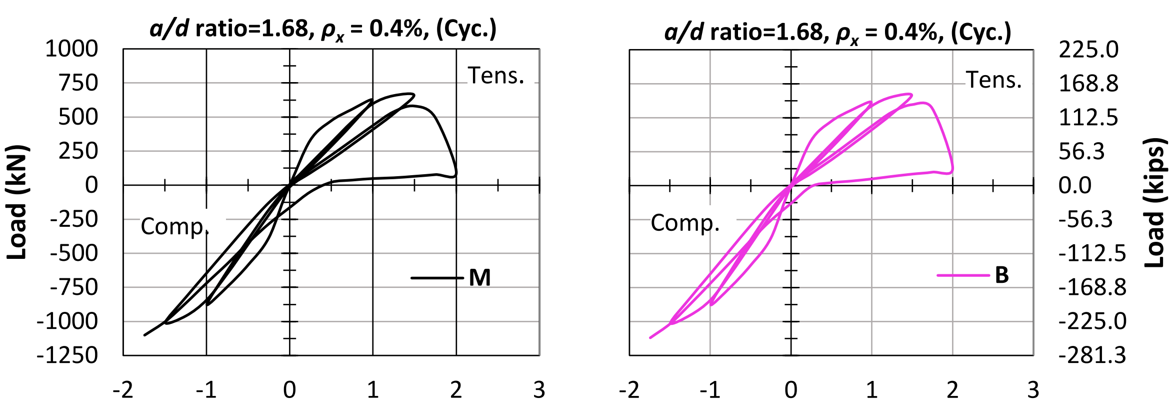

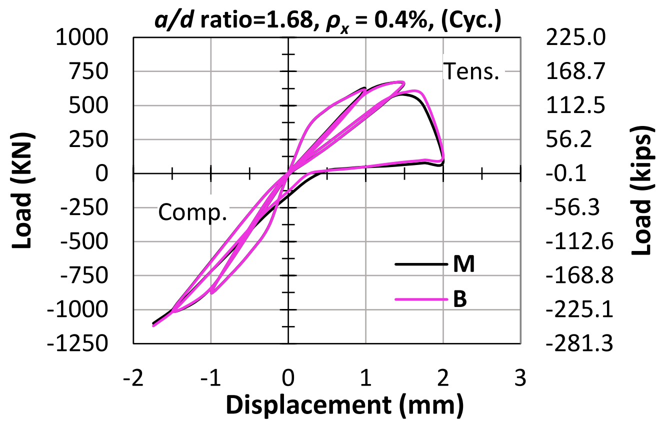

Figure C-40: Load-displacement response-studded bracket type-monotonic tension - *a/d* ratio = 1.68, ρ_x = 0.4%.

Table C-1: Comparison of numerical simulation-studded bracket type-monotonic tension - *a/d* ratio = 1.68, ρ_x = 0.4%.

h_e	*a/d* ratio	Tensile Component				Compression Component				Failure Mode	Bracket Inf.
		P_t (KN)	$P_{t\text{-}T/B}$	δ_t (mm)	$\delta_{t\text{-}T/B}$	P_t (KN)	$P_{c\text{-}T/B}$	δ_c (mm)	$\delta_{c\text{-}T/B}$		
T	1.68	660	0.99	2.00	1.00	1100	0.98	1.74	1.00	Flexural	None
B		665		2.00		1120		1.74		Flexural	None

Tensile component's result

- The load and the displacement capacities remain the same for all the h_e.

Compression component's result

- The load and the displacement capacities remain the same for all the h_e.

a/d ratio = 1.68, ρ_x = 0.8%

h_e	Numerical Model	Crack Pattern
Top (T)	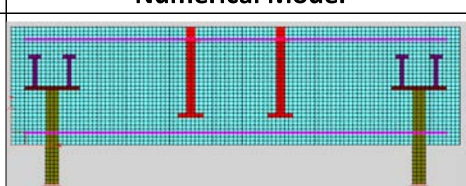	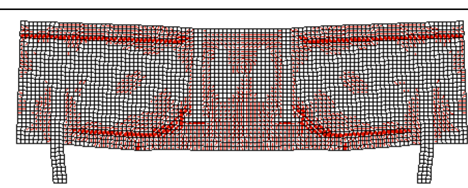
Bottom (B)	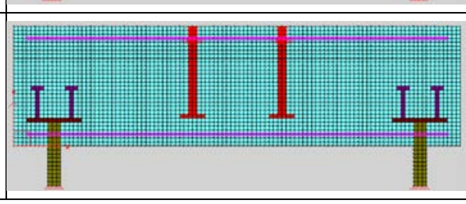	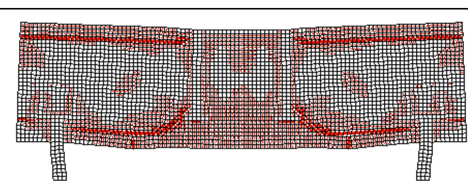

Figure C-41: Numerical model and crack pattern-studded bracket type-monotonic tension - *a/d* ratio = 1.68, ρ_x = 0.8%.

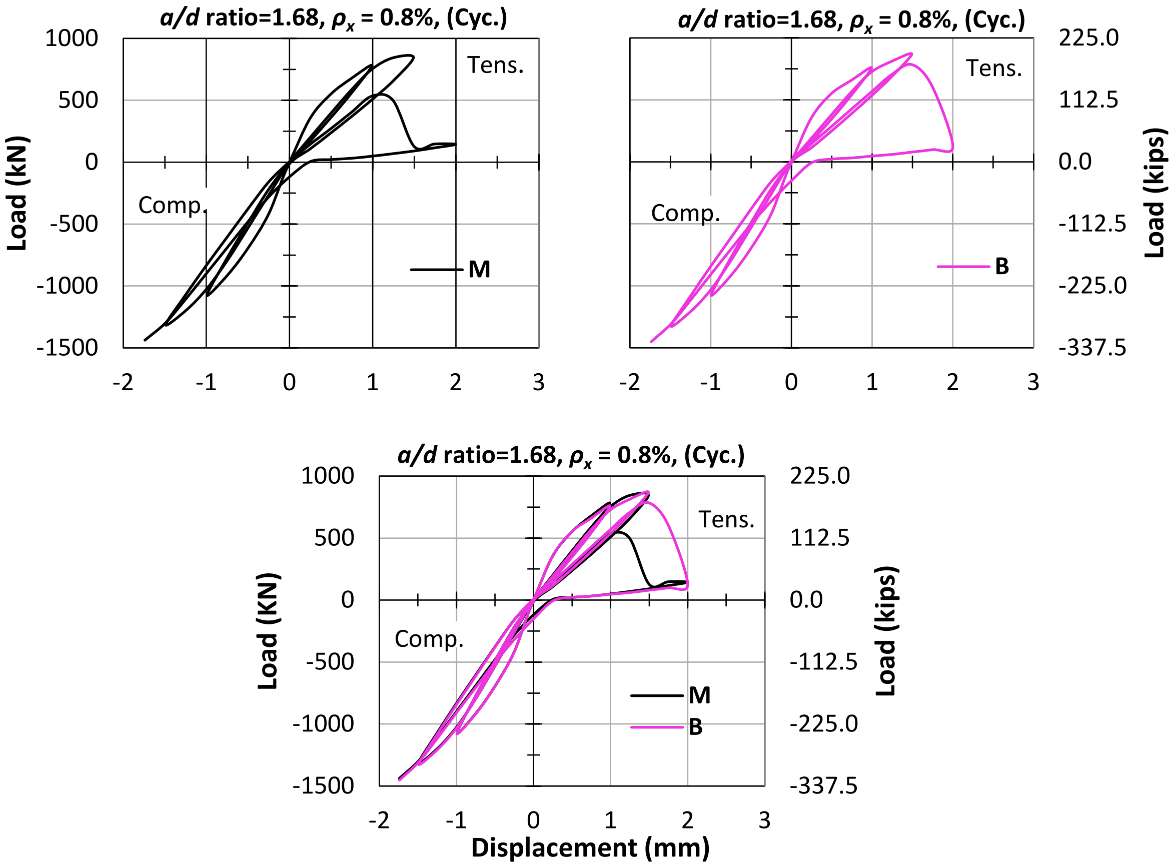

Figure C-42: Load-displacement response-studded bracket type-monotonic tension - *a/d* ratio = 1.68, ρ_x = 0.8%.

Table C-21: Comparison of numerical simulation-studded bracket type-monotonic tension - *a/d* ratio = 1.68, ρ_x = 0.8%.

h_e	*a/d* ratio	Tensile Component				Compression Component				Failure Mode	Bracket Inf.
		P_t (KN)	$P_{t-T/B}$	δ_t (mm)	$\delta_{t-T/B}$	P_t (KN)	$P_{c-T/B}$	δ_c (mm)	$\delta_{c-T/B}$		
T	1.68	846	0.97	2.00	1.00	1438	0.99	1.74	1.00	Flexural	None
B		870		2.00		1452		1.74		Flexural	None

Tensile component's result

- The load and the displacement capacities remain the same for all the h_e.

Compression component's result

- The load and the displacement capacities remain the same for all the h_e.

***a/d* ratio = 1.42, ρ_x = 0.2%**

h_e	Numerical Model	Crack Pattern
Top (T)	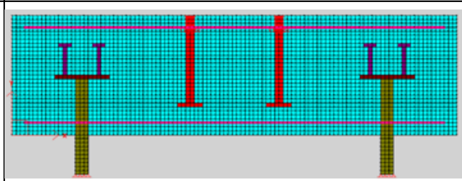	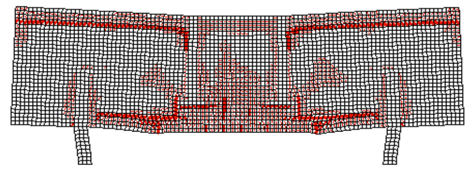
Bottom (B)	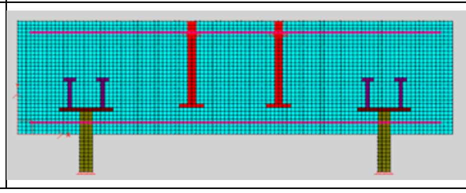	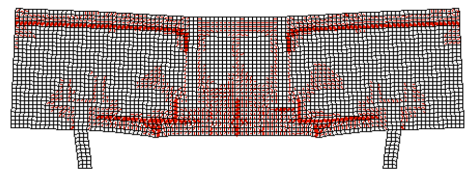

Figure C-43: Numerical model and crack pattern-studded bracket type-monotonic tension - *a/d* ratio = 1.42, ρ_x = 0.2%.

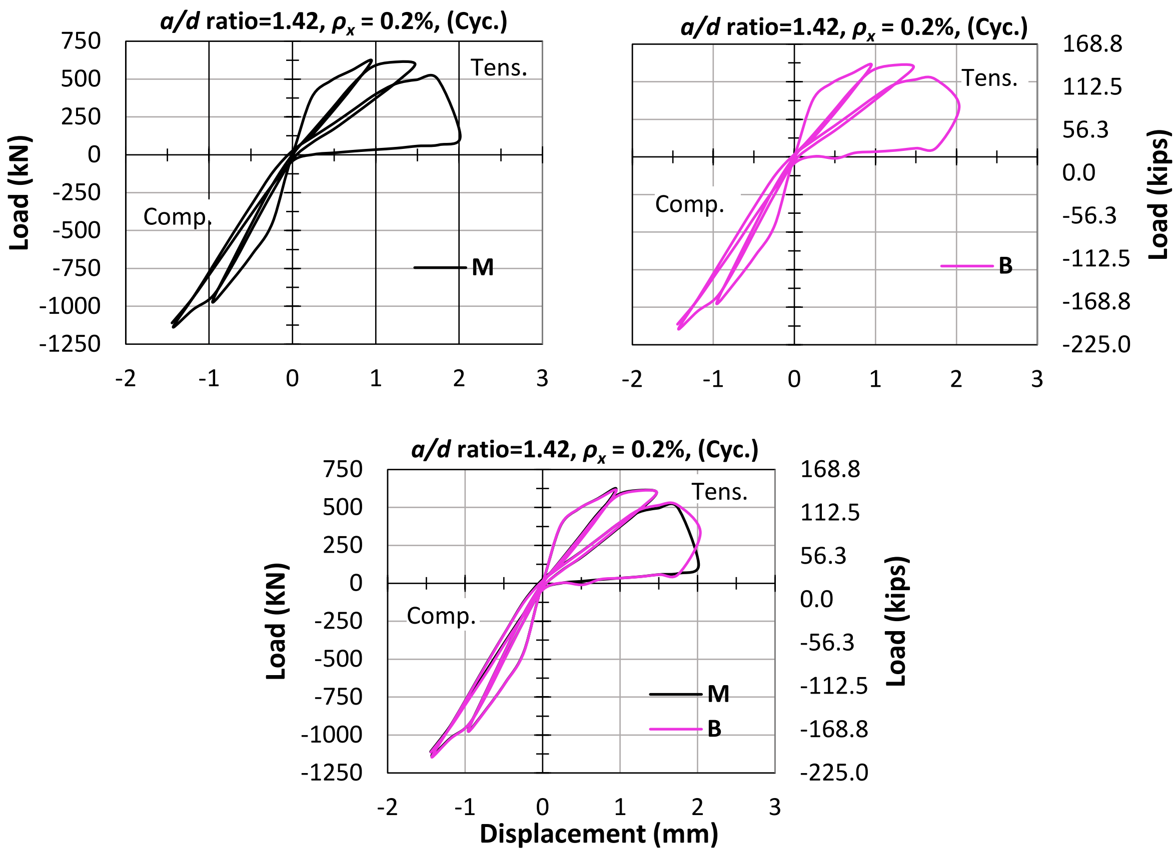

Figure C-44: Load-displacement response-studded bracket type-monotonic tension - *a/d* ratio = 1.42, ρ_x = 0.2%.

Table C-22: Comparison of numerical simulation-studded bracket type-monotonic tension - *a/d* ratio = 1.42, ρ_x = 0.2%.

h_e	*a/d* ratio	Tensile Component				Compression Component				Failure Mode	Bracket Inf.
		P_t (KN)	$P_{t\text{-}T/B}$	δ_t (mm)	$\delta_{t\text{-}T/B}$	P_t (KN)	$P_{c\text{-}T/B}$	δ_c (mm)	$\delta_{c\text{-}T/B}$		
T	1.42	623	1.02	2.01	0.99	1137	0.99	1.45	1.00	Flexural	None
B		614		2.04		1146		1.44		Flexural	None

Tensile component's result

- The load and the displacement capacities remain the same for all the h_e.

Compression component's result

- The load and the displacement capacities remain the same for all the h_e.

a/d ratio = 1.42, ρ_x = 0.4%

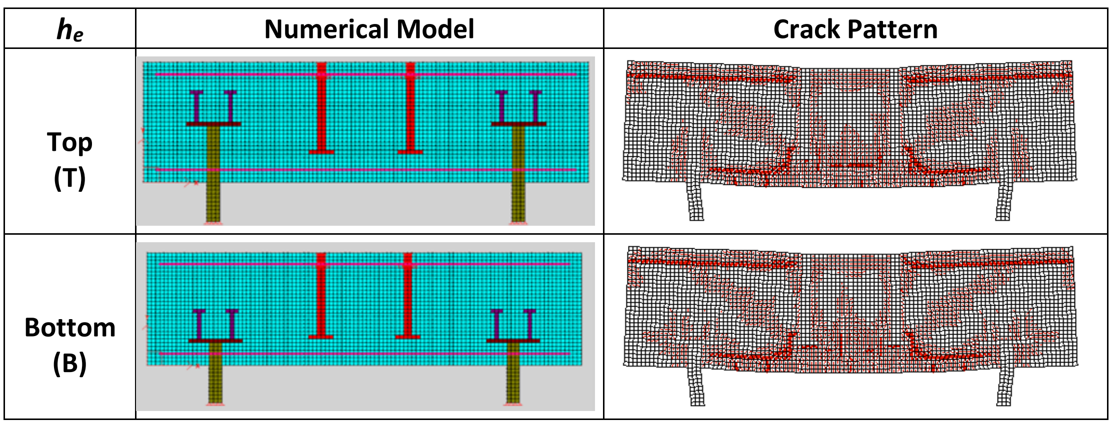

Figure C-45: Numerical model and crack pattern-studded bracket type-monotonic tension - *a/d* ratio = 1.42, ρ_x = 0.4%.

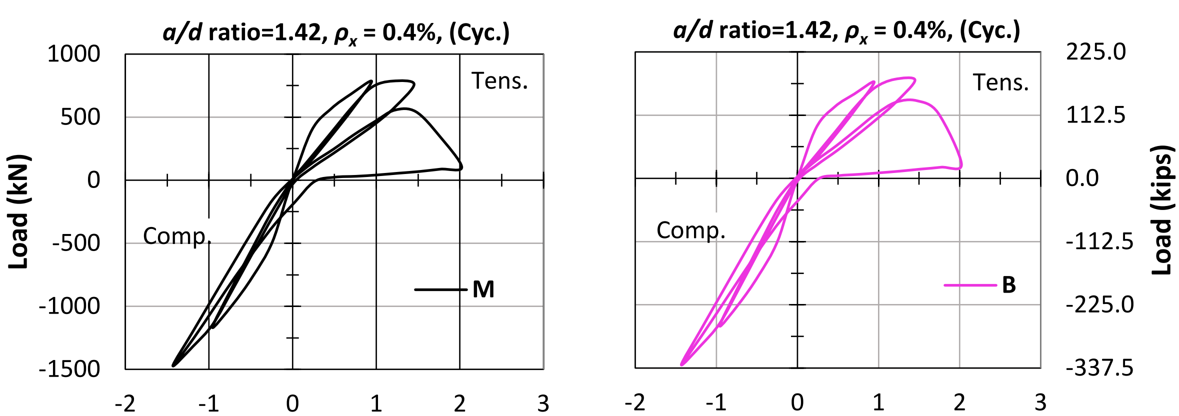

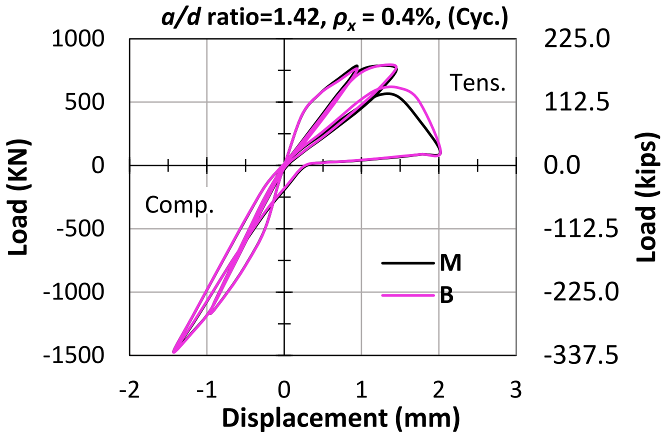

Figure C-46: Load-displacement response-studded bracket type-monotonic tension - *a/d* ratio = 1.42, ρ_x = 0.4%.

Table C-23: Comparison of numerical simulation-studded bracket type-monotonic tension - *a/d* ratio = 1.42, ρ_x = 0.4%.

h_e	*a/d* ratio	Tensile Component				Compression Component				Failure Mode	Bracket Inf.
		P_t (KN)	$P_{t\text{-}T/B}$	δ_t (mm)	$\delta_{t\text{-}T/B}$	P_t (KN)	$P_{c\text{-}T/B}$	δ_c (mm)	$\delta_{c\text{-}T/B}$		
T	1.42	786	1.00	2.02	1.00	1472	1.00	1.43	1.00	Flexural	None
B		783		2.02		1474		1.43		Flexural	None

Tensile component's result

- The load and the displacement capacities remain the same for all the h_e.

Compression component's result

- The load and the displacement capacities remain the same for all the h_e.

a/d ratio = 1.42, ρ_x = 0.8%

h_e	Numerical Model	Crack Pattern
Top (T)	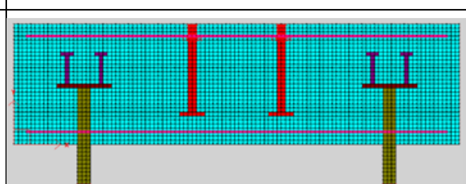	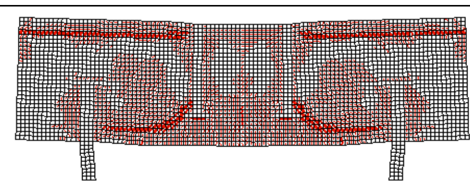
Bottom (B)	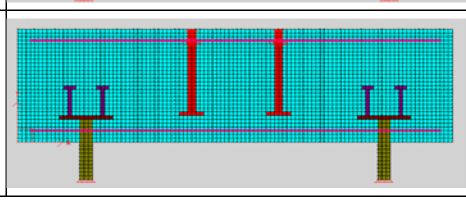	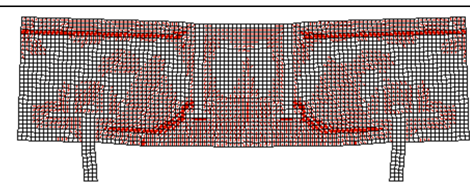

Figure C-47: Numerical model and crack pattern-studded bracket type-monotonic tension - *a/d* ratio = 1.42, ρ_x = 0.8%.

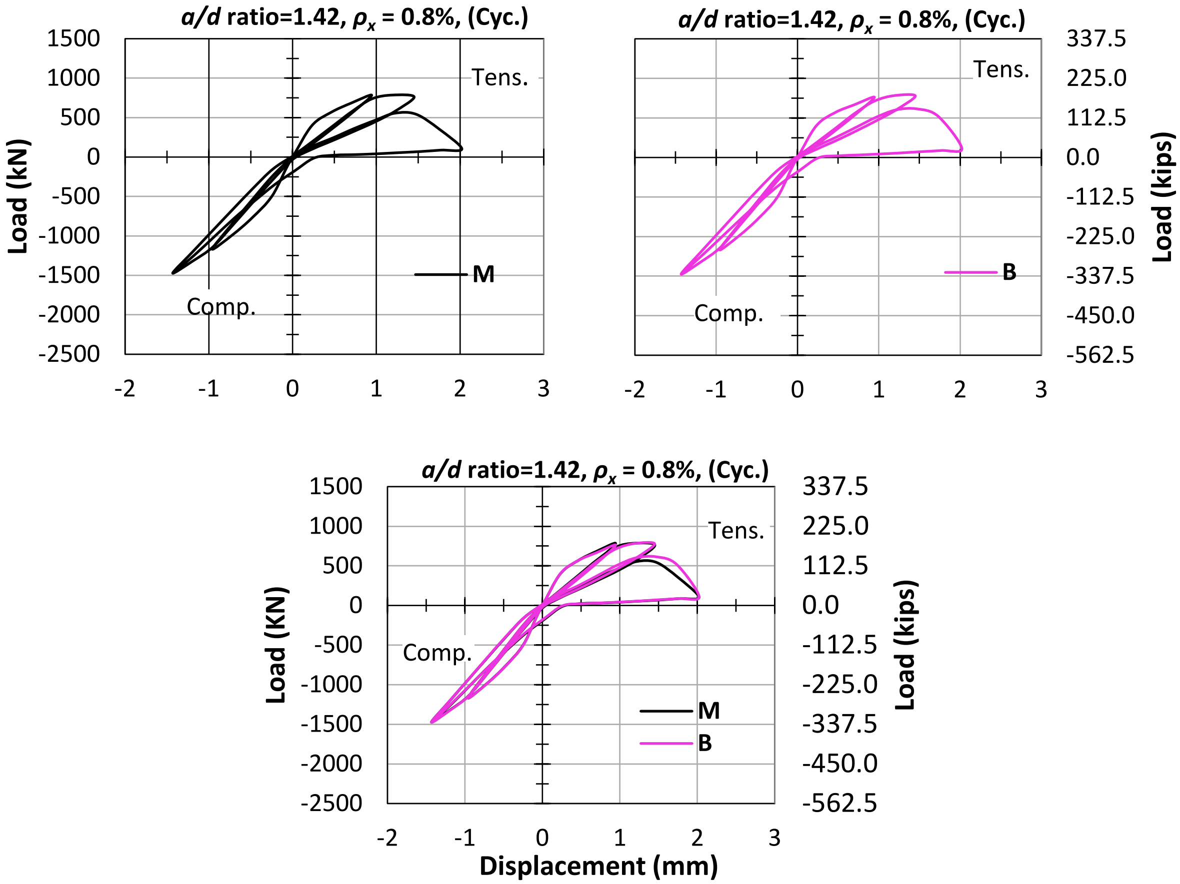

Figure C-48: Load-displacement response-studded bracket type-monotonic tension - *a/d* ratio = 1.42, ρ_x = 0.8%.

Table C-24: Comparison of numerical simulation-studded bracket type-monotonic tension - *a/d* ratio = 1.42, ρ_x = 0.8%.

h_e	*a/d* ratio	Tensile Component				Compression Component				Failure Mode	Bracket Inf.
		P_t (KN)	$P_{t\text{-}T/B}$	δ_t (mm)	$\delta_{t\text{-}T/B}$	P_t (KN)	$P_{c\text{-}T/B}$	δ_c (mm)	$\delta_{c\text{-}T/B}$		
T	1.42	1006	1.02	2.04	1.00	1852	0.99	1.43	1.00	Flexural	None
B		991		2.03		1867		1.43		Flexural	None

Tensile component's result

- The load and the displacement capacities remain the same for all the h_e.

Compression component's result

- The load and the displacement capacities remain the same for all the h_e.

***a/d* ratio = 1.11, ρ_x = 0.2%**

h_e	Numerical Model	Crack Pattern
Top (T)	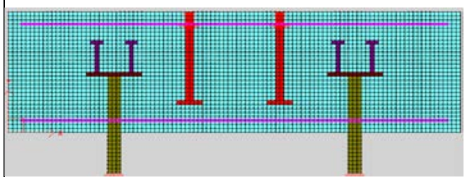	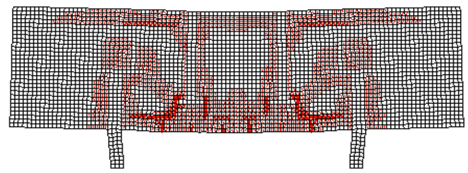
Bottom (B)	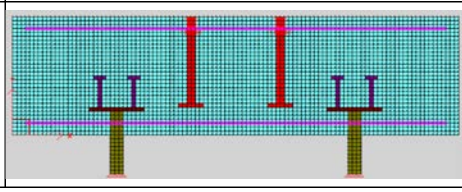	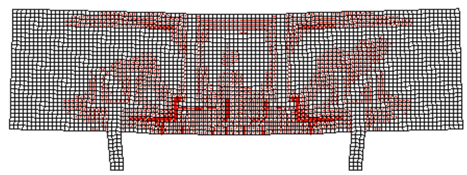

Figure C-49: Numerical model and crack pattern-studded bracket type-monotonic tension - *a/d* ratio = 1.11, ρ_x = 0.2%.

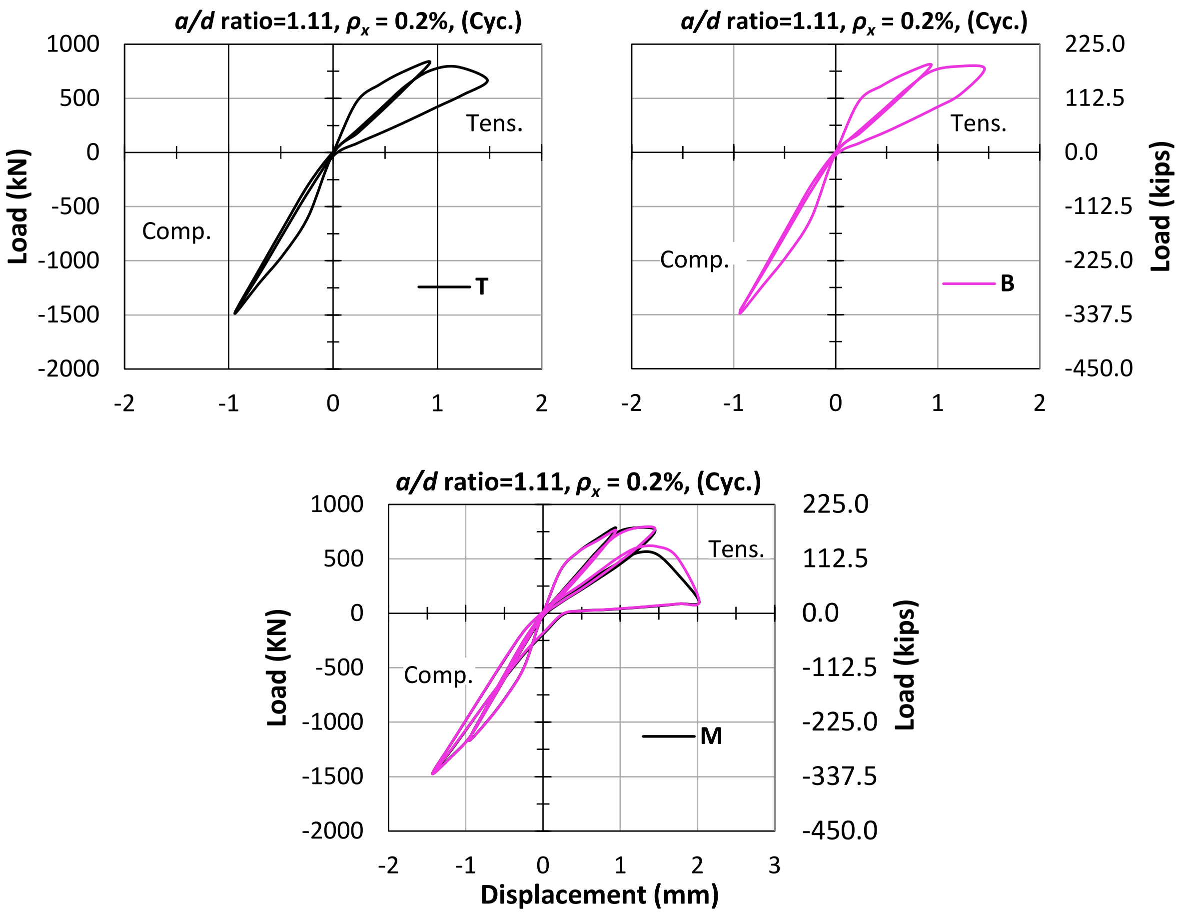

Figure C-50: Load-displacement response-studded bracket type-monotonic tension - *a/d* ratio = 1.11, 0.2 ρ_x%.

Table C-25: Comparison of numerical simulation-studded bracket type-monotonic tension - *a/d* ratio = 1.11, ρ_x = 0.2%.

h_e	*a/d* ratio	Tensile Component				Compression Component				Failure Mode	Bracket Inf.
		P_t (KN)	$P_{t\text{-}T/B}$	δ_t (mm)	$\delta_{t\text{-}T/B}$	P_t (KN)	$P_{c\text{-}T/B}$	δ_c (mm)	$\delta_{c\text{-}T/B}$		
T	1.11	835	1.03	1.48	1.02	1486	1.00	0.94	1.00	Flexural	None
B		810		1.46		1487		0.94		Flexural	None

Tensile component's result

- The load and the displacement capacities remain the same for all the h_e.

Compression component's result

- The load and the displacement capacities remain the same for all the h_e.

***a/d* ratio = 1.11, ρ_x = 0.4%**

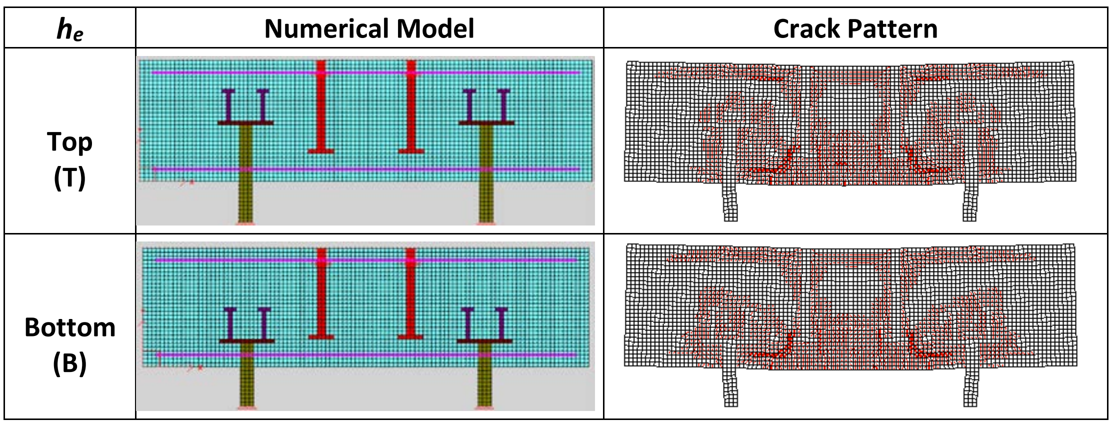

Figure C-51: Numerical model and crack pattern-studded bracket type-monotonic tension - *a/d* ratio = 1.11, ρ_x = 0.4%.

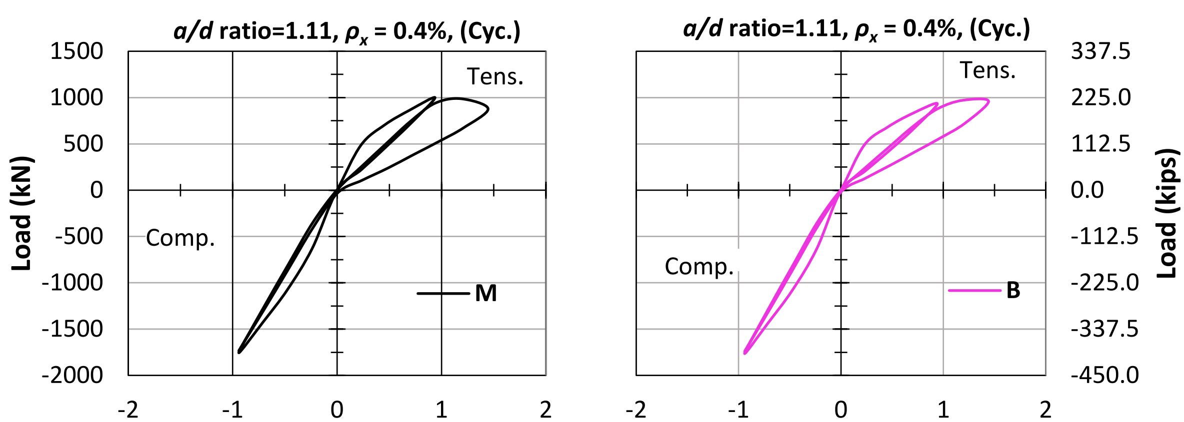

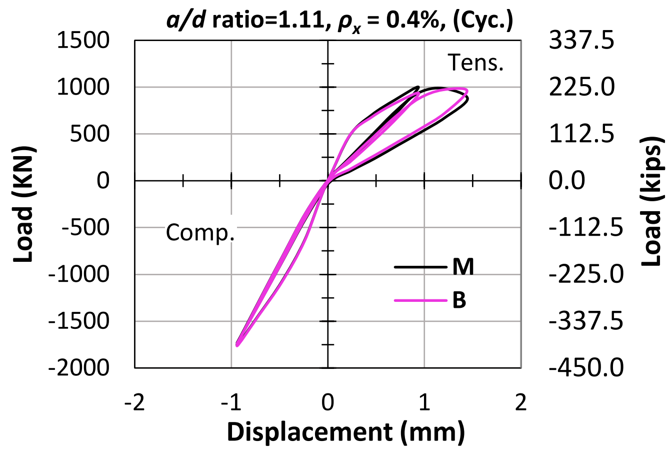

Figure C-52: Load-displacement response-studded bracket type-monotonic tension - *a/d* ratio = 1.11, ρ_x = 0.4%.

Table C-26: Comparison of numerical simulation-studded bracket type-monotonic tension - *a/d* ratio = 1.11, ρ_x = 0.4%.

h_e	***a/d* ratio**	**Tensile Component**				**Compression Component**				**Failure Mode**	**Bracket Inf.**
		P_t (KN)	**$P_{t-T/B}$**	**δ_t (mm)**	**$\delta_{t-T/B}$**	**P_t (KN)**	**$P_{c-T/B}$**	**δ_c (mm)**	**$\delta_{c-T/B}$**		
T	1.11	999	1.03	1.45	1.00	1754	0.99	0.94	1.00	Flexural	None
B		970		1.44		1763		0.94		Flexural	None

Tensile component's result

- The load and the displacement capacities remain the same for all the h_e.

Compression component's result

- The load and the displacement capacities remain the same for all the h_e.

a/d ratio = 1.11, ρ_x = 0.8%

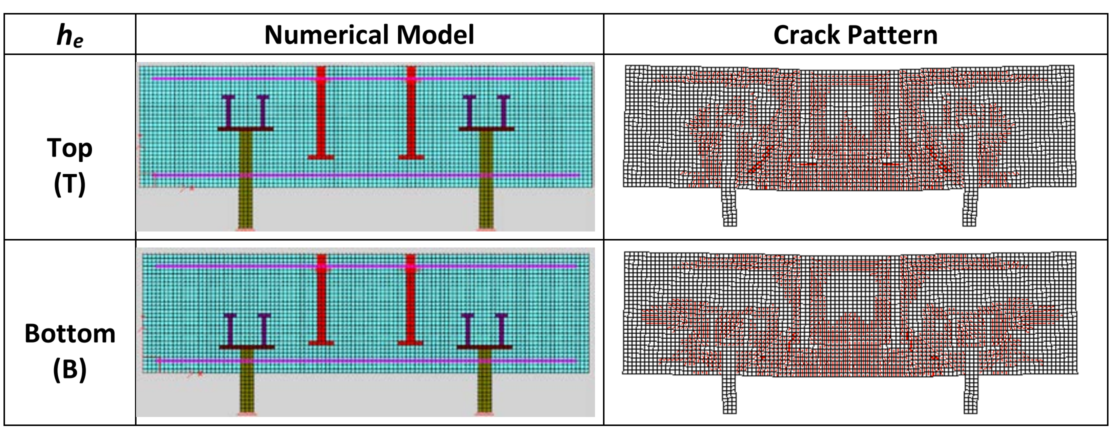

Figure C-53: Numerical model and crack pattern-studded bracket type-monotonic tension - *a/d* ratio = 1.11, ρ_x = 0.8%.

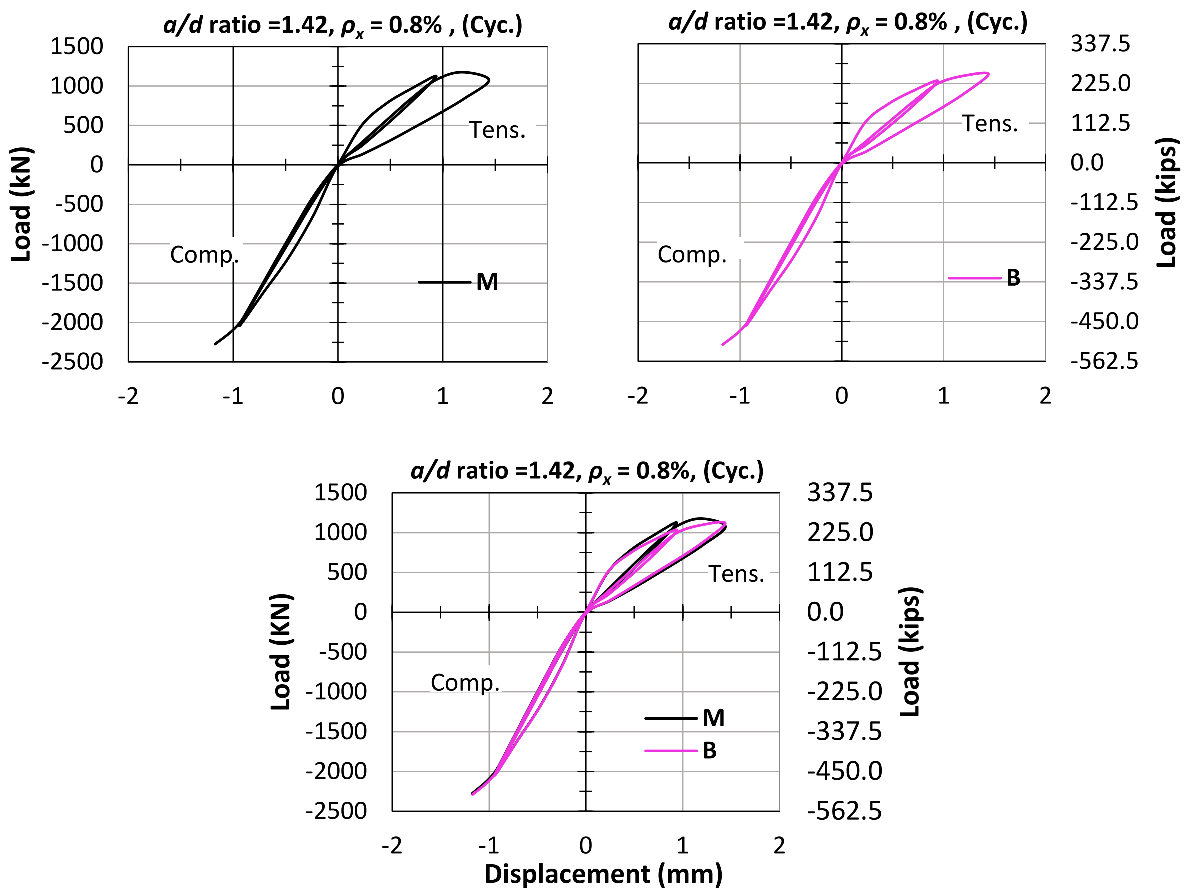

Figure C-54: Load-displacement response-studded bracket type-monotonic tension - *a/d* ratio = 1.11, ρ_x = 0.8%.

Table C-27: Comparison of numerical simulation-studded bracket type-monotonic tension - *a/d* ratio = 1.11, ρ_x = 0.8%.

h_e	*a/d* ratio	Tensile Component				Compression Component				Failure Mode	Bracket Inf.
		P_t (KN)	$P_{t-T/B}$	δ_t (mm)	$\delta_{t-T/B}$	P_t (KN)	$P_{c-T/B}$	δ_c (mm)	$\delta_{c-T/B}$		
T	1.11	1176	1.05	1.44	1.00	2275	0.99	1.17	1.00	Shear	None
B		1117		1.44		2291		1.17		Shear	None

Tensile component's result

- The load and the displacement capacities remain the same for all the h_e.

Compression component's result

- The load and the displacement capacities remain the same for all the h_e.

Appendix D Hand Calculation Details

Pile Cap Sizing by CRSI

Concrete Reinforcing Steel Institute (CRSI) publishes a design guide for pile system (CRSI 2015). Similar dimensions are used in this study. **Tables D-1** and **D-2** provide the pile cap parameters for 80 and 60-ton piles respectively.

Table D-1: Minimum rebar % for 80-Ton steel pile, f_c'=20.7MPa, f_y=414 MPa (CRSI)

No. of Piles	**Length mm (in)**	**Breadth mm (in)**	**Depth mm (in)**	**Minimum Steel mm^2 (in^2)**	**Rebar %**
2	1980 (77.95)	1070 (42.13)	965.2 (38)	2570 (3.98)	0.25

Table D-2: Minimum rebar % for 60-Ton steel pile, f_c'=20.7MPa, f_y=414 MPa (CRSI)

No. of Piles	**Length mm (in)**	**Breadth mm (in)**	**Depth mm (in)**	**Minimum Steel mm^2 (in^2)**	**Rebar %**
2	1680 (66.14)	765 (30.12)	1100 (43.31)	1690 (2.62)	0.2

Minimum Longitudinal Reinforcement for One-way Slabs

Width of a pile cap (B) = 800 mm
Depth of a pile cap (D) = 600 mm
Gross Area of pile cap (A_g) = $B \times D$ = 480000 mm^2
Minimum longitudinal reinforcement ($A_{s,min}$) = $0.002 \times A_g$ (ACI 318-19 Cl.7.6.1.1)
= 960 mm^2 (1.49in^2)
The minimum reinforcement is 0.2% of the gross sectional area for one-way slab.

Global Capacity Predictions using Design Codes

If the simulated results of the helical foundations are smaller than the global concrete foundation checks of the pile caps and the helical piles, it demonstrates that the connection capacity governs. The results from different prediction approaches (i.e., sectional method, one-way and two-way shear method, and STM) are compared with the simulation results to assess the influence of helical pile anchorages.

Diab's Foundation Specimens

Sectional Approach

The flexural capacity of the foundations is calculated according to ACI318-19. Detailed calculations are shown for the Diab foundation specimen T2. The h_e has no influence on the load capacity calculations in this method.

Width of a grade beam $(B) = 500\ mm$
Depth of a grade beam $(D) = 500\ mm$
Effective depth of the grade beam $(d) = 450\ mm$
Effective depth of the compression rebar $(d') = 50\ mm$
Area of tensile rebar $(A_s) = 800\ mm$
Area of compression rebar $(A'_s) = 400\ mm$
Compressive stress of concrete $(f'_c) = 30\ MPa$
Yield strength of steel $(f'_y) = 500\ MPa$
Elastic modulus of steel $(E_s) = 200\ GPa$
Yield strain of tension steel $(\varepsilon_s) = 2.07 \times 10^{-3}$
Yield strain of compression steel $(\varepsilon'_s) = 2.07 \times 10^{-3}$
Ultimate strain of concrete $(\varepsilon_u) = 3 \times 10^{-3}$
Neutral axis $(c) = ?$

$a = \beta \times c$ where, $\beta = 0.85$

Assuming the compressive bars don't yield, and the section is balanced,

$$C_c + C_s + T = 0 \tag{D-1}$$

where,
Compressive force of concrete $(C_c) = 0.85 \times f'_c \times B \times a = 10837.5 \times c$
Compressive strength of compression bar $(C_s) = A'_s \times 200000 \times \frac{0.003(c-50)}{c}$
Tensile strength of bar $(T) = A_s \times f'_y$

Substituting the values in **Equation D-1** and solving, we get
$c = 42\ mm\ (1.65")$, $a = 35.7\ mm\ (1.40")$

Checking the strain in the compression and the tension rebars
$\varepsilon'_s = \frac{(\varepsilon_u \times (c-d')}{c} = 0.6 \times 10^{-3} < 2.07 \times 10^{-3}$ (No yielding) [ok]
$\varepsilon_s = \frac{(\varepsilon_u \times (d-c))}{c} = 29 \times 10^{-3} < 2.07 \times 10^{-3}$ (Yielding) [ok]

Taking moment about extreme compression fiber,
Ultimate Moment $(M_u) = C_c \times a/2 + C_s \times d' + T \times d = 174\ kNm$

The foundation experience maximum moment in the mid-span.
The ultimate load capacity $(P_u) = 2 \times M/L = 436\ kN$
where,
L = span of beam = $800\ mm\ (31.5")$

One-Way and Two-Way Shear Approach

The one-way and two-way shear capacity of the foundations are calculated according to ACI 318-19.

One-way shear

The total nominal one-way shear capacity is the sum of the concrete and stirrup capacities, as per **Equation D-2**.

$$V_{n1} = V_{c1} + V_{s1} \quad \text{(D-2)}$$

where,
V_{n1} = Total nominal one-way shear capacity (in lbs)
V_{c1} = Concrete contribution to the one-way shear capacity (in lbs)
V_{s1} = Stirrups contribution to the one-way shear capacity (in lbs)
The contribution of nonprestressed normal-weight concrete is calculated as per **Equation D-3**.

$$V_{c1} = 2 \times \sqrt{f_c'} \times B \times d \quad \text{(D-3)}$$

where,
f'_c = Concrete compressive strength (in psi)
B = Out-of-plane beam width (in inches)
d = Beam depth (i.e. vertical distance from the top of the beam to the longitudinal reinforcement in inches)
The stirrups contribution is calculated as per **Equation D-4**.

$$V_{s1} = \frac{A_v \times f'_y \times d}{s} \quad \text{(D-4)}$$

where,
A_v = Total area of all vertical stirrup legs (in inches²)
f_y' = Yield strength of the stirrups (in psi)
d = Beam depth (in inches)
s = Stirrups spacing (in inches)

As an example, the calculation of one-way shear strength for the Diab foundations is carried out below. The values of all variables were converted to U.S. customary units to be used in the equations.

Using **Equation D-3** and **D-4**,
One-way shear capacity of concrete $(V_{c1}) = 2\sqrt{4351} \times 19.7 \times 17.7 = 46000\ lbs = 205\ kN$
One-way shear capacity of stirrups $(V_{s1}) = \frac{0.112 \times 76870 \times 17.7}{7.87} = 19363\ lbs = 86.2\ kN$
The total one-way shear capacity of the beam is calculated as **Equation D-2**.

$$V_{n1} = V_{c1} + V_{s1} = 65.36\ kips = 291\ kN$$

Load capacity $\left(P_{1-way\ shear}\right) = 2 \times V_{n1} = 131\ kips = 582\ kN$

Two-way shear

The total nominal two-way shear capacity is the sum of the concrete and stirrup capacities, as per **Equation D-5**.

$$V_{n2} = V_{c2} + V_{s2} \qquad \text{(D-5)}$$

where,
V_{n2} = Total nominal two-way shear capacity (in lbs)
V_{c2} = Concrete contribution to the two-way shear capacity (in lbs)
V_{s2} = Stirrups contribution to the two-way shear capacity (in lbs) which is same as **Equation D-4**.

The contribution of non-prestressed normal-weight concrete is calculated as the minimum of the three formulations in **Equation D-6**.

$$V_{c2} = \text{min. of} \begin{cases} \left(2 + \frac{4}{\beta}\right) \lambda \times \sqrt{f_c^{'}} \times b_o \times d \\ \left(\frac{\alpha_{s*} d}{B} + 2\right) \times \lambda \times \sqrt{f_c^{'}} \times b_o \times d \\ 4 \times \lambda \times \sqrt{f_c^{'}} \times b_o \times d \end{cases} \qquad \text{(D-6)}$$

where,
$\lambda = 1$ for normal-weight concrete
$\alpha s = 40$ for interior column
$b_o =$ Perimeter of a rectangular section d/2 away from the edges of the column

As an example, the calculation of two-way shear strength for foundation with the ρ_x of 0.4% is carried out below. The values of all variables are converted to U.S. customary units to be used in the equations.

The foundations do not have shear stirrups; therefore, the shear strength of the beams are the shear resistance of the concrete.

Using governing **Equation D-6**,

Two-way shear capacity $(V_{c2}) = 4 \times \sqrt{4351} \times 4 \times (1.77 + 17.7) \times 17.7 = 363709\ lbs = 1619\ kN$

Two-way shear capacity of stirrups $(V_{s2}) = \frac{0.112 \times 76870 \times 17.7}{7.87} = 19363\ lbs = 86.2\ kN$

The total one-way shear capacity of the beam is calculated as **Equation D-5**.

$$V_{n2} = V_{c2} + V_{s2} = 383\ kips = 1705\ kN$$

Load capacity $\left(P_{2-way\ shear}\right) = 2 \times V_{n2} = 766 kips = 3410\ kN$

Strut and Tie Method (STM)

Strut and Tie Modelling (STM) is a simple method which represents complex stress patterns with truss models. STM has compression struts and tension ties. Sectional method underestimates the capacity of deep beams such as pile caps and grade beam, to which Euler-Bernoulli theorem does not apply. The foundations in this study are all deep in nature and the STM should be used to estimate their capacities, not the sectional method as discussed above. The STM is valid only for the compression loading because concrete does take tension, a conservative assumption. Detailed calculations are shown for the Diab foundation specimen T2 as shown in **Fig D-1**.

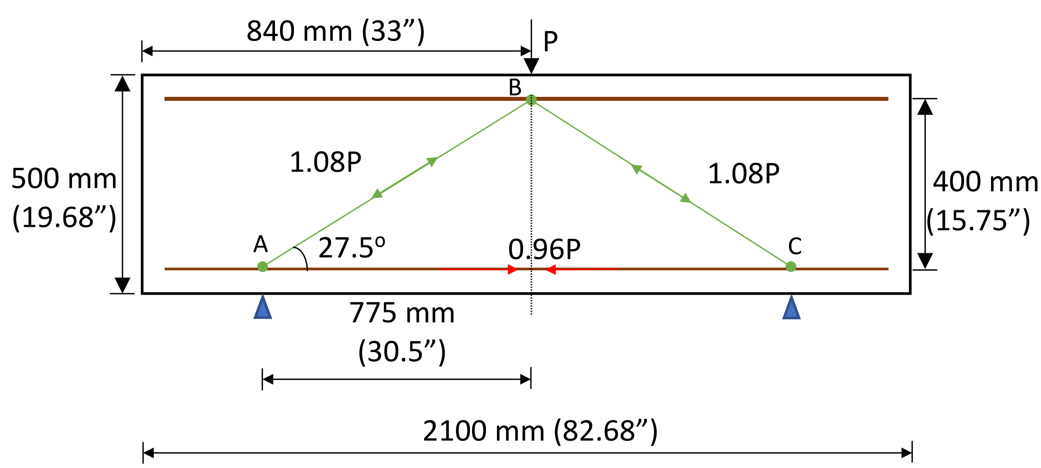

Figure D-1: Strut and Tie Model for one sample foundation.

Step 1: Find member forces

The truss member forces are drawn in **Fig D-1**. AB and BC members are in compression while AC member is in tension.

Step 2: Find the load capacity based on tie capacity
Using A23.3-14,
For tie AC,
$T = \emptyset_s \times A_s \times f'_y = 1 \times 800 \times 500/1000$
where, T = Tie capacity
A_s = Bottom reinforcement = $800\ mm^2$
$\emptyset_s = 1$ (Ultimate Capacity)
or, $0.96 \times P = 1 \times 800 \times 500/1000$
Therefore, $P = 416\ kN$

Step 3: Check nodal zone stresses

Node B – Bearing Check

Bearing strength at node B $(B_{max}) = 0.85 \times f'_c \times A_{bracket} = 0.85 \times 30 \times 165 \times 165$
$= 694\ kN > P$ [ok]
where,
A_{beam} = Cross-section of supporting beam = 260×260

Node A – Bearing Check

Bearing strength at node A $(B_{max}) = 0.75 \times f'_{\boldsymbol{c}} \times A_{brac} = 0.75 \times 20.7 \times 260 \times 260$
$= 1050\ kN > P/2$ [ok]
where,
A_{brac} = Cross-section of bracket = 260×260

Compressive concrete strength in the nodal region B $(s_{max}) = 0.75 \times f'c \times A_{sm}$

where,
$A_{sm} = Beam\ width \times (2 \times concrete\ cover) = 500 \times 140$

$s_{max} = 0.75 \times 30 \times 500 \times 140 = 1740\ kN > 0.96P$ [ok]

Step 4: Check inclined strut capacity

The strut capacity is equated to the strut member force to obtain the strut capacity, as shown in **Fig D-2** and the **Equations D-7**, **D-8** and **D-9**.

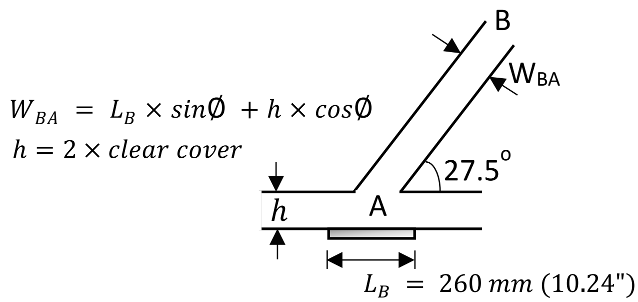

Figure D-2: Strut dimensions to calculate its capacity.

$$\varepsilon_s = \frac{T}{A_s \times E_s} \tag{D-7}$$

where,
ε_s = tensile strength
T = tie member force = $0.96 \times P$
A_s = area of tie reinforcement = $800\ mm^2$

$$\varepsilon_1 = \varepsilon_s + (\varepsilon_s + 2 \times 10^{-3}) \times \cot^2 27.5 \tag{D-8}$$

$$f_{cu} = \text{limiting compressive strength} = \frac{f_c'}{0.8+170\times\varepsilon_1} \tag{D-9}$$

$s_{max} = \emptyset_c \times A_{cu} \times f_{cu} = 1.08\ P$ (Strut capacity)

where,
$\emptyset_c$ = reduction factor = 1 for ultimate capacity
$A_{cu} = L_B \times W_{BA}$

By equating **Equations D-7**, **D-8** and **D-9**,
Shear load capacity $(P) = 754\ kN(179\ kips)$

The minimum of the tie and strut capacities govern the ultimate capacity with flexure or shear/compression failure mode, respectively. Since flexure capacity is governing, the load capacity of the beam is 413 kN (92.9 kips).

Foundations in this Study

Sectional Approach

The flexural capacity of the foundations are calculated according to ACI318-19. Detailed calculations are shown for the foundation beam with a ρ_x of 0.4%, and an *a/d* ratio of 1.42. The h_e has no influence on the load capacity calculations in this method.

Width of a pile cap $(B) = 800\ mm$
Depth of a pile cap $(D) = 600\ mm$
Effective depth of the pile cap $(d) = 530\ mm$
Effective depth of the compression rebar $(d') = 70\ mm$
Area of tensile rebar (A_s) = Area of compression rebar $(A'_s) = 1995\ mm$
Compressive stress of concrete $(f'_c) = 20.7\ MPa$
Yield strength of steel $(f'_y) = 414\ MPa$
Elastic modulus of steel $(E_s) = 200\ GPa$
Yield strain of tension steel $(\varepsilon_s) = 2.07 \times 10^{-3}$
Yield strain of compression steel $(\varepsilon'_s) = 2.07 \times 10^{-3}$
Ultimate strain of concrete $(\varepsilon_u) = 3 \times 10^{-3}$
Neutral axis $(c) = ?$

$a = \beta \times c$ where, $\beta = 0.85$

Assuming the compressive bars don't yield, and the section is balanced,

$$C_c + C_s + T = 0 \qquad \text{(D-10)}$$

where,
Compressive force of concrete $(C_c) = 0.85 \times f'_c \times B \times a = 11964.6 \times c$
Compressive strength of compression bar $(C_s) = A'_s \times 200000 \times \frac{0.003(c-70)}{c}$
Tensile strength of bar $(T) = A_s \times f'_y$

Substituting the values in **Equation D-10** and solving, we get
$c = 69.6\ mm\ (2.74")$, a= 59.2 mm (2.33")

Checking the strain in the compression and the tension rebars
$\varepsilon'_s = \frac{(\varepsilon_u \times (c-d'))}{c} = 0.1 \times 10^{-3} < 2.07 \times 10^{-3}$ (No yielding) [ok]
$\varepsilon_s = \frac{(\varepsilon_u \times (d-c))}{c} = 28 \times 10^{-3} < 2.07 \times 10^{-3}$ (Yielding) [ok]

Taking moment about extreme compression fiber,
Ultimate Moment $(M_u) = C_c \times a/2 + C_s \times d' + T \times d = 416\ kNm$

The foundation experience maximum moment in the mid-span.

The ultimate load capacity $(P_u) = 2 \times M/L = 1616\ kN$
where,
L = span of beam = $515\ mm\ (20.28")$

Table D-3 gives the moment capacity of the pile caps for 0.2, 0.4 and 0.8 ρ_x%.

Table D-3: Moment capacity for different ρ_x%

ρ_x%	**Moment kN.m (kips.ft)**
0.20	220 (162)
0.40	416 (307)
0.80	772 (570)

One-Way and Two-Way Shear Approach

The one-way and two-way shear capacity of the foundations are calculated according to ACI 318-19. Detailed calculations are shown for one of the foundations below as an example. The shear capacities of all the foundations are similar because the capacity depends on the compressive strength of concrete, width of the beam and the effective depth of the reinforcement, which are essentially the same for all the cases.

One-way shear

As an example, the calculation of one-way shear strength for the foundation in ρ_x of 0.4% is carried out below. The values of all variables were converted to U.S. customary units to be used in the equations.

The foundations do not have shear stirrups; therefore, the shear strength of the beams are from the shear resistance of the concrete.

Using **Equation D-2**,
One-way shear capacity $(V_{c1}) = 2\sqrt{3000} \times 31.5 \times 20.9 = 73292\ lbs = 327\ kN$
Load capacity $\left(P_{1-way\ shear}\right) = 2 \times V_{c1} = 146.80\ kips = 653\ kN$

Two-way shear

As an example, the calculation of two-way shear strength for foundation with the ρ_x of 0.4% is carried out below. The values of all variables are converted to U.S. customary units to be used in the equations.

The foundations do not have shear stirrups; therefore, the shear strength of the beams are the shear resistance of the concrete.

Using governing **Equation D-6**,

Two-way shear capacity $(V_{c2}) = 4 \times \sqrt{3000} \times 4 \times (19.69 + 20.89) \times 20.89 = 742901\ lbs$
$= 3305\ kN$

Load capacity $\left(P_{2-way\ shear}\right) = \ 2 \times V_{c2} \ = 1486 kips = 6610\ kN$

Strut and Tie Method (STM)

Strut and Tie Modelling (STM) is a simple method which represents complex stress patterns with truss models. STM has compression struts and tension ties. Sectional method underestimates the capacity of deep beams such as pile caps and grade beam, to which Euler-Bernoulli theorem does not apply. The foundations in this study are all deep in nature and the STM should be used to estimate their capacities, not the sectional method as discussed above. The STM is valid only for the compression loading because concrete does take tension, a conservative assumption. Detailed calculations are shown for the foundation with ρ_x of 0.4%, and *a/d* ratio of 1.42, as shown in **Fig D-3**.

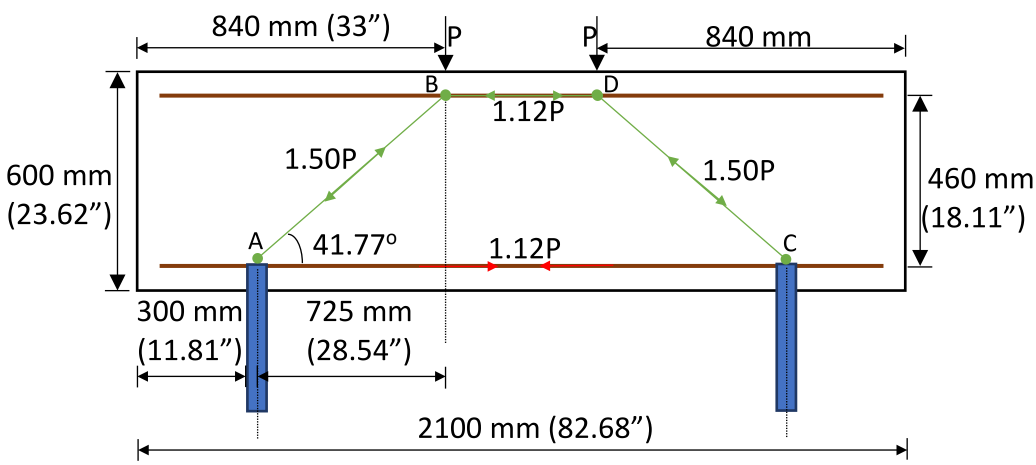

Figure D-3: Strut and Tie Model for one sample foundation.

<u>Step 1: Find member forces</u>

The truss member forces are drawn in **Fig D-3**. AB, BD and CD members are in compression while AC member is in tension.

<u>Step 2: Find the load capacity based on tie capacity</u>

Using A23.3-14,
For tie AC,
$T \ = \ \emptyset_s \times A_s \times f'_y \ = \ 1 \times 1995 \times 414/1000$
where, $T \ =$ Tie capacity
$A_s \ =$ Bottom reinforcement $= 1995\ mm^2$
$\emptyset_s \ = \ 1$ (Ultimate Capacity)
or, $1.12 \times P \ = \ 1 \times 1995 \times 414/1000$

Therefore, $P = 748\ kN$
Total load $(2P) = 1496\ kN(1486\ kips)$

<u>Step 3: Check nodal zone stresses</u>

Node B – Bearing Check

Bearing strength at node B $(B_{max}) = 0.85 \times f'_c \times A_{col} = 0.85 \times 20.7 \times 500 \times 500$
$= 4400\ kN > P$ [ok]

where,
A_{col} = Cross-section of column = 500×500

Compressive concrete strength in the nodal region B $(s_{max}) = 0.85 \times f'c \times A_{sm}$

where,
A_{sm} = Beam width × (2×concrete cover) = 800×140

$s_{max} = 0.85 \times 20.7 \times 800 \times 140 = 1507\ kN > 1.12P\ [ok]$

Node A – Bearing Check

Bearing strength at node A $(B_{max}) = 0.75 \times f'_{\boldsymbol{c}} \times A_{brac} = 0.75 \times 20.7 \times 260 \times 260$
$= 1050\ kN > P$ [ok]

where,
A_{brac} = Cross-section of bracket = 260×260

Compressive concrete strength in the nodal region A $(s_{max}) = 0.75 \times f'c \times A_{sm}$

where,
$A_{sm} = Beam\ width \times (2 \times concrete\ cover) = 800 \times 140$

$s_{max} = 0.75 \times 20.7 \times 800 \times 140 = 1740\ kN > 1.12P$ [ok]

<u>Step 4: Check inclined strut capacity</u>

The strut capacity is equated to the strut member force to obtain the strut capacity, as shown in **Fig D-4** and the **Equations D-7**, **D-8** and **D-9**.

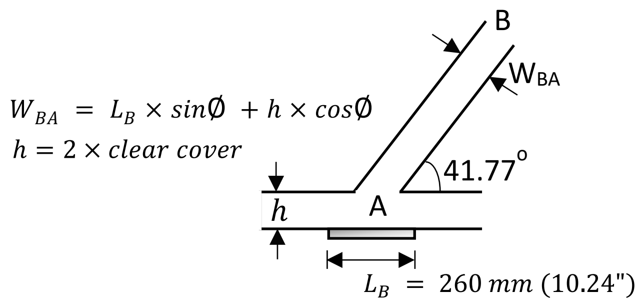

Figure D-4: Strut dimensions to calculate its capacity.

By equating **Equations D-7**, **D-8** and **D-9**,
Shear load capacity $(2P) = 1207\ kN(271.34\ kips)$

The minimum of the tie and strut capacities govern the ultimate capacity with flexure or shear/compression failure mode, respectively. Since strut capacity is governing, the load capacity of the beam is 1207 kN (271.34 kips).